State-of-Health (SoH) and State-of-Charge (SoC) Determination in Electrochemical Batteries and Cells Using Designed Perturbation Signals

By

Andrew James Fairweather

A thesis submitted for the Degree of Doctor of Philosophy in the department of

Electronic and Electrical Engineering, University of Sheffield

June 2015

Dedicated to Donna, William, Poppy and Adam

Summary

Optimisation of battery use and lifecycle is an important aspect of the application of batteries, as the environmental benefits of energy storage schemes can be negated by the carbon footprint of batteries being discarded due to perceived failure. Accurate battery state evaluation helps to reduce the quantity of these batteries entering the recycling chain before the end of their useful life, as in many cases equipment can operate with a reduced battery capabilities if this performance can be accurately reported.

The body of work presented here investigates novel methods of battery state evaluation utilising band-limited white noise in the form of Pseudo Random Binary Sequences. The work includes the building of dedicated test systems, the development of applied battery models, and the realisation of the developed techniques through deployable technology within an embedded environment.

A novel series of experiments were developed utilising a load based test scheme to demonstrate the applicability of the test technique, and batteries were profiled over a full operating temperature range and State-of-Charge (SoC), with equivalent circuit parameters obtained from the tests. New battery types (Ultrabatteries) were examined using these techniques, and compared with battery-supercapacitor parallel networks to investigate the parameters obtained for these systems, and their applicability to EV/HEV usage.

A charger based system was subsequently investigated which allowed the perturbation signal to be applied on line to the power stage in a conventional battery

charger. The benefits of this system were clearly demonstrated in that transitions in multi stage charge regimes could be detected, and clear indications of 100% SoC and indeed 0% SoC were obtained. Furthermore, no energy was wasted in this testing mode, as the test was integral to the charging process.

Combining the load and charge based systems led to a multimode/bipolar PRBS testing scheme which allowed analysis of the battery parameters outside of the frequency range of the previous tests. Using the bipolar test signal, the net effect on SoC was negligible and this therefore facilitated longer duration, with the lower frequency tests giving some insight into the values of the bulk capacity of the battery. Combined mode tests were developed, which, when used in conjunction with mean DC voltage acquisition during bipolar tests, facilitated indicators of battery SoC, State-of-Health (SoH), State-of-Function (SoF) and battery efficiency.

Acknowledgements

I would like to thank:

Professor David A. Stone and Dr. Martin P. Foster for their supervision of this work and their continual support.

Grant Ashley and Tim McCann, owners of VxI Power Ltd for their support and funding during the research, and allowing flexibility in my day job to facilitate the investigations and the presentation of the published work.

The Engineering and Physical Sciences Research Council for their funding over the course of this research.

My colleagues and friends at the University of Sheffield over the course of the PhD, James Holmes, Dan Rogers, Dan Schofield, Dan Gladwin, Huw Price and of course, Chi Tsang.

David Willey, my HND course tutor, who allowed me to step onto the first rung of the ladder.

My parents, Edgar and Rita Fairweather for instilling a work ethic without which the undertaking of this endeavour would have been impossible.

And finally, to my wife, Donna, and my children, William, Poppy and Adam for their support and eternal belief, even in my lowest moments.

"If you're going through hell, keep going."- Sir Winston Churchill

List of publications

1. Fairweather, A.J., M.P. Foster, and D.A. Stone, VRLA battery parameter identification using pseudo random binary sequences (PRBS), in IET Conference Publications. 2010. p. TU244.

2. Fairweather, A.J., M.P. Foster, and D.A. Stone, MLS Testing of VRLA Batteries using Pseudo Random Binary Sequences (PRBS), in EVS 25. 2010: Shenzhen, China. p. 405.

3. Fairweather, A.J., M.P. Foster, and D.A. Stone, Battery parameter identification with Pseudo Random Binary Sequence excitation (PRBS). Journal of Power Sources, 2011. 196(22): p. 9398-9406.

4. Fairweather, A.J., M.P. Foster, and D.A. Stone, State-of-Charge Indicators for VRLA Batteries Utilising Pseudo Random Binary Sequences (PRBS), in PCIM Europe 2011. 2011: Nuremberg, Germany.

5. Fairweather, A.J., M.P. Foster, and D.A. Stone, Modelling of VRLA batteries over operational temperature range using Pseudo Random Binary Sequences. Journal of Power Sources, 2012. 207(0): p. 56-59.

6. Fairweather, A.J., M.P. Foster, and D.A. Stone, MLS Testing of VRLA Batteries using Pseudo Random Binary Sequences (PRBS). World Electric Vehicle Association Journal, 2012. Vol 4: p. 405-412.

7. Fairweather, A.J., M.P. Foster, and D.A. Stone, State indicators for lead acid batteries utilising Pseudo Random Binary Sequences (PRBS) in All Energy 2012. 2012: Aberdeen, Scotland.

8. Fairweather, A.J., D.A. Stone, and M.P. Foster, Evaluation of UltraBattery™ performance in comparison with a battery-supercapacitor parallel network. Journal of Power Sources, 2013. 226(0): p. 191-201.

9. Fairweather, A.J., M.P. Foster, and D.A. Stone, Application of Maximum Length Sequences to Battery Charge Programming for Parameter Estimation in Lead-Acid Batteries, in PCIM Europe 2013. 2013: Nuremberg, Germany.

10. Fairweather, A.J., M.P. Foster, and D.A. Stone, Bipolar Mode Pseudo Random Binary Sequence Excitation for Parameter Estimation in Lead-Acid Batteries, in PCIM Asia. 2013: Shanghai, China.

Contents

Table of figures

List of Symbols

Δt	PRBS clock period		s
$Ah_{Charged}$	Capacity used to charge the battery		Ah
$Ah_{Discharged}$	Capacity of battery during discharge		Ah
C	electric capacitance		F
c_{av}	available capacity		Ah
c_{AS}	Capacity, Ampere-seconds		As
C_{Bulk}	Bulk capacitance		F
c_p	capacity according to Peukert equation		Ah
c_r	rated capacity of battery		Ah
$C_{Surface}$	Surface capacitance		F
E	electromotive force		V
f	excitation frequency		Hz
F	Faraday constant	9.64853×10^4	$Cmol^{-1}$
f_c	PRBS clock frequency		Hz
f_{max}	maximum frequency in PRBS bandwidth		Hz
f_{min}	minimum frequency in PRBS bandwidth		Hz
f_p	frequency of clock pulse		Hz
I	current		A
k	cell capacity constant for Peukert's equation		-
n	PRBS bit order		-
N	PRBS sequence length		-
R	gas constant	8.31441	$JK^{-1}mol^{-1}$

R_d	self-discharge resistance	Ω
R_{EC}	electrolyte resistance (charge)	Ω
R_{ED}	electrolyte resistance (discharge)	Ω
R_i	Ohmic internal resistance	Ω
R_t	charge transfer resistance	Ω
t	time	s
T	absolute temperature	K
t_d	discharge time	hrs
t_r	rated discharge time	hrs
T_s	overall time period of PRBS sequence	s
V	voltage	V
V_{EoD}	End of discharge voltage	V
V_{OCT}	Open circuit terminal voltage	V
WC_{bulk}	Energy stored within bulk capacitor	J
α	activity of component	-
η_{Batt}	Battery efficiency	-
τ	Time constant	s

Chapter 1. Introduction

1.1 Introduction

Electrochemical batteries and cells are a key enabling technology. The developments in mobile telephony, electric vehicles and portable computing would have been impossible without the complementary development of energy storage devices. Energy storage technology has however experienced somewhat of a coming of age in recent years as our energy demands and usage evolve and change, and we seek to address the energy needs within transport and power generation. Whilst lateral technologies such as flywheel energy storage [1] and pumped electrolyte (Vanadium Redox Batteries) [2, 3] are investigated, there remains a heavy focus on the development of electrochemical cells, and it is indeed an exciting time for those individuals involved in applied battery research.

The application of energy storage technologies is becoming increasingly diverse, and multiple charge sources (PV, Wind turbine, regenerative braking etc.) may present themselves to the energy storage system being used. Dynamic charge and discharge cycles, and wide operating temperature range generate the need for battery testing schemes which evaluate performance somewhat independent of any knowledge of the application. Furthermore, the domestic market for power generation is transitioning from grid tied inverters to self-consumption, with large growth seen in this market within Germany [4]. Self-consumption relies on an element of energy storage, unlike grid tie, and as such the battery system represents significant component of the ongoing cost of ownership of such systems [5]. As we enter this

next phase of distributed home generation, there will be much focus on the State-of-Function (SoF) of batteries – the ability of the battery to deliver performance in line with its design window of operation, as it is apparent that with accurate state reporting, the useful life of a battery pack can be extended, or as a minimum, the end-of-life of such a pack could be more accurately predicted, informing the financial and environmental costs of a battery system over its lifetime.

Electric vehicles are regarded as a recent innovation, but the Lohner Porsche with its hub wheel mounted motors was unveiled in 1900[6], and a year later a version was unveiled at the Paris motor show with a complementary internal combustion engine – the world's first hybrid vehicle [7]. This technology has had a recent revival with the moves to reduce emissions from vehicles, leading to growth in the EV/HEV marketplace we see today. This in turn has led to the development of large capacity (10 - 30kWh) Lithium Ion batteries [8], and the market for these batteries within the hybrid and electric vehicle market alone is predicted to be worth $8 billion by 2015 [9]. Government targets for renewable energy adoption [10] have driven the emergence of distributed power generation leading to requirements for large capacity energy storage to buffer Photo Voltaic (PV) installations. 1MW + Lithium Ion systems are already being built [11] to address this need, and a current project under development by the University of Sheffield is concerned with a 2MW system for grid reinforcement [12]. Energy storage is therefore being more widely applied than ever before, and batteries and cells of all chemistries present ongoing problems in terms of measurement of State-of-Function (SoF), State-of-Health and State-of-Charge (SoC) of the battery or cell. These parameters are interrelated, with State-of-Function being

affected by State-of-Health, temperature and State-of-Charge. State-of-Health describes the absolute health of the battery within standard operating conditions, and declining SoH is characterised by loss of capacity or inability to deliver current. State-of-Charge relates to the available battery capacity at any time and is only affected by the level of charge or discharge applied to the battery or cell, and equates to the "fuel tank" of the battery.

The electrochemical "fuel gauge" is notoriously difficult to realise, due to the largely non-linear nature of cell behaviour, with the complex processes within batteries leading to differences in available capacity dependent on magnitude of load, ambient temperature and age of the batteries themselves. Measuring and modelling of these contributing factors is complex, and any method which can obtain a direct value for the energy remaining in a given cell or battery at a specific time is therefore very attractive. Methods of SoC reporting have been used which employ measurement of terminal voltage [13], and this can be effective if the load is constant, but typically the terminal voltage related SoC characteristic requires implementation of an algorithm to allow for cell degradation, and is difficult to implement with a dynamic load/charge profile, (such as is the case in EV/HEV applications). Existing methods involving Coulomb counting have been successful in consumer electronics , but are often subject to periodic recalibration to maintain accuracy [14]. Again, these methods can become ineffective with declining SoH, as the battery degradation can manifest itself in different ways dependent on the nature of the application, and how the powered device has been used during the lifetime of the battery (elevated temperature, high number of cycles, depth of discharge etc.). The cost of large

capacity (10-30kWh) battery packs is driving the need for near 100% utilisation, and an aged battery pack with a 30% capacity reduction is still usable if the SoF can be accurately reported.

Environmental concerns will continually be a focus within applied battery technology, and the potential environmental benefits of EVs and distributed micro generation and storage, will need to be weighed against the consumption of raw materials in battery production and the consequential waste introduced into the recycling loop. The recycling infrastructure for Lithium based chemistries is immature and open loop, with much of the recycled material being used for other purposes (e.g. construction feed material). Research into worldwide lithium reserves indicates that at the projected rate of consumption these reserves could be expended by the year 2100 [15]. It therefore follows that, in conjunction with establishing a closed loop recycling process, the prudent use of batteries to end of life – generally a reduction in capacity to 80% or less [16, 17], is clearly important. As such, new industries are being developed to support the increased reuse of batteries, and much of this activity will concentrate on the EV marketplace, and the reuse of these batteries either in EVs, or in identified opportunities to utilise the remaining function in the batteries for a different application. Already, ABB and General motors are collaborating on a project to reuse EV battery packs in smart grid applications [18], whilst BMW and Vattenfall have a research partnership for similar reuse in power cache applications for fast charge stations and grid stabilisation [19].

The challenges therefore which face the efficient use of batteries and cells throughout their useful life centre on improved methods for establishing battery state, and

developing methods which can dynamically assess the battery condition accurately, irrespective of ambient temperature, rate of charge and rate of discharge.

The "holy grail" in terms of battery testing is a system which can conduct a measurement whilst online to accurately report the overall state of the battery or cell without prior knowledge of its use or age. This work seeks to answer questions regarding measurement of SoH, SoC and SoF for batteries and cells using non-intrusive methods of analysis, in order to develop cross-chemistry techniques which can be used to develop on-line battery fuel-gauge systems.

1.2 Motivation

The motivation for this work was focussed on investigating novel battery state evaluation and testing requirements that may fall outside of the capabilities of existing schemes.

Specifically, the developed technology must add to the pool of knowledge, bringing a new approach to the problem of examining battery state, which may be used alone, or within a hybrid system in conjunction with existing schemes.

Further to this the developed tests should be demonstrated to be useful over a range of battery operating conditions likely to be encountered in application.

The research undertaken within this work was partnered with industry, and as such sufficient development of the techniques examined to allow a first generation implementation of the technology within a commercial product would be a desired output from the research.

1.3 Literature search and background reading

A review of published work was carried out which focused on the current state of battery technology, which follows in chapter 2, and concentrated on the main commercially available chemistries, and those under development. Secondly, current research into methods for SoC, SoH and SoF of these chemistries was examined, with a view to establishing the novelty of the proposed research, and its potential contribution to the pool of knowledge. Investigation of commercially available battery management systems further informed the current state of the technology. In addition to this, as areas of novelty emerged, these were examined for previous research, notably frequency domain analysis of batteries and cells. Library resources within the University of Sheffield, and its affiliated libraries were used for both hardcopy and electronic sources. Further on-line resources were used, notably IEEExplore, Elsevier (Journal of Power Sources), electronic resources from battery manufacturers, and those of organisations researching and developing new battery technologies.

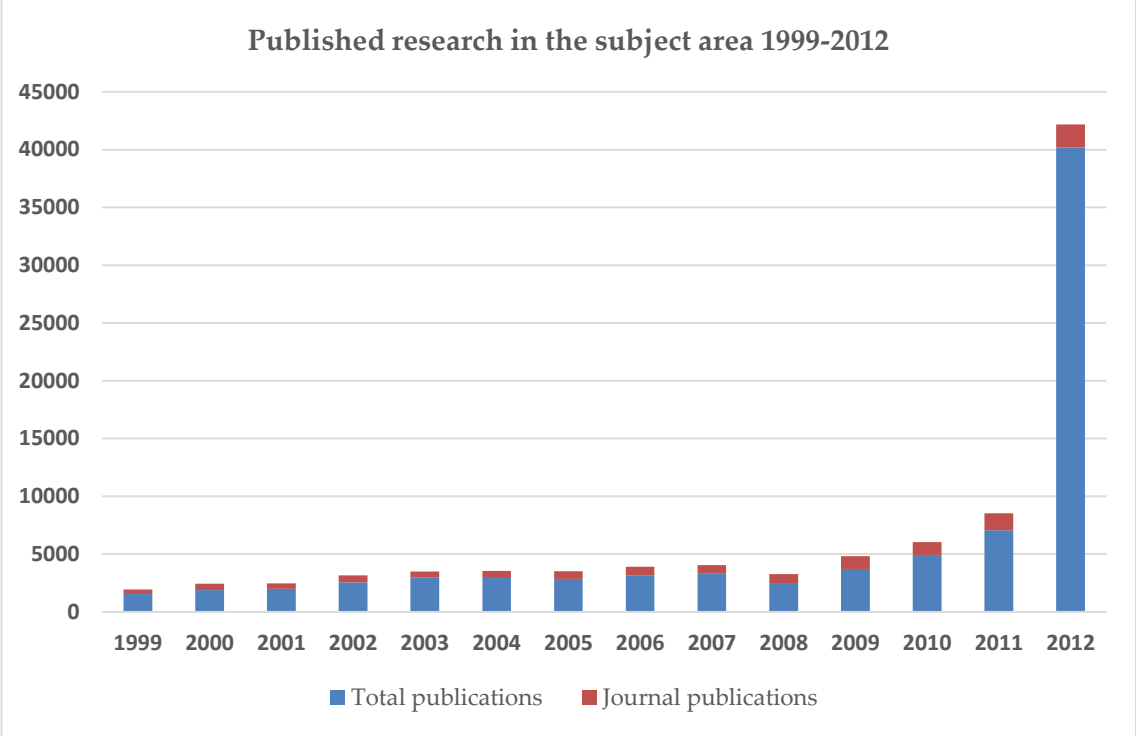

Figure 1. Published research activity within battery and energy storage, 1999-2012

The chart shown in Figure 1 illustrates the timeliness and validity of the research. Using Scopus as a search tool for published work in the subject area [20], searches were carried out using the following keywords:

Battery, storage battery, lithium ion, lithium ion battery, lithium electrode, energy storage system, storage system, charging, electrochemical, battery system, electrolyte, battery storage, cycle life, fuel cell, storage technology, wind power, energy storage li ion battery, lithium battery, battery, cell, electric, grid electrodes, lead acid battery, rechargeable battery, battery systems, cathode, discharging, electric vehicle.

Within the disciplines:

Materials Science, Energy, Engineering, Chemistry, Chemical Engineering and Environmental Science.

It is clear from the observed trends on the chart that there is much focus on energy storage within the research community and that the topic is current. Year on year an upward trend is observed, with the notable exception of 2008, which may be linked to the global economic situation that arose in that year. The 2009-2012 trend shows that the research community is within a period of exponential growth in this area, and certainly the growth in the use of electric vehicles (as seen in Figure 2) will have had a direct relation to this trend [21].

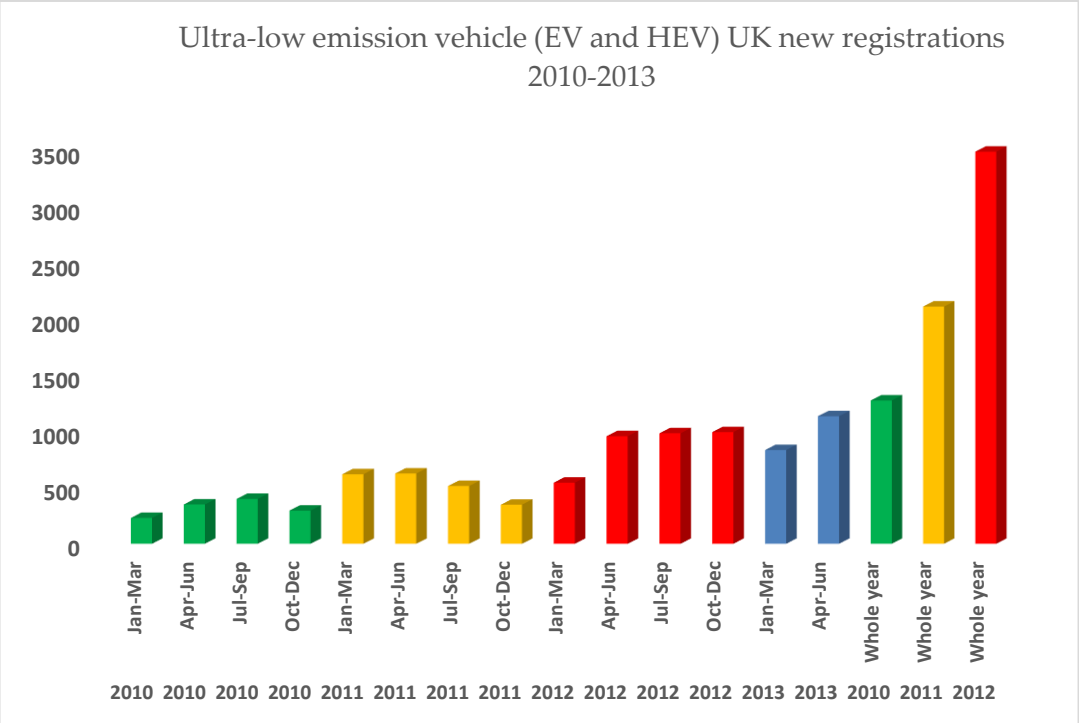

Figure 2. UK Low emission vehicle registrations, 2010-2013

1.4 Outstanding technical challenges

In designing and testing new methods of battery state evaluation, the applicability of the technology over operational conditions that are likely to be encountered by the energy storage system must be understood. Research was therefore needed that

characterised the test batteries against existing test methods, and developed models which could be used to report battery state.

The predominant chemistry that was examined in the body of this work was Lead-Acid. The rationale behind this is that an extensive body of prior research relating to Lead-Acid batteries and cells is available, allowing techniques to be developed, to be subsequently applied to other chemistries. Furthermore the author's prior experience within industry is within the field of Lead-Acid battery charging and testing methods, and therefore existing testing schemes are well understood.

The objective of this work was to develop systems to investigate SoH, SoC and SoF independent of prevailing conditions, and without any need for prior knowledge of the battery state. Therefore the thesis is concerned with:

- Exploring the use of Pseudo Random Binary Sequences as a perturbation signal for battery characterisation.
- The development of test systems which investigate battery state evaluation methods over the operational envelope of the test batteries.
- The establishing of models for the test batteries based on these experiments allowing correlations to be made between battery state and equivalent circuit components.
- The examination of different modes of test for the developed technology, and trends across these methods that facilitate state identification.
- The realisation of this technology in a deployable format which could either be incorporated in a charging system, test instrument or intelligent battery.

The work presented in the following chapters addressed these challenges and resulted in the development of a self-contained battery evaluation system within an embedded environment.

Chapter 2 introduces the competing electrochemistries which currently span the application areas considered, notably HEV, EV, UPS, micro generation and other static applications. Chapter 3 examines problems with batteries in application, associated with rate, temperature and chemical inertia – factors which define the battery test scheme accuracy and applicability. Chapter 4 investigates existing methods of battery testing and evaluation, and presents Pseudo Random Binary Sequences (PRBS) as an excitation signal for the investigations.

Chapter 5 outlines the early work in defining the PRBS test technique in the discharge (load) mode.

Chapter 6 builds on this by introducing the "charge" mode PRBS technique, which is integral to the system battery charger. Chapter 7 combines the two techniques from chapters 5 and 6 to present a bipolar charge/discharge test arrangement, and the benefits of this over the previous schemes are demonstrated. Chapter 8 investigates variations in battery parameters with SoC using the PRBS load technique, and further to this temperature effects are examined in chapter 9. Chapter 10 applies the developed testing to an UltraBattery, and compares this with a parallel battery/supercapacitor combination.

Chapter 11 examines a battery driven to accelerated failure to give an insight into battery parameters as they change over life, and ultimately to end of use. Chapter 12 brings in the applied technology to a product and demonstrates a scheme optimised

for a Microchip dsPIC within an embedded environment. Chapter 13 draws conclusions from the research and suggests opportunities for further work.

1.5 Contribution

The majority of the work presented in this thesis has been presented internationally within learned journals and international conferences, with a further chapter being the subject of a commercial development project, partnered with industry. As such the work has been subject to extensive peer review throughout, and has been demonstrated as a commercially viable technology.

The specific investigations carried out have led to characterisation of energy storage networks using Pseudo Random Binary Sequences, encompassing Lead-Acid, batteries, hybridised batteries (Ultrabatteries) and parallel battery-supercapacitor networks.

The PRBS battery test technique has been explored by examining the charge, discharge and bipolar PRBS test techniques for batteries, and showing that each technique has applicability in identifying SoC, SoH and SoF.

The PRBS charge technique has been developed in the voltage mode to detect SoC and propose its operation as a means for charge stage transition in multi-stage battery chargers.

An overview of the chapters within the thesis, the output from the research, and the connection with the published work are shown in Figure 3.

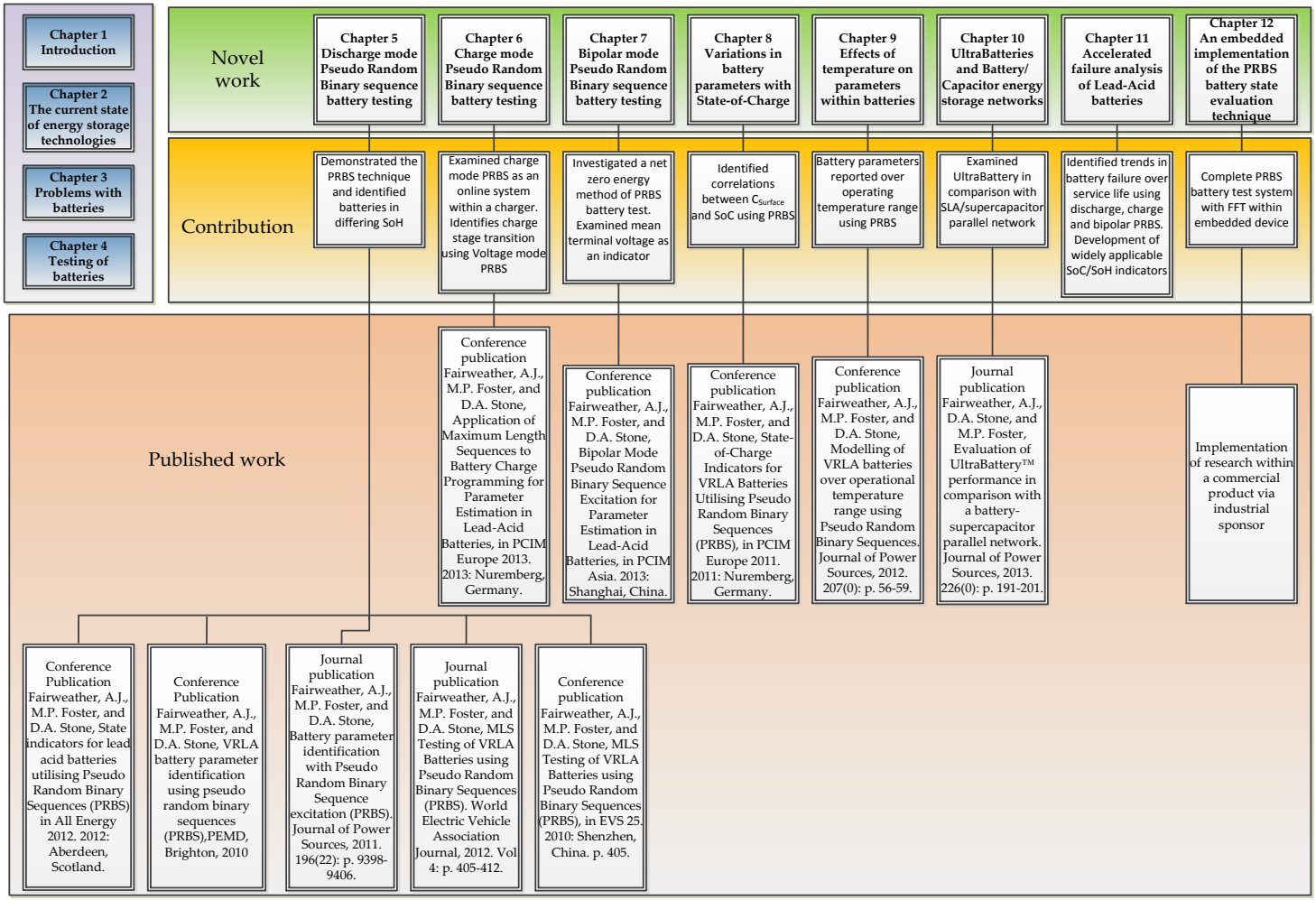

Figure 3. Summary of thesis structure with contribution to the research community

Chapter 2. The current state of energy storage technologies

2.1 Introduction

A review of published work was carried out which focused on the current state of energy storage technology, across commercially available chemistries and those under development.

Library resources within the University of Sheffield, and its affiliated libraries were used for both hardcopy and electronic sources. Further on-line resources were used, notably IEEExplore, Elsevier (Journal of Power Sources), electronic resources from battery manufacturers, and those of organisations researching and developing new battery technologies.

The following section outlines in a concise manner the state of cell and battery technology at the time of this report. The content is based on research into commercially available technologies, experience of the author in using the technologies within a career in research and development, international environmental directives affecting the future of chemistry types, and the pool of current research into new energy storage technologies. Fine detail regarding the chemical composition of the cell types is avoided except where relevant to the application of the cell types, or where classifying the cell family.

2.2 Voltage limits and charging terminology

All battery and cell types have voltage windows of operation for both charge and discharge, and End-of-Discharge (EoD) voltages will be provide by the battery or cell manufacturer. Discharging beyond these limits can permanently damage the battery, and for example, a 12V VRLA battery that has been discharged beyond 1.3 Volts per cell/7.8V (20°C) will experience sulphation and may become unrecoverable [16, 17].

Upper voltage limits for charging are defined by individual chemistry, and are related to the active material in the cell. Similarly charge current recommendations will be provided and generally these are stated as a multiple of the rated capacity (c_r) in Ah.

Constant voltage, float and trickle charging are often used as interchangeable terms, but differ in some aspect. Constant voltage charging can be used for all battery chemistries, but may not be the optimum method for energy transfer into the battery for all types, and may have lifetime limiting effects with some chemistries. The "float" voltage for a lead acid battery is the voltage at which the battery can accept charge, at the defined temperature, and this charge can be applied indefinitely without damage to the battery. A "float" charge is therefore a constant voltage charge profile, and this is often used in UPS systems and battery backed equipment. The charger will be current limited, so initially the charger may be operating in a constant current mode, dependent on the initial battery state. Trickle charge generally refers to a float charge voltage being applied to a battery at low charge current – typically maintaining the battery in a charged state, and by default occurs at the end of a float charge.

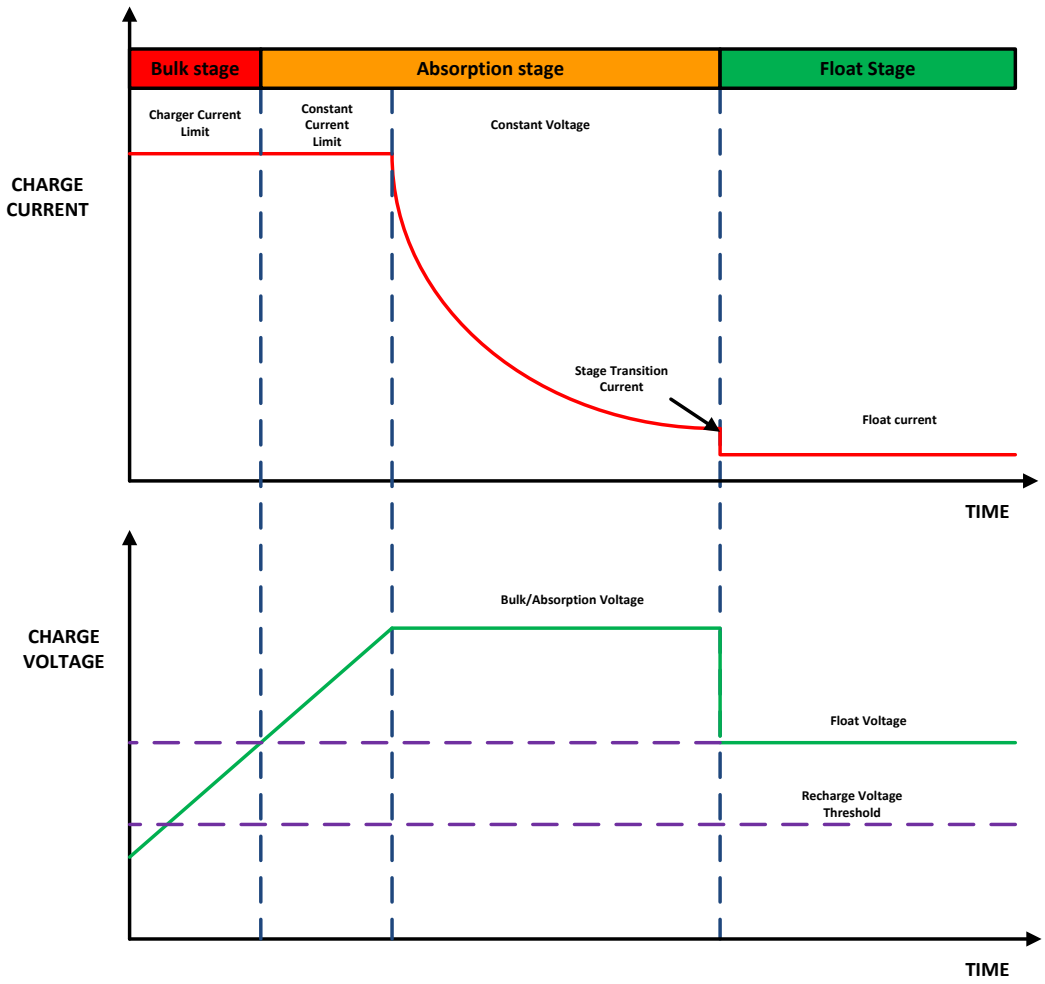

Figure 4. Three-stage charge profile used in Lead-Acid battery charging

Multi stage charge profiles are used for Lead-Acid batteries, and the voltages and currents employed are dependent on the cell type (flooded or VRLA) and the application (cyclic or standby). Figure 4 shows a typical three stage charge profile used in commercial Lead-Acid battery charging [22, 23]. The charge voltage shown is a linear representation of the cycle for clarity. During the bulk stage the charge is in current limit constantly, imparting the "bulk" energy of the charge into the battery, and as the terminal voltage of the battery approaches the bulk/absorption voltage,

the charge current reduces accordingly. As the charge current continues to fall, the stage transition current limit will be met – this is the point at which the majority of charge has been accepted by the battery or cell, and at this point the charger output voltage reverts to the float level, which can be applied indefinitely to the battery. Batteries used in cyclic applications will generally be charged at a higher voltage than those used in standby systems, and flooded batteries may have a periodic equalisation charge to improve battery performance and prevent stratification of the electrolyte.

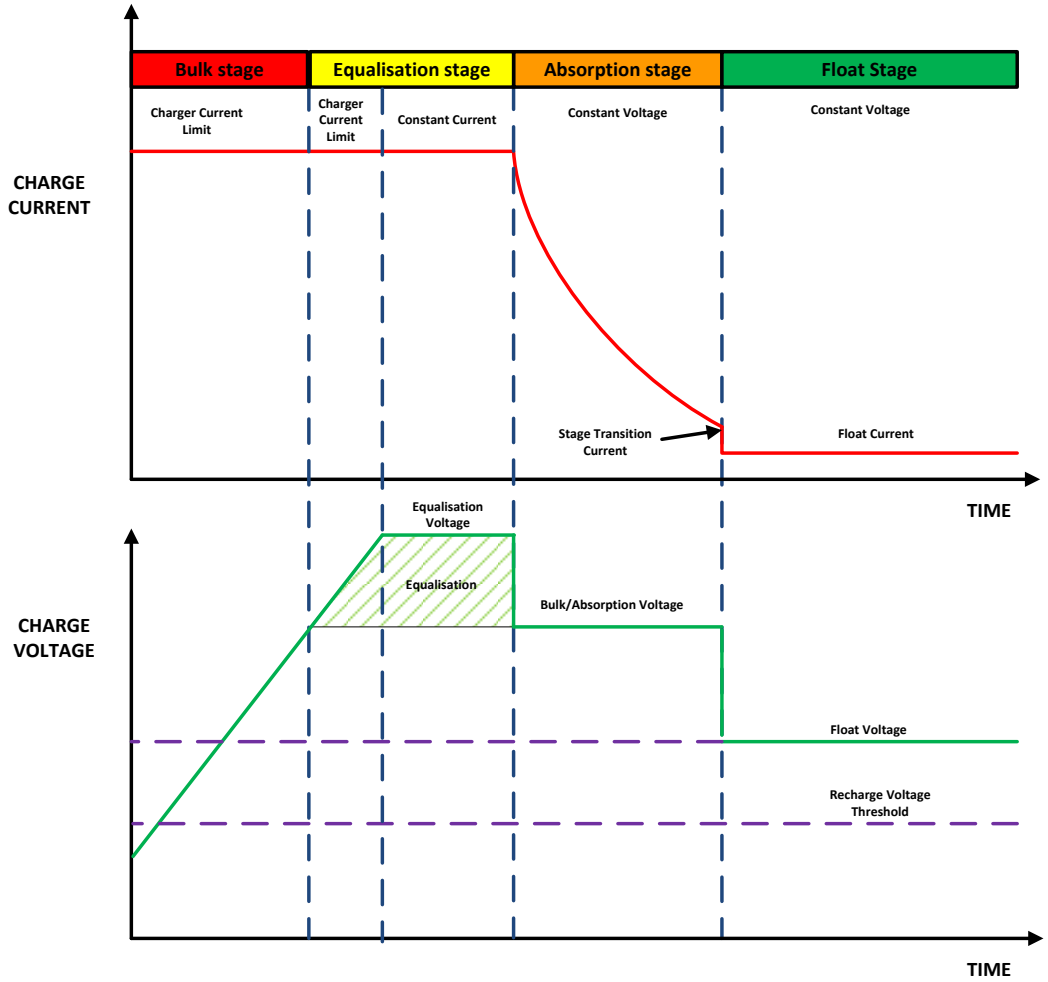

Figure 5. Lead-Acid battery charge profile with equalisation

Figure 5 shows a 4 stage charge profile with equalisation [22, 23]. The stages used are the same as for a three stage charge profile, with an additional, elevated voltage charge phase used in cell balancing. During the equalisation phase, the cells are subject to this increased voltage, which leads to gassing and agitation of the electrolyte. The stage is usually timed, or alternatively, where individual cell voltages can be measured, the end point can be defined by balance being attained using this measurement, or specific gravity measurements can be used. Cell balance is defined when cells are within a 0.4% voltage window or 0.005 points in specific gravity [22, 23].

Equalisation stages are not generally used on every charge cycle and applied periodically dependent on the application. Cells outside of an overall 300mV window within a 12V battery, or have a range of specific gravity measurement of greater than 0.030 points require an equalisation to be carried out [22, 23].

Table 1. Summarises typical voltage limits for Lead-Acid battery charge at 20°C [16, 17, 22-24], along with bulk charge current rates and stage transition currents.

Table 1. Typical Voltage and current levels for Lead-Acid battery and cell charge at 20°C

(Voltages per cell with corresponding 12V battery voltage in brackets)

Technology	Recharge voltage threshold* V	Float Voltage V	Bulk/ Absorption Voltage V	Equalisation Voltage V	Bulk charge current (fraction of rated capacity) A	Stage transition current (fraction of rated capacity) A
Flooded [16, 22, 23]	1.920 (11.52)	2.25 (13.50)	2.470 (14.82)	2.700 (16.20)	0.35	0.03
VRLA [16, 17]	1.920 (11.52)	2.275 (13.65)	2.450 (14.70)	-	0.25	0.05
Spiral Wound [16, 24]	2.00 (12.0)	2.275 (13.65)	2.450 (14.70)	-	0.4	0.05

*open circuit voltage, initial, or steady-state after discharge.

Constant current charging with end point detection is most often used with NiCd, NiMH and Lithium chemistries, and under these conditions a constant current is applied to the battery or cell until an end of charge event is detected, commonly an increase in cell temperature, or for NiMh specifically, a characteristic drop in cell voltage (Figure 6) [25].

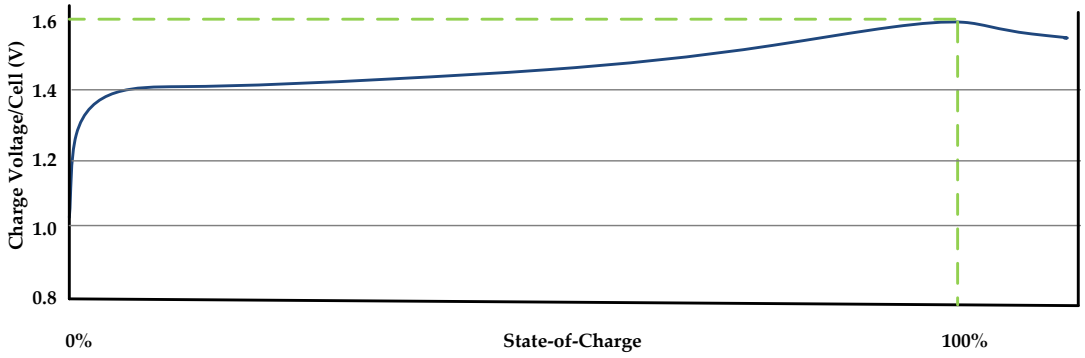

Figure 6. NiMh charge characteristics showing charge end point (20°C)

Temperature compensated charging is used across several battery chemistries, but came to the fore with the invention of Valve Regulated Lead-Acid (VRLA) batteries, where the internal gas recombination processes required that the charging be closely controlled, in order that overcharge does not occur (consuming the electrolyte) and ensuring that full capacity is reached at low temperature. This charging method is equally applicable to flooded cells, despite them being more tolerant of overcharge. Typically, the charge voltage will be specified at 20°C and deviations from this ambient temperature require a 3mV/°C adjustment in the charger voltage with a negative coefficient [17, 24]. The type of charging scheme employed will depend to

some extent on the application, and the Depth of Discharge (DoD) experienced by the battery or cell during each cycle in use.

.

2.3 Lead-Acid

Lead-Acid batteries are a mature technology, which have been in widespread use for many years. The technology was developed by Gaston Planté in 1859 [16], and since that time the chemistry has become extremely widespread in use. Predominately used in starting, lighting and ignition (SLI) for internal combustions engines, the batteries also find widespread employment in electric vehicles, renewable energy, and battery supported systems such as uninterruptible power supplies.

Figure 7. An unused radio 2V 70Ah "accumulator", manufactured by Exide circa 1930-1940 (photograph by author)

Lead-Acid batteries first delivered electricity to the populous when the early electrical appliances became available to the consumer. Lead-Acid "accumulators" (Figure 7) were delivered to domestic premises in order to power the valve radio sets, and the "Accumulator man" would take away the used battery for recharging, exchanging it with a charged unit. This early electric distribution method allowed the first steps in growth within consumer electronics, and this fuelled demand for other electrical appliances, which in turn led to the growth of the electrical distribution network to domestic customers.

The chemistry benefits from a widespread and mature recycling network, which leads to efficient reuse of the constituent materials, predominantly the lead itself.

With more than 98% of all battery lead being recycled [26] Lead-Acid batteries arguably represent the most sustainable incarnation of energy storage within existing technologies. Where the batteries score highly, apart from the mature recycling infrastructure, is that they still represent the best value for money in terms of cost of ownership of all of the current battery technologies, with a well understood cost per Kwh and life cycle cost [5]. Where the technology suffers is energy density as compared to the recent developments in the lithium based chemistries, and as such Lead-Acid batteries have been designed out of the majority of portable equipment. The technology is split fundamentally between the traditional flooded cells (Figure 8a) [23], and the Valve Regulated Lead-Acid (VRLA) battery (Figure 8b) [27], often incorrectly termed "sealed lead-acid".

Figure 8(a) Flooded cyclic Lead-Acid battery and (b) Typical VRLA battery for standby applications

(Photographs courtesy Trojan batteries and Yuasa Europe respectively)

Flooded cells are still in widespread used in Starting, Lighting and Ignition (SLI), traction, and stationary energy storage applications, and offer tolerance to high charge and discharge rates.

For all types of Lead-Acid batteries, available capacity is subject to prevailing conditions and this is demonstrated in the way the batteries are specified, with VRLA types typically having rated capacity quoted for a 20 Hr discharge rate [17]. Similarly, reduced temperature effects capacity, and most Lead-Acid batteries are almost unusable at -20°C. This and other problems associated with application of batteries and their performance are given a thorough treatment in chapter 3.

Charging of Lead-Acid batteries is fairly straightforward, and particularly so for flooded cells. Three-stage charging regimes are generally used for these batteries, using an elevated voltage per cell (equalisation) periodically applied to mitigate stratification of the electrolyte.

The charging process for VRLA batteries is slightly different, with similar charge voltages, although requiring closer control, and without an elevated charge voltage phase. The internal recombination processes involved in these batteries mean that temperature compensated battery charging is generally employed to attain this close

control, and although rapid charging can be carried out, these batteries are intolerant of overcharge, and some form of end-point-detection, or timed charge must be used for increased charge rates.

2.3.1 Flooded Lead-Acid

Flooded Lead-Acid batteries have dominated the automotive SLI marketplace from its inception. The ability of these batteries to deliver very high currents and their tolerance of rapid charge aligns them very well with electric traction applications and they have experienced widespread use in the first generation of widely adopted EVs (mainly utility vehicles) [28]. The main areas of current research within flooded batteries have concentrated on improved plate (grid) construction, seeking to maximise active area with the batteries and reduce corrosion [29]. Traditionally the lead in the plates have been alloyed with antimony by 5 to 12% to reduce brittleness, but modern alloys reduce this content to 1.5 to 2%, which improves water consumption and therefore reduces maintenance of the batteries in service. Other elements have been introduced, such as tin, to mitigate the reduction in antimony, and fractions of silver, cobalt and selenium have been introduced to improve resistance to corrosion [16]. "Calcium grid" is an often used term in modern day Lead-Acid batteries and this umbrella covers several alloys used in grid production with varying percentages of calcium metal. These alloys have improved manufacturability, which in itself facilitates more elaborate plate design, improved overall performance and extended life. Further research is being carried to address the

changing needs of automotive batteries in reduced emission applications [30] as conventional ICE vehicles incorporate start-stop technology and regeneration during braking from the vehicle alternator. Much of this research however has been refocused on to VRLA and AGM technology as vehicle batteries are migrating to these types.

2.3.2 Valve Regulated Lead-Acid (VRLA)

Valve Regulated Lead-Acid batteries were developed in the late 1960s as a non-spillable alternative technology to conventional flooded Lead-Acid batteries, and are split predominantly between "Gel" and "AGM" types. The main differences between the sibling VRLA technologies relates to the way in which the electrolyte is immobilised. In AGM batteries an absorbent glass mat is employed whereas the gel types use silica to form a thixotropic gel with the electrolyte. "Valve Regulated" refers to the integral pressure relief valve within the cell, which allows venting of excess gas should the internal pressure of the cell exceed a recognised maximum. Gas recombination is utilised to reduce the volume of gas liberated from the cell, and this is facilitated by the close proximity of the plates in these types of cells. (In flooded types this gas escapes from the cell to the atmosphere more readily). The reactions involved in this oxygen recombination at the negative plate are as follows:

$$Pb + HSO_4^- + H^+ + \tfrac{1}{2} O_2 \underset{\text{Charge}}{\overset{\text{Discharge}}{\rightleftharpoons}} PbSO_4 + H_2O \qquad (1)$$

When the cell is recharged, particles of lead sulphate are converted to sponge lead at the negative electrode and lead oxide at the positive electrode. As the cell approaches complete recharge, the majority of these conversion reactions have occurred and overcharge reactions begin. For conventional flooded cells this results in the production of hydrogen and oxygen gas, and virtually all of the evolved gas escapes from the cell. In VRLA batteries, the closely spaced plates are separated by a glass mat. This mat allows the cell to be filled with an optimal quantity of electrolyte, which coupled with the proximity to the plate itself facilitates recombination of the majority of evolved gases, if charged at recommended rates [31].

Commercially available VRLA batteries are available in a range of industry standard form factors, in the sub 100Ah capacity range, being used for applications ranging from uninterruptible power supplies to low level EV (golf carts etc.). Power density in VRLA batteries is similar to flooded types, leading to them appearing less attractive to the Lithium chemistries for many applications.

Despite this current focus on the Lithium chemistries, research in VRLA batteries remains popular as they displace flooded batteries in SLI use [32], and offer potential as a cost competitive alternative to Lithium chemistries in HEV/EV applications [33, 34]. Atraverda have developed a bipolar VRLA technology, which offers an increased energy density, reduced internal impedance, and due to the plate design, uniform current distribution over the plate [35]. The addition of carbon in the negative plate has also led to

performance improvements in VRLA batteries and several investigations are ongoing in this area [36-38].

2.3.3 Spiral wound VRLA

Spiral wound VRLA cells offer an alternative approach to conventional VRLA batteries in that the "plates" comprise spiral wound lead foils separated by an AGM suspended electrolyte. It is interesting to note that spiral wound cells represent the first generation in AGM technology, with conventional plate designs following afterwards [39]. This construction leads to the cells having a high effective area allowing high discharge rates. As such batteries constructed from spiral wound cells (Figure 9) find applications in motorsport, in starting of high compression engines [40].

Figure 9. Spiral wound Lead-Acid SLI battery for motorsport applications (image courtesy Optima batteries)

This high effective area also offers advantages with low temperature operation, and typically spiral wound cells outperform conventional VRLA batteries

under these conditions [17, 24]. The technology has been evaluated for HEV use, and enhanced spiral wound cells were developed in conjunction with Enersys, employing terminals duplicated at both ends of the cell plates, allowing an even distribution of temperature in the cell during high rate charge and discharge. The cells were demonstrated as a viable alternative to NiMh cells in a Honda Insight HEV test vehicle [41].

2.3.4 Lead-Acid Ultrabatteries

"Ultrabatteries" relate to a VRLA technology that has been developed to address the application of Lead-Acid batteries to HEVs. It is widely recognised that a Lead-Acid cell in parallel with a supercapacitor offers benefits in applications where rapid changes from charge to discharge are made, such as during regenerative braking and acceleration [33]. The use of this peak power buffer overcomes some of the issues associated with Lead-Acid batteries in HEV use, and this requirement has led to the technology pioneered by the Commonwealth Scientific and Industrial Research Organisation (CSIRO), Australia's national science agency. CSIRO have developed a "hybridised" lead-acid battery technology which integrates a Lead-Acid battery and a super capacitor in one unit [42], addressing these HEV applications requiring a peak power buffer [33, 37]. Lead-Acid cells comprise a positive and negative plate, consisting of lead-dioxide and sponge lead respectively. The CSIRO investigation developed asymmetric supercapacitors using the conventional positive plate with a carbon based negative plate. Connecting these different

cell configurations in parallel leads to a battery with integral capacitance which is suitable for HEV duty [42].

Figure 10. Lead-Acid "UltraBattery™" manufactured by Furukawa for HEV applications (photograph by author)

These batteries are now being manufactured under licence by the Furukawa Battery Co Ltd in Japan [43] (Figure 10), and East Penn Manufacturing Co Inc. [44] in the United States.

2.4 Nickel Cadmium (NiCd)

Nickel Cadmium cells were first developed by Waldemar Jungner of Sweden in 1899 [45] and have been in widespread use since that time. Until recently NiCd cells were widely used as rechargeable power sources for consumer electronics, offering around 500 to 2000 cycles and hence a usable power source for a cyclic device, compared to 200-700 cycles for Lead-Acid [16, 46]. However, heavy metals such as Cadmium are damaging to the environment, and are a known human carcinogen. As such a

European directive [47] has led to the use of small NiCd cells being banned in consumer goods, however exemptions in the directive still allow the use of this chemistry in emergency and alarm systems and emergency lighting (where limited alternatives are available for the specified high temperature operation). The cells are still permitted for use in medical equipment (due to issues with approving replacement technologies) and cordless power tools, as the cells exhibit good performance under high current pulse discharge, although Lithium chemistries are advancing on this marketplace and have gained significant ground. Finally, the cells are still permitted in military applications, and this will be due to a combination of upper temperature range performance, pulse current capability, and the fact that military equipment has a requirement for a long maintainable life (flooded NiCd cells can have a service life in excess of 20 years, whereas Lead-Acid batteries have a service life of 5 years for commodity batteries, and 10-12 years for high quality standby batteries) [24, 48].

Manufacturers such as Saft are still extremely active in the production of large NiCd cells and flooded NiCd cells (Figure 11.) also remain readily available, with manufacturers such as Alcad and Storage Battery Systems producing these cells in capacities ranging from 10Ah to over 1500Ah [48]. In spite of the "memory effect" exhibited by this chemistry [49] – the effective loss of capacity due to repeated partial discharge - the cells still find applications where wide temperature range and long service life (particularly the flooded cells) are desirable attributes. The low temperature performance of NiCd cells eclipses Lead-Acid, with the cells remaining operable at -20°C, and whilst lead-acid batteries experience a steep reduction in

service life at temperatures over 30°C, NiCd are more resilient, with some cells operating to 70°C [17, 50]. In terms of charging, a constant current regime is employed, and for longevity of the cells themselves a charge rate of 10% of rated capacity (c_r) in amps ($c_r/10$), or ideally $c_r/20$ should be used, effectively a "float" charge, with a factor applied for cell efficiency (typically 120-140% of capacity) [16].

Figure 11. Flooded NiCd stationary cell (image courtesy of Storage Battery Systems Inc.)

Higher charge rates can be used, and have been essential in the widespread use of cordless power tools, with the trade-off of service life being reduced. Research activity with NiCd has been somewhat impacted by the environmental concerns in using the chemistry, and is regarded as a dying technology by many in the research community. The wholesale replacement of NiCd cells by NiMH in consumer products, and the success in Lithium chemistries in subsequently replacing NiMH means that NiCd cells have a less than bright future.

2.5 Nickel Metal Hydride (NiMH)

Nickel Metal Hydride (NiMH) cells were developed in the in the 1960s originally as a potential power source for electric vehicles [51]. This was not fully realised until the late 1990s, and predominantly the cells have served as an alternative chemistry to Nickel Cadmium in consumer electronic applications. Because of the desire to replace cadmium, the technology has largely displaced NiCd in the consumer marketplace, which has been further progressed due to the inception of the battery directive mentioned above. In terms of power density (90-110Wh/kg) they offer an improvement of up to 50% over their predecessor [52], whilst retaining a similar charging regime, allowing NiMH chargers to be generally designed as backwardly compatible with NiCd batteries used in the same application. Chargers tend to incorporate end point detection, which can be achieved by terminal voltage measurement, as a characteristic of the chemistry is a reduction in terminal voltage at the transition into overcharge. Alternatively cell temperature sensing is used to detect overcharge, as the cell temperature increases as the energy absorbed by the charge process diminishes [25]. NiMH cells were the chemistry of choice for the first wave of widespread commercially available HEV vehicles, and were utilised in the first generation Honda Insight (Figure 12) [53] and now familiar Toyota Prius battery packs [54].

Figure 12. Honda Insight NiMH battery pack (image courtesy Bumblebee Batteries LLC)

Research in NiMH batteries and cells has been somewhat eclipsed by the focus on lithium technology, but their adoption in the early EVs and HEVs has a legacy, and latterly there is much interest in the recycling of the cells [55, 56].

2.6 Lithium Chemistries

Lithium based cells are perhaps the chemistry which currently attracts most attention in the area of energy storage research. From initially finding applications in consumer products such as mobile telephones, lithium based cells and batteries are now becoming commonplace throughout the wider marketplace. The technology is characterised by high energy density (>200 Wh/kg) as compared with other chemistries, and high voltage-per-cell (3.7V) [16]. There are several sub chemistries of "Lithium Ion" cell, but generally these are descriptively lumped together, with Lithium Polymer being generally regarded as a separate technology using a solid polymer electrolyte unlike the liquid organic electrolyte used in Lithium Ion cells [16].

"Lithium Ion" has become a generic term for a family of cells which share a basic chemical make-up which comprises an anode, cathode and electrolyte in which the cathode and electrolyte contain Lithium compounds. The Lithium-Ion chemistry for secondary cells was first proposed in the 1970s, but came to commercial prominence in 1991 when the Sony Corporation of Japan started to market the cells in consumer electronics [57].

Virtually all portable computing relies on the technology, and increasingly markets previously dominated by NiCd and NiMH, portable power tools a notable example, have been taken over by Lithium Ion cells. In contrast to NiCd and NiMH cells and batteries, which tend to derive their dimensions from IEC 60086 [58], many Lithium Ion cells have specific form factors which are separate from those adopted by other secondary cells. Dominant is the 18650 cell, which is used in laptop batteries, and many consumer applications use this cell type, and as a result pricing has rapidly dropped - in 2009 laptop battery pricing was around $1200 per kWh, which had dropped to $500 per kWh in 2013 [59]. The cells are used in packs with an overall protection and safety circuit (Figure 13), but more recently this protection circuit has been incorporated into loose cells allowing use in consumer products. The electrochemical processes are different to other cell types, and during discharge the Li+ ions transfer charge from the negative to positive electrode, through the electrolyte, and during charge the reverse reaction occurs. Li+ ions bury themselves in the porous electrode of the cathode - a process known as "intercalation" [16].

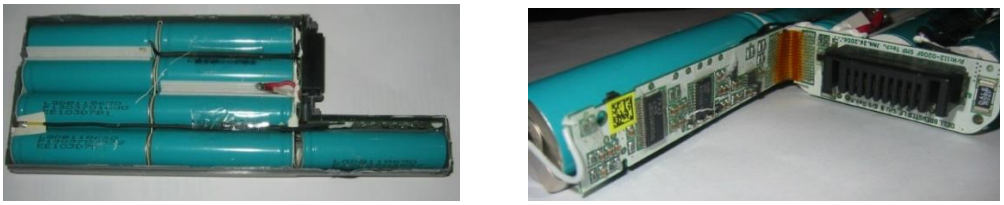

Figure 13(a) Dell laptop battery with cover removed showing 18650 cells and (b) close up of protection circuit and on board "fuel gauge" (photograph by author).

Due to the highly reactive nature of lithium metal, there are hazards associated with misuse of Lithium Ion cells. If the cells are overcharged, they can experience thermal

runaway if the electrolyte begins to react with the carbon anode, which further heats the cell and allows these reactions to continue otherwise unaided. Similarly, this process can be initiated outside of charging if the cells are sufficiently overheated [60, 61].

Amongst the battery manufacturers, A123 systems have a large presence in the emerging EV marketplace, and have the largest Lithium Ion battery manufacturing plant in North America manufacturing their advanced nanophosphate cells [62]. The rapid progress within lithium technology has not come without some growing pains, and despite supplying cells to the major automotive manufacturers (among them GM and BMW) A123 systems filed for bankruptcy in November 2012. The company, now under Chinese ownership is viable and continues to be a market leader in supplying to the EV/HEV sector.

The drive for increased energy density centres on increasing the effective surface area within the cell, and reducing the nano-scale "bottlenecks" in the reaction processes [63]. Altair Nanotechnologies research and manufacture cells and batteries exploiting these techniques and they are active in markets ranging from EV to smart grid energy storage. Their cells feature nano-structured lithium titanate instead of carbon as an anode material leading to improvements in cycle life, with 16,000 cycles reported from experimental cells which will ultimately reduce the life-cost of EV battery packs [64].

Researchers from MIT have reported improvements in power density in Lithium Ion cells using carbon nanotubes which could see increases in energy density of an order of magnitude (200 W h/$kg_{electrode}$) [65]. Other current research reflects the focus on

carbon nanostructures in the formation of Lithium based secondary cells [66, 67], and this technology tends to lead the way in attempts to increase power density.

The use of Lithium Ion batteries in stationary applications was initially hindered by the comparatively high price of the chemistry as compared to Lead-Acid (with Lithium Ion having at least twice the cost per kWh [59]). However, reductions in this cost have led to growth in this area. Exide now offer a range of medium capacity stationary packs with on board battery management. Sanyo [68], Enerdel [69], Electrovaya [70], Mitsubishi Heavy industries [71], and Valance [72] have all developed large capacity batteries which have arisen due to application crossovers from HEV/PHEV to stationary, and these batteries have been specified for backup UPS, generator start, switchgear, renewable energy and spun off technologies like hybrid generator sets.

Despite the Lithium chemistries showing the greatest potential currently for HEV and EV applications, the environmental impact of the cells themselves in the waste stream shows some concern [73]. The rapid evolution of the technology is currently one of the obstacles to the development of an efficient and ecological recycling infrastructure, and specific problems exist in the process which relate to disposal of harmful waste removed from the cells and prevention of cell explosion due to radical oxidation of lithium metal during the recycling process [74]. Additionally, much of the mineral extraction processes associated with Lithium chemistries occur on the African sub-continent, which itself is subject to environmental scrutiny due to extensive deforestation, and the area is plagued with political unrest and human rights violations.

The differences in the Lithium Ion chemistries are predominantly characterised in the cathode materials, each presenting trade-offs in application over alternative materials. The following sections give a brief overview of the main Lithium cell types with application examples.

2.6.1 Lithium Cobalt Oxide (LCO) ($LiCoO_2$)

Lithium Cobalt Oxide ($LiCoO_2$) is a positive electrode material with a layered structure, developed in the 1980s [75], which has gone on to become the most predominate Lithium Ion cell type on the market at the time of writing. LCO is the de-facto cell material used in 18650 cells for laptop computer batteries and the chemistry is used generally for applications where discharge currents up to 1C, which falls within the bounds of most portable computing, and digital still and video cameras.

$LiCoO_2$ cells are generally manufactured in the Far East, and the process for designing a battery using these cells involves enlisting a pack builder who configures the packs in the correct voltage and capacity arrangement before connecting the within-pack protection circuit module (PCM). This has made the incorporation of Lithium Ion technology a reasonably straightforward undertaking for an Original Equipment Manufacturer (OEM).

Research continues in these cells, and there is much interest in thin film batteries utilising processes allied to semiconductor manufacture [76], as moves towards solid-state batteries progress [77].

2.6.2 Lithium Nickel Manganese Cobalt Oxide (NMC)

Lithium Nickel Manganese Cobalt Oxide ($LiNiMnCoO_2$) cells are less expensive than Lithium Cobalt Oxide, but this differential is somewhat eroded by the large numbers of LCO cells which are manufactured. With a slightly lower energy density than LCO (100-150 Wh/kg against 150-250 Wh/kg) [16], but being slightly safer, use in application is based on trade-offs in these properties. NMC cells have been adopted in EV applications, with the Zero motorcycle company using cells from Molicel (Canada) providing energy storage within the vehicles. The bikes battery packs range from 8.5 kWh to 14.2kWh capacity with a claimed battery life equating to between 231,000 and 385,000 miles [78].

2.6.3 Lithium Manganese Oxide (LMO)

Lithium Manganese Oxide ($LiMn_2O_4$) cells complement Lithium Cobalt Oxide in that they are available in the same form factors (18560 cells predominantly) and approximate voltage, but are more suitable for discharge rates > 10C. As such they find wide application within power tools and EVs, notably the GM Volt (Compact Power/LG Chem battery option), Nissan Leaf and Renault Fluence [79].

2.6.4 Lithium Iron Phosphate

Lithium Iron Phosphate ($LiFePO_4$) offers attractive discharge performance with increased safety over other lithium chemistries. The cathode material is more stable that that used in $LiCoO_2$ and therefore requires a much higher energy input to promote undesirable reactions within the cell [16]. This, coupled with compatible cell voltages (3.2V cell voltage, allowing a 4 cell 12.8V battery) has assisted the technology gaining a presence in the automotive market in SLI applications. The chemistry, at around 1/3 the weight of Lead-Acid is very attractive, especially for motorcycles where the battery is significant in overall machine weight.

Figure 14. 12V 12Ah $LiFePO_4$ battery for SLI applications in the automotive marketplace (image courtesy of Super-B batteries)

Specific energy for these batteries is less than that of other Lithium types, but this is traded off against the benefits of $LiFePO_4$ being a safer battery in use.

Aftermarket SLI batteries for cars and motorcycles are becoming readily available in this technology (Figure 14), with benefits over conventional Lead-Acid being low self-discharge, extended cycle life and rapid charge [80], although widespread adoption by automotive OEMs is delayed by the higher

comparative cost. $LiFePO_4$ batteries have been demonstrated to have very good life cycle performance as compared to other chemistries in applications such as renewable energy [81]. $LiFePO_4$ cells also find applications in EV usage, with the A123 systems offering for the GM Volt employing the technology.

2.6.5 Lithium Polymer (LiPo)

Lithium polymer batteries are a development of Lithium Ion technology in which the organic electrolyte is replaced with a polymer. During the 1970s polymer electrolytes were invented by a research team within the University of Sheffield, Department of Chemistry, which led to the development of the technology [82]. The energy density of these batteries is demonstrated by their widespread adoption in radio controlled aircraft, but they take a large share of the mobile telephony and computing battery market due to this energy density.

Although intolerant of overcharge as other lithium chemistries, (decomposition of the electrolyte and liberation of gas can result) [83], the cells tend to be manufactured in unconstrained packaging, allowing some expansion without explosion - a feature which has led them to be used most readily in the consumer marketplace. Lithium Polymer batteries look set to replace the bulk of applications traditionally dominated by initially NiCd and latterly NiMH, with the batteries being capable of very high discharge rates. Figure 15 shows a 2 cell 7.4V pack with 2200mAh capacity, $40c_r$ discharge rate, weighing only 143g.

Figure 15. Lithium Polymer radio controlled model battery (photograph by author)

The safety issues associated with Lithium Polymer (cell expansion, thermal runaway and possibly fire) [83] are tolerated as a trade off against the desirable performance attributes, and low rate applications such as mobile telephony and tablet computing offer little risk with closely controlled charge and discharge. Model vehicle batteries however used at high rate are known to self-heat, and expand within their packaging, and "charging pouches" made of fireproof material are supplied with battery/charger sets to mitigate fire risks in the event of a catastrophic battery failure.

2.7 Supercapacitors

Capacitors traditionally have found applications in short term energy storage applications, with capacitance values rarely surpassing 1 Farad. High value capacitors were subsequently developed and used as alternatives to small lithium cells in memory retention applications. Further development in this area has led to the high value supercapacitors (Figure 16) [84] we see today being employed in a

range of applications from wind turbines [85] to uninterruptible power supplies [86]. Supercapacitors, or electrochemical capacitors differ in some respects from traditional capacitors in that they do not employ a conventional dielectric. High-area porous materials are used in a very thin layer that facilitates a large double layer capacitance at the electrode-electrolyte interface where the energy is stored – leading to very high capacitance [87]. The thin dielectric does however lead to the low working voltage (mostly below 3V) [84, 87, 88] of these capacitors generally, often requiring series connection in application.

Figure 16. Maxwell Technologies 2500F 2.7V supercapacitor used in peak power buffer applications (photograph by author)

The technology is expensive when compared to other energy storage technologies ($10,000 - $20,000/kWh) [89], but does offer some clear advantages over conventional batteries and cells. The way in which batteries and capacitors store energy is fundamentally different. Batteries store electrical energy indirectly as potential chemical energy. To release this energy oxidation and reduction reactions occur which allows charges to be released facilitating electrical work when these flow

between two electrodes at different potentials. In contrast, capacitors store energy directly in an electrostatic way, as negative and positive charges on the plates of a capacitor, a process known as non-Faradaic energy storage. Electrochemical capacitors operate in a similar way, but store the electrical energy in an electrochemical double layer within the electrolyte [87]. This facilitates high rate charge and discharge performance which is characteristic of capacitors generally.

Furthermore, within batteries, the chemical interconversions of the anode and cathode materials in the cell take place with phase changes, and some irreversibility of the conversion of the anode and cathode reactive materials occurs. This leads to the limitations on cycle life experienced by batteries (1000-1500 cycles typically). As these chemical processes do not exist within capacitors, 10^5-10^6 cycles are commonplace [87].

The main disadvantage with capacitors however is energy density. At the molecular level, limitations exist which restrict this energy in capacitors to 20% of that of batteries of similar active area [87], and conventional capacitor technologies use only a small proportion of this. However, with the development of electrochemical supercapacitors active area utilisation has improved, allowing the complementary characteristics of the two energy storage technologies to be more adequately exploited.

2.8 Fuel cells

"Fuel cells" describe a group of galvanic devices that convert the chemical energy of a fuel and corresponding oxidant to electrical energy. This process is carried out electrochemically, so very high efficiencies can be attained (>80%) [90], and as long at the fuel and oxidant are supplied to the electrodes, electrical energy is produced. Typically the active materials are gaseous or liquid fuels and are either hydrogen or hydrocarbons. Energy density is high when compared to conventional batteries, with very high theoretical energy densities possible for hydrogen in particular (200-500 Wh/kg for small cells with 800+ Wh/kg possible for larger designs [16, 91]. Hydrogen fuels cells present the most potential for use within vehicular applications [92], due to their ability to rapidly re fuelled, and have made some progress within applications involving public transport [93, 94]. Major obstacles exist in the adoption of fuel cells in that the fuelling infrastructure does not yet comprehensively exist [93, 94]. A detailed examination of these storage devices is available in many texts, and is outside of the scope of this work [95, 96].

2.9 Flow batteries

Flow batteries are regarded a relatively recent innovation, with the technology of the zinc/chlorine battery in being patented 1973 [97], however use of the technology predates this patent, and the French military Engineer, Charles Renard, developed the airship "La France" which was powered by a zinc/chlorine flow battery in 1884 [98]. Applications of the batteries include hybrid power systems with renewable energy, micro grids, smart grid power shaving and UPS. The technology

encompasses various chemistries, with Vanadium Redox (Figure 17) being one of the most popular and successfully implemented. All flow batteries employ a pumped electrolyte which is introduced into a cell with an ion exchange membrane. During both charging and discharging the electrolytes are pumped through the cell stack, facilitating the ion exchange processes, but remain separated by the ion exchange membrane. As such the electrolytes do not "mix" chemically, which to some extent avoids the undesirable reactions in conventional batteries, and does not directly expend the electrolyte, leading to a long life.

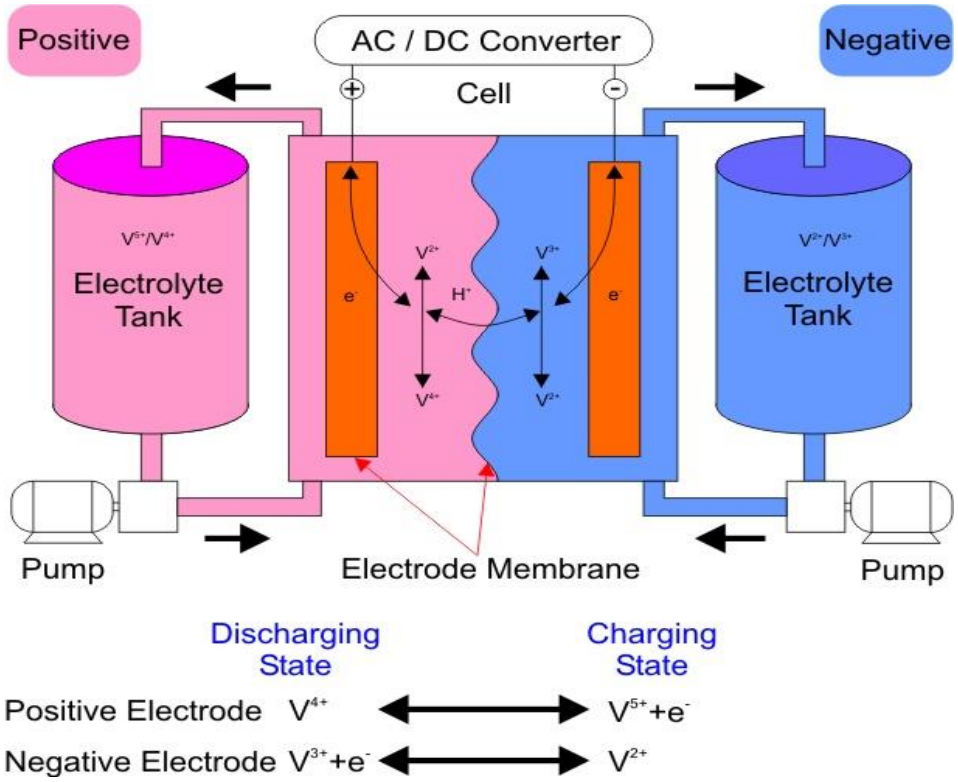

Figure 17. Vanadium Redox battery block diagram (image courtesy of REDT Ltd)

The cell stack size therefore controls the rate at which the "battery" can deliver current, with the capacity based on the volume of the external electrolyte storage tanks. The systems tend to be in the tens to hundreds of kWh range, with systems as larger as 1MW in existence [99]. Figure 18 shows a 30kWh Vanadium Redox battery

system manufactured by REDT Ltd in the UK. The overall height of the enclosure is 2.2m demonstrating the scale of these batteries [100].

Figure 18. 30kWh Vanadium Redox battery system (image courtesy of REDT Ltd.)

Energy density is currently lower than other technologies (30-50 Wh/kg), and the overheads of losses due to pumping of the electrolyte lead to efficiencies in the 70-80% range [100]. However, the advantages of this technology, such as a typical 20,000 cycle life at up 90% Depth-of-Discharge (DoD), with a reusable electrolyte are clearly attractive. The additional benefit of the ability to recharge these types of batteries by replacing discharged electrolyte with charged electrolyte has attracted some interest in the EV sector, and research into self-contained flow battery systems for vehicle use are being explored [101].

2.10 Competing electrochemistries – summary of performance and applications

Table 2 presents a comparative summary of the competing electrochemistries.

Table 2. Performance comparisons for competing energy storage technologies

Chemistry	Typical Applications	Advantages	Disadvantages	Cycle life (100% DoD)	Specific energy	Cell Voltage	Temp range
Lead-Acid (flooded) [16, 22, 23, 102]	SLI (Automotive), stationary applications, UPS, micro renewables.	Good high-rate performance. Low cost. Mature recycling infrastructure.	Risk of acid spill. Lower energy density than other technologies. Capacity affected by discharge rate. Hydrogen liberated during operation.	200-700 cycles	30-50 Wh/kg	2.0V	-40°C to +55°C (SLI)
Lead-Acid (VRLA) [16, 17]	SLI (Automotive), stationary applications, UPS, micro renewables, portable equipment.	Maintenance free, no acid spill risk. Mature recycling infrastructure.	Intolerant of deep discharge. Charging more closely controlled than flooded. Capacity affected by discharge rate.	200-700 cycles	30-50 Wh/kg	2.0V	-40°C to +55°C (SLI) -10°C to +40°C (Stationary)
Lead-Acid (VRLA spiral wound) [16, 24, 40]	Specialist SLI (Automotive), Stationary applications, UPS, portable equipment.	High rate. Better low temperature operation than conventional Lead-Acid. Long relative calendar life.	More expensive than other types. Single cell types can need cycling to establish working capacity.	200-700 cycles	~30 Wh/kg	2.0V	-10°C to +40°C
Lead-Acid (Ultrabattery) [16, 44, 103-105]	HEVs	Performance of a Lead-Acid battery with parallel capacitance.	Lower energy density than conventional Lead-Acid	Tests ongoing – expected to have twice the cycle life of conventional Lead-Acid	~25 Wh/kg	2.0V	-20°C to +40°C
Super capacitors [16, 84, 87]	Peak power buffers, regenerative braking (HEV). Complementary technology for batteries.	Rapid charge and discharge. No minimum EoD voltage. Very high cycle life.	Low energy density and expensive when compared to batteries. Low working voltage.	Up to 10^6 cycles. Short calendar life.	Up to 12 Wh/kg	2.3-2.85V	-30°C to +65°C
NiCd [16, 106, 107]	Portable equipment, power tools.	Tolerant of rapid charge and discharge, low cost.	Memory effect. Environmental issues (largely removed from consumer products for this reason)	500 + cycles	10-40 Wh/kg	1.2V	-20°C to +70°C
NiCd (flooded) [16, 48]	Stationary applications (particularly in the rail industry)	Long service life (up to 30 years). Wide operating temperature range.	Expensive when compared to Lead-Acid. Sintered plate types exhibit memory effect.	2000+ cycles	30-80 Wh/kg	1.2V	-50°C to +60°C
NiMH [16, 25, 46]	Portable equipment, power tools	Direct replacement for NiCd in most applications, with higher energy density.	Some memory effect, although better than NiCD. Charging at moderate temperatures preferred.	Up to 1000 cycles. (300000 cycles are possible for HEV specific cells).	90-110 Wh/kg	1.2V	-20°C to +65°C

Chemistry	Typical Applications	Advantages	Disadvantages	Cycle life (100% DoD)	Specific energy	Cell Voltage	Temp range
Lithium Cobalt Oxide $LiCoO_2$ [16, 46, 108]	Portable consumer products (laptop batteries). Portable power tools, EV batteries, Lead-Acid replacement applications.	High energy density, high cell voltage.	Not tolerant of fault conditions in charge or discharge. (Requires external protection circuit.) Mechanical damage can result in overheating/fire.	500 typical, 1000+ cycles possible	150-250 Wh/kg	3.7V	-20°C to +50°C
Lithium Nickel Manganese Cobalt Oxide (NMC) $LiNiMnCoO_2$ [16, 108, 109]	Portable power tools, EV batteries, Electric bicycles, Lead-Acid replacement applications.	High energy density, high cell voltage. Safer than $LiCoO_2$.	Energy density not as high as $LiCoO_2$.	500 typical, 1000+ cycles possible	100-150 Wh/kg	3.7V	-20°C to +50°C
Lithium Manganese Oxide (LMO) $LiMn_2O_4$ [16, 110]	Portable power tools, EV batteries, Electric bicycles, Lead-Acid replacement applications.	High energy density, high cell voltage. Safer than $LiCoO_2$.	Poor high temperature stability. Energy density not as high as $LiCoO_2$.	500 typical, 1000+ cycles possible	100-150 Wh/kg	3.7V	-20°C to +50°C
Lithium Iron Phosphate $LiFePO_4$ [16, 80]	SLI batteries, replacement for Lead-Acid generally, power tools, EVs.	High cycle life/ energy density. Safer than $LiCoO_2$.	Initial energy density lower than $LiCoO_2$. Discharge rate lower than Lead-Acid.	1000+ cycles, with 2000-7000 cycles developed for HEV applications.	100-120 Wh/kg	3.2V	-20°C to +50°C
Lithium Polymer [16, 111]	Cellphone batteries, tablet computing power, mobile devices generally, toys and RC models. Electric bicycles, Some EVs.	High energy density, high cell voltage.	May explode if overcharged. Requires similar care to Lithium Ion. Chargers should incorporate thermal sensing/end point detection.	500 typical, 1000+ cycles possible	250-300 Wh/kg	3.7V	-20°C to +50°C
Fuel cells (general) [16, 112]	Backup power, portable power, micro renewables, speciality vehicles	Fuel based- rapid energy replenishment. Scale-able technology.	Relatively expensive. Very little fuelling infrastructure.	Mainly measured in cycling service hours. 5000-20000 hrs dependent on technology.	200-500 Wh/kg (small cells) 800+ Wh/kg larger designs	1V	Self-heating
Flow batteries [2, 3, 101, 113]	Stationary applications (peak power shaving, UPS)	Long life, capacity theoretically unlimited (tens of kWh to MWh range). Can be charged by replacing electrolyte.	Physically large. Low relative energy density (similar to Lead-Acid). Difficult to implement in mobile/vehicle applications.	10000 – 20000 cycles	30-50 Wh/kg	1.3-1.4V	-0°C to +40°C (temperature control of the electrolyte can be employed to widen range)

2.11 Conclusion

The competing storage mediums discussed within this chapter give a snapshot of electrochemical energy storage at the time of writing. These technologies are complementary, although there are some migrations in progress which will become pronounced in the near future. Lead-Acid batteries in particular have had a long reign and maintain their firm hold within the marketplace, particular in conventional vehicles with Internal Combustion Engines (ICE), however LiFePO4 is positioned to compliment Lead-Acid batteries in these applications somewhat as prices fall.

Lithium chemistries have a strong ongoing presence in EV and HEV energy storage, whilst mild hybrid ICE using turbo generators and/or starter generators may see UltraBattery technology taking a share of this market.

NiCd batteries have a limited future due to their heavy metal content, and the advance of Lithium chemistries also threatens NiMH. It is likely that all portable equipment and power tools will adopt some form of Lithium technology within the next five years, which may overlap with supercapacitors with further improvements through research.

Developments in flow batteries are likely to see this technology start to displace Lead-Acid in large stationary applications, but for the immediate future electrochemical batteries and cells will retain a firm hold on the portable device and EV marketplaces.

Chapter 3. Performance characteristics and limitations of batteries

3.1 Introduction

An ideal battery would exhibit a shallow, linear discharge curve, with performance independent of temperature or rate of discharge. Unfortunately, this is not the case, and this leads to issues associated with use of batteries in application, and in turn establishing State-of-Charge and State-of Health of the batteries. Electrochemical cells and batteries employ chemical reactions in order to affect charge storage and delivery of current. It therefore follows that batteries will have response times and performance based on the basic controlling criteria for speed of chemical reactions, (concentration of reactant, temperature, and addition of catalysts).

The following chapter gives an overview of the problems associated with the use of batteries, and gives some treatment to the chemical processes at work from an applied perspective. The issues described apply generally across all chemistries, but where specific examples are described, Lead-Acid examples will be used.

3.2 Electrochemical reaction rates and battery performance

In seeking to understand the limitations of the performance of batteries some understanding of reaction processes within the battery must be made. There are several well-known phenomena attached to battery performance which have implications for direct modelling of batteries and cells under operational conditions. The change in reaction rates with temperature can be directly related to two known

battery behaviours. Firstly, the observed loss of capacity of batteries at low temperature, and secondly, the reduction in service life of batteries with increased operational ambient temperatures. It can be appreciated that plate corrosion and other degrading reactions will increase with temperature, but there are other mechanisms at work generally in the battery which require consideration for a complete picture. Additionally, batteries suffer performance limitations when used in applications where rapid transitions from charge and discharge exist. Moving from a state of charge to discharge in electrochemical batteries and cells requires opposing chemical processes to occur which in themselves give rise to voltage drops as these reactions proceed.

3.3 Mass transport processes and chemical inertia

Within electrochemistry, three basic modes of mass transport exist, and some understanding of these, without detailed reference to chemistry, is required in order to explain the observed performance metrics of the battery under prevailing conditions. Mass transport to and from an electrode can occur by three processes - convection and stirring, electrical migration in an electric potential gradient, and diffusion in a concentration gradient [16]. These mechanisms control the performance of the cell, and in conjunction with temperature acting as a catalyst, define the predominate behaviour of the electrochemical system.

3.3.1 Diffusion

Diffusion is well known and occurs in all solutions, arising from the natural tendency towards high entropy in all systems. Work carried out by Fick [87] in 1855 defined laws describing diffusion which are applicable to the processes within batteries. The rate of diffusion within the electrolyte of the battery or cell will be a limiting factor in performance, as concentration gradients arise during charge and discharge. Stratification in flooded batteries, and some of the requirements for closely controlled charging in VRLA batteries (which have suspended electrolytes) are in part due to diffusion. Mitigation of these effects can be effected in flooded batteries by equalisation charge rates – elevated charge causes hydrodynamic effects and therefore assisted diffusion of the electrolyte.

Additionally, reduction in capacity with both temperature and discharge rate is also attributed to diffusion and is discussed in the following sections.

3.3.2 Convection

Convection occurs due to forces acting on the electrolyte, caused by density or thermal differences within the solution. Convection will help reduce stratification in flooded batteries, but the effects of convection are reduced in a suspended electrolyte. Increasingly, the active area within cells is increasing, with the separation of plates and the effective depth of electrolyte between the

plates being reduced. As such convection effects represent less of an issue in spiral wound cells typical of current designs.

3.3.3 Migration

Migration is the third and final form of mass transport. This is the process that occurs during charge and discharge of the battery and is the actual movement of ions within the electrolyte. Electrical migration occurs due to an electric potential gradient within the cell and is limited by the available charge carriers at any time.

3.4 Coupe de fouet and the effect of load application to batteries

In addition to the chemical processes outlined above, a phenomenon exists with Lead-Acid batteries particularly which effects terminal voltage on application of load. "Coupe de fouet" is a phenomenon observed in Lead-Acid batteries and the term derives from the French for the "crack of the whip" [114, 115]. Figure 19 shows a discharge curve for a lead-acid battery at 20°C carried out during this work, and the temporary reduction in terminal voltage can be seen at the application of load.

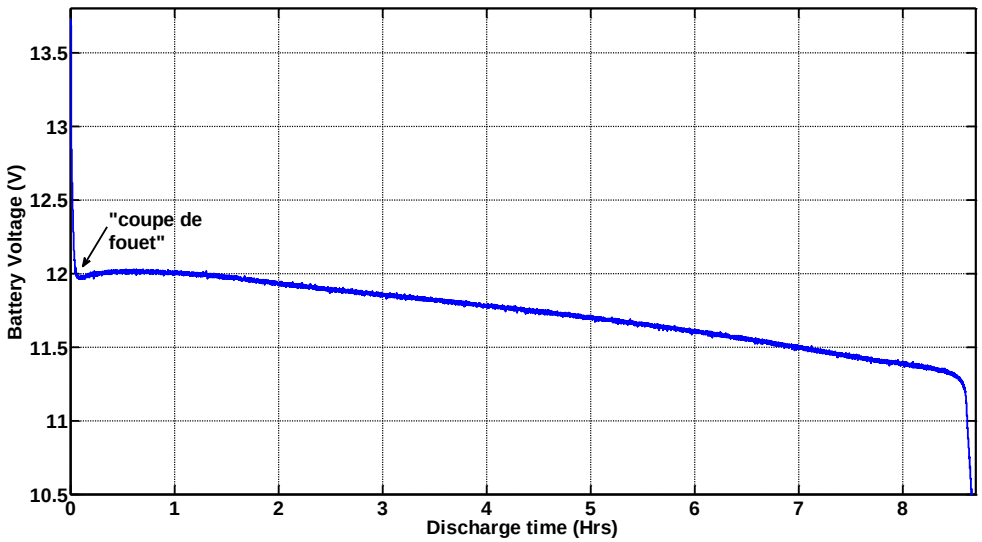

Figure 19. Battery terminal Voltage on application of load showing "Coupe de Fouet"

The phenomenon has been variously described electrochemically, with Berndt and Voss first proposing crystallisation overvoltage as the mechanism for the voltage reduction 50 years ago [116]. Subsequently several theories have been investigated [115, 117, 118], and whilst the mechanism of the phenomenon is of interest to the electrochemist, the manifestation of the terminal voltage drop is the main concern of the battery engineer. The author, in the course of his professional career has developed several battery testing schemes for Lead-Acid batteries, incorporating methods to remove coupe de fouet from the measurement system. These techniques have been incorporated into this body of work, and are described in the following chapter.

3.5 Mass transport over potential

Mass transport over potential controls the performance of batteries at high rates of charge and discharge. Under these conditions, the region around the electrode is subject to a depletion of reactants, and further reactants diffuse towards the electrode. If the discharge rate causes these reactants to be depleted at a rate greater than they can arrive at the electrode the battery voltage decreases.

In simple terms a concentration gradient exists in the electrolyte, which is caused by a high rate of charge or discharge. The result of this is that the battery terminal voltage reduces to the minimum voltage earlier than expected, and some of the reactants are not used.

This supports the findings of Maneti [119], in that after a high rate discharge, a period of rest allows the battery to recover to a point where the remaining energy is accessible, and one would assume that an equalisation has occurred within the electrolyte at this time. During charging similar processes occur, which therefore explains somewhat why elevated charge voltages are required for increased charge rates [16].

3.6 Discharge rate issues

3.6.1 Loss of capacity with discharge rate

Electrochemical batteries and cells generally exhibit a reduced capacity with increased discharge current. This phenomena is well known from the work of

Peukert [120] who described the reduction in effective capacity of Lead-Acid cells with discharge rate at constant temperature:

$$C_p = I^k t_d \quad (2)$$

Where C_p is capacity according to Peukert, at the specified discharge rate.

I is discharge current in Amperes

k is the Peukert constant for the battery

t_d is the time of discharge in hours

The relationship can more usefully be expressed in the following way:

$$It = c_r \left(\frac{c_r}{It_r} \right)^{k-1} \quad (3)$$

Where I = Actual discharge current (A)

c_r = rated battery capacity (Ah)

t_r = rated discharge time

therefore

It = available Ah capacity (c_{av})

$$c_{av} = c_r \left(\frac{c_r}{It_r} \right)^{k-1} \quad (4)$$

Plotting this for a 100Ah battery with a rated 20 Hr capacity, with a Peukert coefficient of 1.3 gives rise to the graph shown in Figure 20.

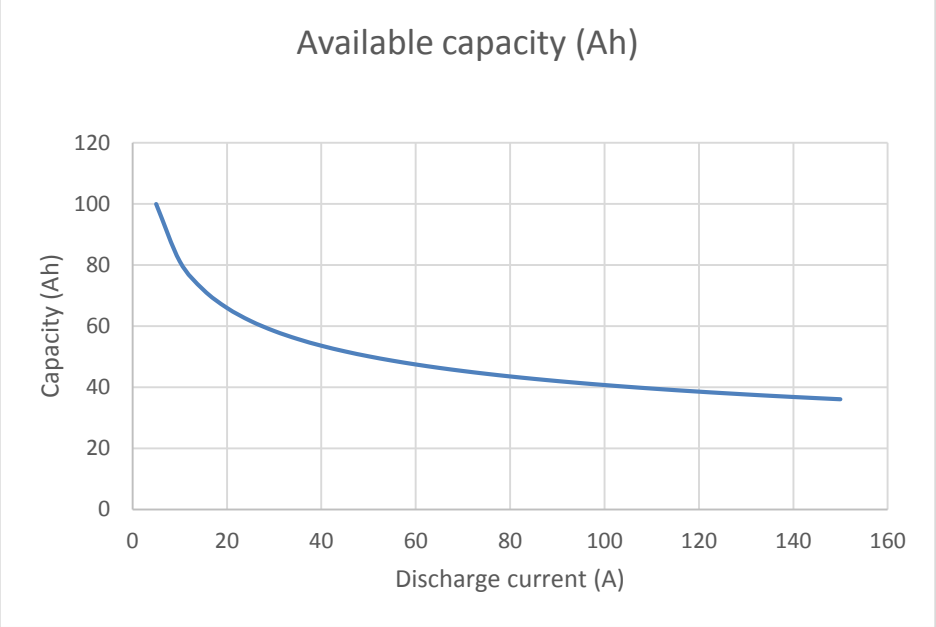

Figure 20. Lead-Acid battery capacity with discharge rate (100Ah at 20 hr discharge rate, 20°C)

This is demonstrated in the way Lead-Acid batteries are specified, with VRLA typically having rated capacity quoted for a 20Hr discharge rate. Similarly, reduced temperature effects capacity, and most Lead-Acid batteries are almost unusable at -20°C. Peukert's equation has been also demonstrated to be applicable to Lithium Ion batteries [121].

3.7 Effect of temperature on battery and cell performance

For most battery and cell types, optimum operating conditions exist at around 20-25°C, offering the best mix of operational life expectancy and performance generally.

It is well known within chemistry that heat is a catalyst, and this applies equally to energy storage technologies. As temperature falls, reactions within the battery become less active, the manifested effects being a reduction in terminal voltage, a corresponding loss in capacity, and a reduced capacity to deliver high currents. This is demonstrated in the way that SLI batteries are specified, being quoted in Cold Cranking Amps (CCA) as a measure of their performance at low temperatures. These effects can in turn be correlated to the equivalent circuit developed for the subject battery, and it therefore follows that identifying these parameters allows some establishing of predicted battery performance under these conditions.

3.7.1 Terminal Voltage variations with State-of-Charge and temperature

Figure 21 shows the variation in terminal voltage for a VRLA battery at 20°C over State-of-Charge [17]. This terminal voltage varies with prevailing conditions (recent load or charge) and also with temperature.

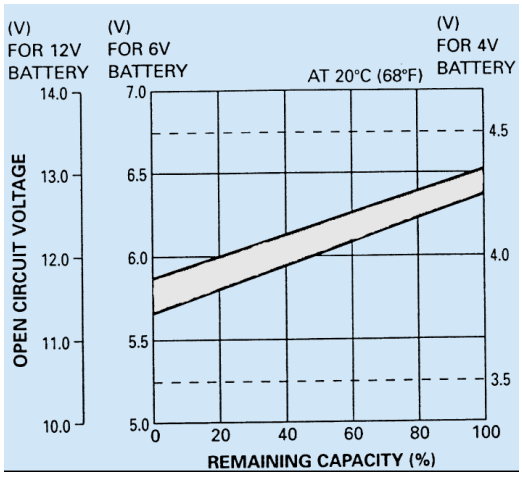

Figure 21. Steady state open circuit terminal voltage with State-of-Charge (Image by kind permission of Yuasa Battery Sales UK)

The equilibrium voltage of a Lead-Acid battery with temperature is a linear relationship described by the Nernst equation:

$$E = 2.047 + \frac{RT}{F} ln\left(\frac{\alpha H_2SO_4}{\alpha H_2O}\right) \quad (5)$$

Where E is the voltage across the cell, R is the gas constant, T is the temperature in Kelvin, F is the Faraday constant and α is the chemical activity of the relevant species.

An experiment was carried to investigate this change in terminal voltage with temperature. Two new 65Ah batteries in good SoH at close to 100% SoC were used for the investigation, and the initial steady-state OCV measured. Subsequently one of the batteries remained in a 25^0C ambient as a "control" sample whilst the other was cooled to -10^0C, and the terminal voltages were measured again after 2 weeks. It is known from previous work by the author that application of a small load pulse will remove overvoltage due to recent charge or change in temperature, so identical load pulses were applied to both batteries in order to obtain a more representative steady state voltage for the test batteries. The response to the load steps can be seen for battery 1 and battery 2 in Figure 22.

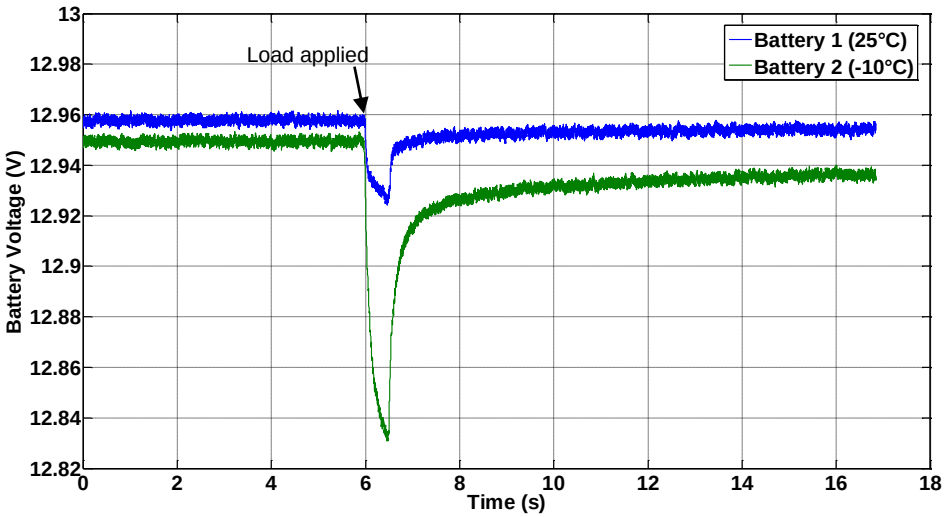

Figure 22. Battery terminal voltage response to an applied load step

It can be seen that battery 1 (25°C) responds well to the load step and recovers to close to the original OCV quickly. Battery 2 at -10°C clearly undergoes a much larger voltage deviation when subject to the same load step, but recovers in a way that tends towards a lower steady-state voltage.

The batteries were left for 1 hour to establish a steady state and the terminal voltages measured. The recorded results are shown in table 3.

Table 3 - battery terminal voltage at ambient and reduced temperatures

	Initial OCV	OCV after 2 weeks	OCV after load pulse	Overall change in terminal Voltage
Battery 1	12.973V (25°C)	12.953V (25°C)	12.952V (25°C)	21mV
Battery 2	12.982V (25°C)	12.945V (-10°C)	12.936V (-10°C)	46mV

The results in table 3 for the battery at -10°C in particular are not completely as expected if we consider the Nernst equation shown in (5). Using a normalised

approach, and based on the measured terminal voltages at 25 °C a terminal voltage of 12.897V was expected at this temperature.

This highlights some of the problems associated with using terminal voltage as a state indicator, and the issues in defining an absolute condition for a steady-state battery condition under which reference measurements can be taken.

3.7.2 Temperature effects on cell capacity

The reduction in cell voltage with temperature discussed in the previous section has an impact on battery capacity as this indicates reductions in electrochemical activity. This is manifest in a reduction in both effective area of the cell plates and reaction speed, leading to an effective reduction in battery capacity.

It is important to understand that temperature reductions do not result in the energy in the battery being "lost". Increasing the temperature of a battery which has been discharged to its EoD voltage at -10°C will result in an increase in terminal voltage and electrochemical activity, with further energy becoming available. Figure 23 shows the variation of VRLA Lead-Acid battery capacity with temperature and discharge rate [17]. The curves shown in the figure refer to discharge rates expressed as a fraction of rated capacity.

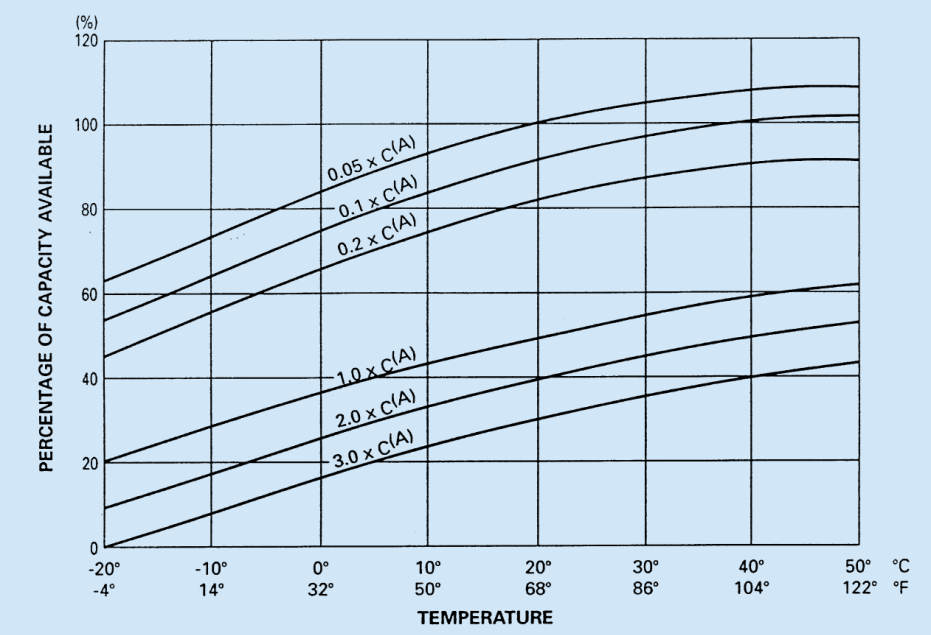

Figure 23. VRLA Lead-Acid battery capacity with temperature and discharge rate (image reproduced with kind permission of Yuasa Battery sales UK)

As can be seen, typically, a lead-acid battery discharged at a moderate rate will see a reduction in capacity to around 60% at -10°C, compared to the published Ah rating, being specified at 25°C. At temperatures above 25°C the battery capacity will exceed 100% levelling off towards 110%. This is not "free" energy, but a result of increased terminal voltage and reaction efficiency increase with temperature, thus allowing energy supplied during the charging process to be released more readily.

3.7.3 Undesirable reactions with increased temperature

The desirable effects of increased ambient temperature in battery and cell performance are offset by the degenerative process which occurs due to the

undesirable reactions which also proceed at an accelerated rate at elevated temperatures.

Plate corrosion, electrolyte depletion and increased self-discharge are some of the issues associated with increased ambient temperature, but from an applied perspective all of these mechanisms result in reduced service life.

Manufacturer's data regarding service life with temperature [17] (Figure 24.) tends to support the general statement of the Arrhenius equation (6), in that for common chemical reactions, reaction rate doubles for every 10 °C increase in temperature [122].

$$k = A^{\left(-\frac{E}{RT}\right)} \tag{6}$$

Where k is the reaction rate constant, A and E are constants characteristic of the reactants, R is the gas constant and T is absolute temperature.

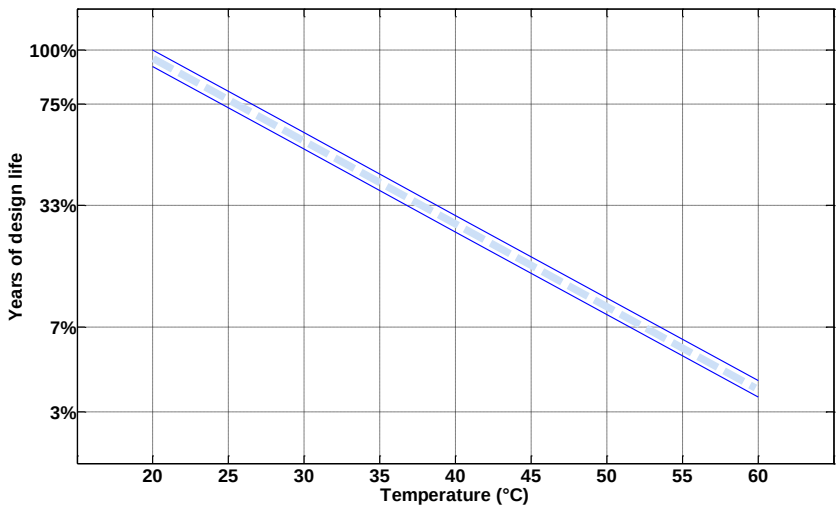

Figure 24. Lead-Acid battery service life with ambient temperature

This reduction in service life with increased temperature can be exploited to provide accelerated testing of batteries and cells over lifetime (to 80% of rated capacity). This characteristic is used in chapter 11 in order to provide lifetime parameters for the developed tests by accelerating failure of the test battery.

3.8 Conclusion

The non-linear nature of batteries and cells, within their operating environment highlights the problems associated with establishing SoH and SoC. Mass transport processes (diffusion, convection and migration) are controlling factors in battery or cell operation, and with this, other phenomena affecting available charge carriers within the battery further govern the way batteries can supply energy.

As has been discussed, most battery types experience optimum operating conditions at around 20-25°C, but it is very rare that these conditions can be guaranteed, and as such any battery state evaluation scheme must factor in temperature. Additionally discharge rate presents issues with available capacity, and the test system developed must be able to accommodate such factors. As such characterisation of test batteries must be carried out over a range of operational conditions in order to prove any developed test techniques.

The values of the preliminary experiments carried out within this section have shown that caution must be observed in collecting test data from batteries, as the Nernst equation applies only when residual overvoltage is removed from the battery, and all terminal voltage measurements need to be taken in a controlled fashion with a steady-state being established. This highlights the problems with using terminal

voltage as an indicator of SoC, and this is clearly not possible without prior knowledge of battery state, which somewhat negates the value of the technique.

Additionally, the application of current pulses to batteries as part of developed test schemes must consider the effects on the battery terminal voltage, in order that false reporting is not encountered.

Chapter 4. Battery characterisation

4.1 Introduction

Battery characterisation has been very much in the forefront of the application of batteries and cells from the inception of the technology. The need to establish the SoC of batteries in use has led to a number of schemes being adopted to monitor battery status. As part of the literature review for the research, a review of current methods for establishing SoC, SoH and SoF was carried out, and as areas of novelty emerged, these were further examined for previous research, notably frequency domain analysis of batteries and cells. This chapter reviews a number of widely used techniques and equipment before discussing pseudo-random binary sequences and their application to battery technologies in detail.

4.2 Specific gravity of electrolyte

Traditionally, early batteries or accumulators were largely flooded Lead-Acid types, and with access to the electrolyte a measurement of specific gravity was carried out to establish battery state. This type of testing provides an accurate means of establishing State-of-Charge, and State-of-Health can be established somewhat by inspection of the electrolyte condition. This technique is however only applicable to flooded cells, and requires an operator to carry out the test with a glass bodied hydrometer. This involves removing a sample of the fluid from the cell in order to measure the density of the electrolyte. Most instruments use a scaled, weighted float which is factory calibrated using water as the relative medium.

Table 4 shows specific gravity over a range of states-of-charge for flooded lead-acid batteries [22, 23].

Table 4. Specific gravity with SoC for flooded Lead-Acid batteries

State-of-Charge (%)	Specific gravity
100	1.255 – 1.275
75	1.215 – 1.235
50	1.180 - 1.200
25	1.155 - 1.165
0	1.110 - 1.130

Specific Gravity is dependent on the electrolyte temperature. The values in table 5 are taken from manufacturer's data and are valid for a temperature of 27°C. Correction for other temperatures can be achieved by adjusting the above figures by 0.003 for every 5°C (negative coefficient).

The test method has become somewhat redundant with VRLA batteries superseding conventional flooded types, as this is not a viable test for cells having anything other than a pure, unsuspended electrolyte.

Much of the research around using specific gravity as a state indicator has concerned measurement using ultrasonic or optical methods [123, 124], but tends to date from the 1980-1990 period, reflecting that the techniques have somewhat become redundant.

4.3 Terminal voltage measurement

Terminal voltage measurement as a means of battery state evaluation can be applied, but should be used within a controlled environment. As discussed in chapter 3, there are problems associated with the history of the battery before the measurement is made, and unlike capacitors which offer direct SoC evaluation from voltage measurements, batteries are non-linear in this respect and therefore these measurements need to be carefully considered.

An example of the problems encountered is shown in Figure 25. The graph illustrates an experiment where four different new batteries manufactured by Yuasa were charged to 100% SoC and then open circuit terminal voltage measured over time using a high-impedance instrument.

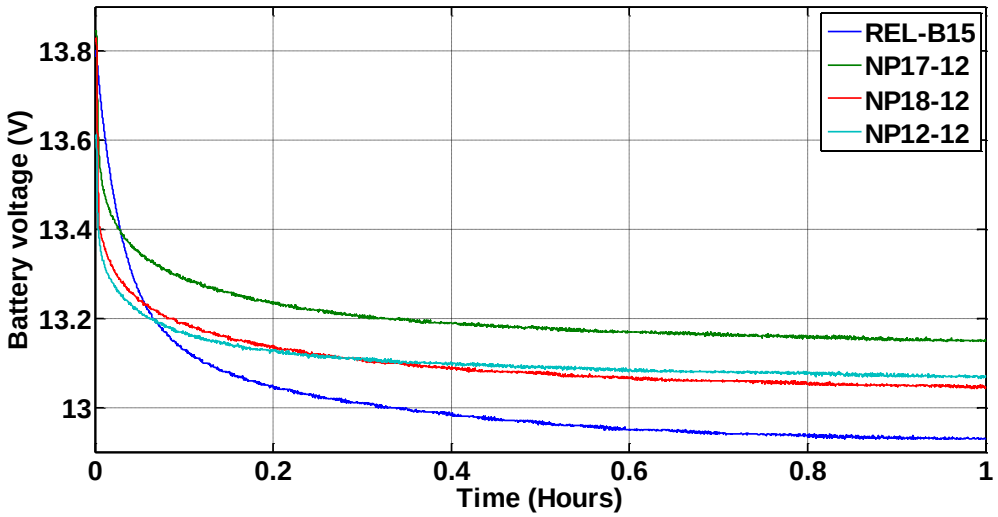

Figure 25. Comparative terminal voltage of Lead-Acid batteries post-charge (20°C)

The REL-B15 is a long design life 12V 15Ah battery, and shares a case design with the NP17-12 and NP18-12 which are 17Ah and 18Ah capacity respectively. To the untrained observer these batteries are superficially the same, but the off charge

characteristics are clearly different. The NP12-12 is a 12V, 12Ah battery, but has an off charge voltage profile similar to the 18Ah battery.

This clearly shows that the use of terminal voltage as an indicator requires some controlled conditions, and as an isolated test technique, can only offer rudimentary indications. The method is therefore employed mainly in hybrid test schemes as one of several parameters used to assess battery state, with some understanding of the current flow in or out of the battery prior to the test.

4.4 Load testing

Load testing has a long history in SLI batteries and gives a reasonable indication of battery performance. Traditionally, load testing has been known as a "drop test" where a low resistance load is applied to the battery, with a test current of at least $1c_r$. A voltmeter integral to the test apparatus indicates the voltage drop over the test period, with distinct pass/fall limits. This type of testing, in conjunction with measurements of specific gravity were the only tests of SoH and SoC that were available for Lead-Acid batteries in their early application and is still commonly used today in car repair workshop where there is a need for robust and easy-to-use equipment. Load testing has developed somewhat, and has facilitated battery analysis in diverse excitation schemes, developing on straightforward discharge testing and simple load pulses. Testing of batteries using a suitable load is therefore subdivided into several test schemes, which are described in the following sections.

4.4.1 Constant current long duration discharge tests

Long duration constant current discharge remains the definitive method for establishing the capacity of a battery or cell. The test generally comprises discharging the fully charged battery into a constant current load and measuring the elapsed time to the End of Discharge (EoD) Voltage. Figure 26 shows a typical discharge curve for a 65Ah VRLA battery at 20°C.

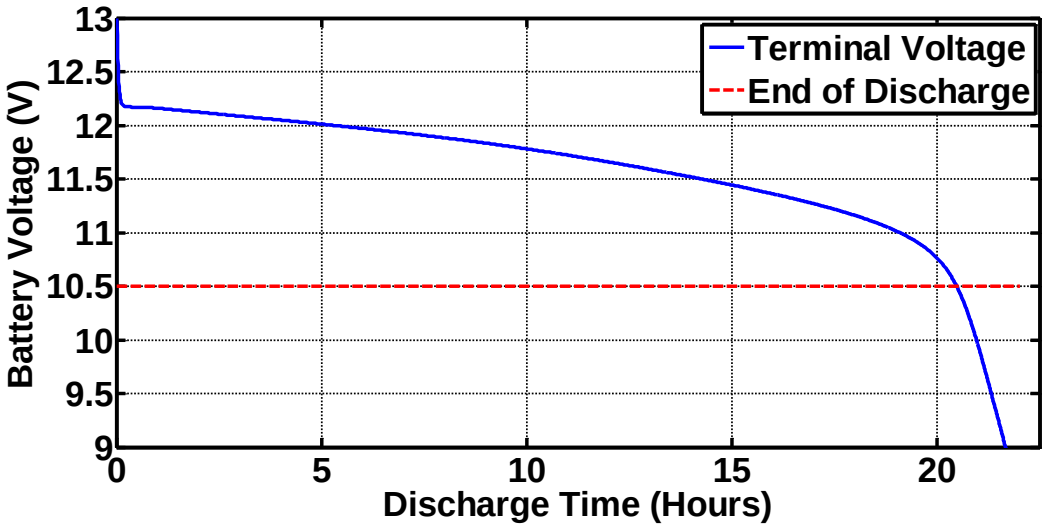

Figure 26. Typical discharge curve for 65Ah VRLA battery at 20°C

The EoD Voltage is established from manufacturer's data and will correspond to the prevailing discharge rate during the test. Figure 27 shows the EoD Voltage (dotted line) for a range of discharge currents [17]. Additionally, the temperature at which the test is carried out must also be taken into account, as discussed in chapter 3. The major disadvantage of this type of test is the duration of the discharge, and the fact a charge-discharge-charge cycle is expended during the process. As such the use of this test is generally limited to research, and verification of new evaluation methods.

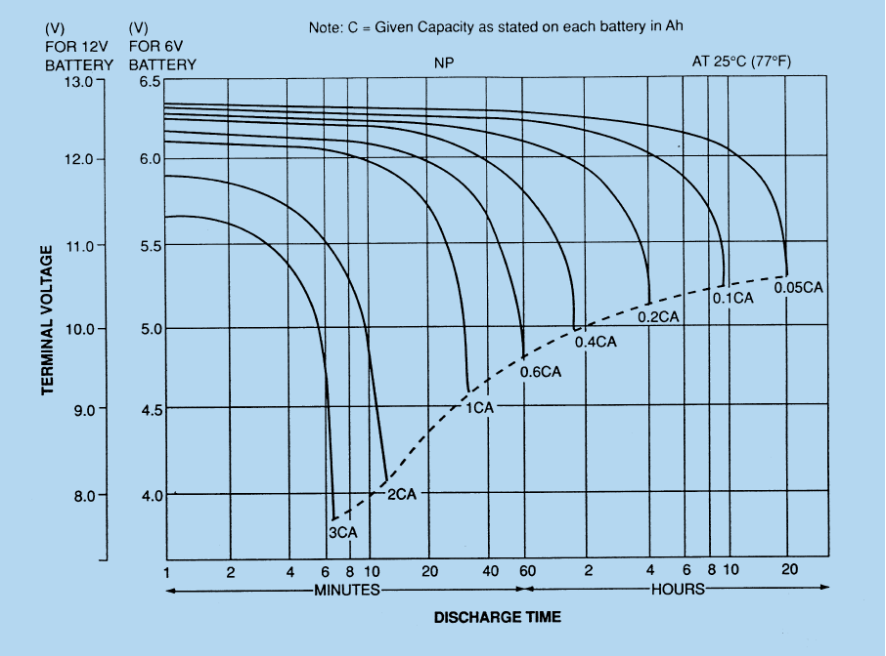

Figure 27. Variation of battery capacity with discharge rate showing EoD Voltage (Image courtesy Yuasa battery Sales Europe)

4.4.2 Short duration pulse load testing

Pulse load tests can be used as means for establishing SoH and to some extent SoC, but in many cases the technique is used to report the battery health alone, and operational restrictions on when such tests are applied can be implemented in order to avoid false test results. Applying a single load pulse can report battery SoH, but a false result can be reported if the battery has recently been charging, or the ambient temperature in which it has been stored has changed significantly. Furthermore, the problems associated with terminal voltage measurement discussed in the previous sections prevail with simple tests. A two pulse test was developed by the author in 2001 within Bulgin Power Source Plc, which has been in use commercially since that date by VxI Power Ltd [125].

This testing scheme has also appeared independently in published work by Coleman et al in 2008 [126].

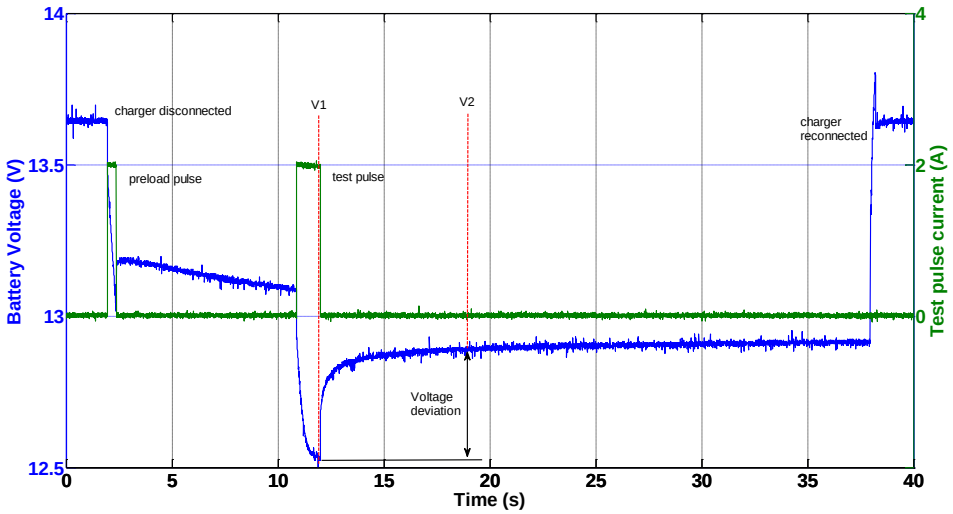

Figure 28. Two pulse battery test as applied to a 24Ah VRLA battery as part of on board SoH testing

Referring to Figure 28, as the charger is turned off, the battery remains at the charge voltage, which over time would decay towards a steady-state in a similar fashion to the characteristics shown in Figure 25. To accelerate this process the battery is given an initial load pulse (preload pulse) which arrests the terminal voltage and "clips" the overvoltage due to recent charge. There follows a relaxation period under which the battery terminal voltage is falling towards a steady-state value, which is followed by the actual test pulse. At V1, the battery voltage is measured before the test pulse is turned off. The battery is then allowed to recover for 5 seconds before V2 is measured and V1-V2 is the test voltage deviation. Durations for pulses and measurement intervals are based on bench characterisation of the battery types used at constant temperature. Voltage deviations during the test can be compared to historical

results or absolute limits. Limitations of the technique relate to the level of interpretation placed upon the data, and the most effective implementation of this type of testing scheme is in conjunction with historic data from previous tests where degradation of the battery has been observed as an increase of the test voltage deviation.

4.4.3 Charger margin test

"Margin" test refers to a type of discharge testing that can be implemented within equipment with battery backup during a defined charge period and was developed for high availability DC UPS systems for utilities applications [127]. The testing is most applicable to uninterruptible power supplies, and other equipment with regular, long charge cycles. IEE standards for testing batteries rely on disconnection from the supported equipment followed by controlled discharges of the system batteries [128, 129]. This may be undesirable for high availability systems so an alternative approach is required which does not compromised the equipment in use. During a margin test the charger voltage is reduced to a level below the open circuit terminal voltage of the connected battery, and as a result the battery takes up supply of the load. The load discharges the battery during this period, and the voltage measurements are taken throughout the test to develop a discharge curve. The test may not encompass a full discharge, but will be carried out over a time period deemed suitable based on load and battery pack capacity. The charger voltage is digitally controlled and kept just below the battery voltage, in order that a

faulty battery does not jeopardise the operation of the equipment. The test is terminated either at a pre-set time or when the battery has reached a specified voltage threshold. If the application facilitates a long test, and the load is well understood (stable, constant loads are preferred), performance of the battery can be evaluated. Over time a history can be built, and in turn, predictions made for end of life of the battery.

An alternative approach is to provide an on board constant current load within the equipment which undertakes a partial discharge of the connected battery periodically. This offers benefits where load is unpredictable, but has the downside in that the energy is dissipated, which can be unattractive thermally, and is undesirable in terms of environmental impact.

4.5 Coulomb counting

Coulomb counting methods employ measurement of the current flowing and out of the battery in order to establish the state-of-charge [14]. This technique is relatively successful, and has been widely adopted in portable computing, but it does suffer from some drawbacks as a stand-alone battery test scheme. Cumulative errors can be introduced and these may be due to varying efficiency of the battery being evaluated, deteriorating SoH and inaccuracies in the measurement acquisition system. These shortcomings were manifest in early implementations of the technique where a healthy SoC could be indicated for a battery in poor SoH, leading to unpredictable shutdown of the powered equipment. Coulomb counting can be improved by periodic recalibration, which involves a charge and discharge cycle of

the battery, however this can be inconvenient to the user, and more commonly hybrid SoC evaluation schemes are used in conjunction with this type of evaluation system [130].

4.6 AC impedance measurement

AC impedance measurement has been used in battery state evaluation for some time, being developed during the 1970s, with the technique allowing spot frequency analysis of the battery being examined [131]. Typically a perturbation is applied to a constant current load and the voltage deviations observed in order to calculate the impedance at the subject frequency. Outside of this research the method has been adopted in commercially available instruments for use in battery testing, the most widely used being hand held meters (Figure 29) used in preventative maintenance of Uninterruptible Power Supplies (UPS) [132].

Figure 29. Hioki 3354 hand held battery test instrument using AC impedance to establish battery health (Image courtesy Hioki UK)

The batteries in these applications are connected in series string arrangement with a large number of similar parallel branches. Absolute impedance measurement is

possible with these instruments but rarely used, a comparative approach using SPC being preferred. Typically cell or battery impedances are recorded at the service interval and retained for historical analysis. Any cell or battery that has moved away from the median impedance value by a defined percentage will be subject to further examination, usually requiring replacement of that battery string. AC impedance is used widely within research for battery characterisation [133, 134], and some embedded battery testing schemes exist within commercial products. The primary limitations of the AC impedance technique, is that is does require a frequency sweep to examine the equivalent circuit components, and where spot frequency schemes are used, only limited parameter information becomes available. SoC and SoH reporting can be carried out, but this is dependent on the excitation frequencies selected.

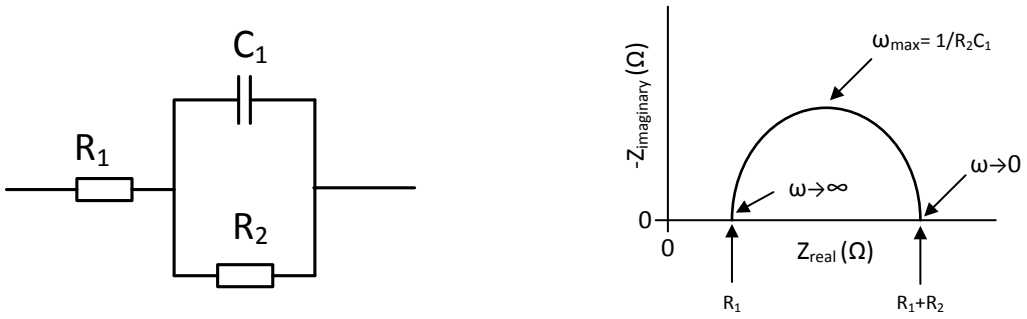

Figure 30. Electrode equivalent circuit and typical EIS plot with parameter identification

AC impedance is most commonly implemented in electrochemical cells as Electrochemical Impedance Spectroscopy (EIS) [131], and Figure 30 shows a typical equivalent circuit for the electrode-electrolyte interface, and the corresponding EIS plot [16].

4.7 Battery management integrated circuits

The growth in the adoption of battery packs manufactured specifically for portable equipment and computing has led to the development of a range of "battery management" integrated circuits. Initially used in NiCD and NiMH packs the technology has expanded to encompass the requirements of Lithium chemistries and the safety in use of these cells. These ICs are the destination for many of the developed battery test technologies, and they employ elements of coulomb counting, terminal voltage measurement, load testing and AC impedance measurement.

Figure 31 shows a LCO battery in its raw, uncased form, showing the Protection Circuit Module (PCM).

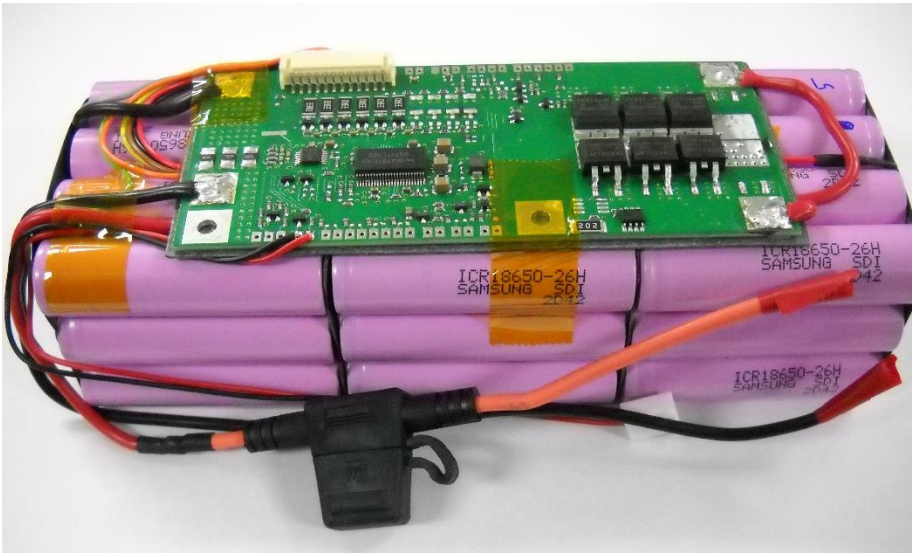

Figure 31. Lithium Ion Cobalt pack used in one of the author's current projects (photograph by author)

Figure 32 shows the circuit in more detail with the main control and protection ICs highlighted. The bq77pl900 cell protection IC provides the safety control functions within the pack, controlling the output MOSFETs, sensing temperature and cell to

cell balance [135]. The fuel gauge IC is particular relevance to this research, as it incorporates the commercialisation of existing SoC and SoH technologies.

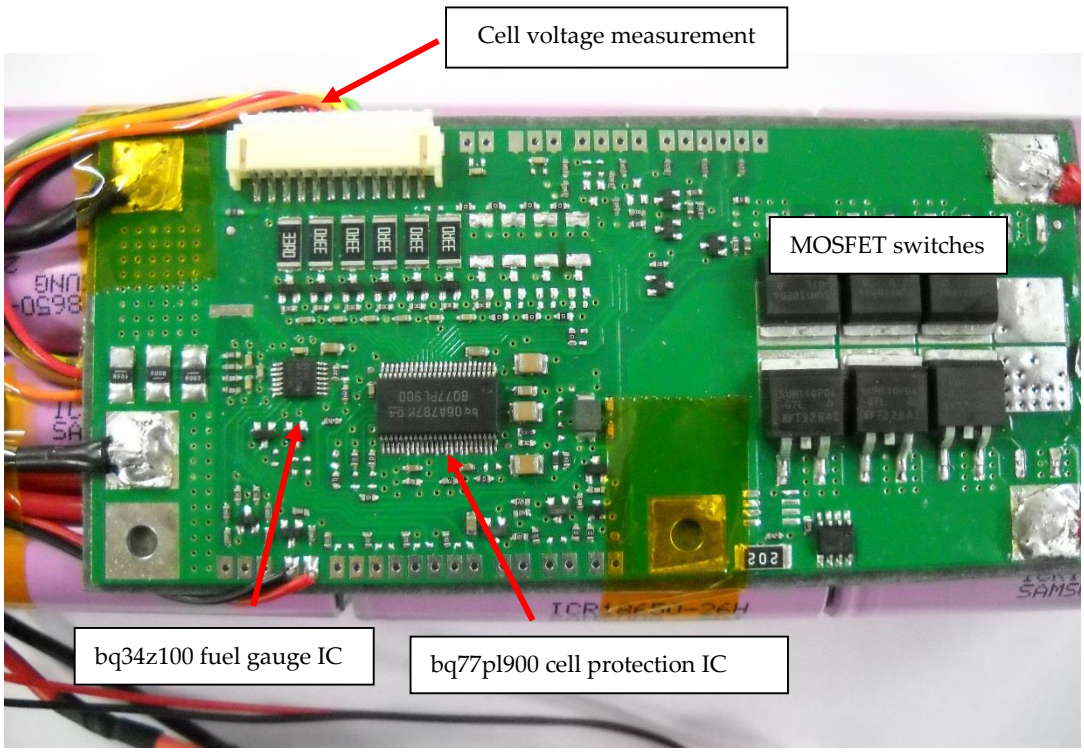

Figure 32. Close up of PCM board (photograph by author)

The bq34z100 is a Texas Instruments device and predominantly incorporates an historically calibrated coulomb counting scheme to establish SoC, using the load to derive calibration factors for the algorithms used [136]. Typical of such schemes, and battery state evaluation generally, it employs historic data to improve the accuracy of the reporting. A microcontroller implementation of this type of device could potentially employ the novel methods of state evaluation developed during this work.

4.8 Frequency domain (spectrum) analysis

Many of the battery test schemes discussed here operate at fixed frequency points giving either response to low frequency pulses, DC loads or spot frequency AC impedance.

An alternative approach is to employ a range of frequencies, or frequency rich signals in order that impedance spectra may be obtained for the batteries under test. Using Fast Fourier Transformations (FFT) frequency responses can be obtained, and in turn models for the batteries and cells under test can be developed using curve fitting or other methods to arrive at a satisfactory approximation to the test battery or cell. The following sections outline some of the competing methods for examining batteries in this way, and offers the PRBS technique as an alternative approach for experimental analysis of batteries.

4.8.1 Swept sinusoids

Traditionally, frequency response analysis techniques have relied on the application of a swept sinusoid to establish the response of the system being examined [137, 138]. This technique remains valid, but the use of sine waves to analyse frequency response requires analogue generation of the perturbation signal, or a filtered pulse width modulated representation of an appropriate sinusoid. The hardware and software overhead in generating this perturbation digitally (if it is considered that the resultant response will be processed digitally also) is greater than that required to generate a comparable digital

signal, which can in itself be swept and analysed at the individual frequency steps.

4.8.2 Digital signals

Applying digital signals for frequency domain analysis offers clear benefits for equipment with some computing component, either embedded or otherwise. Generating square waves as perturbation signals is straightforward, but as with swept sinusoids, appropriate frequency steps need to be selected and this can lead to a long test, dependent on the resolution of the frequency steps. An alternative approach was proposed employing designed digital signals which are frequency rich to battery analysis [139]. Periodic signals which exhibit this property are widely used and are introduced in the following section.

4.8.3 Pseudo Random Binary Sequences as a perturbation signal

It is conveniently straightforward to generate signals which use deterministic logic to create signals with properties of randomness. Pseudo Random Binary Sequences offer a digitally generated signal which on inspection appears random in nature, but is actually periodic, and therefore has properties which are extremely useful in several application areas. There are a class of PRBSs termed Maximum Length Sequence (MLS) that exhibit properties similar to white-noise and this apparent randomness of a signal, which actually repeats finds applications in communications cryptography [140] using the PRBS

modulate the signal. From here on the term PRBS refers to MLS. The sequences have extensively been used to establish audio frequency response [141], and system frequency response analysis generally [142]. Integrated circuits such as the Texas Instruments MM5437 [143] were marketed as noise generators for these applications, being essentially within-a-chip implementations of the PRBS generator seen in Figure 33, using shift registers with modulo 2 (XNOR) feedback at predetermined "tap" positions.

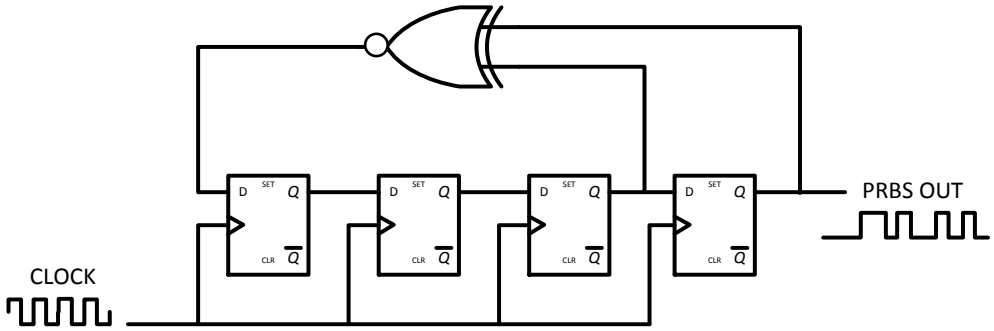

Figure 33 4-bit PRBS generator constructed from shift registers with determined "tap" positions and XNOR feedback

Within a PRBS generator the number of shift registers defines the bit order, n. Considering that all states apart from "all zeros" are represented, the number of terms, N in the sequence is defined by:

$$N = (2^n - 1) \qquad (7)$$

Figure 34 shows the output from the 4 bit PRBS generator in Figure 33. The total number of terms at which the sequence repeats (N) is 15 and the PRBS amplitude is +/- a. The autocorrelation function is also shown, where Δt is the period of the PRBS clock and T_s is the time before the PRBS repeats.

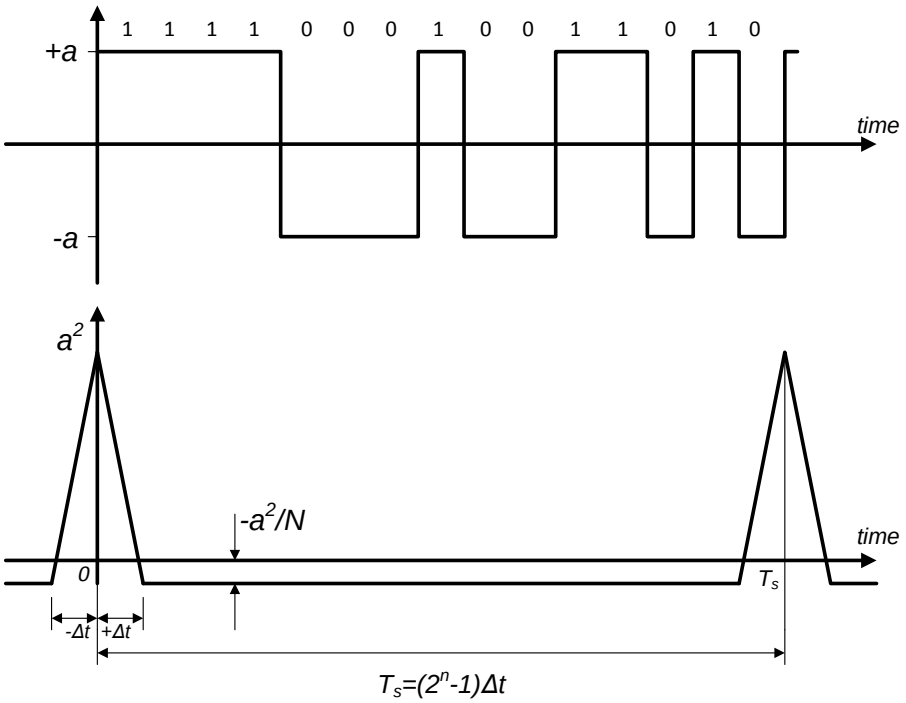

Figure 34. Example PRBS sequence and autocorrelation response

The autocorrelation function is continuous, with the waveform totally uncorrelated with itself if shifted more than one clock period in either direction [107, 144].

The "tap" positions for the shift registers have been defined mathematically in various texts [107, 144], and their derivation is outside the scope of this work, however, common taps are shown in table 5 [145].

Table 5. Feedback tap positions for PRBS bit sequences up to 16 bit

n	Feedback taps	N	n	Feedback taps	N
3	3,2	7	**10**	10,7	1023
4	4,3	15	**11**	11,9	2047
5	5,3	31	**12**	12,6,4,1	4095
6	6,5	63	**13**	13,4,3,1	8191
7	7,6	127	**14**	14,5,3,1	16383
8	8,6,5,4	255	**15**	15,14	32767
9	9,5	511	**16**	16,15,13,4	65535

Alternative tap positions can be used for some bit sequences, with n = 7 for example also having valid taps at 7, 6. Hardware shift registers however, along with dedicated ICs for PRBS implementation have largely been rendered obsolete, with the general adoption of embedded processing within electronic equipment. Within this environment, either memory registers, or a look up table for the sequence may be used.

The power spectral density of a PRBS, as shown by Davies [144] is a line spectrum, having an envelope described by the *sinc* function (sin*x*)/*x*, reaching its first value of zero at the frequency of the clock pulse (fp). This spectrum has been further described in other work [146, 147] giving rise to the following equation:

$$\Phi_{xx}(f) = \frac{a^2}{f_p}\frac{(N+1)}{N}\left[\frac{\sin f\pi / f_p}{f\pi / f_p}\right]^2 \qquad (8)$$

Where a is the amplitude of the PRBS (Figure 34) and N is as in equation (7). The minimum frequency step being defined by the number of terms in the sequence and the frequency of the clock pulse. The minimum frequency step is shown in equation (9).

$$f_{\min} = \frac{f_p}{N} \qquad (9)$$

The PRBS is bandwidth limited at a frequency which is less than the clock frequency, and Davies [144] derives this as the half power point:

$$f_{\max} = \frac{f_p}{3} \tag{10}$$

This useful frequency band is shown in Figure 35. The power spectrum of the PRBS is an equally spaced series of spikes spaced at f_P/N intervals and it can be seen that the FFT reaches zero value at the PRBS clock frequency and its harmonics.

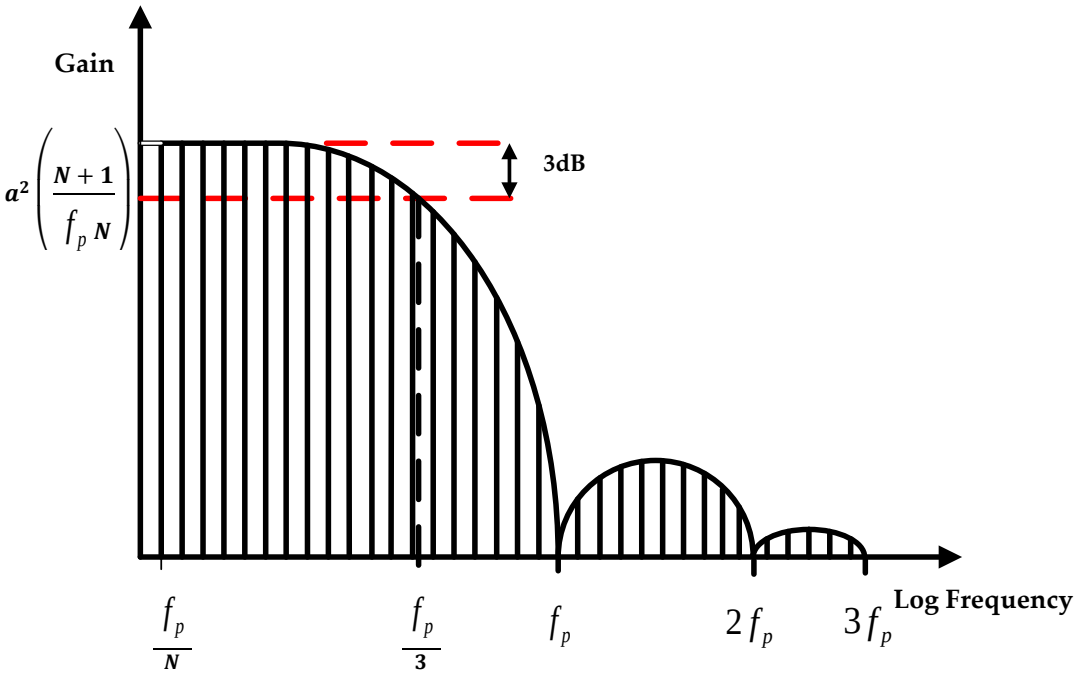

Figure 35. Power spectrum (FFT) of a PRBS showing usable frequency band

This band limit has been explored somewhat during the course of this and other research [147] with a wider band technique, with verified results using an incremented clock was developed during this work.

The duration of a test using a PRBS will be defined by the overall period of the PRBS. This period (T) is defined by the clock pulse width and the bit length, in the case of a 4 bit sequence clocked at 1Hz,

$N = (2^n - 1) = 15$ terms

Therefore T=15 seconds.

It therefore follows that using a high bit sequence with a low frequency clock leads to a long duration test. The design of the PRBS should therefore consider usable bandwidth, frequency of interest and the resulting test duration. The relationship between these three key parameters can be seen in Table 6.

Table 6. Relationship between bandwidth, bit length (n) and test duration for a PRBS clocked at 1kHz.

PRBS bit length (n)	PRBS sequence length (N)	Clock frequency (Hz)	Test duration (s)	Bandwidth (Hz)
4	15	1000	0.015	66.6-333
6	63	1000	0.063	15.9-333
8	255	1000	0.255	3.92-333
10	1023	1000	1.023	0.98-333
12	4095	1000	4.095	0.24-333
14	16383	1000	16.383	0.06-333
16	65535	1000	65.535	0.015-333
18	262143	1000	262.143	0.0038-333
20	1048575	1000	1048.575	0.00095-333

As the bit length of the PRBS increases, there are diminishing returns with the increase in usable bandwidth. The disadvantage of the use of excessively long sequences can therefore be seen with the increase in required test duration to capture a complete sequence.

The developed approach to utilising the PRBS as an excitation signal required examination of how that signal could be applied to a battery or cell under test. Clearly a battery presents itself as a low impedance, and as such applying a voltage perturbation requires a low impedance source. As such it was decided that a current mode approach would be developed where constant current

pulses would be applied to the battery in either charge or discharge mode during the tests, and three modes of test were devised for the investigation.

4.8.4 Monopolar Pseudo Random Binary Sequence excitation (discharge mode)

Monopolar excitation was examined as a test type for the research and the operation of this testing concerns application of a load to the battery under control of the designed PRBS excitation. The motivation for adoption of this test mode was based on the hardware being relatively easy to develop, and limiting the operational criteria for the test battery. Under a test load, the battery would not experience any charge to discharge transient conditions, there is no possibility of overcharge, and the mode would be used as the first method for proving the technique.

It was accepted that the actual test does discharge the battery to some degree, so short test durations were devised. Additionally, the current perturbation test signal should not be designed to unnecessarily provoke Peukert effects, but should have an appropriate current level to provide a meaningful and noise immune result.

The amount of energy removed from the battery is clearly relevant in that any correlations sought to be made between the test results and the battery SoC will be compromised by the test itself. Peukert's effect [120] – loss of capacity with increase discharge rate, can be avoided by using a test load at or around the c_r/t_r discharge rate.

"Coup de fouet" can be significant in battery testing results, so the test load was selected to ensure the effect is not excessively pronounced, and the data examined for the characteristic drop in terminal voltage followed by a partial recovery. The initial investigations with this test mode are explored in chapter 5, and the technique is used extensively throughout the work.

4.8.5 Monopolar Pseudo Random Binary Sequence excitation (charge mode)

The charge mode testing was devised in order to explore any differences in applying a charge pulse to a test battery, in comparison with the discharge mode testing. Furthermore, the effect of adjusting the charge ceiling voltage was of interest as a means for SoC evaluation in this mode. The method is explored in chapter 6, and yielded valuable comparative results to the discharge mode tests.

4.8.6 Bipolar Pseudo Random Binary Sequence excitation

Bipolar mode PRBS battery excitation offers the least intrusive test to the battery, in that the net energy applied by the test is zero, and only the battery efficiency at the perturbation current amplitude should apply. The test mode requires complementary power stages delivering and removing current under influence of the PRBS. The technique is given a thorough treatment in chapter 7, and demonstrated the envisaged benefits of a net-zero energy test.

4.9 Conclusion

In reviewing the existing battery testing technologies it becomes clear that no single battery test scheme offers "all things to all men", and as such various methods are employed to establish battery state. Table 7 shows a summary of the technologies examined, and their limitations and applicability. With the exception of specific gravity, the commercial battery management integrated circuits commercially available exploit the majority of the test techniques and implement a hybrid scheme.

The areas of novelty identified for investigation were concerned with the detailed examination of frequency-rich perturbation signals for a battery parameter estimation scheme in the frequency domain.

Further to this, an examination of three specific modes of PRBS application (load, charge and load/charge) were to be carried out to establish if there were discernible differences in the respective test modes.

The development of on-line hybrid battery testing schemes in one or more of the described modes, allowing the battery to be continuously evaluated without disconnection from the host equipment, using current and voltage responses to provide indicators of battery state.

And finally, development of the PRBS technique into a software based embedded solution allowing low cost implementation of the technology and possible incorporation into hybrid schemes such as commercially available battery management ICs.

An investigation of these techniques using PRBS is detailed in the following chapters.

Table 7. Battery testing technologies investigated in the course of the research

Battery test scheme	Suitable batteries	Calibration factors	General applicability	Limitations	Equivalent circuit parameter identification*
Specific gravity	Flooded Lead-Acid	Temperature	SoC	Operator interaction required, acid burn risk	C_{Bulk}
Terminal voltage measurement	All chemistries	Temperature, load, charge	SoC/SoH	Requires known load conditions and history	C_{Bulk}
Discharge testing	All chemistries	Temperature, load	SoC	Long duration test, carried out off-line.	C_{Bulk}
Pulse load testing	All chemistries	Temperature	SoH	Requires close to 100% SoC for repeatability	Ri and Cs possible with careful design)
Charger margin	All chemistries	Temperature, load	SoC/SoH	Requires a known constant load, lengthy test	C_{Bulk}
Coulomb counting	All chemistries	Temperature	SoC	Unsuitable for standby systems. Requires periodic recalibration	C_{Bulk}
AC Impedance testing	All chemistries	Temperature	SoH	Spot impedance result at chosen frequency	Ri, Rt, Cs
Battery management ICs	Predominately Li Ion	Historical data	SoH, SoC	Requires historical data to calibrate algorithms. Designed for OEM LiIon battery packs	Potentially all parameters

*For parameter definitions see figure 36, page 118.

Chapter 5. Discharge mode Pseudo Random Binary Sequence battery testing

5.1 Introduction

The following chapter examines the PRBS technique for evaluating battery state using a constant current load being excited by the designed sequence. The work was carried out early in the body of research and the motivation for the investigation was concerned with proving the technique in terms of its ability to identify impedance for the test batteries, and indeed to be able to differentiate between batteries in different states-of-health (SoH). This chapter introduces the test method, and seeks to make initial comparisons between the results obtained and those obtained through conventional testing. Further to this observations are made in relation to a standard model for batteries and cells, and the foundations laid for further model development.

5.2 Battery Models

Basic electrical models for electrochemical cells are widely employed to aid the analysis of energy storage systems, and in the analysis of batteries, several models are in widespread use. These models may be borrowed from their usage in analysis of electrochemical cells which may not specifically be electrical energy storage devices, and this is demonstrated with the diverse application of the models, with

examples ranging from DNA analysis [148] to modelling of reinforced concrete corrosion [149].

In the general approach to battery modelling an R-C linear equivalent circuit model is employed, which in its most simplistic form, comprises a capacitor, representing the bulk energy store, and a series resistor. This model, however, is limited in use, as it does not fully describe the chemical processes within the battery. It therefore follows that an improved model, with representation of the predominant chemical phenomena, should be used as the basis for further evolution of the described system. Detailed models have been developed for secondary cells using this approach [52], which generally evolve from the familiar Randles' model [150] which is used for the work described in this chapter. The model is a straight forward electrical representation of the complex electrochemical processes, with lumped parameters representing dominant battery behaviour. The model assumes the cell behaviours under both charge and discharge conditions are identical, and charge transfer is achieved with 100% efficiency.

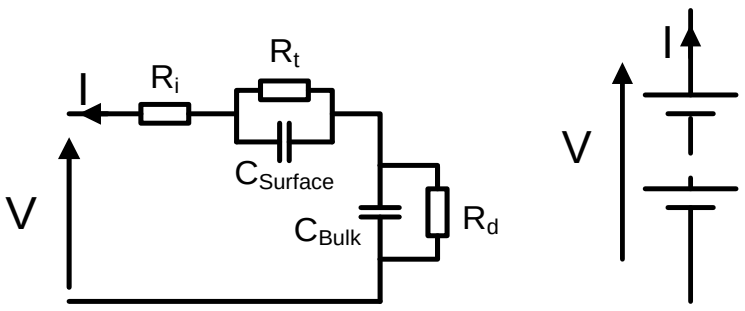

Figure 36. Randles equivalent circuit

Figure 36 shows the Randles' model which was used for the basis of the initial model development. R_i is the lumped resistance for the electrolyte and cell interconnections

and represents the major series resistance for the cell. $C_{Surface}$ is a double layer capacitance, which is a result of the charge separation at the interface between the electrolyte and the cell plate [13, 16]. R_t, connected in parallel with the double layer capacitance is the charge transfer polarisation, and this parallel branch controls transient behaviour of the battery.

C_{Bulk} represents the dominant capacitive element of the cell and R_d is the self-discharge resistance of the cell. R_d is typically high for a healthy cell, and is most commonly quoted by the manufacturer in terms of a percentage discharge in a specified time. Yuasa provide a figure of 3% per month self-discharge at 20ºC for their NP battery range, which translates into a value for Rd of approximately 5kΩ, for the 65Ah batteries used in the experiments [12].

Calculation of R_d can be carried out as follows:

3% per month self-discharge at 20°C

3% of 65Ah = 1.95Ah capacity loss in the first month

One month = 30 days at 24 hours, 720 hours total

Therefore 1.95Ah/720 hours = 2.71×10^{-3} A discharge current

Assuming a fully charged battery, terminal voltage will be approximately 13V

Using Ohm's law, V= I x R

$$13 = 2.71 \times 10^{-3} \times R_d$$

Therefore, $R_d = 4.797k\Omega$

So the general formula for evaluating R_d:

$$R_d = \frac{V_{OCT}}{\frac{\frac{SD}{100} \times c_r}{720}} \qquad (11)$$

$$R_d = \frac{720 \times V_{OCT}}{\frac{SD}{100} \times c_r} \quad (12)$$

Where V_{OCT} = battery open circuit terminal voltage

SD = self-discharge rate (%/month)

c_r = rated battery capacity in Ah

5.3 Cell parameter estimation by conventional methods

Analysis of cells and batteries by conventional means is well understood, and a number of methods can be employed to determine appropriate vales for the equivalent circuit components. In order to validate the results of the PRBS testing, it was necessary first to establish the equivalent circuit parameters using conventional tests employing step load pulses, and controlled constant-current discharges.

5.3.1 Determination of C_{Bulk}

Establishing the overall capacity, and from that the bulk capacitance, of a test battery employs a straightforward, albeit lengthy, discharge test. The test battery had a specified capacity at a 20 hour discharge rate, and as such a constant current load of $0.05c_r$ was applied. Manufacturers data for the battery [17] was consulted for the End-of Discharge voltage (V_{EoD}). This V_{EoD} (10.5V for this battery @ 20°C) allows direct calculation of C_{Bulk} from the published capacity and the initial terminal voltage at 100% SoC. Therefore, these initial estimates of the bulk capacitance value of a battery can be made before

verification by experiment, based on estimated initial open-circuit-terminal (V_{OCT}) and end (V_{EoD}) voltages. Discharging the battery then provides the actual battery capacity, by measurement of discharge time to V_{EoD} from the steady state V_{OCT}.

Prior to the capacity discharge test the batteries were charged at a constant (float) voltage, using a temperature compensated battery charger (VxI Power Oracle 200E). The batteries were then left for a period of 4-6 hours in an open circuit condition for the internal chemical processes to stabilise in order to establish a stable off-charge terminal voltage (V_{OCT}). A discharge test was performed, corresponding to the 20 hour discharge rate, ($0.05c_r$) and the two test batteries were discharged. Figure 37 shows the discharge profile for the batteries.

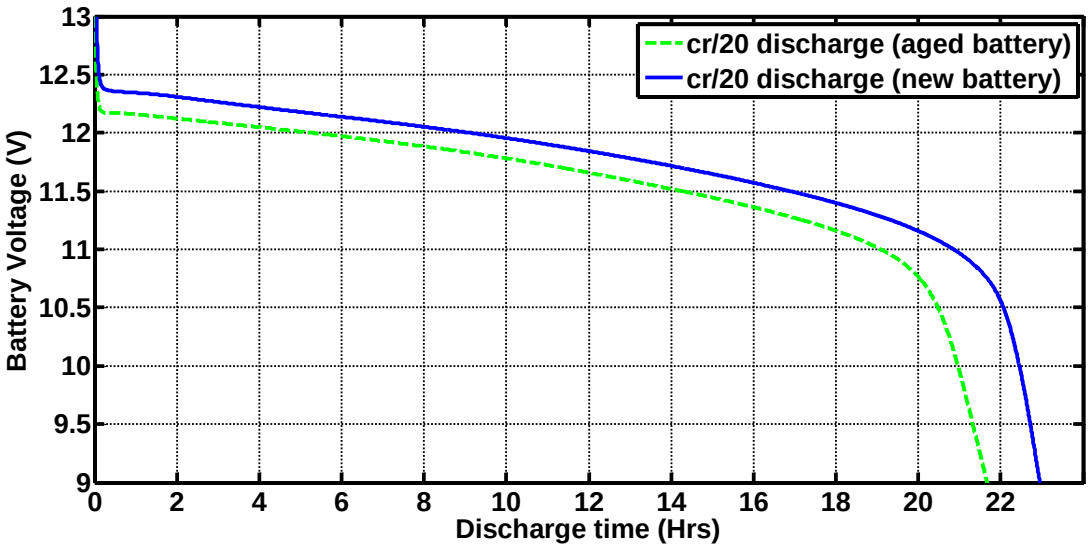

Figure 37. Actual discharge curves for the batteries tested, $c_r/20$ discharge rate, 20°C.

The capacity in Ah is calculated, from which the energy transferred from the battery to the load, W_{CBulk}, can be determined. A value for the bulk capacitor is obtained by equating from the capacitor energy equation.

$$W_{CBulk} = \frac{1}{2} C_{Bulk}(V^2) \quad (13)$$

$$= \frac{1}{2} C_{Bulk}(V^2{}_{OCT} - V^2{}_{EoD}) \quad (14)$$

Capacity in Ampere-seconds:

c_{AS} = discharge current (A) x time (s) (15)

Therefore,

$$C_{Bulk\ Initial} = \frac{C_{AS} \times V_{OCT}}{\frac{1}{2}(V_{OCT}^2 - V_{EoD}^2)} \quad (16)$$

Analysis of the discharge curves for the new and aged batteries revealed a difference in capacity of 7% as shown in table 8.

Further tests were therefore carried out to establish the variation in C_{Bulk} with increased discharge. As discussed in chapter 3, Peukert's equation describes how Lead-Acid cells and batteries vary in available capacity for different rates of discharge, and it is known from the authors work in industry that the Peukert coefficient of a battery can be affected be declining SoH. The batteries were subjected to $c_r/4$, $c_r/2$ and $1c_r$ discharges, and the results from the discharge tests for both batteries can be seen in Figure 38. With increased discharge rates deviations from expected performance were observed. For the higher rate discharge tests capacity differences between the two batteries increased, rising to around 20% for the 1c test on the aged battery, with a characteristic steep fall in terminal voltage seen on application of the load. This further indicated the degrading SoH of the aged battery

and possible trends towards end of life. The tabulated values for bulk capacitance are presented in table 8.

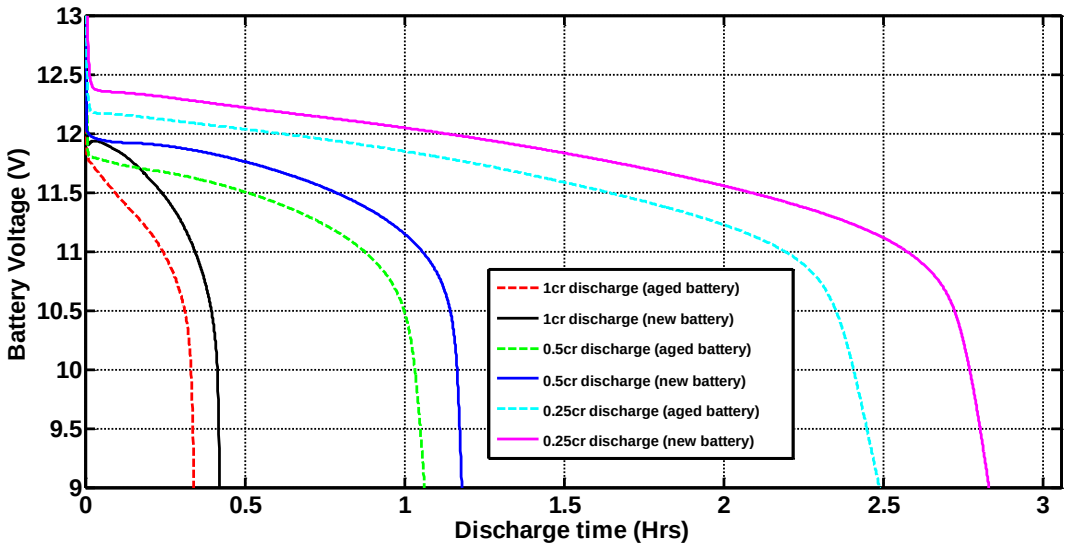

Figure 38. Discharge curves for the test batteries at discharge rates of 0.25c_r, 0.5c_r and 1c_r (20°C)

Table 8. Bulk capacitance with discharge rate

Discharge rate / C_{Bulk} (F)	1cr	0.5cr	0.25cr	0.05cr
New battery	29,210	48,020	62,730	121,960
Aged battery	23,300	43,160	54,150	115,205

5.3.2 Determination of $C_{Surface}$, R_i, R_t

The evaluation of $C_{Surface}$ requires a slightly different approach to that of C_{Bulk} in that $C_{Surface}$ is most apparent during transient conditions from discharge to off-load situations, and it is important that the method employed is not affected by C_{Bulk}. Previous work [151] has shown that the time constant associated with

C_{Bulk} is very much larger than that associated with $C_{Surface}$, and therefore a test pulse duration of short duration compared to the time constant associated with C_{Bulk} can be easily selected to reveal $C_{Surface}$. Typical pulse widths of 500mS (2Hz) have been quoted in previous work for small capacity cells [41].

The test employed a constant current discharge of 20A from a fully charged state, during which, short interruptions to the load were made in order to observe the transient terminal voltage of the batteries. Figure 39 shows the terminal voltage of one of the batteries, observed during the test, with figure 40 showing the response zoomed to show more detail.

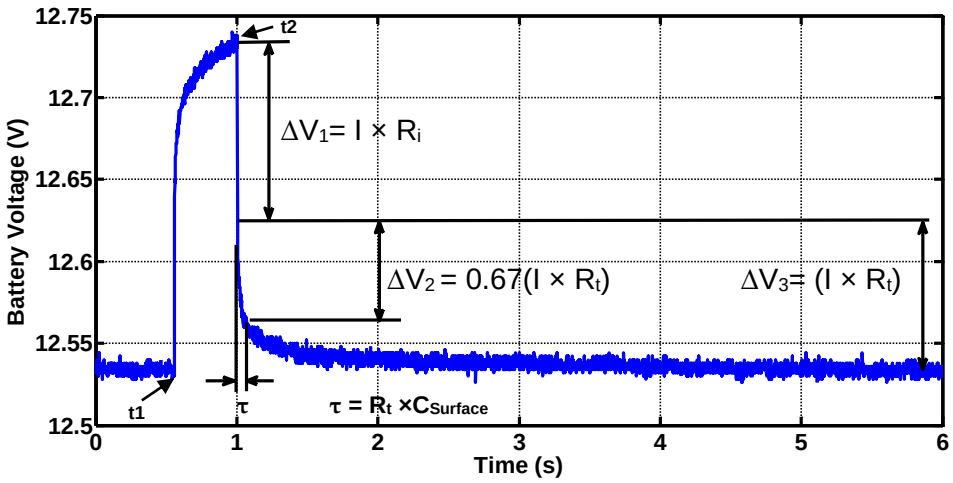

Figure 39. Off-load step response used in calculation of model parameters

Prior to time t_0 the battery has been discharging to some time at a constant current and the terminal voltage is considered to be in a time-limited pseudo steady-state. During this time it can be assumed that the decay in terminal voltage is completely attributable to the discharge of the bulk capacitor. As the load is removed ($t=t_1$), a step change in the terminal voltage occurs, which is predominantly due to the series impedance, R_i. Following the step

change $C_{Surface}$ begins to charge (previously discharged during the load period).

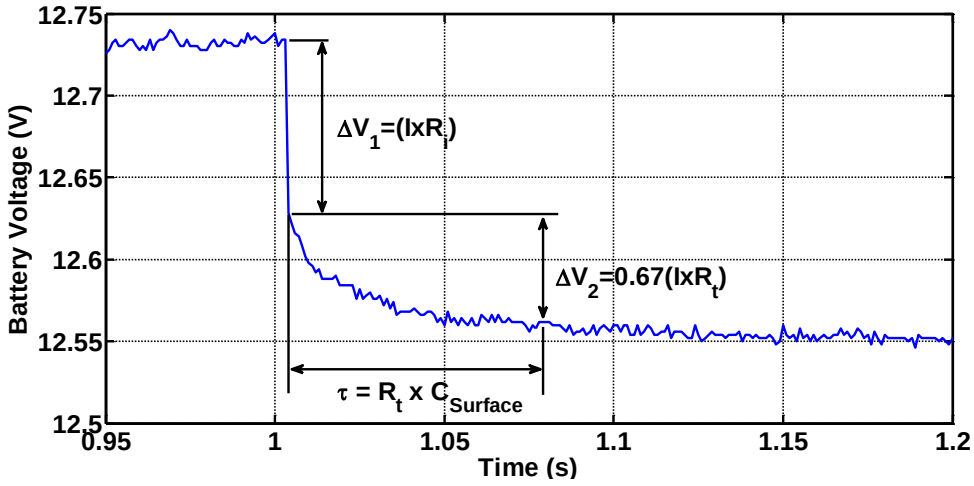

Figure 40. Off-load step response zoomed to show detail

The load is re applied ($t=t_2$), and again the effect of R_i is seen, followed by the discharge of $C_{Surface}$ (time duration τ). As previously discussed the value of $C_{Surface}$ is several orders of magnitude smaller than C_{Bulk} allowing a reasonable degree of clarity regarding measuring the time constant.

From the responses obtained, the equations below were used to obtain the parameters of interest, shown in table 9.

$$R_i = \frac{\Delta V_1}{I} \tag{17}$$

$$R_t = \frac{0.67I}{\Delta V_2} \tag{18}$$

$$C_{Surface} = \frac{\tau}{R_t} \tag{19}$$

5.3.3 Determination of R_d

The measurement of R_d is carried out by observing the decay of V_{OCT} for a fully charged battery that has been allowed to achieve a steady-state terminal voltage subsequent to the charging process. The test batteries were fully charged and connected to a data acquisition system of sufficiently high input impedance (>1MΩ) as not to effect the self-discharge caused by R_d. The decay in terminal voltage was measured over several weeks in order that the value of R_d could therefore be calculated using equation 11 in section 5.2.

5.3.4 Experimental results

The parameters obtained from the conventional tests can be seen in table 9.

Table 9. Parameters obtained from the test batteries using the conventional tests

	New battery	Aged battery
V_{OCT} (V)	12.846	12.807
V_{EOD} (V)	10.5	10.5
Capacity (As)	259,992	241,839
C_{Bulk} (F)	121,960	115,205
$C_{Surface}$ (F)	14.81	5.59
R_i (mΩ)	5.08	5.6
R_t (mΩ)	5.18	6.5
R_d (Ω)	5,034	4,955

5.4 Pseudo Random Binary Sequence (PRBS) battery analysis

In order to design the PRBS tests, the conventional test data was used to make predictions regarding the PRBS design parameters. Simulations were carried out using a sampled data model, which informed the PRBS design.

5.4.1 Sampled data model analysis

The parameters obtained from the conventional tests (Table 9) allowed an examination of the impedance response for the battery using computational techniques. The results of this approach were used to inform the PRBS design process, in presenting the frequencies of interest, and therefore facilitating the choice of clock frequency, and the required bandwidth.

Throughout this work the magnitude of complex impedance is used, and based on the selected Randle's model, the overall battery impedance can be expressed in complex form, assuming constant temperature:

$$Z_{Batt} = \frac{1}{\frac{1}{R_d} + \frac{1}{XC_{Bulk}}} + \frac{1}{\frac{1}{R_t} + \frac{1}{XC_{Surface}}} + R_i \qquad (20)$$

A sampled data model was created in MATLAB, with a PRBS sequence generated and applied to the Randles' model, with values for the equivalent circuit established earlier (Table 9). For completeness the sampled data model (sdm1a.m) is included in the appendices in 15.8.1. FFTs of both the input current waveform and the corresponding battery terminal voltage were

evaluated (Figures 41 and 42), with the evaluated impedance over the usable frequency band shown in Figure 43.

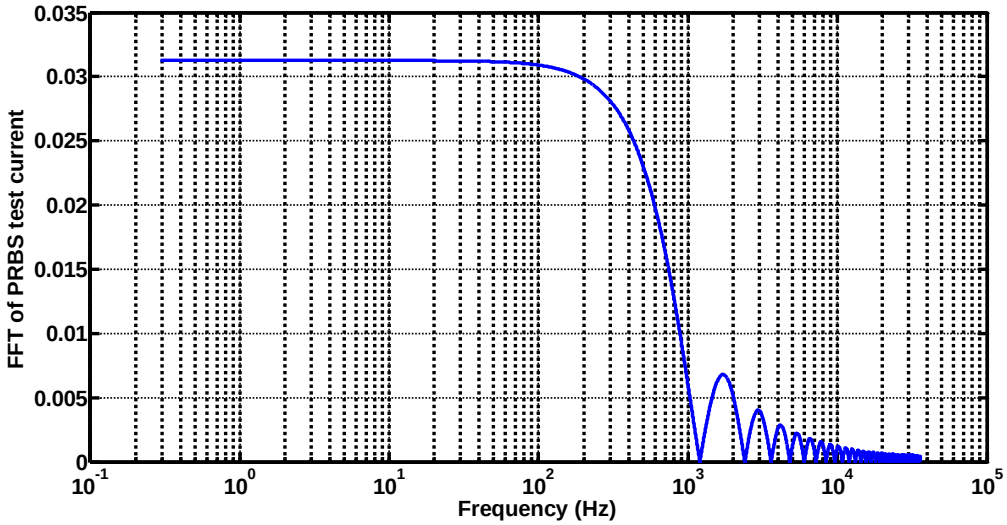

Figure 41. Simulated current FFT plots using experimental battery data

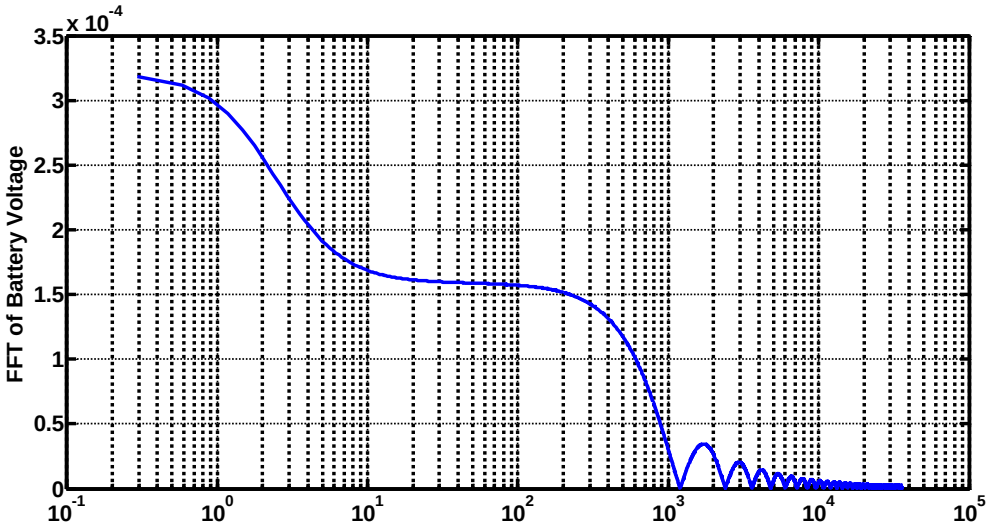

Figure 42. Corresponding Voltage FFT with the PRBS applied to the Randle's model

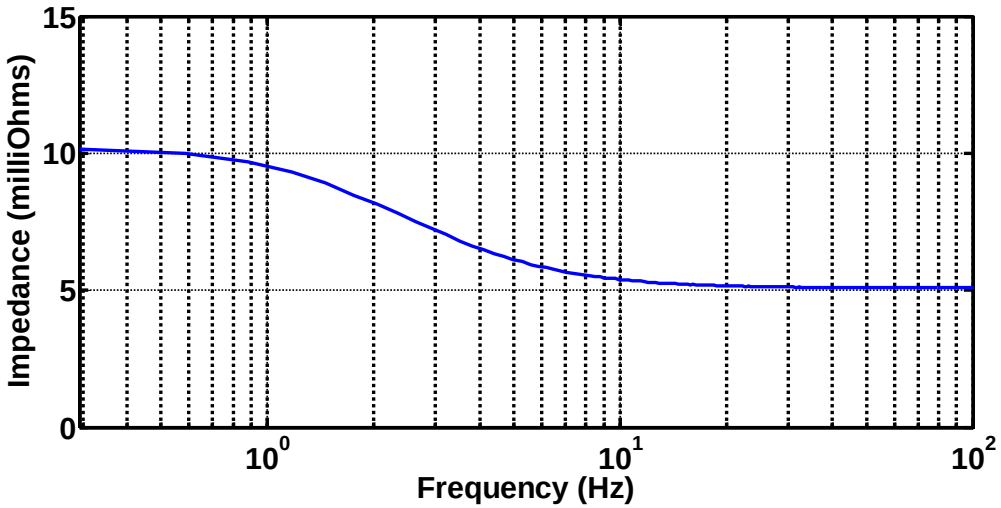

Figure 43. Impedance plot resulting from the experimental data

A number of simulations were carried out, and it became apparent that exciting C_{Bulk} would prove a problem due to the high value of this component leading to an extremely long test. For example, if we consider C_{Bulk} to be in the order of 120,000F for the new battery at the $0.05c_r$ discharge rate (table 9), the frequency response range over which the impedance is of interest is in the order of 10^{-7} Hz and lower. Hence the clock frequency for the PRBS would need to be in the same order and $1/10^{-7}$ H_z = 165 days - for the clock pulse alone.

Applying similar analysis to the other circuit parameters from table 9, a clock frequency of 1200Hz was chosen, in conjunction with a 12 bit PRBS sequence, giving a sequence length of 4095 (2^{n-1} where n=12). This would excite the remaining components in the equivalent circuit and give a test duration of around 3.4 seconds (4095/1200Hz). This investigation is expanded in later chapters to provide correlations between the readily examinable parameters to C_{Bulk}.

5.5 Experimental PRBS investigation

Tests were devised to explore the PRBS test technique in comparison to the conventional tests. The objective of these tests were to form a basis for the work in later chapters.

5.5.1 Temperature considerations

Tests were carried out at constant temperature, with consideration given to self-heating of the battery during the test. An estimate for self-heating was made based on overall battery impedance of tens of milliohms and a PRBS current amplitude of 10A at 50% duty cycle.

Power = $I^2R = (10/2)^2A \times 20m\Omega$ (approximately)

= 0.5 Watts, or 0.5 Joules for every second of test

Specific heat capacity of Lead = 112 J/kg°C [152]

If the test battery mass = 23kg and we assume 70% of the battery mass is lead:

112 J/kg°C x 16.1kg = 1803.2J to raise the battery temperature by 1°C

It was therefore decided the PRBS tests would not significantly affect the battery temperature.

5.5.2 Test system description

A high-power battery cell characterisation apparatus, (Figures 44 and 45), was developed featuring data acquisition, high-bandwidth current amplifier and

PRBS generator. The test rig was developed in a modular format allowing later expansion, and eventual incorporation into a combined-mode test system.

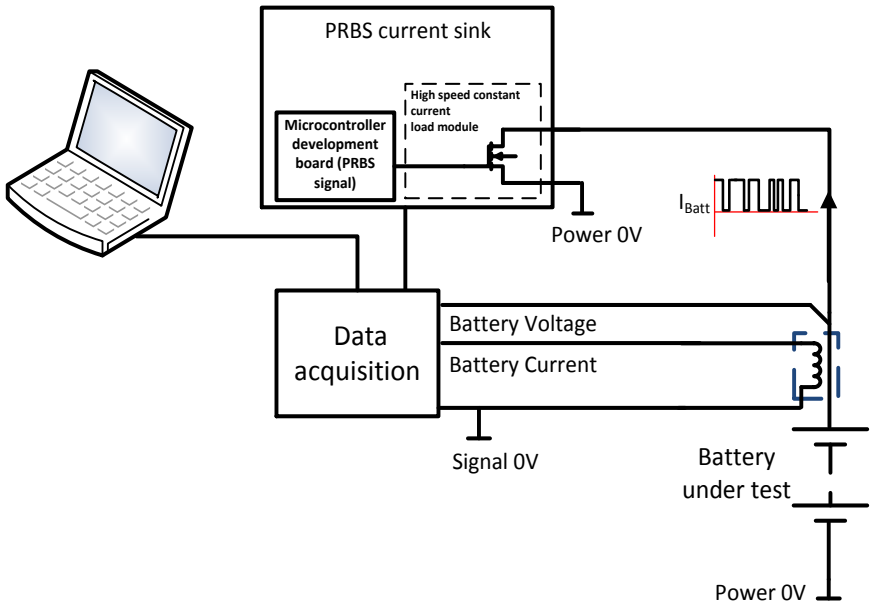

Figure 44. Test system block diagram

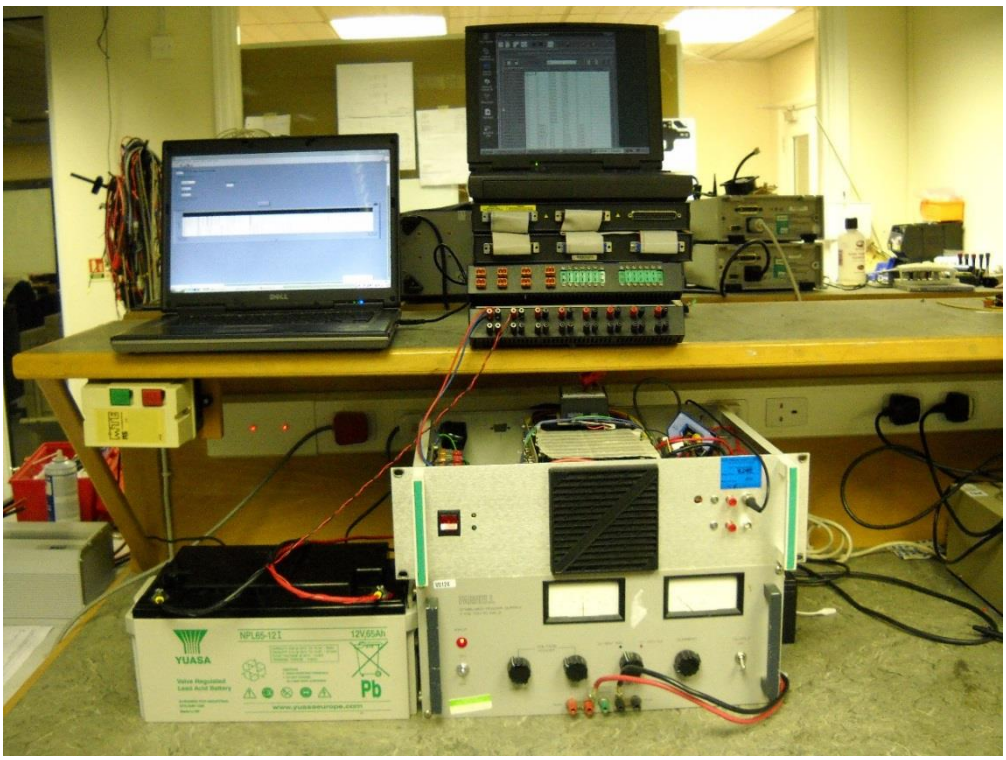

Figure 45. Photograph of test rig

The system comprised a high speed constant-current load module (Figure 46) with PRBS signal input provided by an external embedded processor, allowing straightforward implementation of the input signal.

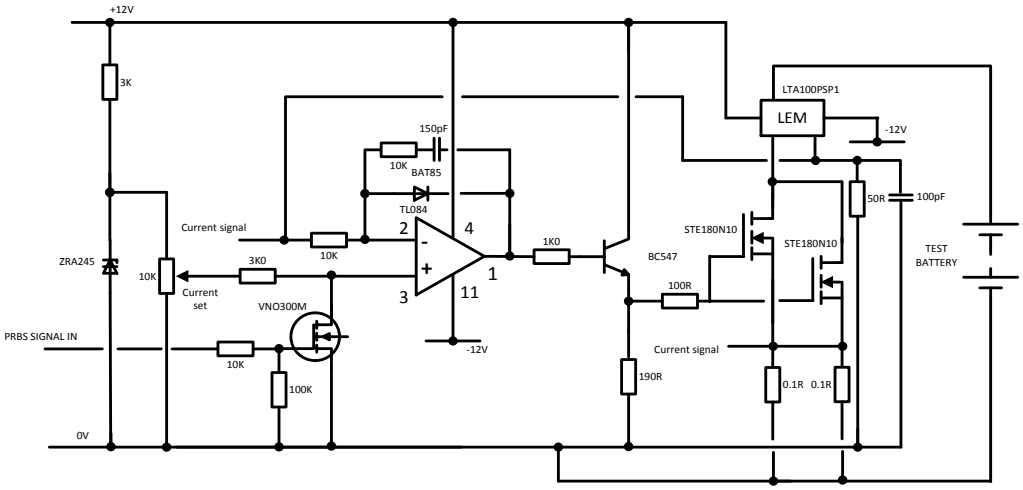

Figure 46. Power stage schematic, PRBS discharge tests

A pair of parallel connected MOSFETs with low value series resistors reduced the dissipation within the semiconductor devices. The current programming was user selectable up to 20A, and the control system itself was supplied from an instrumentation grade linear power supply to avoid noise issues. Closed loop analogue control of the MOSFET bank provided rapid operation and close control over the transient response which allows drive by the PRBS to be replicated with minimal settling time and reduced rise/fall times. A two channel, redundant current measurement system was implemented, with a raw current signal being able to be captured from any one of the MOSFET series resistors, with a second channel acquiring data from the output of a LEM LTA-100PSP1 current transducer.

Data acquisition was provided by a proprietary system from IOTech (full specification can be found in appendices, 15.6) at sampling rates of up to 32kHz available with 16 bit resolution. Initial charge is provided by a closely controlled battery charger manufactured by VxI Power Ltd [153].

5.5.3 Test procedure

The battery was fully charged, and allowed to establish a steady-state terminal voltage over four hours, before the tests were carried out. The current pulse amplitude was selected in order to provide good signal to noise ratio, without producing a significant discharge (PRBS pulse amplitude set to 10A, 0.15 c_r).

The excitation signal was applied to the test system using a Microchip development board, running a simple routine in C. The PRBS sequence was generated by a software implemented 12 bit shift register, with a clock frequency in the order of 1.2 kHz allowing a good combination of test duration, bandwidth and resolution.

5.5.4 Test results

Examples of the acquired data can be seen in Figures 47 and 48. The evaluation of impedance from battery test results was carried out using MATLAB code written to evaluate FFTs of both the PRBS current and voltage waveforms, then evaluate these using Ohm's law. In the literature it is well acknowledged, [144, 154, 155] that to minimise the effects of spectral leakage and other artefacts,

complete PRBS sequences must be processed. This was demonstrated during the off line processing, in that the capture of non-exact sequences gave rise to considerable signal spectral content degradation. Correspondingly the analysis routines written in MATLAB extracted exact sequences of acquired data to be processed. Initially, using inspection, the data start of the PRBS was established, and from that the sequence length was calculated by a MATLAB function (fourseq.m), based on sampling rate, bit length and clock frequency. The code also provided a check of data integrity, by plotting the current FFT, which easily confirms the data sample by inspection, providing a clean PRBS FFT. The routine is included in section 15.7.4 of the appendices. Once the data start and sequence length were verified, the data was processed using evalprbs.m which carried out the impedance calculation using the FFTs of PRBS terminal voltage and excitation current. The routine is included in the appendices (15.7.5).

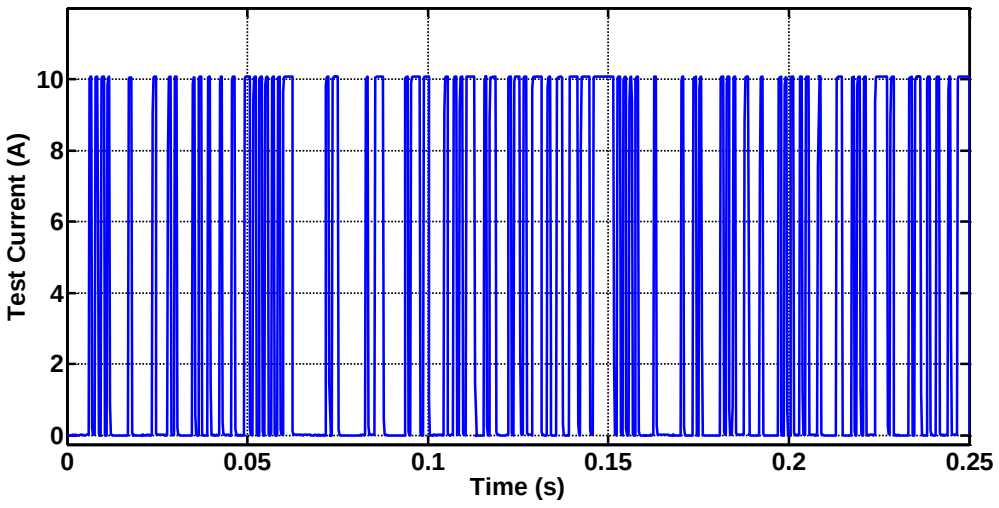

Figure 47. Extract from the PRBS current perturbation signal

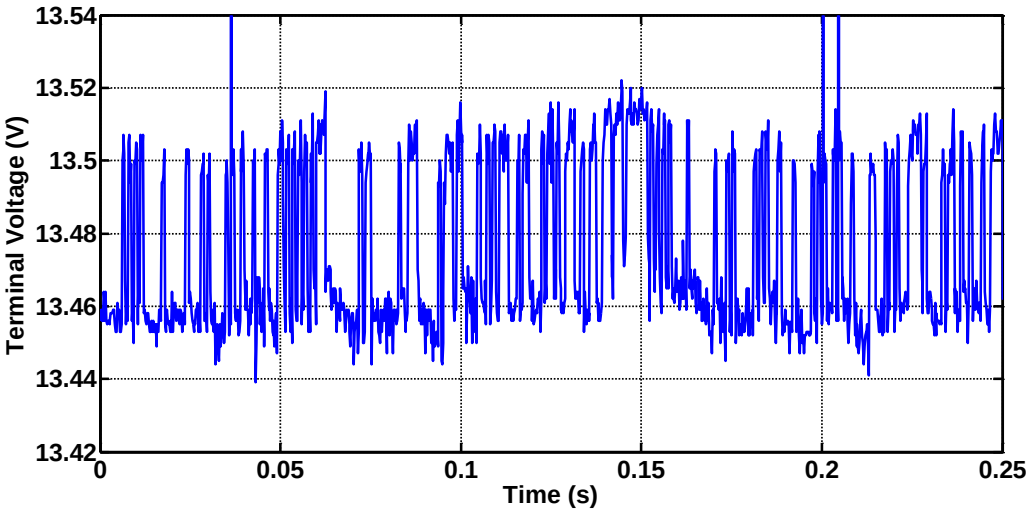

Figure 48. Battery terminal voltage during PRBS test

As previously discussed, the values of R_i, R_t and $C_{Surface}$ were examined within these experiments.

The values for R_i, R_t and $C_{Surface}$ can be obtained directly by inspection and calculation. Considering points on the response, multiple impedances present themselves corresponding to the components at these frequencies, which will be directly influenced by $C_{Surface}$ itself.

Referring back to Figure 34, the response tends to R_i at high frequency. Moving towards the lower frequencies the effect of $C_{Surface}$ increases and the impedance of the parallel combination of $C_{Surface}$ and R_t becomes significant. This impedance is (in complex form):

$$Z(\omega) = \frac{1}{\frac{1}{R_t^2} + \frac{1}{XC_{Surface}^2}} + R_i \qquad (21)$$

Calculating a value for $C_{Surface}$ without R_t can be carried out by taking more than one point from the impedance results, and solving simultaneous equations at frequencies ω_1 and ω_2. Therefore, if Z_{t1} and Z_{t2} are two complex impedances at frequencies ω_1 and ω_2 respectively, the impedance of the parallel combination of R_t and $C_{Surface}$ at these frequencies will be:

($XC_{Surface1}$ and $XC_{Surface2}$ are the reactance of $C_{Surface}$ at ω_1 and ω_2 respectively).

$$Z_{t1} = \frac{1}{\left(\frac{1}{R_t} + \frac{1}{XC_{Surface1}}\right)} + R_i \qquad (22)$$

Therefore:

$$\frac{1}{R_t} = \frac{1}{Z_{t1} - R_i} - \frac{1}{XC_{Surface1}} \qquad (23)$$

And

$$\frac{1}{R_t} = \frac{1}{Z_{t2} - R_i} - \frac{1}{XC_{Surface2}} \qquad (24)$$

Equating:

$$\frac{1}{Z_{t1} - R_i} - \frac{1}{XC_{Surface1}} = \frac{1}{Z_{t2} - R_i} - \frac{1}{XC_{Surface2}} \qquad (25)$$

Solving for $C_{Surface}$:

$$\frac{1}{Z_{t1} - R_i} - \frac{1}{Z_{t2} - R_i} = \frac{1}{XC_{Surface2}} - \frac{1}{XC_{Surface1}} \qquad (26)$$

$$\frac{1}{Z_{t1}-R_i}-\frac{1}{Z_{t2}-R_i}=\frac{1}{j\omega_1 C_{Surface}}-\frac{1}{j\omega_2 C_{Surface}} \tag{27}$$

$$\frac{1}{Z_{t1}-R_i}-\frac{1}{Z_{t2}-R_i}=j\omega_1 C_{Surface}-j\omega_2 C_{Surface} \tag{28}$$

$$C_{Surface}=\frac{\frac{1}{Z_{t1}-R_i}-\frac{1}{Z_{t2}-R_i}}{(j\omega_1-j\omega_2)} \tag{29}$$

Figures 49 and 50 below show responses from the batteries under test.

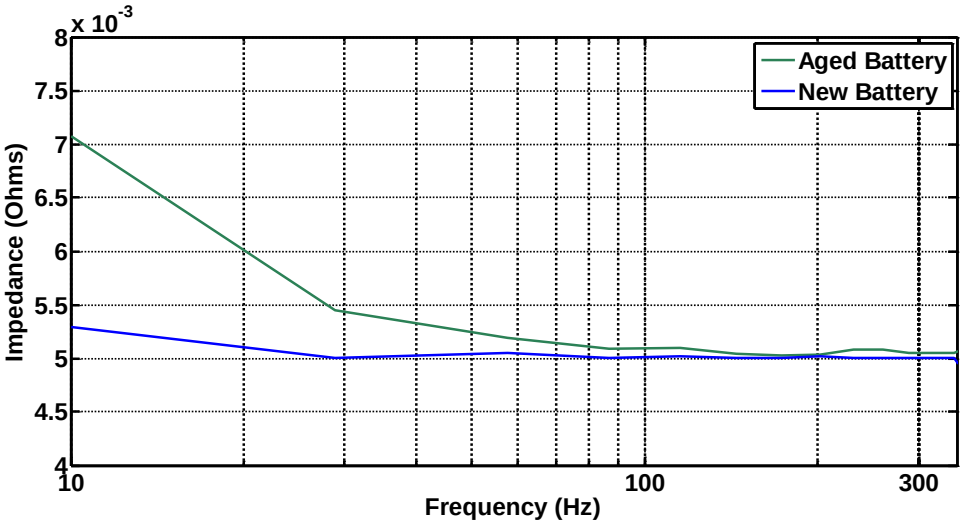

Figure 49. 10Hz-300Hz, Impedance responses, showing effect of $C_{Surface}$ and R_t in parallel, in series with R_i

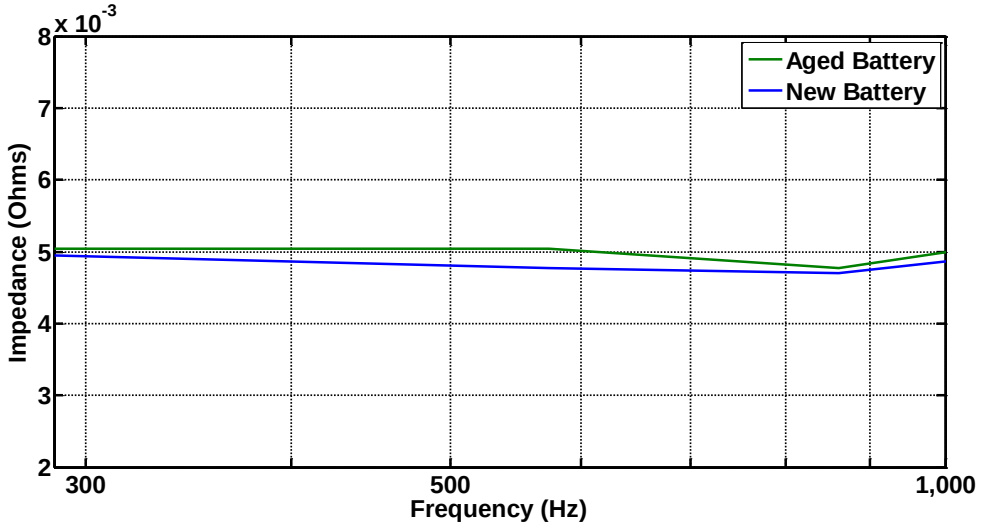

Figure 50. 300Hz-1000Hz Impedance responses showing response tending to the value of R_i

Using equation 29 above $C_{Surface}$ was evaluated in MATLAB using two frequency points at 10Hz and 300Hz, This was carried out within evalprbs.m (15.8.5, do_z_calc) allowing phase to be taken into account from the impedance results. The value for $C_{Surface}$ was then subsituted back in to equation 23 within the same MATLAB routine to obtain Rt. A summary of the results are found in table 10.

The PRBS analysis of the two batteries yielded some interesting results in that the values obtained for R_i for the load-step test in section 5.3.2 and frequency domain tests were in the healthy range expected for both batteries. The manufacturer's data sheet is included in 15.7.1 indicates an impedance of 5mΩ at 1 kHz, (which corresponds to R_i) and an internal resistance of 10.51mΩ (R_i + R_t). This is interesting in that the aged battery was expected to be more obviously degraded, yet measurement of C_{Bulk} revealed a reduction in rated

capacity of only 7%. The value of $C_{Surface}$ yielded the most information, the aged battery showing a considerable reduction in this value. Despite appearing relatively healthy this hinted at the underlying age of the battery and therefore a potential indicator of SoH.

This confirmed the earlier findings of the higher rate discharge capacity tests in section 5.3.1 where the differences in capacity between the aged and new batteries increased (Figure 37). The tests indicated the aged battery tending towards 20% reduction in capacity at the $1c_r$ discharge rate, further indicating the degradation of the aged battery (table 10).

Table 10. Experimental results, pulse test results from table 9 in parentheses.

	New battery	Aged battery
C_{Bulk} (F) (static test)	**121,960**	**115,205**
$C_{Surface}$ (F)	**16.4 (14.8)**	**4.5 (5.6)**
R_i (mΩ)	**5.0 (5.1)**	**5.1 (5.6)**
R_t (mΩ)	**4.0 (5.2)**	**4.2 (6.5)**

5.6 Conclusion

The work within this chapter demonstrated the PRBS parameter identification technique as applicable to the test batteries. The PRBS tests were successfully verified

through experimental comparison to results obtained by the conventional established testing methods. Comparisons to conventional current pulse and discharge test methods showed clear advantages of the PRBS technique. The parameters were identified with short duration tests, and it was shown that battery in declining SoH could be identified by differences in the frequency response and in turn equivalent circuit parameters.

Commercial battery test equipment generally operates at singular frequencies in the 1 kHz range [132], only R_i can be examined, and in the case of the test batteries the comparative conventional tests showed this value to be in a healthy range.

Similarly, the PRBS tests showed these indications for R_i, however, in the older battery, the value of $C_{Surface}$ had reduced by some margin, and C_{Bulk}, although not measurable directly using the PRBS was established via controlled long duration discharge tests and was found to be reduced, albeit to a lesser extent.

The observed frequency range in the PRBS tests therefore allowed deeper analysis of the battery than the conventional testing methods, but was not sufficiently broad to facilitate curve fitting, which is required to observe more subtle changes in battery equivalent circuit parameters over operational conditions of temperature, load and charge. Additionally the test time required to explore the excitation of C_{Bulk}, prohibited direct identification, and as such, seeking to find correlations between SoC and other, more readily identified, equivalent circuit elements was identified as a relevant body of work for investigation.

The identified limitations of the PRBS techniques were therefore found to be bandwidth and test time leading to the work which is explored in later chapters.

Chapter 6. Charge mode Pseudo Random Binary Sequence battery testing

6.1 Introduction

This chapter builds on the work carried out in the previous chapter to establish the PRBS battery evaluation technique, and introduces a current source (charge) approach.

The motivation for the work was to investigate the application of PRBS perturbation using positive current injection into the battery. Specifically, the investigation was concerned with exploring the use of charge current injection as a battery evaluation technique, with the obvious advantage that this can be applied to battery charger designs with minimal additional hardware.

Furthermore, comparisons to the discharge technique were of interest, as it is known that batteries exhibit different characteristics during charge and discharge [16].

The investigations carried out in chapter 5 were able to distinguish between batteries in differing states of health, but the bandwidth of the test results did not facilitate the use of curve fitting. As such further specific goals within this work were to expand the bandwidth of the test results, and develop characteristic responses in order that more subtle effects can be observed.

Furthermore, during the work carried out in chapter 5, it was observed that the overall effect on the battery state by the test itself required further investigation. This is explored by using a reduced test current, with comparative tests for the two techniques at specific states of charge.

6.2 Selection of test parameters

In addition to examining the effects of reducing the test current to limit the invasiveness of the test, alternative MLS lengths and clock frequencies for the PRBS required investigation to explore the wider behaviour of the test battery. Finally, the upper voltage threshold for the PRBS charge test required some attention, as the selection of this level should not be arbitrary, and with control could potentially yield useful state information.

6.2.1 PRBS bandwidth

During the investigation in chapter 5 it became apparent that a high bit order PRBS sequence could not be used with a low frequency clock in these tests without a prohibitively long test. In order to investigate a wider band of frequencies a PRBS test was developed allowing a quantized bandwidth approached to be used. This was implemented by running a 6 bit PRBS sequence with a specific clock frequency, applying a step change to the frequency and repeating the sequence. A number of frequency steps allowed generation of a sequence which able to cover the required test bandwidth for curve fitting, without introducing excessively long test times. The embedded code also had dual clock range control by selection of the pre-scaler value of the in-built timer. The clock frequency range spanned 0.5Hz to 1250Hz with eight frequency steps, with a divide by eight option for lower frequency tests. The embedded hardware comprised a Microchip Technology Explorer 16 development board (Figure 60), with a dsPIC 33FJ256GP10 microcontroller

[156, 157]. The embedded code used is provided for reference in the appendices (15.9.1).

6.2.2 Test current amplitude and voltage thresholds

During the tests in chapter 5, it became clear that minimising the test current, whilst retaining a reasonable signal to noise ratio would lead to a less intrusive test. The work in chapter 5 gave rise to the overall voltage envelopes shown in Figures 51 and 52. The response was obtained during a 10A PRBS test, running continuously over an extended period. It can be clearly seen that the battery terminal voltage is reducing during the test, and during the processing of results in chapter 5, data sets were used from the steady-state portion of the envelope to avoid indeterminate results.

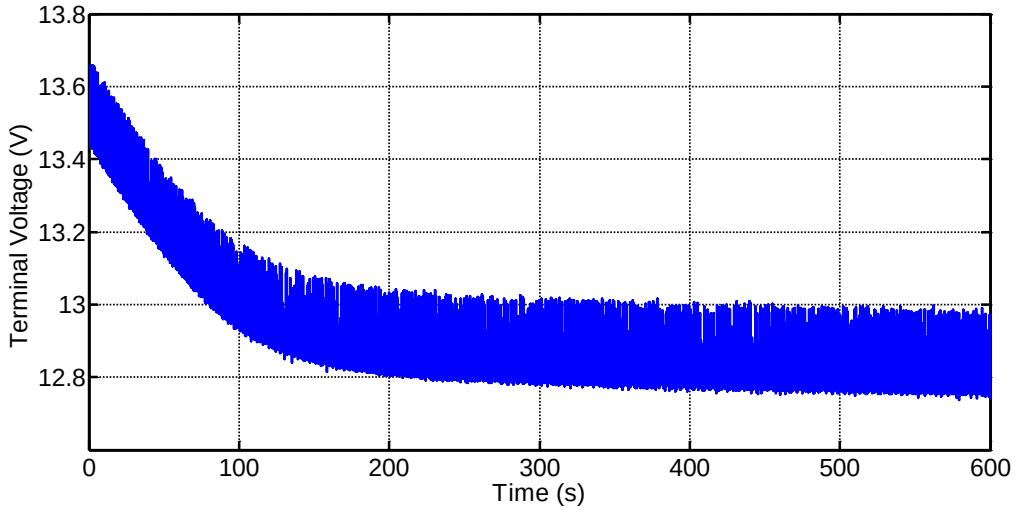

Figure 51. Overall voltage envelope during PRBS discharge testing

These levels were chosen specifically to examine well understood battery states, with provisions made to detect indeterminate results from initial test

data taken from the PRBS perturbation tests. As such the duration of tests carried out at all States-of-Charge was again designed to allow examination of several consecutive data sets in order to identify any such data.

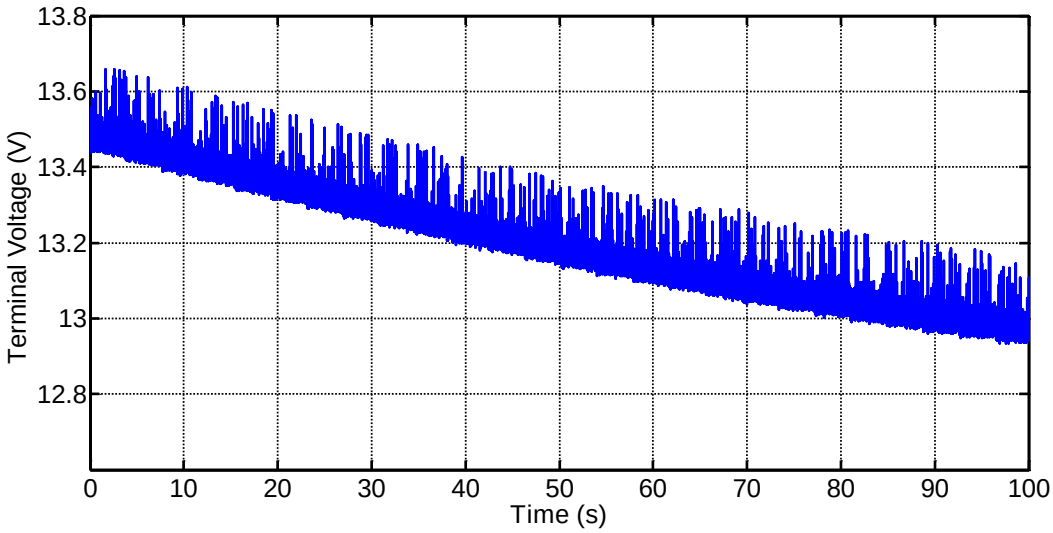

Figure 52. Terminal voltage over first 100 seconds of test

The test at 85% SoC was chosen as a stable battery state and finally the 0% SoC test was selected again as a known state with stable terminal voltage.

The discharge PRBS tests were also re-evaluated at the 85% SoC test condition and with a reduction in current amplitude used in order to reduce effects of the test, and a corresponding charge current used for the charge investigation.

The amplitude for the test current were therefore revised, and current amplitudes close to the rated discharge current were chosen. In the case of the Yuasa batteries used, this current was 0.05 c_r (20 hour rate, 3.25A for the 65Ah battery). A 4A test amplitude was therefore chosen for the work in this chapter. As the experimental set up was based on a constant current charger, the upper charge voltage limit for this system was very relevant to the battery under test.

Charge voltages for the test battery from manufacturer's data were taken into consideration, as it was important that the battery should not be overcharged. It was decided also that by using the manufacturer's recommended voltage levels further information could potentially be gleaned at near to 100% state of charge. Table 11 shows the thresholds devised for the charge PRBS tests over the range of temperatures likely to be encountered during the tests.

Table 11. Voltage thresholds for the PRBS charge stage used in the tests

Battery temperature (°C)	Voltage threshold (V)
20	13.65
21	13.632
22	13.614
23	13.596
24	13.578
25	13.56

It was important that temperature compensated voltages be used for the voltage thresholds, if the results were going to be used to indicate battery state. Additionally, the thresholds used in table 11 are based on float charge limits suitable for batteries used in standby applications [17], as this was deemed generally applicable for the batteries under test.

6.3 Battery model development

During the work carried out in chapter 5, the Randles' model was used, and for the work described in this chapter this model required modification to encompass both the charge and discharge behaviour of the test battery.

As discussed in chapter 5, R_i from the Randles' model (Figure 36, page 118) comprises the resistance of the cell interconnections (R_{int}) and the electrolyte resistance (R_e) within the cell itself.

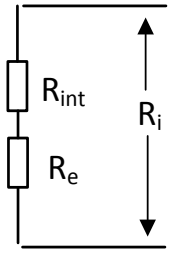

Figure 53. R_i broken out into its component impedances

Figure 53 shows the series R_{int} and R_e which are in real terms impossible to separate. However, it is know that different processes occur within the battery during charge and discharge, and this is shown in the work of Salameh et al [158] in developing models for lead-acid batteries. As such the values for electrolyte resistance were separated into parameters that describe charge and discharge processes (Figure 54).

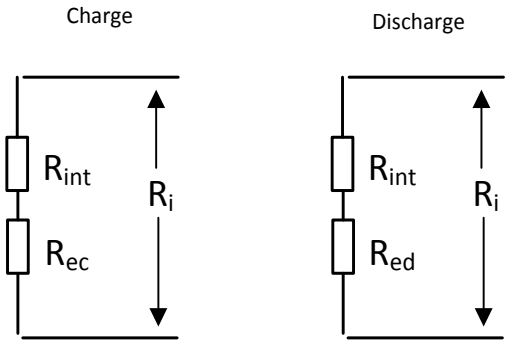

Figure 54. R_i broken out as separate models for charge and discharge

Therefore, during charge: $$R_i = R_{\text{int}} + R_{ec} \quad (30)$$

And discharge: $$R_i = R_{\text{int}} + R_{ed} \quad (31)$$

This leads to a separate model being required for charge and discharge, so to incorporate both of the circuit legs shown in Figure 54 into one model it is necessary to observe the respective current flows during the charge and discharge processes. This is achieved in a non-linear model by the addition of theoretical ideal diodes with zero volt drop and recovery time as shown in Figure 55 [159].

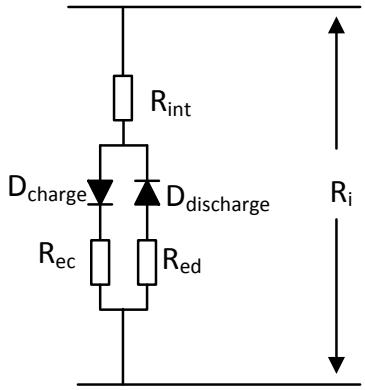

Figure 55. Combined model for Ri separating electrolyte resistance into charge and discharge elements

The modified Randles' model incorporating the electrolyte resistance for charge and discharge is shown in Figure 56.

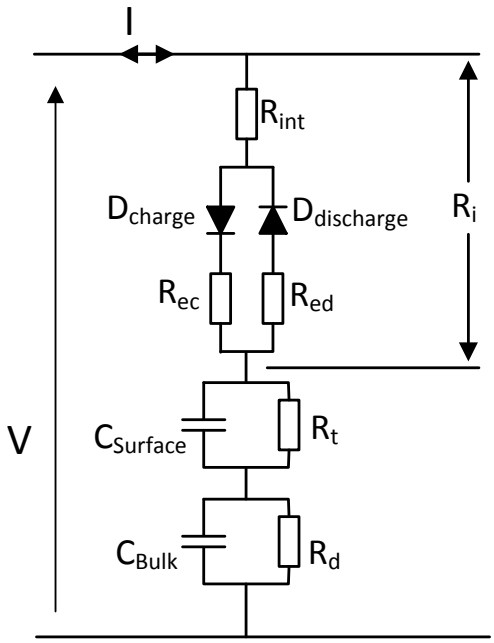

Figure 56. Modified Randle's model incorporating active charge and discharge resistance elements

It was found during investigations into complementary energy stores, that the addition of a parallel branch element to the Randles' model could facilitate an improved curve fit to VRLA batteries when tested using the PRBS technique. These findings were presented at the 13th European Lead Battery Conference (Paris, 2012) and were subsequently published in the Journal of Power Sources [160]. Examination of other published work indicated that this parallel branch may be related to mass transport effects, due to the reservoir of electrolyte at the electrode boundary [161], supporting justification of the addition to the model of R_x and C_x (Figure 57). It was intended that an investigation into electrochemical mechanisms associated with the parallel branch would be a subject of further work, encompassing both VRLA and flooded Lead-Acid batteries.

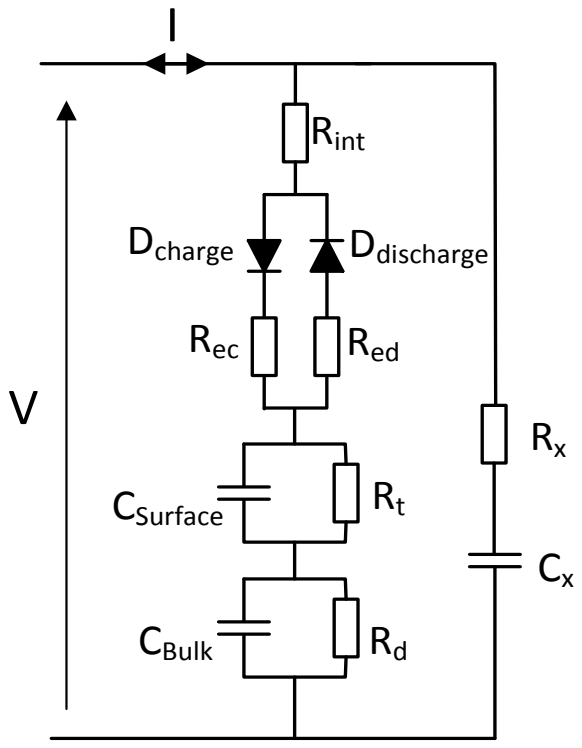

Figure 57. Developed model

Transfer function analysis was carried out to allow curve fitting using MATLAB. The series combination of electrolyte resistance and cell interconnections in Figure 56 reverts to R_i in the transfer function (as the components cannot be separated out).

This therefore retains a Randle's model for the major branch of the circuit with a parallel RC network (Figure 58):

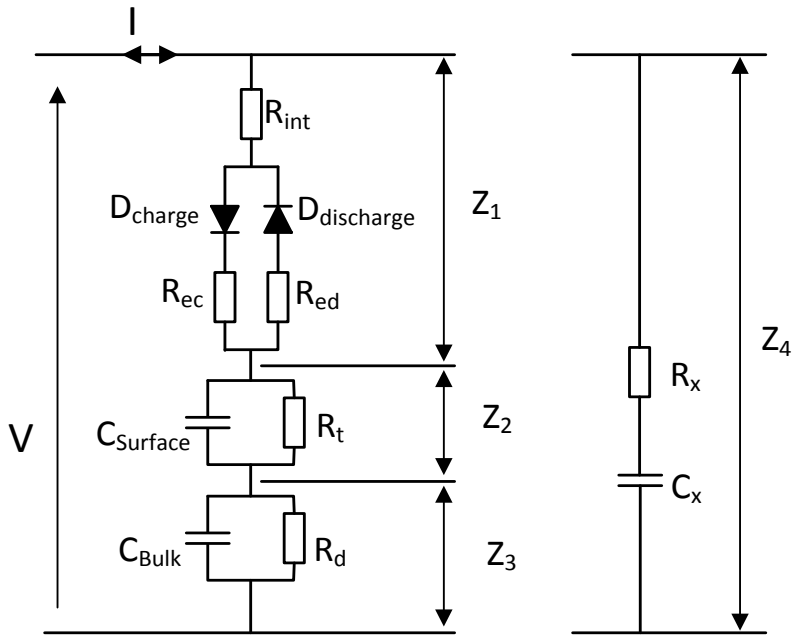

Figure 58. Equivalent circuit broken into branches for analysis

Referring to Figure 58, the respective impedances of the branches leads to the relationship in equation 32.

$$Z_{Batt} = (Z_1 + Z_2 + Z_3) // Z_4 \qquad (32)$$

(Individual impedances, in complex form)

$$Z_1 = R_i \qquad (33)$$

$$Z_2 = \frac{1}{(\frac{1}{R_t} + \frac{1}{XC_{Surface}})} \quad (34)$$

$$Z_3 = \frac{1}{(\frac{1}{R_d} + \frac{1}{XC_{Bulk}})} \quad (35)$$

$$Z_4 = \sqrt{R_x^{\,2} + XC_x^{\,2}} \quad (36)$$

The derivations above were incorporated into a MATLAB routine which is included in the appendices (curve_fit.m, 15.8.10) used in establishing the battery parameters in section 7.5.1.1.

6.4 PRBS charge test investigation-experimental set up description

The experimental test system was devised as a module for the AM-1 battery test system. Figure 59 shows an overall system block diagram for the complete hardware used in this chapter.

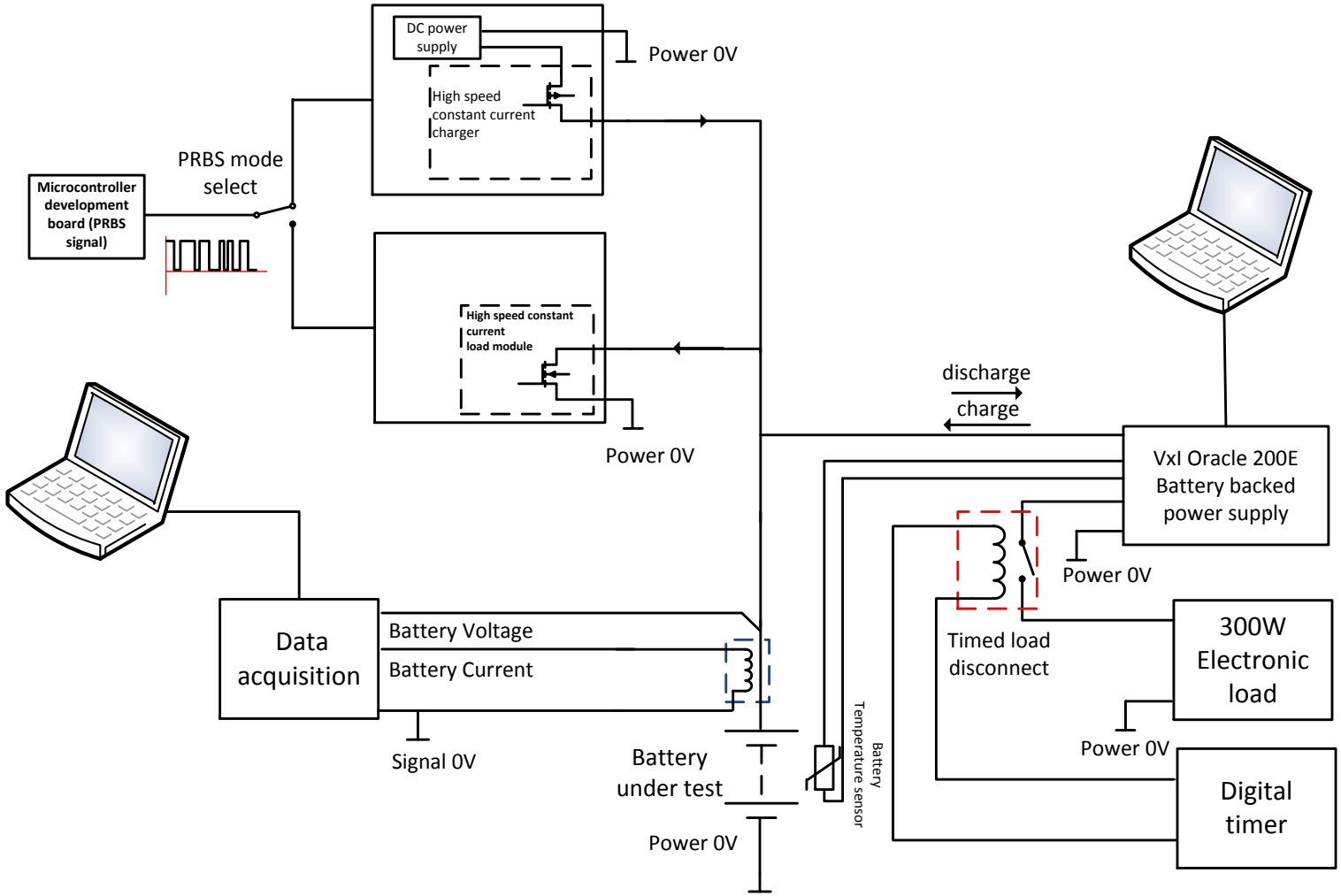

Figure 59. Overall test system block diagram

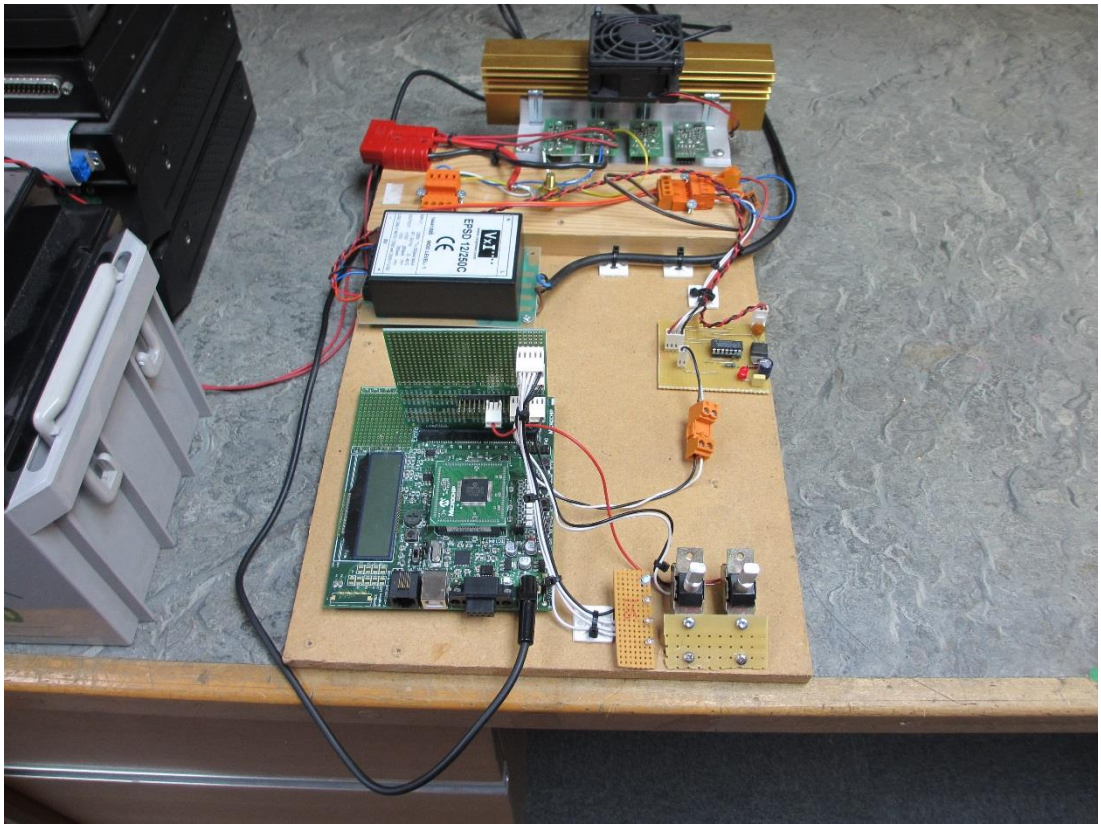

Figure 60. PRBS discharge system photograph

The system comprised a revised PRBS discharge system (Figure 60), to be used for the comparative tests to the charge technique. The hardware consisted of a high speed constant current load with integral current sensing.

The developed charge PRBS hardware (Figure 61) comprised a constant current charge module, driven by an adjustable 500W power supply. Downstream of the charge circuitry a switching FET was provided in order to apply PRBS charge to the battery.

Both of the hardware modules were driven using a Microchip development board programmed to provide a PRBS demand signal to the active current sink/source modules. The hardware developed in this chapter would later be used to develop

the tri-mode battery test module, and schematic diagrams can be found in the appendices in chapter 15. Once again high resolution voltage and current measurements were obtained using a dedicated data acquisition system along with the external battery temperature logged via the RS232 port on the VxI Oracle unit.

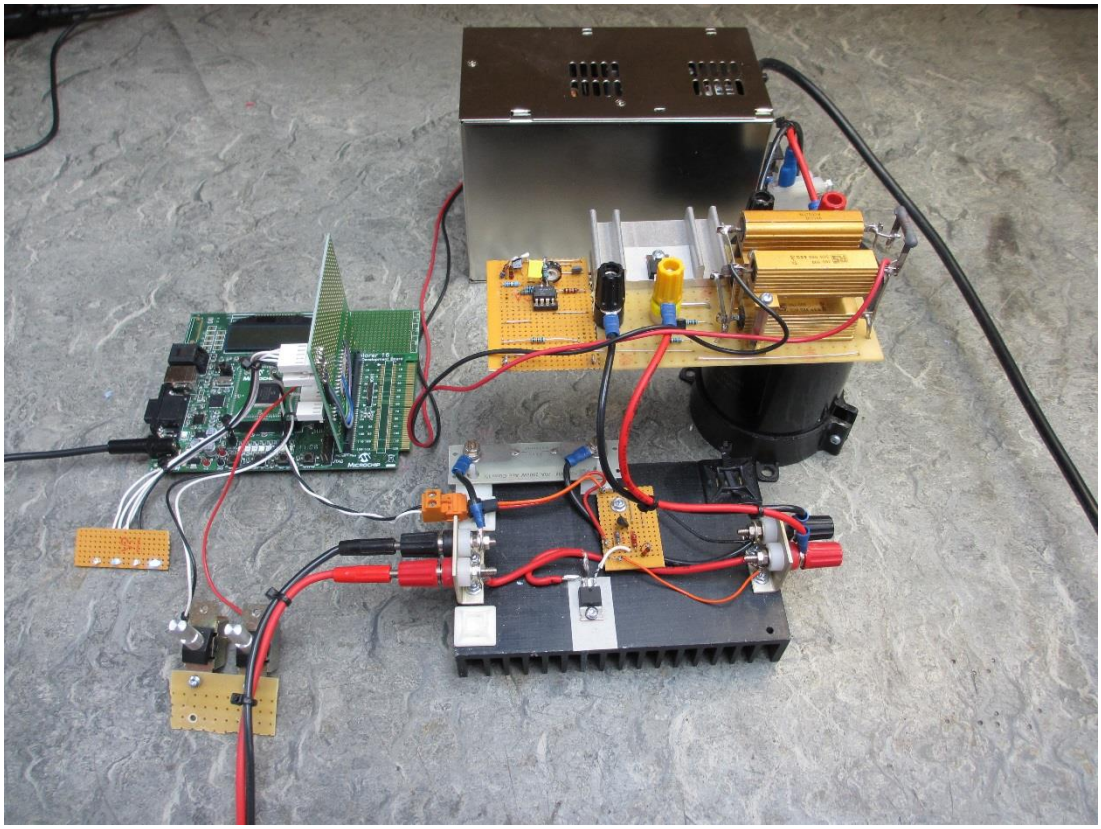

Figure 61. PRBS charge system photograph

A controlled charge and discharge system (Figure 62) was used to remove a pre-determined amount of energy from the test battery. The overall discharge was monitored using a VxI Power Oracle 200E battery backed power supply. The battery is connected to the electronic load via the contactor and the VxI unit. The digital timer allows a discharge to proceed for a set time after which the contactor is interrupted and the battery is disconnected. Additionally, as the VxI unit incorporates automatic disconnect of the battery at the EoD voltage with datalogging, full discharge of the battery to 0% SoC was possible if required. The Oracle unit also provided

temperature controlled charging of the test battery (the temperature sensor can be seen on the positive battery terminal), separately to the PRBS dynamic charge system used in applying the test perturbation.

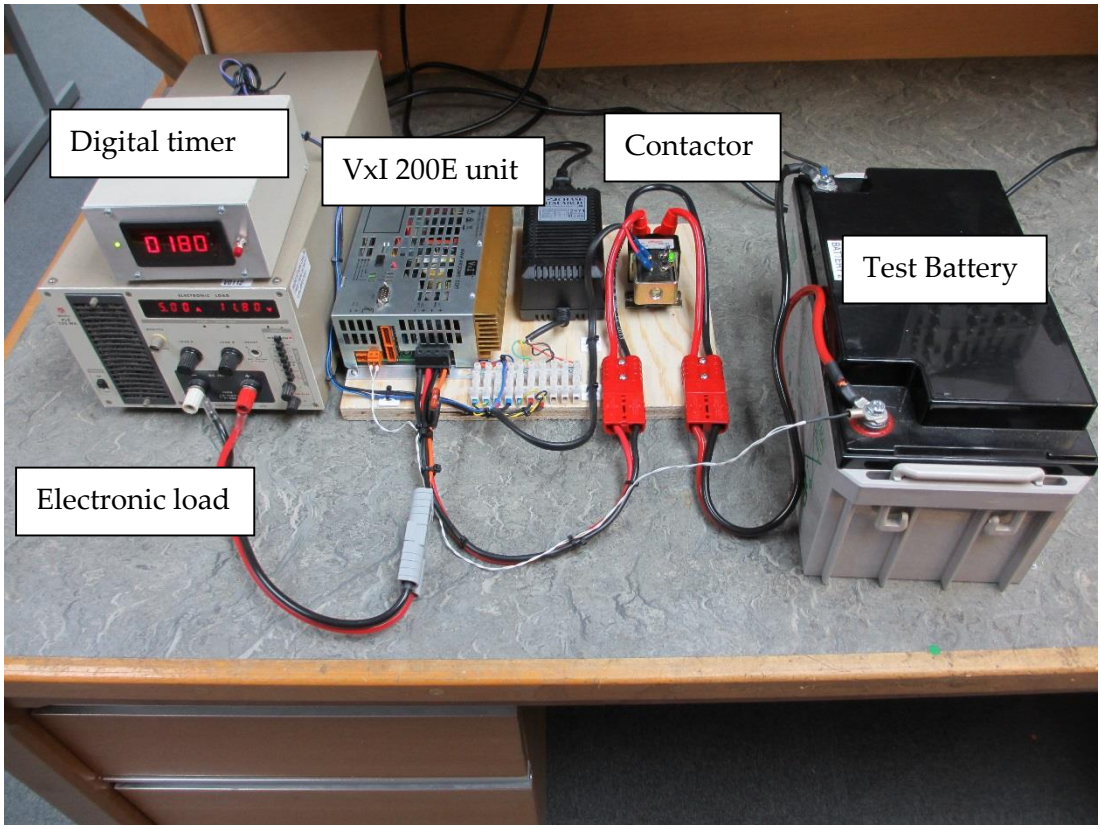

Figure 62. Controlled charge/discharge system photograph

6.5 Test procedure

The battery used during the tests was a 65Ah 12V VRLA (Yuasa NPL65-12i) type.

The battery was in a good state of health, being previously used in the work in the preceding chapter, being new prior to these tests.

The battery was conditioned with a number of charge and discharge cycles before

being charged to 100% SoC using the temperature controlled charger (VxI Oracle 200E unit).

PRBS tests (charge, and comparative discharge) were then carried out on the batteries. Subsequent to this test the batteries were discharged at 5 amps for 2 hours to remove around 15% of the rated capacity before carrying out the next test. The third stage was to discharge the battery at a 20 hour discharge rate to the manufactures specified End-of-Discharge (EoD) Voltage before carrying out the final test. A summary of the tests is shown in the flowchart in Figure 63.

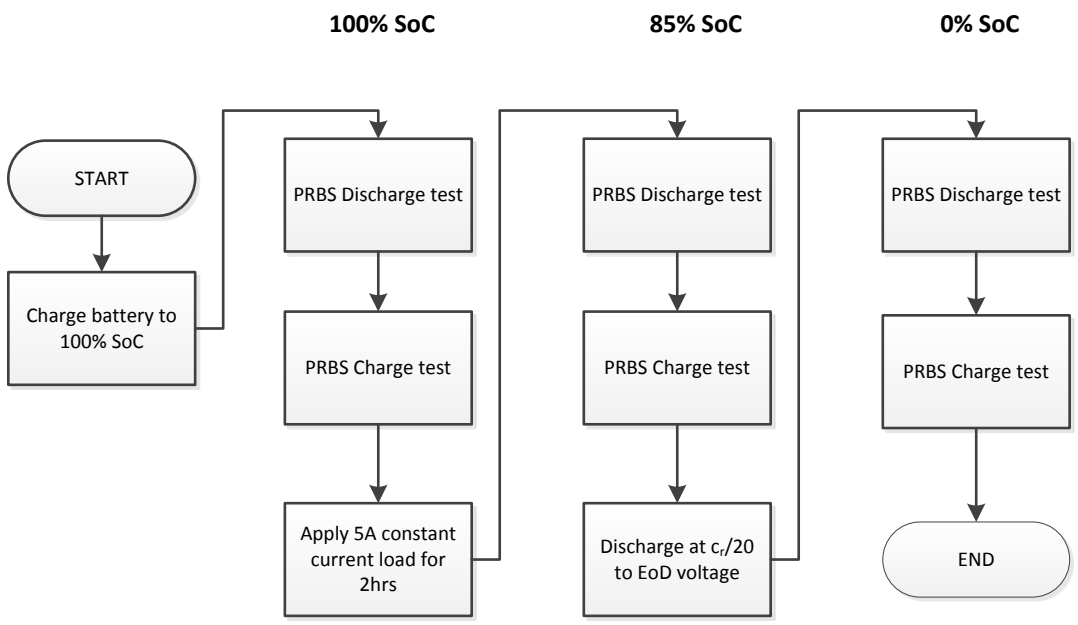

Figure 63. Charge test procedure flowchart

6.6 Test results

Example current and voltage data are seen in Figures 64 and 65 at 85% SoC during one of the dynamic charge (PRBS) tests.

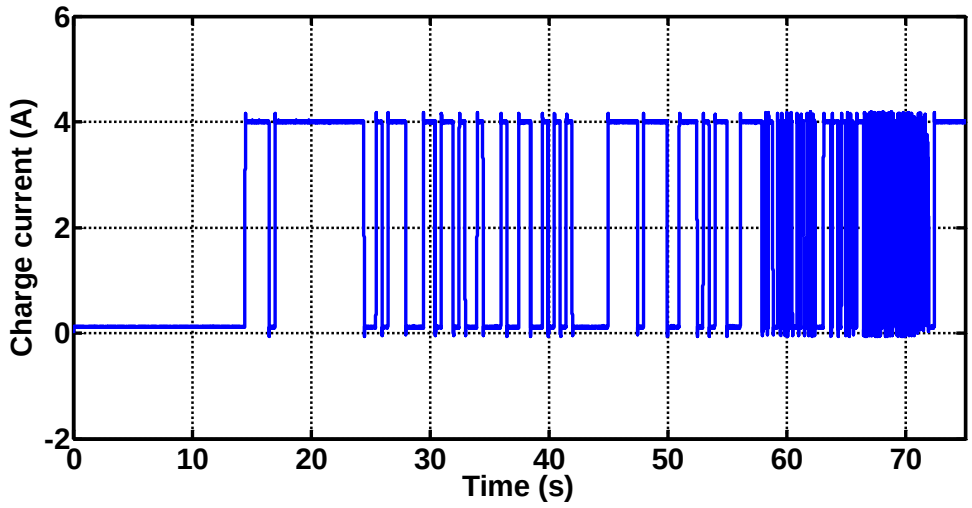

Figure 64. Current waveform, 85% SoC, charge test

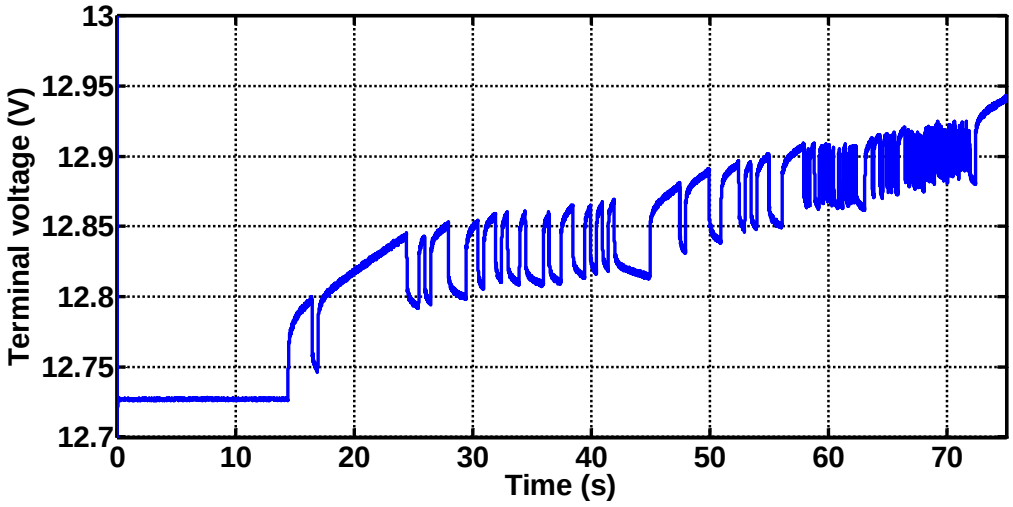

Figure 65. Voltage response, 85% SoC charge test

The impedance information obtained from the tests is shown in Figures 66 to 71. Transfer function analysis of the adopted model (Figure 57) was employed to obtain a curve fit for each of the results using curvefit.m in appendix 15.8.1. The curve fits were obtained by inspection of the responses to obtain initial values for R_i (as the response tends to R_i at high frequencies (towards 1kHz). An initial value for Rt is obtained by inspection for the low frequency area of the response. These start

parameters are then used with initial values for C_{Bulk} and R_d (using methods from 5.3.1 and 5.3.3) to iteratively establish the battery parameters.

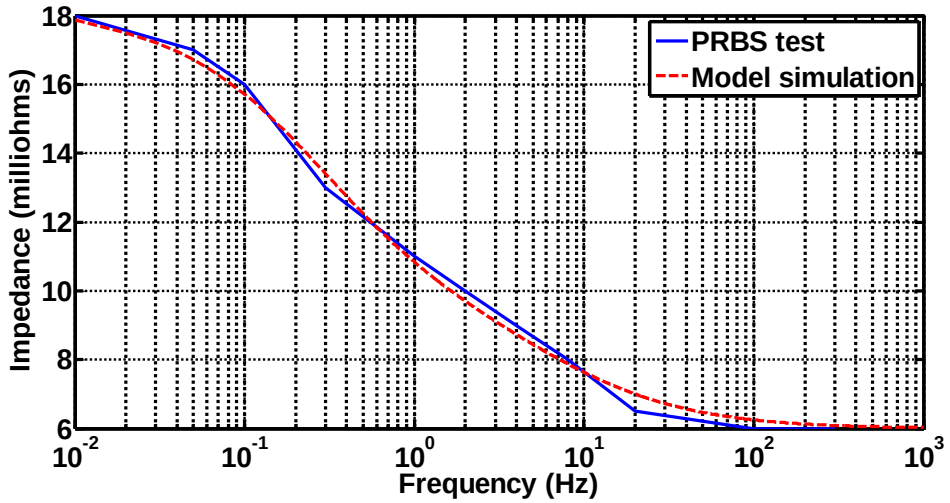

Figure 66. 100% SoC, discharge mode PRBS

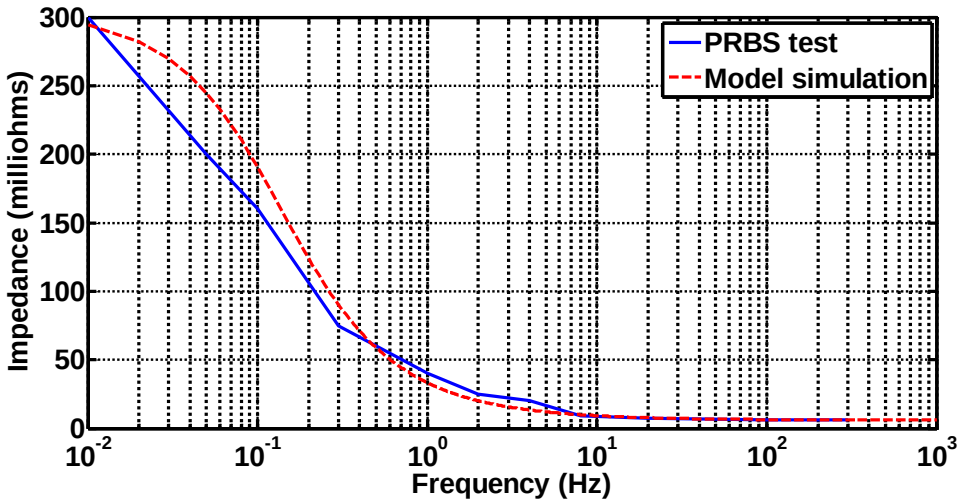

Figure 67. 100% SoC, charge mode PRBS

Figures 66 and 67 illustrate the comparative results at 100% SoC. As mentioned, testing at this state of charge can lead to an indeterminate result, as the battery may not be at a steady state terminal voltage. This has been addressed previously in battery pulse testing by applying a preload to the battery [126], and in PRBS discharge

tests by disregarding initial data sets until a pseudo steady-state voltage envelope is observed. However, the PRBS charge technique does not have this facility as the test mode inherently charges the battery. This led to an elevation of terminal voltage during the 100% SoC test which resulted in "clipping" in the PRBS charge current (Figure 73). Importantly, this is observed in Figure 67 as the high magnitude of low frequency impedance, whilst the high frequency impedance approaches the expected level. This phenomenon clearly shows detection of end of charge, in conjunction with the carefully selected upper voltage limits in table 11. The voltage limits chosen define the reporting of this high impedance and as such indicate elevated charge levels, whilst showing healthy impedance results for the higher frequency part of the response.

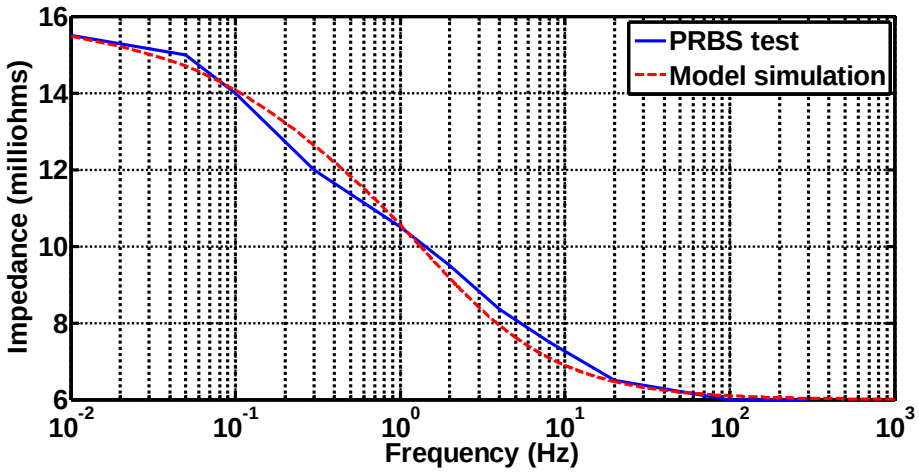

Figure 68. 85% SoC, discharge mode PRBS

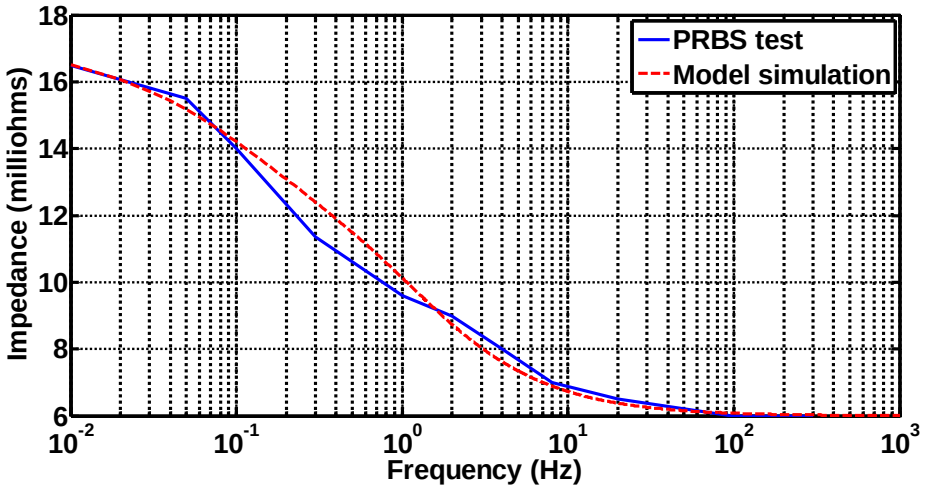

Figure 69. 85% SoC, charge mode PRBS

Figures 68 and 69 show the test results at 85% SoC for both test modes. Both results show similar results but the differences in the charge and discharge processes are apparent in elements of the curve fitting.

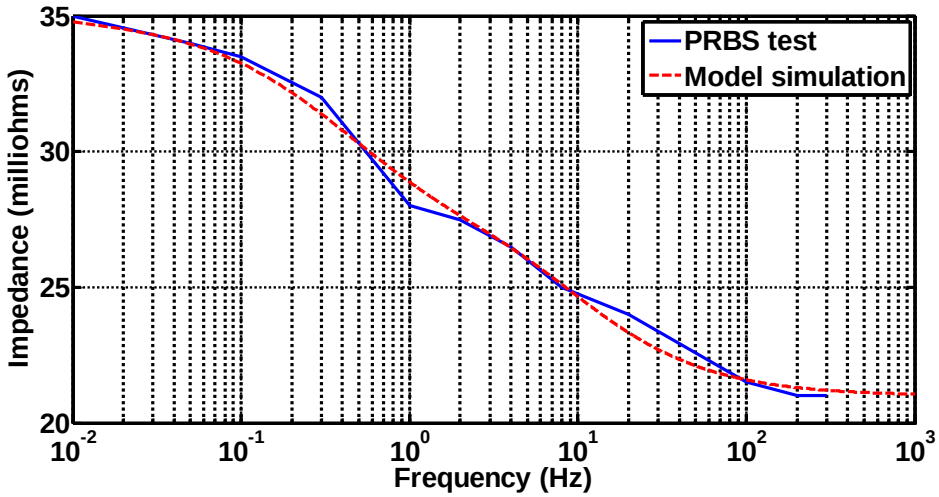

Figure 70. 0% SoC, discharge mode PRBS

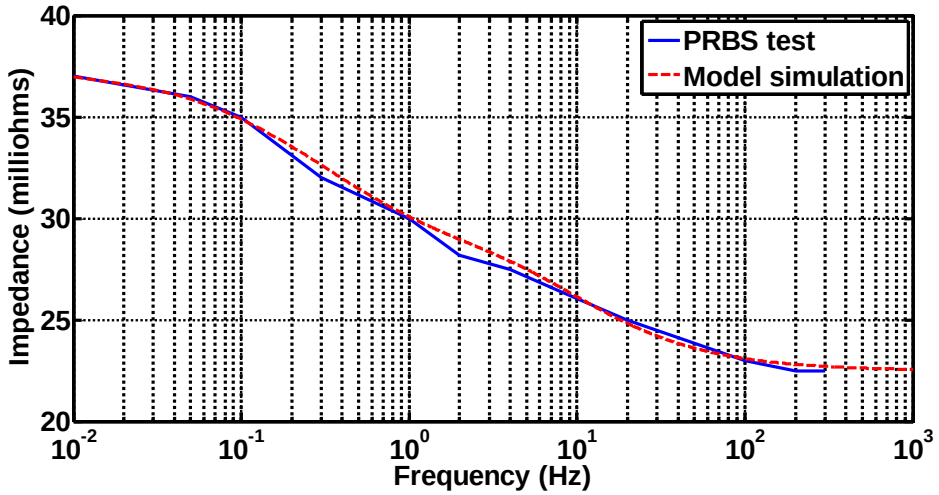

Figure 71. 0% SoC, charge mode PRBS

Figures 70 and 71 show the results for 0% SoC. The battery shows an elevation in impedance across the test frequency range which shows two test modes which shows both charge and discharge PRBS tests exhibit similar results but with some differences for the two test methods over the frequency range, with the discharge mode showing lower impedance over the frequency range. Figure 72 shows the comparative impedance results for the PRBS discharge and charge tests.

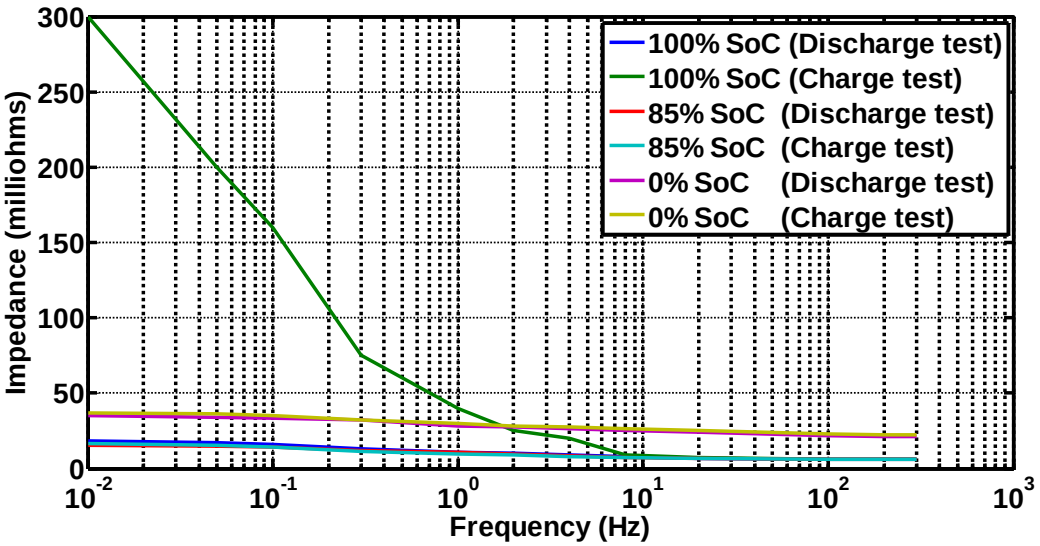

Figure 72. Comparative impedance results, PRBS discharge and charge tests.

The analysis yielded the model parameters shown in table 12.

Table 12. Obtained model parameters

Battery state and test mode	$R_{int}+R_{ec}$ (R_i)	$R_{int}+R_{ed}$ (R_i)	R_t	$C_{Surface}$	C_x	R_x
100% SoC (discharge)	-	6mΩ	12mΩ	6F	34F	4mΩ
100% SoC (charge)	6mΩ	-	300mΩ	4F	2F	9mΩ
85% SoC (discharge)	-	6mΩ	9.5mΩ	16F	35F	9mΩ
85% SoC (charge)	6mΩ	-	10.75mΩ	20F	60F	9mΩ
0% SoC (discharge)	-	21mΩ	13.8mΩ	2.5F	16F	9mΩ
0% SoC (charge)	22.5mΩ	-	14.6mΩ	2.5F	22F	9mΩ

The results in the table show the differences between the charge and discharge technique mainly related to the elements of $C_{Surface}$. This demonstrates somewhat the different reactions involved in the charge and discharge processes [16] and overall observations on the validity of the charge technique are satisfied in that clear results are observed for the various charge states as compared to the discharge technique with trends that are recognisable for both methods.

6.7 Conclusion

The work within this chapter demonstrated the benefits of a charge based excitation signal as a means for parameter estimation within batteries.

Specifically:

- Able to identify a battery at 100% SoC by increased low frequency impedance
- Gave comparable results to discharge mode PRBS at other states of charge
- Potentially can be implemented in a battery charger as part of the charge hardware
- Does not consume energy during the test

The system was able to identify a battery at 100% SoC by showing a significant increase in the overall magnitude of the impedance spectrum. This could further be observed by examining the PRBS current waveform (Figure 73) which shows the transition from current mode to voltage mode charge during the test.

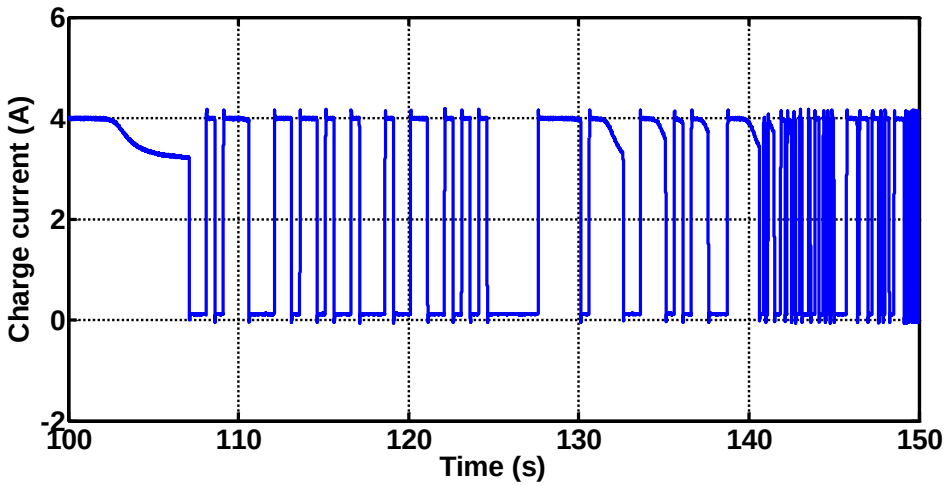

Figure 73. Current waveform "clipping" 100% SoC, charge test

In spite of this observed increase in low frequency impedance, the higher frequency impedance for the battery appears healthy, allowing both SoC and SoH to be reported, provided the upper voltage threshold for the PRBS charge is carefully selected with reference to manufacturer's data for charge voltage, compensated for ambient temperature [17]. Choice of voltage thresholds that are too high could lead

to overcharge of the battery during the test, and impedance reporting which is outside of the operational envelope of the battery.

This behaviour has potential for examination within further work, beyond pure indication of 100% SoC, having potential applications in multi-stage charge profiles as a facilitator for stage transition.

Chapter 7. Bipolar mode (Charge/Discharge) Pseudo Random Binary Sequence battery testing

7.1 Introduction

The work carried out within this chapter builds on the investigations carried out in chapters 5 and 6, developing a bipolar method of applying the PRBS perturbation to the test battery.

In applying this test mode, it was anticipated that the observation of the battery state would be less-intrusive than the techniques already explored, thus offering advantages over the discharge and charge techniques.

Additionally, the specific motivation for the work extended to investigating the applicability of the test at 100% SoC - an area that is open to indeterminate results using the discharge test method, but was however shown to be a valuable state indicator using the charge test technique.

Finally, since the bipolar signal should present a net-zero energy exchange from the battery, there was interest in the actual effects of the test itself, as observed changes in terminal voltage of the battery during the test could potentially be employed in indicating battery efficiency.

7.2 Battery efficiency

The importance of battery efficiency can be overlooked in SoC and SoH evaluation systems, or its effects placed outside of the scope of the predictive algorithms used. During earlier chapters the behaviour of the battery during charge and discharge conditions has been discussed, and it is well understood that a battery does not

behave as an ideal capacitance. It follows therefore that that the amount of energy used in charging a battery will exceed that used during discharge, and this difference in energy is most commonly expressed as the charge efficiency of the battery. This relationship is shown in equation 37.

$$\eta_{Batt} = \frac{Ah_{Discharged}}{Ah_{Charged}} \tag{37}$$

Where $Ah_{Discharged}$ is the discharge capacity of the battery and $Ah_{Charged}$ is the Ah capacity imparted to the battery during charging.

η_{Batt} is influenced by prevailing conditions and battery state, and Figure 74 shows the efficiency of Yuasa NP series VRLA batteries used in the tests, over SoC from the manufacturer's own data [17]. Figure 75 shows the characteristic for the same batteries over a range of charge currents, where xCA is the manufacturer's terminology for charge current as a fraction of rated capacity [17].

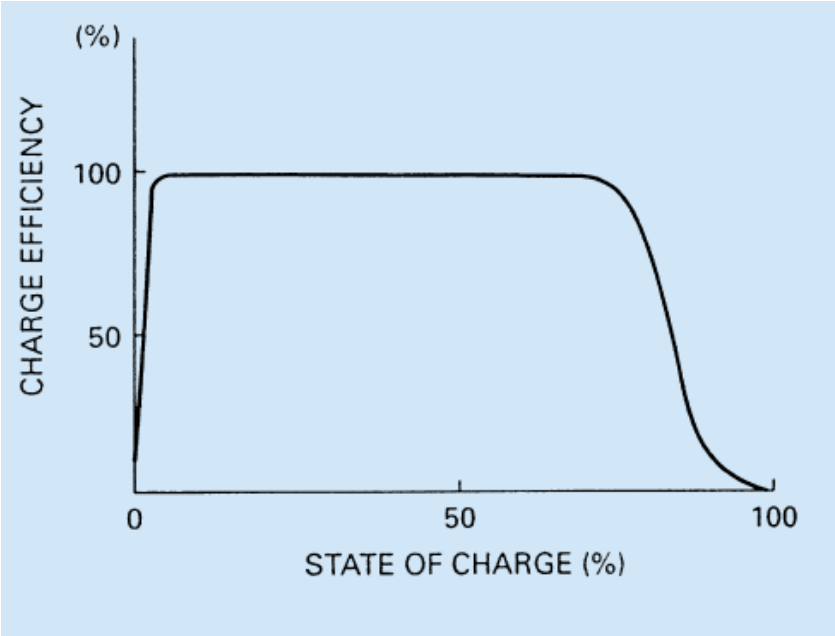

Figure 74. Charging efficiency with SoC from manufacturers data (image reproduced by permission of Yuasa Batteries Europe)

This behaviour has implications in optimised energy use, notably renewable energy, EV/HEV and electric traction. Within photovoltaic systems Maximum Power Point Tracking (MPPT) charge controllers have been developed, allowing the PV panels to be used at the optimum operating point. This technology is only partially utilised if the batteries within the system are operating at low efficiency, potentially at or near to 100% SoC during periods of peak irradiation [162, 163]. Similarly, systems using regenerative braking can also suffer the same inefficiencies.

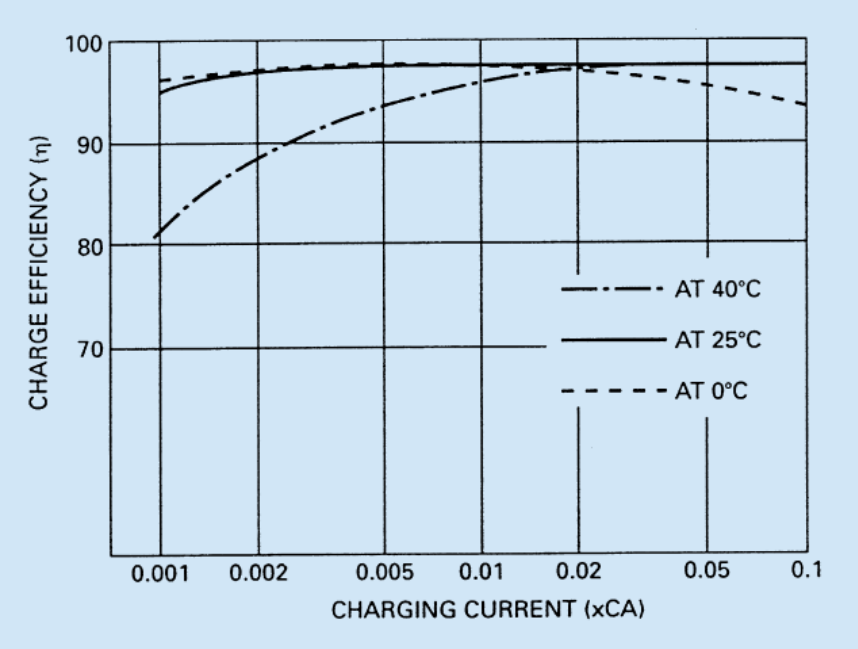

Figure 75. Charging efficiency with charge current from manufacturer's data (image reproduced by permission of Yuasa Batteries Europe).

Battery efficiency also declines with declining SoH, so it therefore follows that battery efficiency is a parameter of interest. As such it was decided to investigate this effect by performing the tests over a longer duration and examine the mean terminal voltage within the PRBS voltage envelope.

The findings from these experiments are presented in section 5 of this chapter.

7.3 Hardware modifications

The power stages developed in the previous discharge and charge PRBS tests were combined using an amplitude offset drive circuit to the power stages in order to generate a PRBS perturbation signal centred around zero current (Figure 76.) The hardware was configured in order that switching between the 3 modes of test (charge, discharge and bipolar) could be carried out easily, and via digital control from the test system if required. This allowed consecutive tests for each of the three modes to be carried out, in order that direct comparisons could be made between the results.

The controlled discharge apparatus, was as introduced in section 6.4, comprising the VxI charger, Kikusui 300W load and the digital timer controlling the timed battery disconnection.

A photograph of the bipolar PRBS test apparatus is shown in Figure 77. The completed hardware forms the basis of the tri-mode PRBS test apparatus and is discussed in detail in chapter 15.

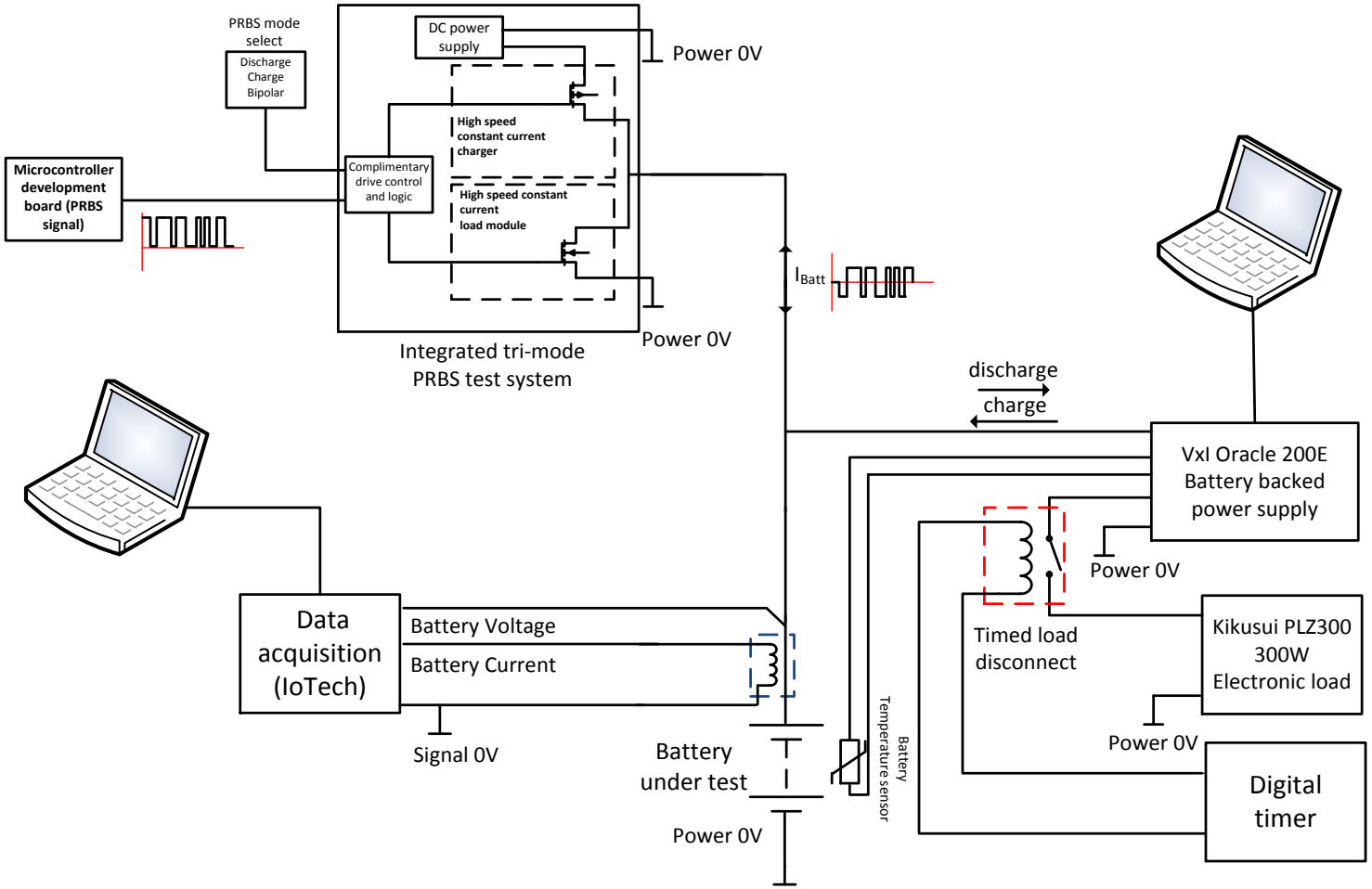

Figure 76. Bipolar PRBS test system block diagram

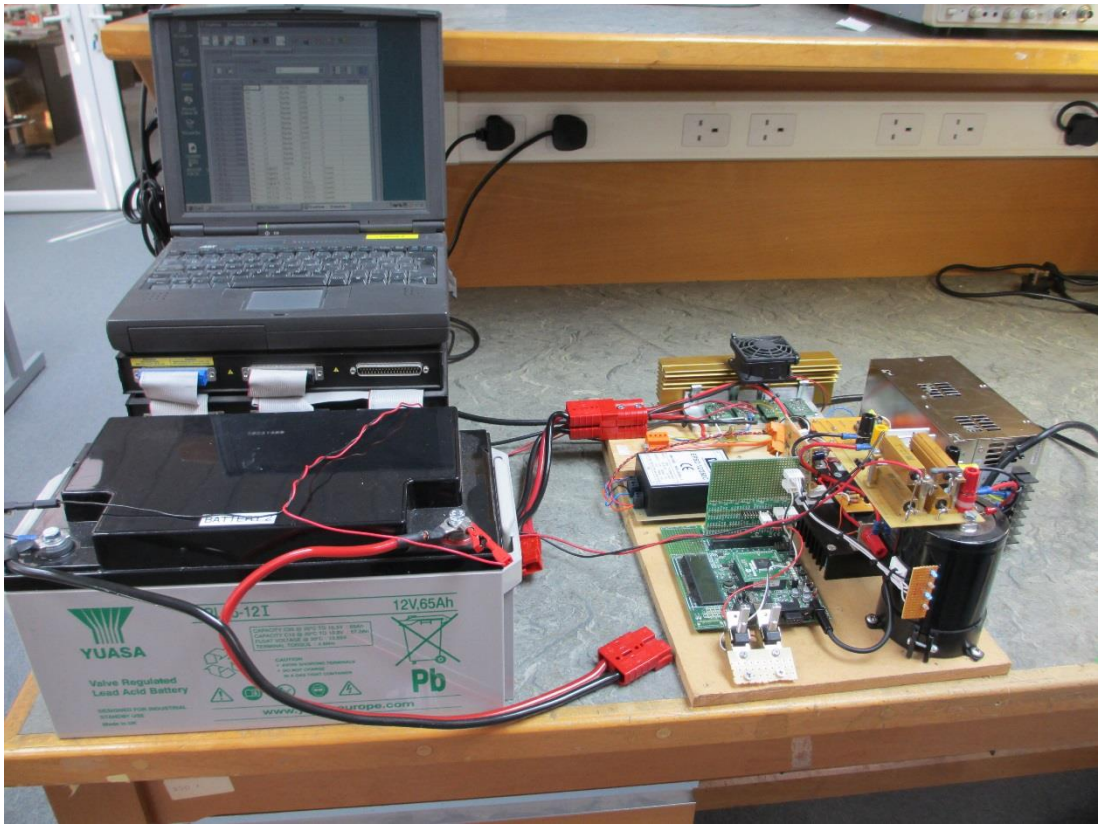

Figure 77. Bipolar PRBS test system photograph

7.4 Test procedure

The battery used during the tests was a 65Ah 12V Valve Regulated Lead Acid (VRLA) (Yuasa NP65-12i) type, which was used for the previous investigations using the charge and discharge tests.

The battery was conditioned with five charge and discharge cycles before being charged to 100% SoC using the temperature compensated Lead-Acid charger within the test controlled charge/discharge apparatus used in the previous chapter (Figure 60).

To allow direct comparisons with the previous experiments, the tests were again carried out at 100%, 85% and 0% SoC. The flowchart shown in Figure 78 outlines the

test procedure.

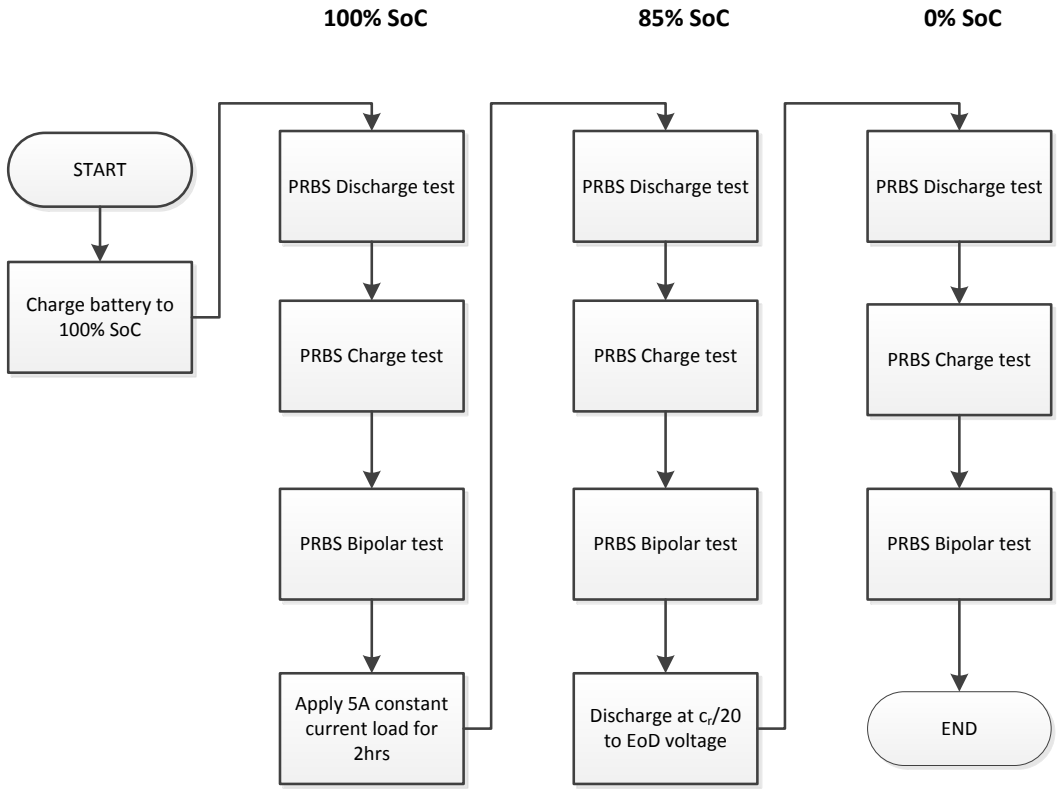

Figure 78. Bipolar test procedure flowchart

The bipolar PRBS was developed with prior work in mind and the test level used was +/- 4A, using the sequence introduced in 6.3.1. The upper voltage limit for the charge pulse was fixed before the test dependant on temperature (13.65V, 20°C), with the level adopted was the same as that chosen for the charge PRBS tests in chapter 6, table 11.

PRBS tests were then carried out on the battery at 100% SoC before it was discharged at 5 amps for 2 hours to remove around 15% of the rated capacity in preparation for the next test at 85% SoC. The third stage was to discharge the battery at the 20 hour discharge rate to the manufacturers specified End-of-Discharge (EoD) Voltage before carrying out the final PRBS test at 0% SoC.

7.5 Test results

Example current and voltage waveforms are seen in Figures 79 and 80 for the test at 85% SoC.

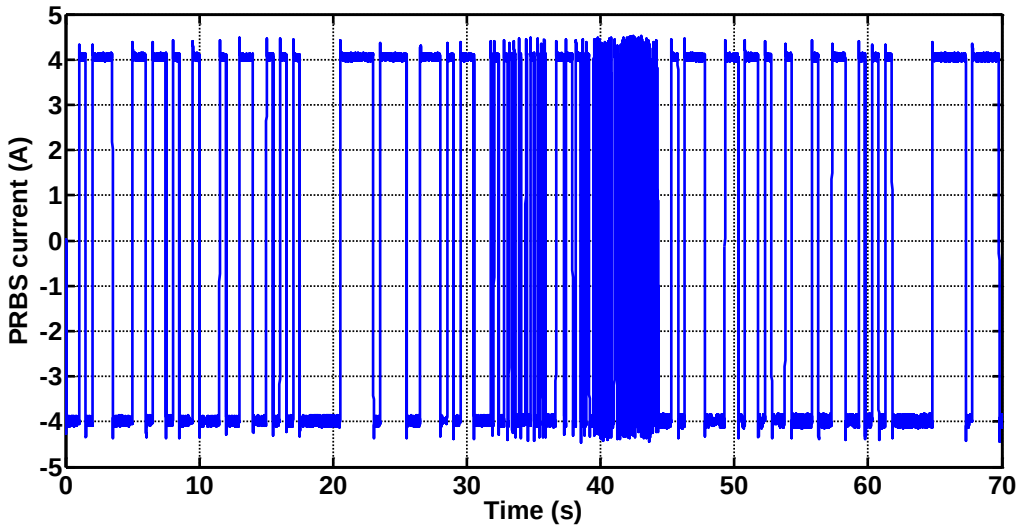

Figure 79. Bipolar PRBS test current waveform, 85% SoC.

The test voltage response shown in Figure 80 illustrates the difference between the Bipolar PRBS and the Charge and Discharge PRBS tests. The voltage envelope shows a much reduced net change to the average level, especially for the higher frequency

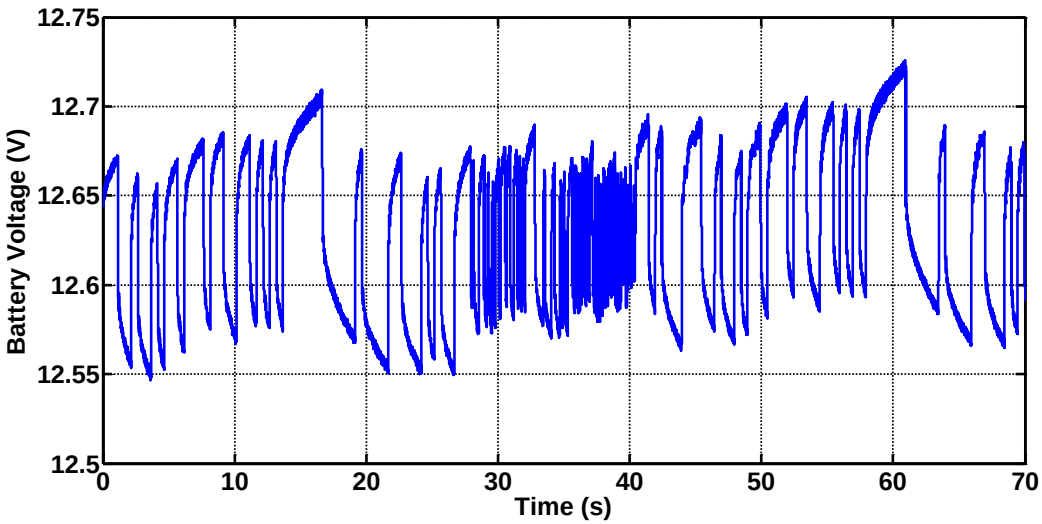

Figure 80. PRBS test voltage response, 85% SoC

PRBS content. Due to this reduced effect on battery state it becomes possible to carry out PRBS tests with a lower clock frequency or higher bit order, without significantly affecting the battery SoC during the observations. It was therefore considered that any observed changes in the average terminal voltage of the battery during the PRBS test could be an indicator of battery efficiency at the prevailing States-of-Charge.

7.5.1 Impedance results

The voltage and current data was processed using MATLAB (evalprbs.m, appendix 15.8.5) leading to the impedance information shown in Figures 81 to 83. Transfer function analysis of the adopted model as (Figure 57, page 148) as carried out in chapter 6 was employed to obtain a curve fit for each of the results using curvefit.m (15.8.10) as previously described in chapter 6. This analysis yielded the model parameters shown in table 13.

Figure 81 shows the impedance results at 100% SoC. Using the bipolar PRBS it was possible to carry out a test at this state, where previously the discharge mode PRBS could show indeterminate data, if the initial data sets were not carefully selected by inspection of the overall test envelope. The test shows an

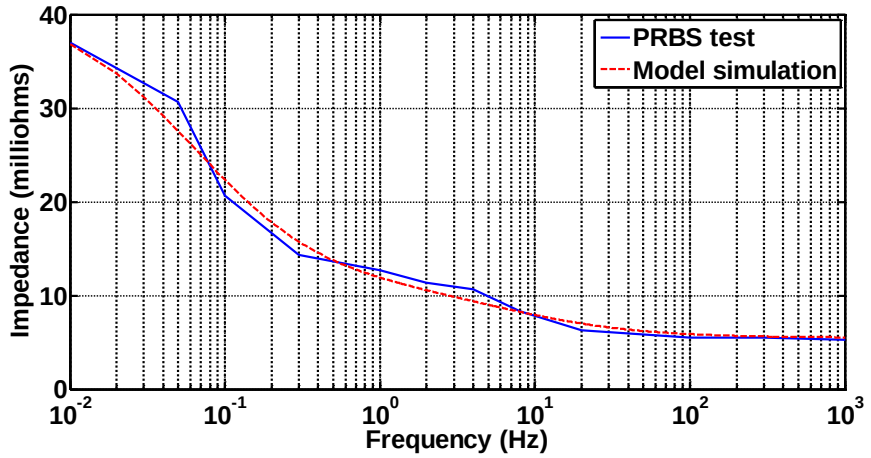

Figure 81. Test results and curve fitting, 100% SoC

elevated low frequency impedance, consistent with known characteristics for lead-acid batteries at 100% SoC [16].

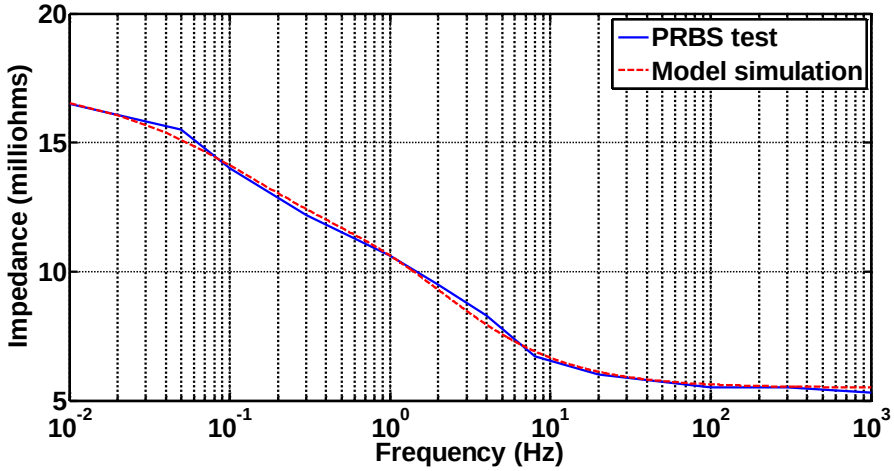

Figure 82. Test results and curve fitting, 85% SoC

Figure 82 shows the impedance plot for 85% SoC. This is consistent with the discharge and charge PRBS methods, within the quasi-linear area of operation of the battery. The low frequency impedance of the battery is therefore more representative of typical performance, and the plot generally would be used to indicate battery SoH, with initial calibration carried out using

manufacturer's data if available or profiling of new batteries. A thorough treatment is given to battery parameters over lifetime in chapter 11.

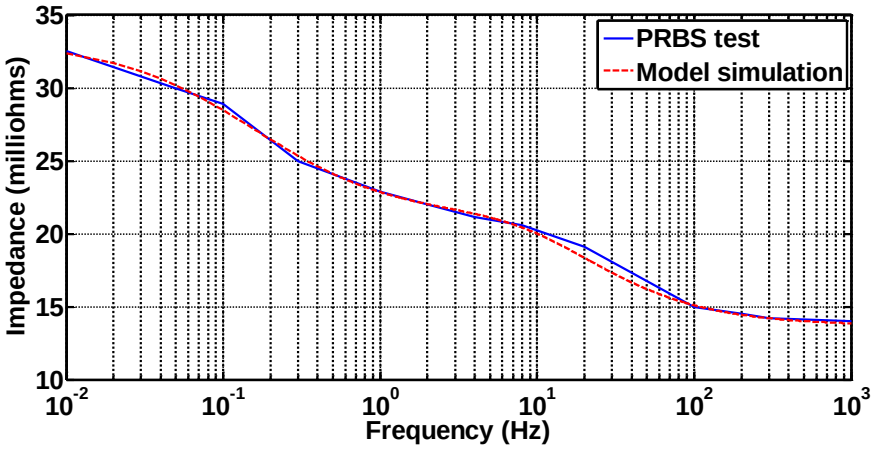

Figure 83. Test results and curve fitting, 0% SoC

Figure 83 shows the impedance plot for the test at 0% SoC. The battery in this state shows an elevation in impedance across the test frequency range. This gives a distinct indication of a discharged battery and can be compared to the 100% SoC results (Figure 81) which show similarly the increased LF impedance, but preserve the healthy HF result.

7.5.1.1 Battery parameters

Table 13 shows the parameters obtained during the curve fitting using the bipolar tests, with the corresponding discharge and charge test parameters. R_{int}, R_{ec} and R_{ed} are combined parameters for the bipolar tests as no distinction can be made between the individual components, and are therefore compared to $R_{int}+R_{ec}$ for the charge mode tests and $R_{int}+R_{ed}$ for the discharge mode tests.

At 85% SoC the three modes of test show similar impedance and parameter results, but it is at the extremes of charge states 0% and 100% where the individual methods show the significant differences.

Table 13. Obtained model parameters

Battery state and test mode	$R_{int}+(R_{ec}+R_{ed})/2$ (R_i) (mΩ)	$R_{int}+R_{ec}$ (R_i) (mΩ)	$R_{int}+R_{ed}$ (R_i) (mΩ)	R_t (mΩ)	$C_{Surface}$ (F)	C_x (mΩ)	R_x (mΩ)
100% (Bipolar)	**5.5**	**-**	**-**	**35.3**	**3.9**	**60**	**5.8**
100% SoC (discharge)	**-**	**-**	**6**	**12**	**6**	**34**	**4**
100% SoC (charge)	**-**	**6**	**-**	**300**	**4**	**2**	**9**
85% (Bipolar)	**5.5**	**-**	**-**	**11.3**	**12**	**60**	**10**
85% SoC (discharge)	**-**	**-**	**6**	**9.5**	**16**	**35**	**9**
85% SoC (charge)	**-**	**6**	**-**	**10.75**	**20**	**60**	**9**
0% (Bipolar)	**13.7**	**-**	**-**	**19.2**	**1**	**31**	**12.5**
0% SoC (discharge)	**-**	**-**	**21**	**13.8**	**2.5**	**16**	**9**
0% SoC (charge)	**-**	**22.5**	**-**	**14.6**	**2.5**	**22**	**9**

Across the test methods, the elements of surface capacitance ($C_{Surface}$ and C_x) remain indicators of the ability of the battery to deliver energy, as this capacitance directly indicates the effective plate area and in turn capacity.

Further profiling of this capacitance against actual discharge tests may reveal direct correlations to bulk capacity

7.5.2 Battery efficiency results

Examining the voltage envelopes using low frequency PRBS tests revealed a net change in terminal voltage that could be attributed to battery efficiency. As discussed in chapter 4, using battery terminal voltage as a state indicator can only be used in controlled conditions, and the bipolar PRBS facilitated this in that the alternating current applied to the battery served to remove the electrode overpotential [164], and move the battery into a pseudo steady-state terminal voltage.

The mean DC terminal gradients observed for each state (Table 14) are normalised representations of the battery efficiency, which can be compared to manufacturer's data in Figure 74. The manufacturer's graph is deliberately vague, and in the literature battery efficiency has not been extensively researched, however, the correlations between the battery data and the PRBS tests do show interesting results.

Table 14. Mean DC voltage gradient during PRBS tests (20°C)

State of Charge	Overall change in mean terminal voltage over test duration (mV)	Mean DC Voltage gradient (mV/minute)
0%	148.6	6.85
85%	11.1	0.51
100%	439.5	20.28

Examining the gradient at 100% SoC this is clearly the area of the tests where the battery charge efficiency is the lowest. This ties in with the Yuasa data

indicating a sharp fall in efficiency at 100% SoC. At 85% SoC (Figure 84) the gradient of the average voltage has reduced dramatically indicating the battery has moved into a more efficient area. The almost flat DC terminal voltage at this point of high efficiency for the battery verifies the net-zero energy exchange of the Bipolar PRBS, at this state, under these conditions.

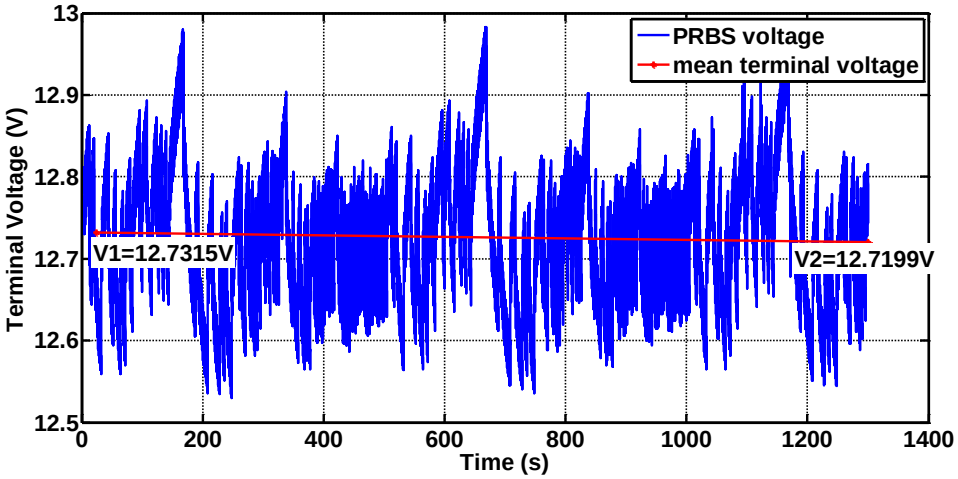

Figure 84. Voltage envelope, 85% SoC

The gradient at 0% SoC (Table 14) clearly indicates a reduction in efficiency in line with manufacturers data (Figure 74) falling off dramatically below 4-5% SoC.

7.5.3 Mean DC terminal voltage as a SoC indicator

The data from the efficiency analysis was used to examine the possibility of using the mean DC terminal voltage to inform SoC prediction. Figure 85 shows the manufacturers data for SoC in relation to terminal voltage [17].

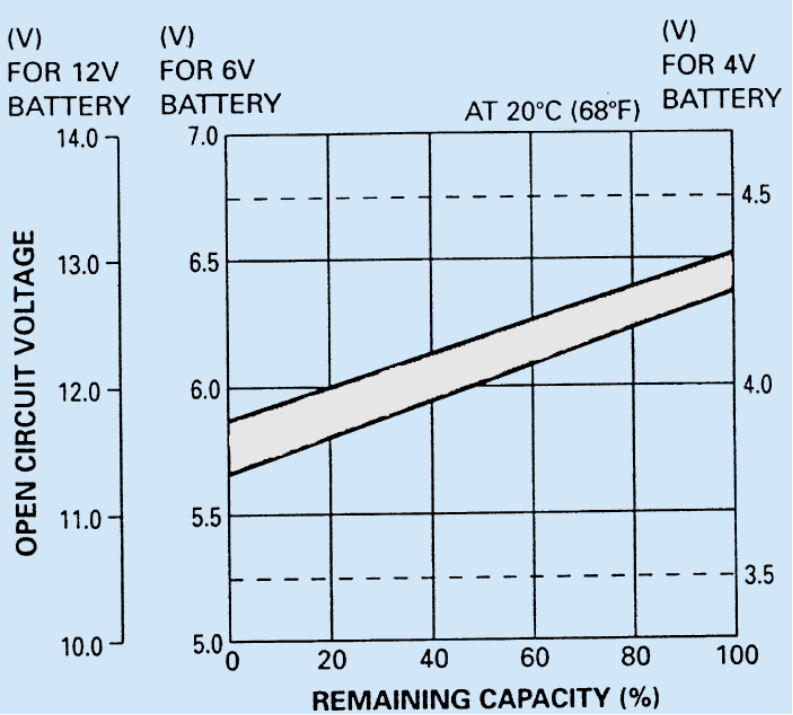

Figure 85. SoC in relation to terminal voltage from manufacturer's data (image courtesy Yuasa Batteries Europe).

The relationship assumes prior control over battery state, in that the battery would have been allowed to reach a steady-state terminal voltage over some hours. It therefore does not immediately follow that the test procedure carried out during this chapter should produce terminal voltage based state information, as at each of the three state-of-charge values chosen the PRBS test was carried out directly after the prior test step (charge for the 100% test, and controlled discharges for the 85% and 0% states of charge.) The observations in Figure 86 however show interesting correlations at these charge states.

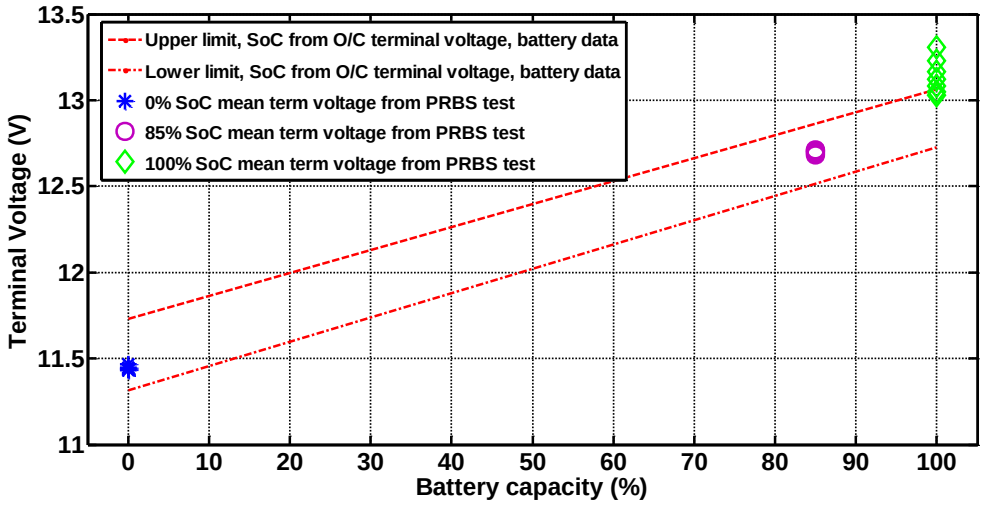

Figure 86. Mean DC terminal voltage clusters obtained during the bipolar PRBS tests plotted against battery data for SoC with terminal voltage (20°C).

Unsurprisingly the battery terminal voltage at 100% SoC is elevated, but the application of the bipolar PRBS arrests this overvoltage and it then remains in the ranges for that state. The 85% and 0% results show mean DC voltage levels which are reflective of the manufacturer's data, albeit over a wide band with the limited results obtained in this chapter.

7.6 Conclusion

The effect of applying a bipolar PRBS perturbation signal with an average value of zero was observed to have several characteristic benefits. Examining the overall voltage envelope for the battery during the test showed the average DC terminal voltage is much less affected than by using the discharge and charge PRBS techniques. The test is designed to have a net energy exchange between the test system and the battery of zero, with the only losses being efficiency of the battery during the charge and discharge pulses of the PRBS. It followed, therefore, that the

excitation signal facilitates long duration tests which can be used on line, which may lead to a broader understanding of the battery parameters at lower frequencies. The test system did consume energy, so its use would be most suitable to battery test instruments rather than on board tests in portable equipment, however this could be mitigated somewhat by storing the discharged energy and reusing it. The bipolar system was applicable at 100% SoC, and showed repeatable results at this state, with a characteristic, elevated low frequency impedance at the fully charged state. Similarly this elevated low frequency impedance was seen at 0% SoC, but an increase in the high frequency impedance was also present, allowing identification of the respective states.

Further analysing the overall voltage envelope of the PRBS, the average DC level of the PRBS voltage was used to make approximations to battery efficiency at the selected test states-of-charge, by using the gradient of this DC level as an indicator.

The intention was that this gradient could be used to report battery charge efficiency and could, historically inform SoH of the batteries over time. This indicator is revisited in chapter 11 in testing a battery to accelerated failure.

The mean DC voltage was observed to tie in with the manufacturer's data for SoC, for the tests carried out. This was interesting as the battery had been subject to either charge or discharge before these measurements were made, suggesting that application of the bipolar signal assists the battery in moving towards a steady-state terminal voltage.

This data therefore has potential for being useful in informing a combined mode SoC evaluation system and is explored further in the work within the following chapters.

Chapter 8. Variations in battery parameters with state of charge

8.1 Introduction

It is known that over a charge and discharge cycle a battery will undergo changes in the rate at which energy is exchanged [16], and this can be characterised by examining the battery parameters using an appropriate model. The most easily observed areas for these parameters are at low and high states-of-charge (SoC), where the battery has characteristic behaviours which are reflective of these states. This is of use, but the SoC at other times represents the predominate areas of interest in most applications – a fuel gauge which only indicates full or empty has limitations.

The motivation for this work was to build on the findings of chapter 7 and investigate the applicability of the PRBS technique in indicating state of charge over a full range of charge states. The work encompasses early investigations during the body of this research investigating battery parameters over SoC using a discharge based PRBS[165], and was expanded to encompass the later work using the bipolar PRBS method, which had demonstrated applicability over the full range of SoC, with the additional ability to report mean terminal voltage of the battery during the test itself. The mean terminal voltage is further examined to establish if these measurements can be used as an indicator in informing the SoC evaluation process.

8.2 Correlations between SoC and processes within the battery

The SoC of battery or cell can be equated to the voltage across the bulk capacitance, but this voltage is not always directly accessible, or completely reflective of the

battery state. The effective capacity of the battery is also subject to the dynamic behaviour of the processes controlling transport within the battery, leading to the need for analysis of other equivalent circuit components within the battery model.

The ability of the battery to accept charge and deliver current can be related to the $C_{Surface}$ and R_t from the standard Randles' model [16], and the effective value of these components, and others, can change over a discharge cycle at constant temperature. Understanding these changes can therefore facilitate SoC indications if the prevailing conditions are well understood.

8.3 PRBS test procedure

Tests were designed to allow the parameters for the batteries (Yuasa NPL65-12i) to be obtained after periodic discharge steps. The battery was initially charged to 100% SoC using the temperature compensated charger within the test equipment, and the PRBS perturbation was then applied before a timed discharge to the next test step. The flowchart in Figure 87 shows the test procedure.

The test equipment used comprised the discharge mode apparatus developed in chapter 5 for the early work, and the combined mode bipolar test apparatus described in chapter 7 for the later tests, which is detailed in the appendices.

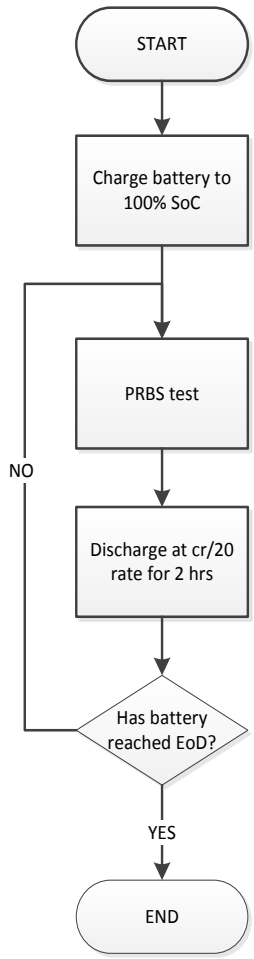

Figure 87. Test schedule flowchart, SoC tests

8.4 Discharge PRBS test results

The discharge PRBS tests were carried out during the early research [165] prior to the development of the bipolar PRBS technique. The tests were therefore subject to the limitations of the method that have been identified, particularly the indeterminate results at 100% (resulting in the discarding of initial data sets from the results) and the effect of discharge of the battery during the tests. The model used for this work was the standard Randles' circuit and the impedance results in Figure 88 shows the findings from these tests for the parameters R_i and R_t.

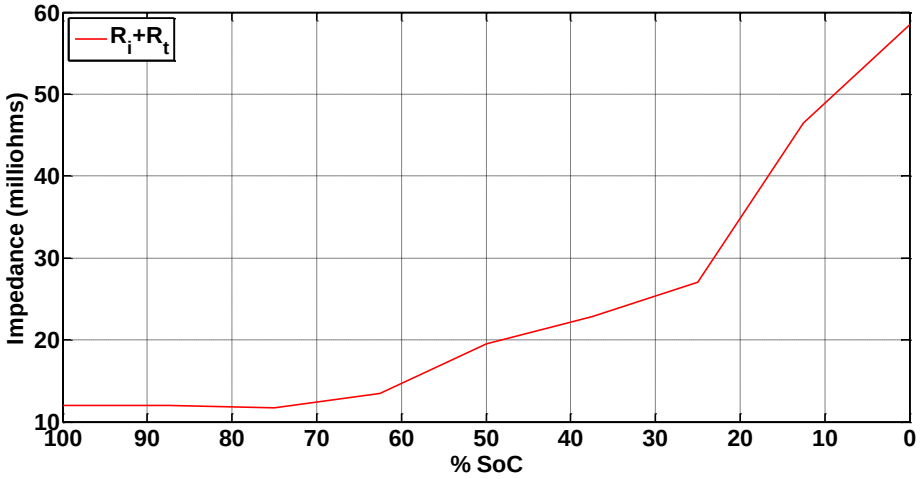

Figure 88. Battery impedance against SoC for the test battery, (discharge PRBS tests)

The impedance results show a good indication of battery state, but the characteristic elevation in impedance at 100% SoC is not apparent due the some data sets being discarded at the early part of the test. This was due to the more intrusive nature of a discharge based system, affecting the initial terminal voltage of the battery, leading to an aggregate impedance being used at this charge state.

Figure 89 shows the surface capacitance over SoC for the PRBS discharge tests, over the same data range, established using a combination of the evaluation techniques used in the early work. Indications from the results were that the activity within the battery decreases over state of charge, manifested in a reduction in surface capacitance. As such the discharge tests presented a view of the test battery which showed areas from 100% to 80% SoC which were broadly similar from the graphs in Figures 88 and 89, yielding usable results.

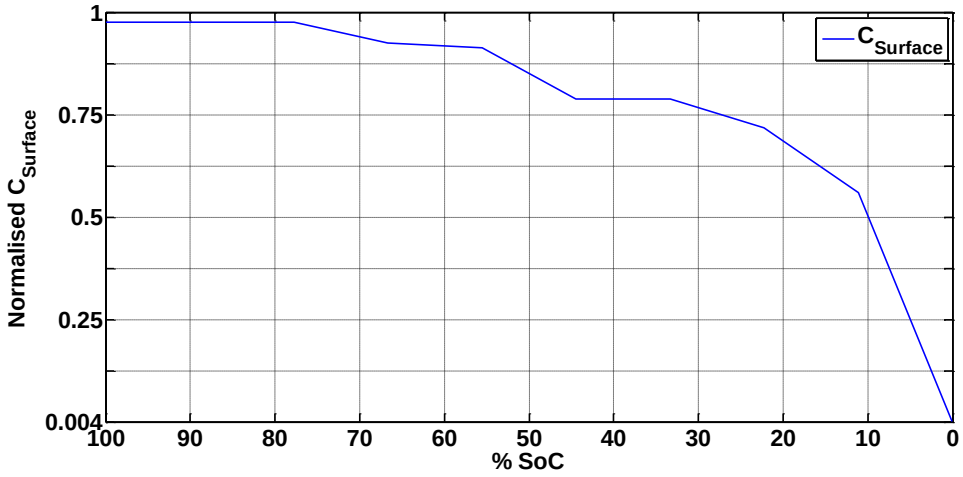

Figure 89. Surface capacitance over SoC ($C_{Surface}$ normalised=14F)

However the knowledge gained later in the research led to revisiting the tests with the bipolar PRBS, as it was imagined that more detailed results could be obtained using these techniques.

8.5 Bipolar PRBS test results

Subsequent to the work carried in chapter 7, the tests were repeated using the bipolar method, using the 6 bit PRBS with the frequency step as introduced in chapter 6. The impedance analysis was carried out using multiprbs.m (appendices, 15.8.8) which was devised to process the frequency step PRBS automatically, calling evalprbs2.m to calculate the impedance of the PRBS test. The battery model was also revisited from Figure 54, section 6.2 with modifications for clarity in its application, with consideration to known battery characteristics [161, 164].

8.5.1 Developed battery model

The model used to analyse the data acquired during these tests was based on the model used in chapter 6, Figure 54, with some modifications and is shown in Figure 90. Referring back to Figure 53, Ri is the sum of the resistance of the cell interconnections (R_{int}) in addition to the electrolyte resistance (R_e), a combined parameter for both charge and discharge as tests carried out used bipolar PRBS where no distinction could be made between charge and discharge processes.

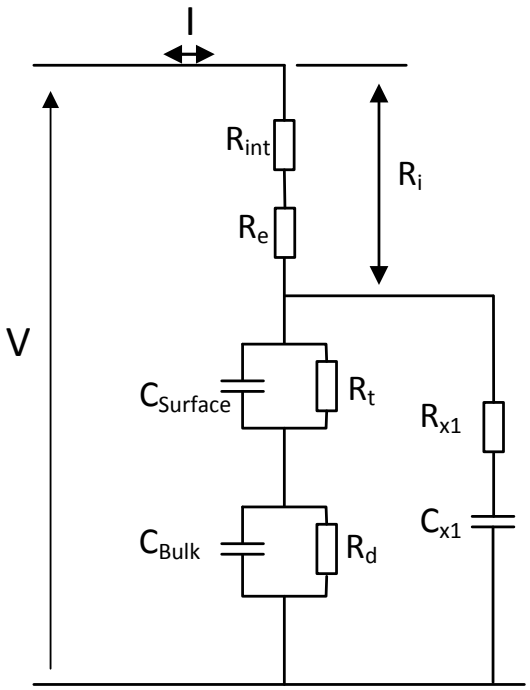

Figure 90. Developed battery model for the Bipolar PRBS SoC investigation

The parallel network in this model C_{x1} and R_{x1} can be equated to the parallel C_x, R_x (a parallel branch element of $C_{Surface}$ and R_t) used in the previous iteration of the model, but it is connected to the bottom of R_e in this case which was deemed to be more representative of actual conditions. The model developed from

previous investigations [160], and with consideration to work of Armenta-Deu [164] and Jossen [161] whose work in dynamic battery behaviour and the transition from charge to discharge informed the positioning of R_i outside of the parallel circuit branch. The impedances of a battery or cell which contribute to the overall impedance are split into three main groups, those related to the structure and electrodes (R_{int}), electrolyte resistance (R_e) and impedance due to reactions at the electrode double layer [16, 161, 164]. It made sense therefore at this fairly mature stage of the model development to place these parameters accordingly in the equivalent circuit. As such R_e and R_{int} were placed outside of the parallel branch with all of the parameters associated with $C_{Surface}$ in the lower circuit branch. C_{Bulk} is very low impedance at the perturbation frequencies used (0.5 to 1250Hz), therefore R_{x1} and C_{x1} sit effectively in parallel with $C_{Surface}$ providing the improved curve fit.

Impedance analysis of the circuit branches was carried out to allow incorporation into the MATLAB routine curvefit.m within the appendices (15.8.10) for later analysis of the PRBS impedance results. The analysis is shown below in equations 38 to 43.

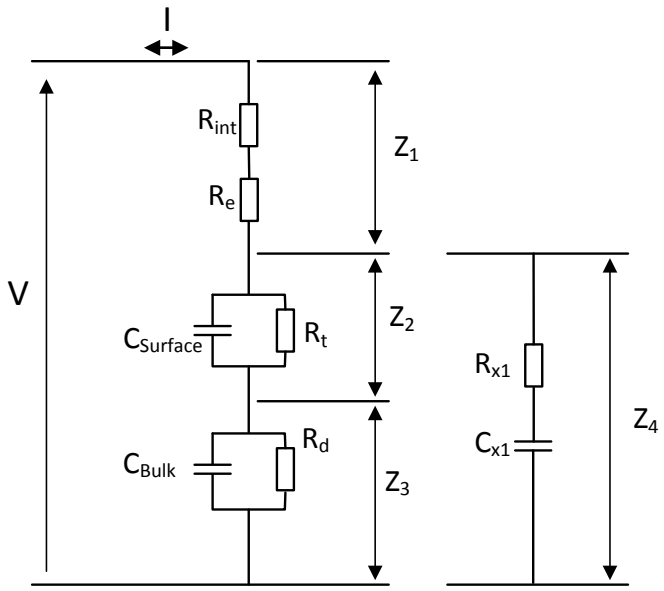

Figure 91. Equivalent circuit broken into branches for analysis

$$R_i = R_{\text{int}} + R_e \tag{38}$$

$$Z_{Batt} = Z_1 + (Z_2 + Z_3) // Z_4 \tag{39}$$

$$Z_1 = R_i \tag{40}$$

$$Z_2 = \frac{1}{(\frac{1}{R_t} + \frac{1}{XC_{Surface}})} \tag{41}$$

$$Z_3 = \frac{1}{(\frac{1}{R_d} + \frac{1}{XC_{Bulk}})} \tag{42}$$

$$Z_4 = \sqrt{R_{x1}^{\ 2} + XC_{x1}^{\ 2}} \tag{43}$$

8.5.2 Bipolar investigation test results

Impedance results for the test battery states were plotted in order to observe the changes over battery state. These findings are shown in Figure 92.

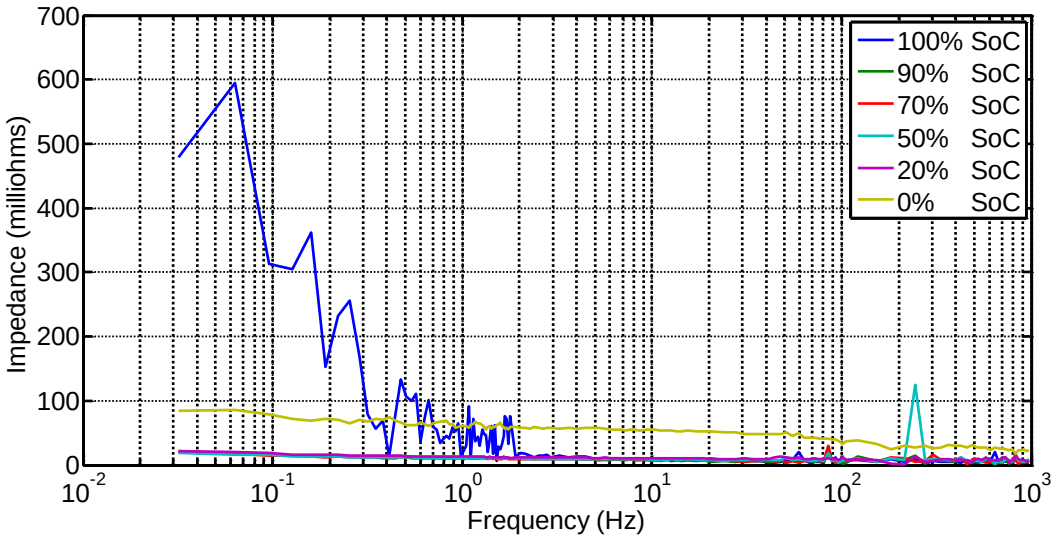

Figure 92. Impedance over SoC - Bipolar tests

The figure shows the plots for the battery impedance over SoC and for clarity not every 10% SoC step is plotted but the characteristics are clearly seen. 0% SoC shows a sharply elevated impedance over the full frequency range, indicating the inability of the battery of this stage to operate as a useful energy storage medium.

The responses from the other states-of-charge are similarly interesting (Figure 92). The higher states of charge (70%, 50%) show lower impedance across the frequency band than the 20% SoC result, but the 100% SoC result shows the characteristic increase of impedance known to exist with this state. This can be seen more clearly with the expanded plot in Figure 93.

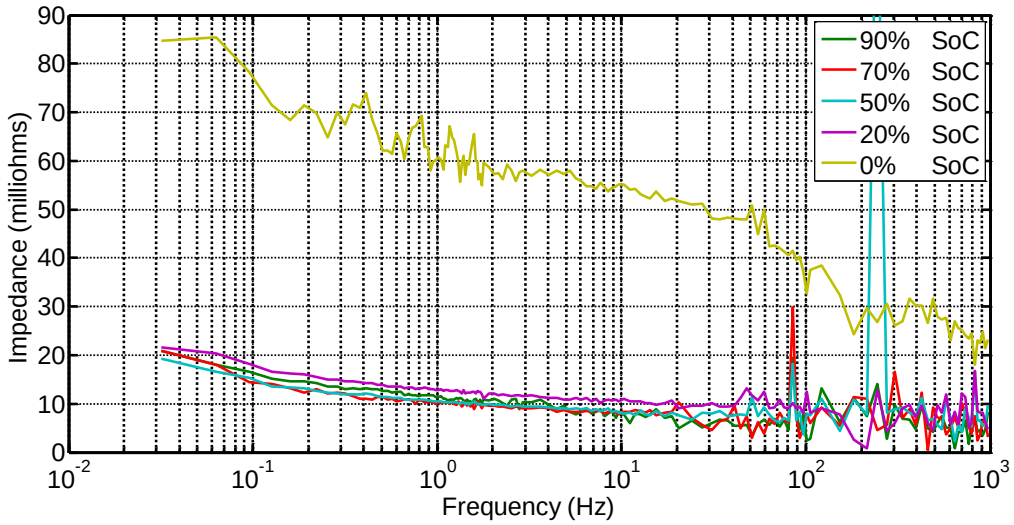

Figure 93. Impedance over SoC - Bipolar tests, expanded to show more detail (0 - 90% SoC)

From the responses seen in Figure 93, it can be seen that the impedance/SoC relationship has a crossover point around 50% SoC, which corresponds to the quasi-linear area of discharge for a VRLA battery at a 20 hour rate (Figure 26, page 97). Since increased impedance is seen at both high and low states of charge the PRBS alone is not sufficient to fully characterise SoC and so some further tests would need to be applied to inform a SoC evaluation system to allow blind tests of batteries.

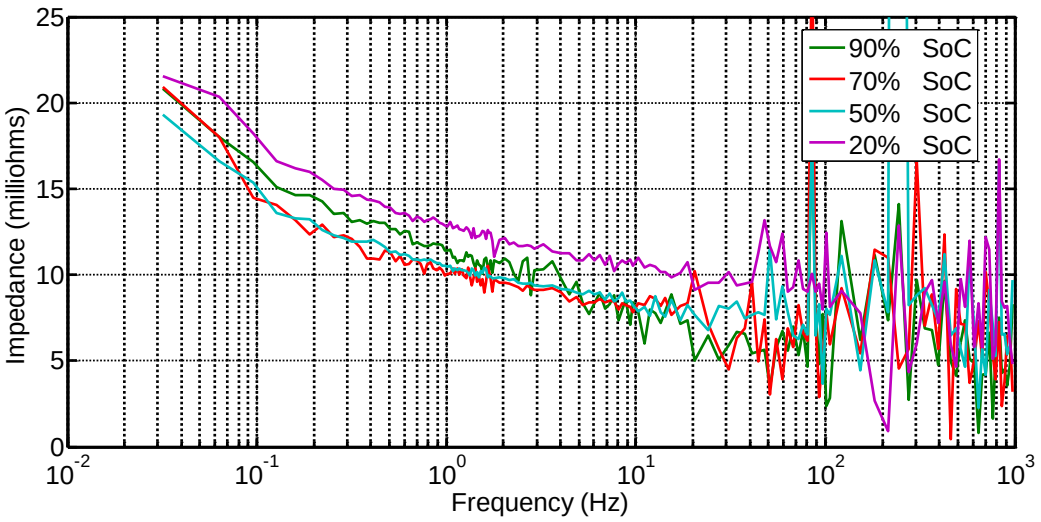

Figure 94. Impedance over SoC - Bipolar tests, expanded to show more detail (20% - 90% SoC)

Using the developed model, curve fits were carried out (curvefit.m, 15.8.10) using an iterative approach in order to establish the battery parameters over SoC and these are presented in Table 15. The parameters for 100% SoC were notable for showing a distinct indication of this state, and the model parameters are dominated by the elements of surface capacitance, apparent reduction in bulk capacitance and the series resistance.

Table 15. Battery parameters over SoC

SoC (%)	$R_{int} + R_e$ (mΩ)	$C_{Surface}$ (F)	R_t (mΩ)	R_{x1} (mΩ)	Cx1 (F)	C_{Bulk} (F)
100	5.8	20	20	14	0.1	4
90	4.6	4.5	18	14	75	88400
80	6.3	5.5	15	5	85	88400
70	4.7	2.5	15	8	85	88400
60	6.3	2.5	15	4	85	88400
50	6.1	2.5	15	6.5	90	88400
40	6.4	2.5	16	6.5	90	88400
30	7.0	2.5	16	6.5	90	88400
20	8.7	6.5	14	6.5	60	88400
10	9.3	1	16.5	5.5	40	88400
3	16.7	0.1	38.5	20.5	25	88400
0	21.6	0.05	70.5	30.5	0.05	88400

Towards 100% SoC the chemical reactions facilitating charge slow down, and this is indicated by the characteristic reduction in charge current as a battery is float charged. The battery no longer accepts current significantly and any attempt to charge it further, up to the upper charge (cyclic) voltage limits only result in this excess voltage being developed across the surface capacitor.

At 100% SoC therefore the model is not completely applicable into the low frequency area of the response, and an indicated value of 4F for the bulk capacitance demonstrates this. This is clearly an apparent capacitance due to the high SoC, as during the remainder of the tests the battery delivers the rated capacity. The response at 100% SoC however remains significant in that despite the low frequency impedance being high, the high frequency impedance is in the healthy range. From these indications alone it could be established that the battery is in a fully charged state.

The key indicators from the testing are presented in the following graphs, with Figure 95 showing the values of the major impedances of the battery over SoC.

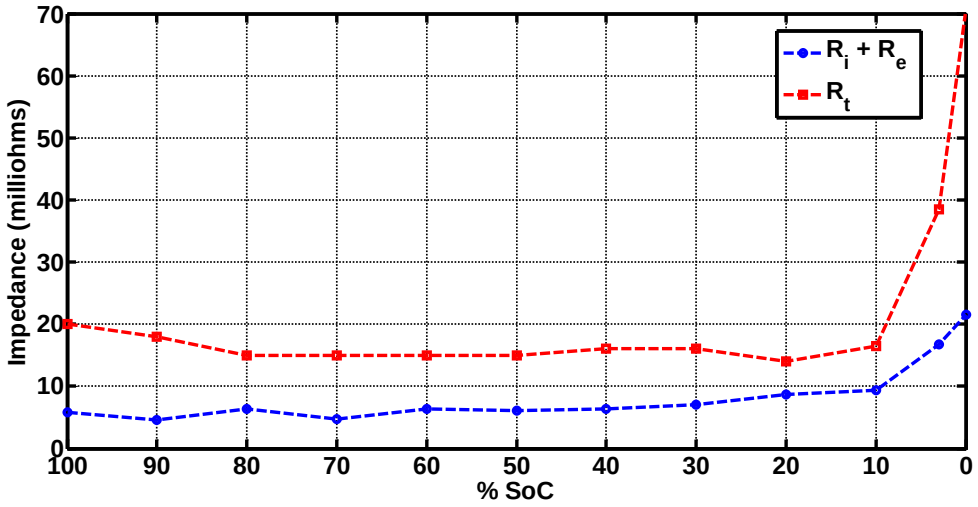

Figure 95. Major controlling impedance over SoC

Figure 96 shows the value of C_{x1} over SoC.

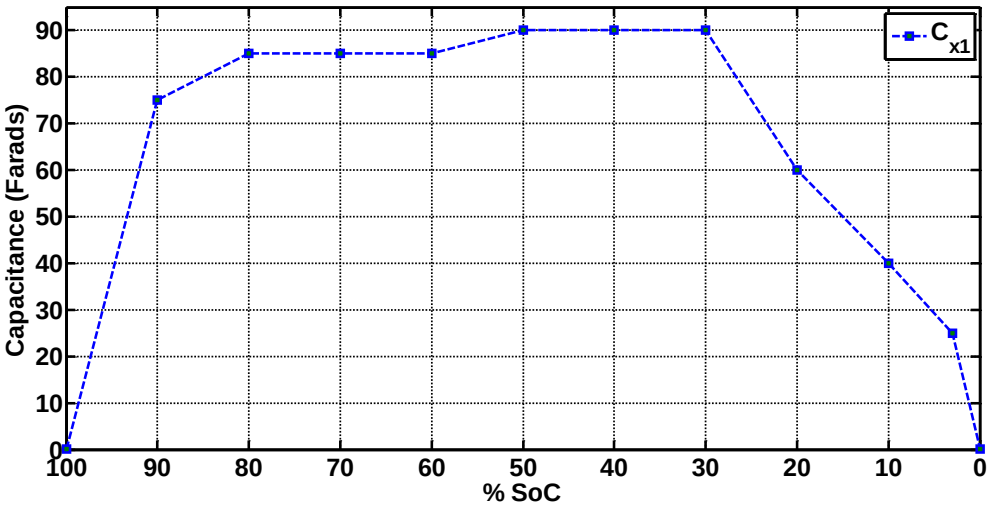

Figure 96. C_{x1} over SoC

The findings from the tests indicated that observation of battery status can be made from battery impedance and model parameters, however, the increased impedance at high and low charge states required some examination of additional indicators in order that the states could be differentiated. As such

the mean DC terminal voltage was extracted from the test data in order that this could be evaluated for such use.

8.5.3 Mean DC terminal voltage

The elevated impedances at both low and high states of charge could lead to some confusion over actual battery state during a blind test. As such, the findings of chapter 7 in regard to mean DC terminal were re-examined to establish whether these results could further inform a SoC indication system. Figure 97 shows the results obtained from the bipolar tests, bounded by the limits from manufacturer's data for the battery terminal voltage over SoC.

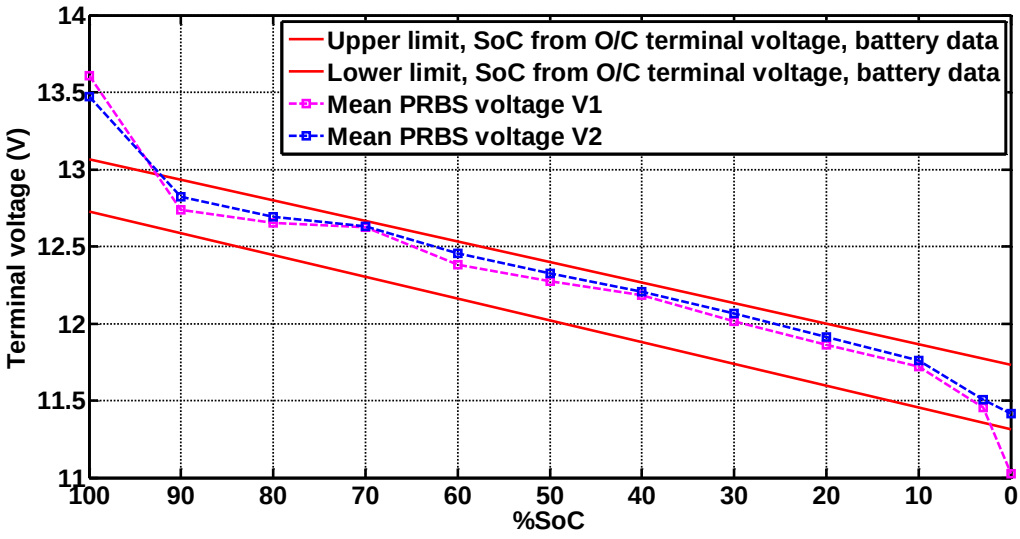

Figure 97. Mean PRBS DC terminal voltage over SoC

The findings are clearly useful in providing additional information for the state prediction process. The voltages V1 and V2 are the mean DC terminal voltages at the start and end of each PRBS test. As can be seen the voltages fall within

the manufacturers band for open circuit terminal voltage at 20°C for the indicated state, apart from 0% and 100% SoC where the experimental results deviate, but the deviations are such they confirm the status reporting. This means, referring back to Figure 94, that the impedance responses for each state can be indexed with the PRBS mean terminal voltage.

8.6 Conclusion

The investigation within this chapter demonstrated that bipolar PRBS battery testing facilitates SoC evaluation within batteries and cells, and allows very clear identification of 100% and 0% charge states. The elevated low frequency impedance at 100% SoC was accompanied by high frequency impedance indicating a healthy battery, which clearly indicated the 100% charged state. In contrast, the test results from the early work [165] using the discharge method showed trends which could be correlated to battery state, but the test data at 100% SoC required some indeterminate data to be rejected, thus not showing the elevated battery impedance at this point.

The discovery that the bipolar test facilitated useful mean terminal voltage measurement was important in that it allowed further identification of the charge state, particularly in intermediate states-of-charge, and this additional indicator, could therefore find application as part of a combined mode SoC indication system. This investigation therefore led to opportunities for expanding the work, based on the concept shown diagrammatically in Figure 98.

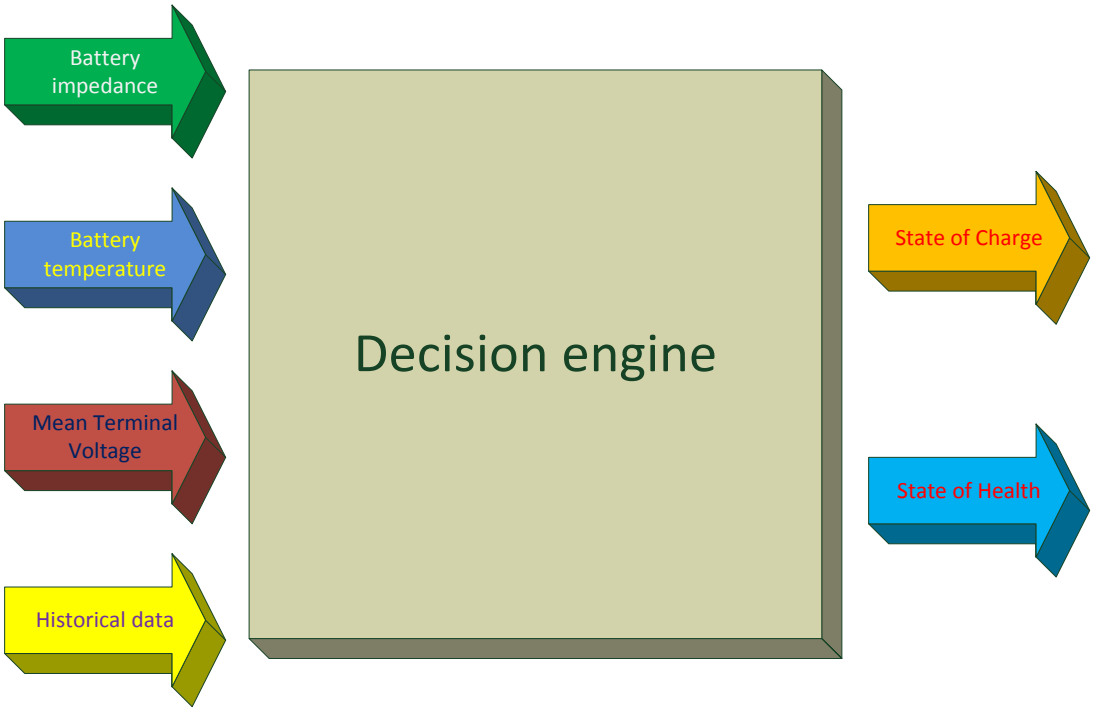

Figure 98. Battery SoH/SoC system

Figure 97 shows a proposed state evaluation system based on the work up to this point and sets out the work which follows. Based on the results of this chapter, the PRBS analysis could be used to inform a battery SoH/SoC system, based on a fixed temperature and with either initial data from a battery in a known good state-of-health, or a sufficiently comprehensive manufacturer's datasheet.

As such it remained to examine these system inputs in more detail, thus requiring examination of batteries over operating temperature range and lifecycle.

Chapter 9. Effects of temperature on parameters within batteries

9.1 Introduction

The previous chapters showed how PRBS testing coupled with suitable analysis could be used to provide useful SoC and SoH indicators should the battery and load conditions be known, and this chapter further explores these ideas by examining the temperature dependence of the equivalent circuit parameters in an effort to develop a more comprehensive battery monitoring system.

As discussed in chapter 3, Lead-Acid batteries suffer considerable performance reductions at low temperature, with both the ability to deliver high discharge currents and the effective capacity being impacted by reduced temperature. Performance increases with higher temperatures, but this is accompanied by undesirable degradations in battery health.

This chapter examines the parameters of test batteries over operating temperature range, and encompasses early work using the discharge based PRBS technique [166], reinforcing this work by again revisiting the experiments with the less intrusive bipolar PRBS.

9.2 Test setup and schedule

The test batteries used were again Yuasa NPL65-12i, as used in previous tests in a good SoH (new condition). Tests were devised to examined the batteries over a

typical operating temperature range, with a temperature range of -10°C to + 50°C for the PRBS discharge tests, with this expanded to -20°C to + 50°C for those carried out using the bipolar method.

The apparatus comprised two test chambers, the primary chamber being a Montford scientific environmental chamber with heating and cooling capability from -50°C to + 150°C.

Figure 99. Test battery in Montford environmental chamber

The Montford chamber (Figure 99) was used for the tests above 0°C with active heat/cool being used to maintain the battery temperature. Despite the fact this equipment has the ability to cool to -50°C, a modified domestic freezer with an industrial temperature controller was used for the temperature tests below 0°C. This "chamber" had been devised for previous low temperature battery experiments as it

proved more cost effective to run over long periods of time, as the Montford chamber employed a total loss refrigerant system in the form of liquid CO_2. The chambers, including their specifications, are described in more detail in the appendices.

In order to evaluate the battery performance over operating temperature range it was necessary to ensure the subject batteries were stable at the test temperatures before any testing was carried out. To achieve this at each test increment the battery was allowed several hours at each temperature step in order to reach a thermal equilibrium before carrying out the PRBS test. The flowchart in Figure 1 shows the test procedure.

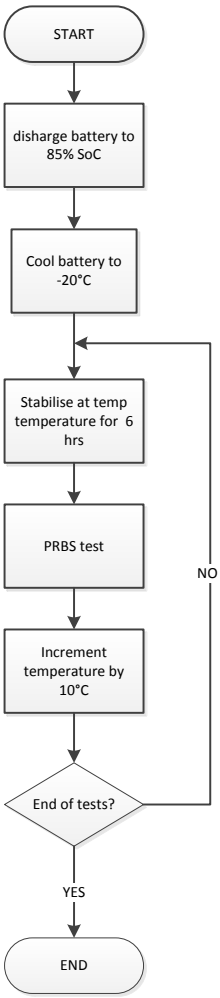

Figure 100. Test schedule flowchart, temperature tests

As can be seen in the flowchart, the battery was discharged to 85% SoC before the tests, and remained in this state throughout the tests. 85% was chosen as a SoC where the battery is in a stable state, and it was prudent to avoid very high and very low states-of-charge, where other dynamics may have inadvertently affected the results.

Figure 101. Test battery in low temperature chamber

Figure 101 shows the test battery in the low temperature chamber prior to being cooled to -20°C. The temperature sensing thermocouple can be seen connected directly to the battery terminal, which is the most effective method of sensing the plate temperature without actually opening the battery case. As such the controller shows the "warm" battery at 22°C, rather than the temperature of the surrounding

ice. This chamber has no direct heating only insulation losses, so the autotune function of the controller was used initially on a dummy cool cycle in order to optimise the system.

9.3 Test results

The test results for the work carried out in examining the test batteries over temperature are found in the following sections. The test results for the early work carried out using the discharge PRBS is included, with the detailed analysis being carried out on the bipolar PRBS, providing more comprehensive results.

9.3.1 Discharge PRBS tests

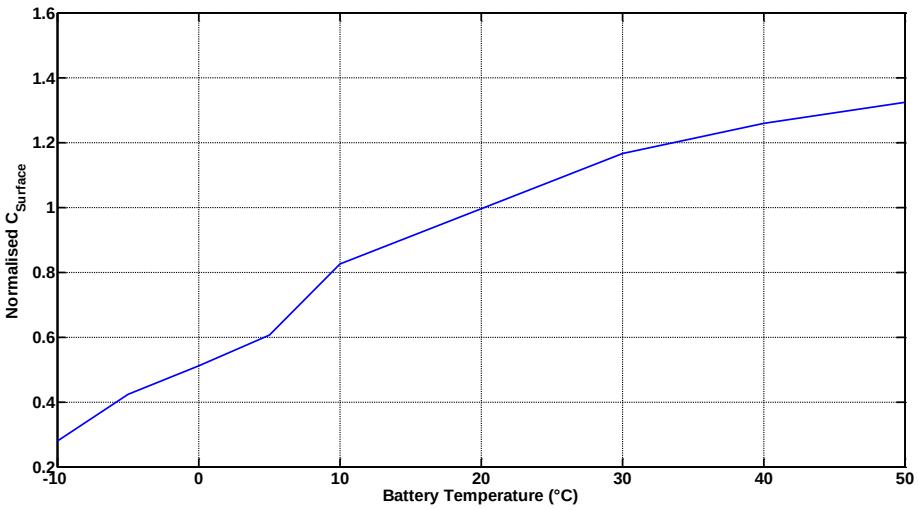

Figure 102. Normalised surface capacitance over temperature, discharge PRBS tests ($C_{Surface}$ = 14F at 20°C).

The discharge PRBS tests (Figure 102) were originally devised to explore correlations between surface capacitance and temperature using Randles'

model (Figure 36, page 118), as a potential indicator for effective capacity. Using the analysis in chapter 5 the value of $C_{Surface}$ over temperature was established, with the battery being maintained at a known SoC (95%). The work was presented at LABAT 2011 and published in the Journal of Power Sources [166].

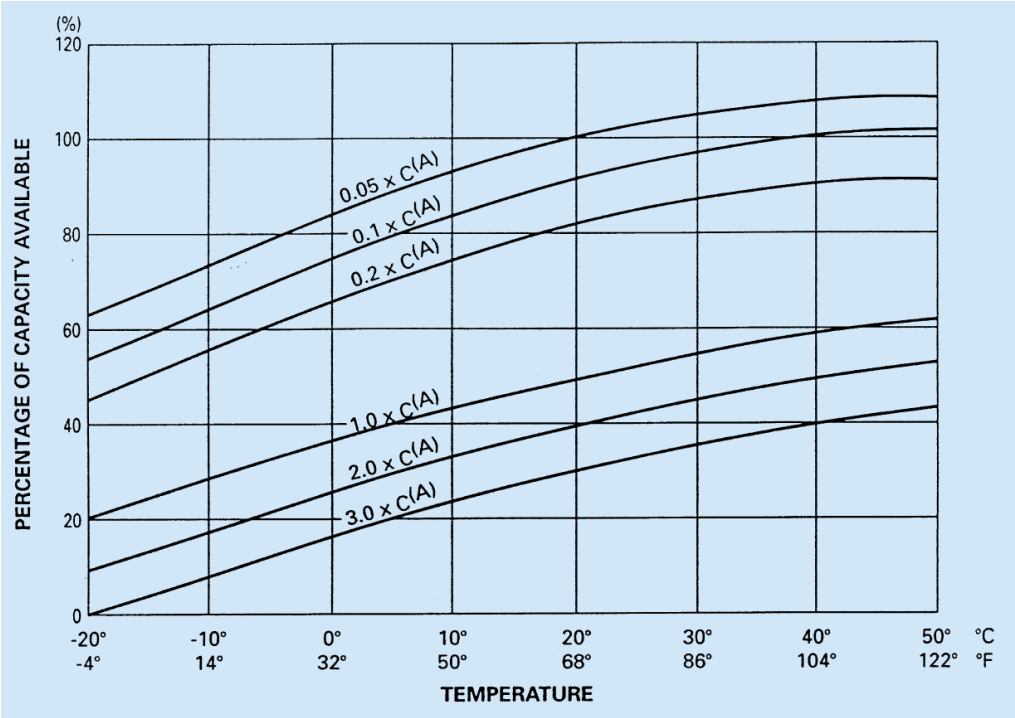

Figure 103. Available battery capacity with temperature from manufacturer's data (image courtesy Yuasa Batteries Europe)

The tests show satisfactory results, when compared with figure 103, which shows manufacturer's data for available capacity over temperatures. The value of $C_{Surface}$ reduces with decreases in temperature, albeit following a steeper gradient than that for the capacity values from Figure 103. The work was revisited later in the research, and it was imagined that a developed test system

from this work may ultimately use the bipolar PRBS test, so the investigation was refocused on this method, which is detailed in the following sections.

9.3.2 Bipolar PRBS test results

The bipolar tests carried out on the test battery were able to expand on the work carried out using the discharge PRBS by providing a less intrusive test to the battery, particularly as the battery was cooled, and using the model developed for the SoC tests in chapter 8 (Figure 90, page 186). Figure 103 indicates the battery has a severe loss of capacity at -20°C, so therefore further discharging the battery with the test itself is undesirable.

Considerations had to be made for the upper voltage limit of the bipolar PRBS on the positive going "charge" section of the PRBS waveform. The battery would, at low temperature, require an increased charge voltage, and the headroom on the test apparatus had to be set in order that this would not become an issue during the lower temperature tests. The voltage levels for cyclic charge at -10°C indicated the voltage should be around 15.3V and the Yuasa data stopped at this temperature. The majority of VRLA batteries, with the exception of some spiral wound types [24], are effectively unusable at temperatures below -10°C, however, the charge voltage limits were extrapolated to allow the tests at -20°C.

The tests results were examined and curve fitting applied using MATLAB, using the model developed for the SoC tests in chapter 8.5.1, and the plotted results are presented in Figures 104, 105 and 106.

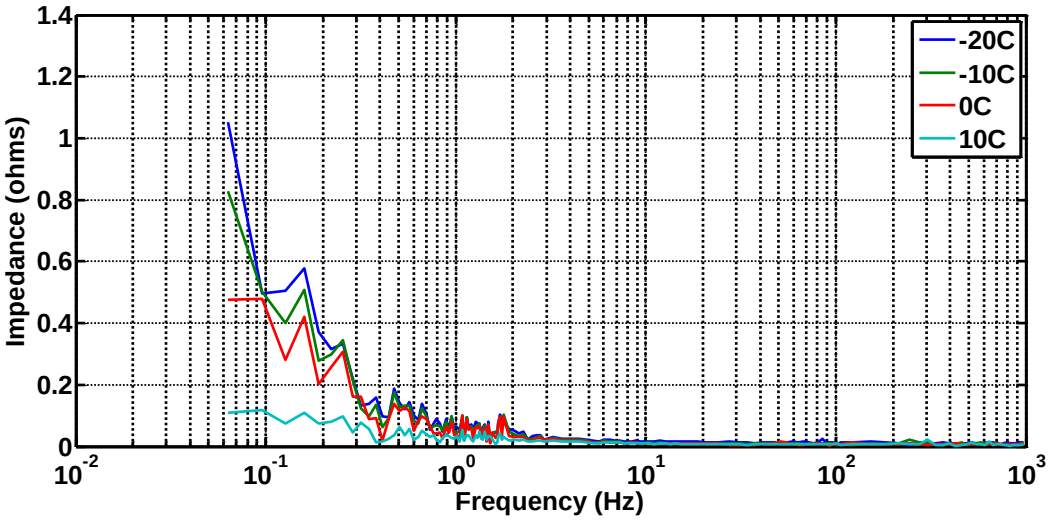

Figure 104. Impedance over -20 to 10°C temperature range - bipolar tests.

Figure 104 shows a spread of the results obtained for the test battery. The tests between 0°C and -20°C show the elevated impedance in this area due to the decreased ability of the battery to accept charge. Responses for 20°C to 50°C are shown in Figure 105.

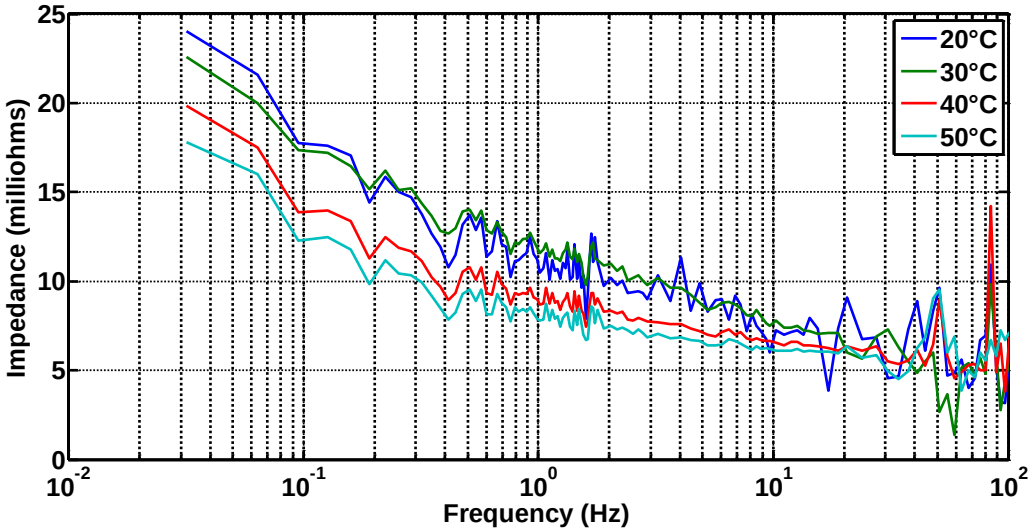

Figure 105. Impedance over 20-50°C temperature range - bipolar tests.

The results in figure 105 show more predictable area of operation for the test battery. High frequency impedance (R_{int} +R_e) is representative of battery state across the range of tests, and this relationship is shown in Figure 106.

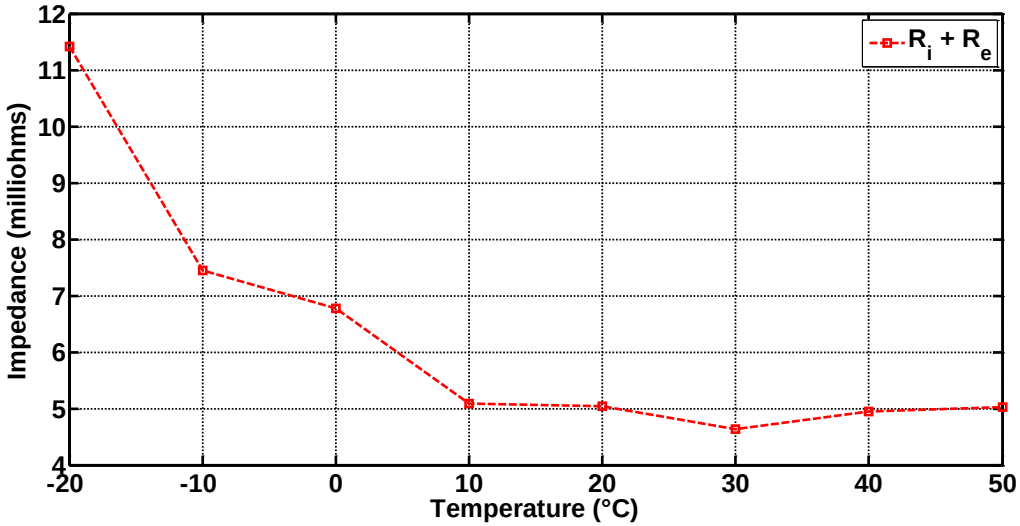

Figure 106. High frequency impedance (R_i+ R_e) over temperature

Curve fitting was carried out using the MATLAB routine curvefit.m, comparing impedance plots to iteratively derived responses in order to establish parameters. The complete results are shown in Table 16.

Table 16. Test battery parameters over temperature

Temp (°C)	R_{int} + R_e (mΩ)	$C_{Surface}$ (F)	R_t (mΩ)	R_{x1} (mΩ)	Cx1 (F)	C_{Bulk} (F)
-20	11.42	1	5	5	1	1.5*
-10	7.44	1	5	5	1	2*
0	6.77	1	5	5	1	3*
10	5.09	2	15	8	5	88400
20	5.04	5.0	20	11	50	88400
30	4.63	5.5	20	14	75	88400
40	4.94	6.5	18	5	95	88400
50	5.03	6.5	14	3	105	88400

*The values for C_{Bulk} at the lower temperatures are representative of the impedance response, and the actual capacity of the battery is much higher than this.

9.3.3 Mean PRBS DC terminal voltage

For completeness, the mean terminal voltage of the PRBS at the battery terminals was again examined for each test carried out during the investigation.

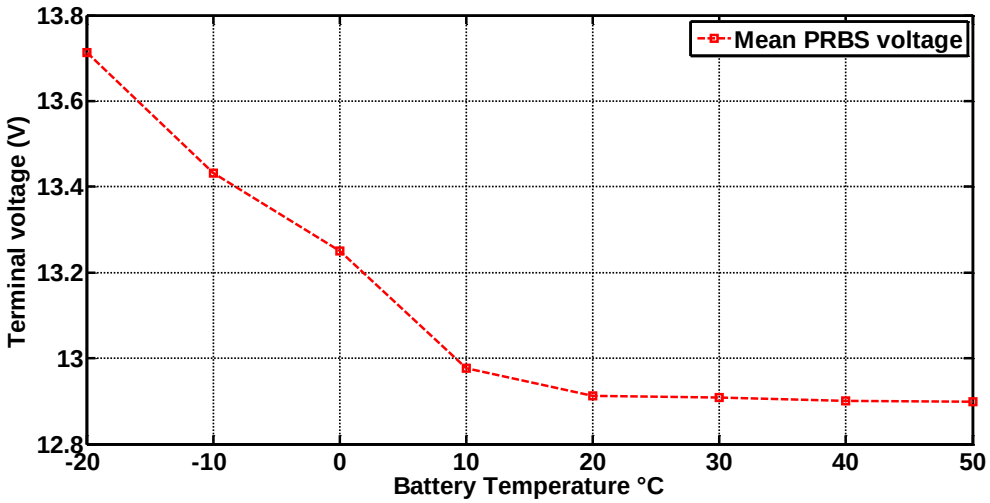

Figure 107. Mean DC terminal voltage over battery temperature

The results seen in Figure 107 are interesting in that the mean terminal voltage at lower temperature is shown as elevated. As the battery cools the mobility of the electrolyte due to diffusion naturally decreases. It is known that electrolyte circulation reduces overvoltage – a common phenomenon known in batteries dependant on current density during normal operation at normal ambient temperatures [164]. At low temperatures the reduction in electrolyte

mobility therefore reduces the ability of the battery to deliver current, tending to promote an overvoltage on the positive going portions of the PRBS waveform. If the battery was discharged at this temperature however, this voltage would immediately collapse before recovering to a level more representative of the activity within the battery.

9.4 Conclusion

The findings for the investigation revealed useful indicators of battery performance at the test temperatures. The battery, when tested at -20°C indicated a severe drop in performance in line with general characteristics with low temperature operation of Lead-Acid batteries [16]. The electrochemical activity within the battery at this temperature, and the effective capacity, were clearly shown in the values obtained in the model capacitances and the charge transfer resistance. Towards 0°C the performance of the battery improved somewhat, but the suppressed performance was still indicated by the model parameters. Significant improvements began to be seen beyond this point with the familiar range of parameters seen at 20°C.

Towards 50°C the indication were that the performance of the battery was further improved, but as is known and discussed in chapter 3, increasing battery temperature to this level brings with it the undesirable degrading reactions within the battery which reduce operational life.

The tests carried out therefore demonstrated characterising the battery against its prevailing SoC, and are useful in providing an input to the battery state evaluation system proposed in chapter 8.

Chapter 10. PRBS analysis of Ultra batteries and battery/supercapacitor energy storage networks

10.1 Introduction

The work carried out in this chapter concerns the examination of parallel energy storage networks using the PRBS tests developed in earlier chapters. The motivation for this study was to examine the applicability of the developed test techniques to parallel energy storage networks, as these find applications in electric vehicles [167] and renewable energy systems [168]. The work was carried out early in the overall body of research leading to the parallel branch battery model used in chapter 6 (Figure 56, page 149) and its later iterations in other chapters.

Within the work, it was of interest to gain an understanding of the benefits of a lead-acid battery/supercapacitor parallel network, examining the respective roles of the battery and capacitor by applying the spread frequency PRBS perturbation, and obtaining parameters for the networks tested.

Going further, examination of an UltraBattery™ using the same techniques in order to make comparisons to the parallel networks, and their respective parameters would allow the advantages of each energy storage system to be assessed.

10.1.1 Capacitor and battery parallel networks

In chapter 2 the differences in the way energy is stored in batteries and capacitors were discussed. As batteries store electrical energy indirectly as

potential chemical energy and capacitors store energy directly in an electrostatic way, this presents opportunities for complementary energy stores operating at differing rates of charge and discharge.

The response times of batteries led to the technology being inefficient during rapid charge/discharge cycles, such as those observed in regenerative braking and subsequent acceleration in electric vehicles. These types of current profile are more suited to capacitors, but their overall energy density generally precludes capacitors being used alone in these applications, with the technology available at the time of writing. As such a parallel supercapacitor/battery network can offer advantages for use in EV and HEV duty [33].

10.2 Conventional battery tests

The investigation was focused on examining a conventional VRLA battery in comparison to an UltraBattery. Further to this two different super capacitor banks were assembled to be assessed as parallel, complementary storage elements with the conventional VRLA battery. The intention of these experiments was then to compare the performance of the parallel capacitor/battery networks against the UltraBattery, and also to use the parallel battery/capacitor combinations to give some insight into the respective roles of the parallel storage elements.

The batteries used were a Furukawa FTZ12-HEV UltraBattery™ as discussed in the review of current energy storage technologies in chapter 2. The battery is housed

within a generic 8-9Ah case size for commodity automotive SLI batteries, so a comparable capacity/case size motorcycle battery (Continental Batteries CTX-9) was chosen as the test subject for the conventional technology. A schedule of comparative tests was devised, and these are described in the following sections.

10.2.1 Discharge capacity tests

Initially, discharge tests were carried out on the two batteries, at a rate around $1c_r$ (8A) to compare capacity, using the apparatus in Figure 108.

Figure 108. Controlled charge/discharge system photograph

The overall control was implemented by using a VxI Power Oracle 200E battery backed power supply with custom firmware. This allowed controlled discharge of the battery to 0% SoC with automatic cut-off of the connected load

at the EoD voltage. As detailed manufacturer's data was not available for the batteries under test generic guidelines for VRLA batteries from Yuasa were used to establish appropriate EoD voltage levels for the discharge rates selected (9.6V for a $1c_r$ rate at 20°C) [17]. The system was also used for the temperature controlled charging of the test battery. Figure 109 shows the discharge curves for the batteries at the $1c_r$ rate, 20° Celsius.

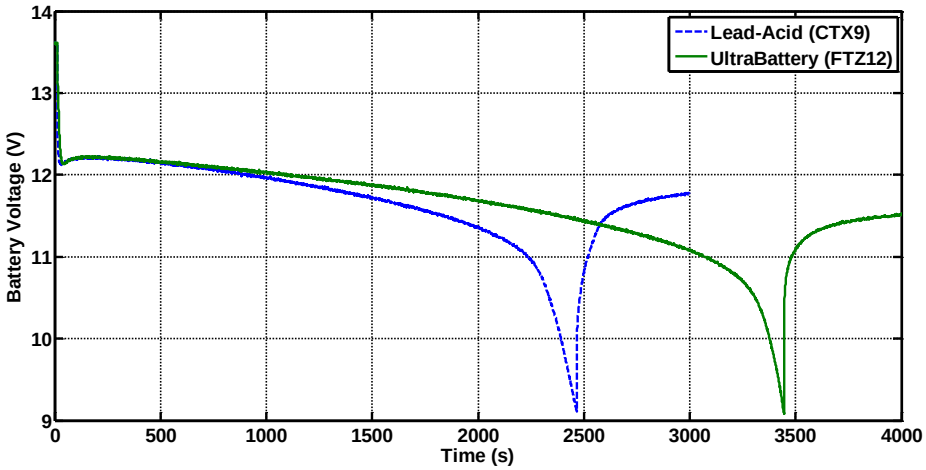

Figure 109. $1c_r$ discharge, 20° Celsius, both batteries

A further test at the same discharge rate in a -20° Celsius ambient was carried out to examine the low temperature discharge performance of the test samples (Figure 110). The calculated capacities for both batteries (using equation 16, page 122) during the tests, along with values for C_{Bulk} at 20°C are shown in Table 17.

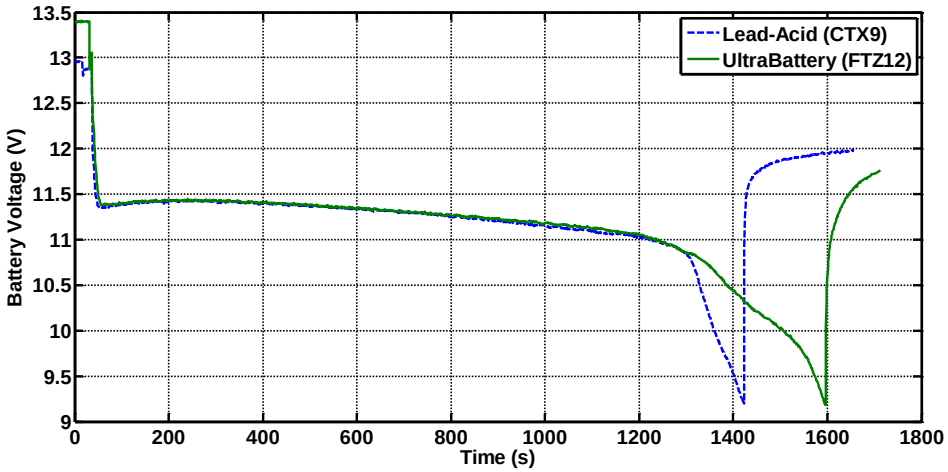

Figure 110. 1c_r discharge, - 20° Celsius, both batteries

Table 17. Discharge test results, UltraBattery and conventional VRLA

	Discharge time (s)	Capacity (Ah)	Capacity (%)	Capacitance (F)
Conventional (CTX9) (20°)	**2451**	**5.45**	**71.4**	**7561**
UltraBattery (FTZ12) (20°)	**3433**	**7.63**	**100**	**10586**
Conventional (CTX9) (-20°)	**1415**	**3.14**	**89.11**	**-**
UltraBattery (FTZ12) (-20°)	**1588**	**3.53**	**100**	**-**

The observations from the tests were that at 20°C the UltraBattery had approximately 30% more capacity than the CTX-9 battery. However, at -20°C the two batteries only show a difference of around 10%. This may indicate that the parallel capacitor structure of the battery leads to some reduction in

capacity at low temperature, although further testing would be required to verify this.

10.2.2 Static parameter evaluation

The batteries were subject to short duration pulse load tests in order to establish the parameters for the Randles' circuit. (Figure 36, page 118). The batteries were subjected to an 8A constant current load (approximately $1c_r$ discharge rate) which was interrupted to provide parameter information. The results for the Lead-Acid battery (CTX9) and UltraBattery (FTZ12) are shown in Figures 111 and 112 respectively.

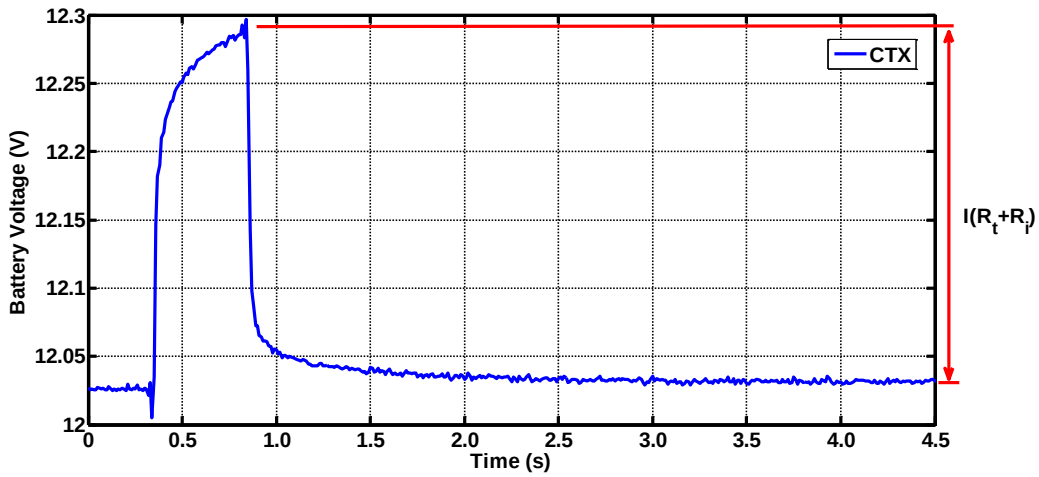

Figure 111. CTX-9 static parameter test, 8A off load transient (20°C)

On inspection of the responses distinguishing R_i from R_t proved difficult, precluding accurate evaluation of $C_{surface}$. As such the total of $R_i + R_t$ was recorded as a reference for the later PRBS tests:

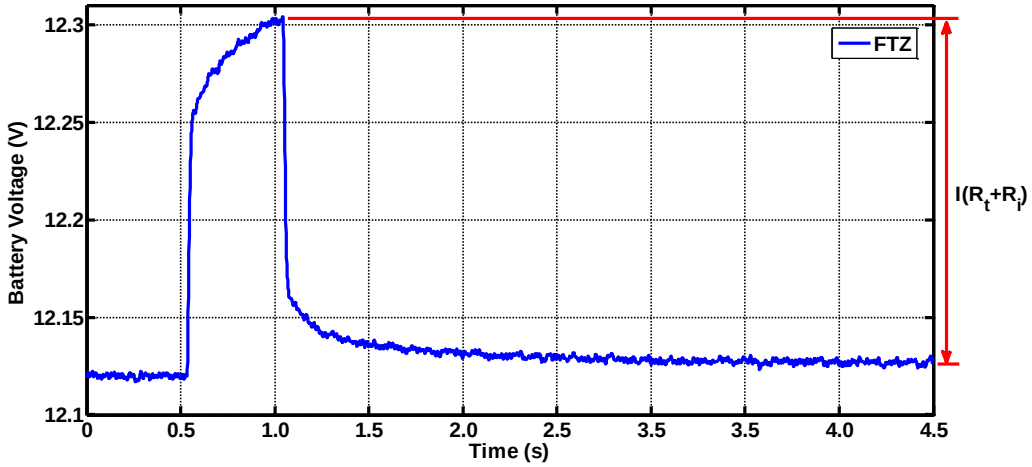

Figure 112. FTZ-12 Ultrabattery static parameter test, 8A off load transient (20°C)

Lead- Acid (CTX9)

Voltage deviation = 248mV

$I(R_t + R_i) = 0.248$

I=8A, therefore $R_t + R_i = 31m\Omega$

UltraBatttery (FTZ12)

Voltage deviation = 168mV

$I(R_t + R_i) = 0.168$

I=8A, therefore $R_t + R_i = 21m\Omega$

The results are presented in table 18 below.

Table 18. Randles' parameters (from static tests)

Battery	Ri+Rt (mΩ)
Lead-Acid (CTX9)	**31**
UltraBattery (FTZ12)	**21**

The static tests gave rise to results which were as expected generally, with the UltraBattery battery being lower in overall impedance by around 30%.

10.2.3 Battery mass

The batteries were weighed for completeness, bearing in mind the UltraBattery is designed for HEV usage and it was found to be significantly heavier than the conventional Lead-Acid (table 19).

Table 19. Battery mass

Battery	Mass (kg)
Conventional	**2.85**
UltraBattery	**3.75**

10.3 Testing of parallel energy storage networks

The following section concerns tests developed using the conventional battery with parallel capacitance. The capacitor banks chosen were significantly different in order to inform the model already developed for the UltraBattery.

10.3.1 Test configuration - Supercapacitor Bank 1

The super capacitors used were Wima DS-C-09-01-C200-XB-M-SS rated at 200F, 2.5V DC [88]. In order to achieve the terminal voltage of the battery, capacitors in series were used to increase the working voltage. This in turn reduced the

overall capacitance by the same factor, resulting in a pack 1/6 of the rated capacitance value per capacitor (33F).

10.3.2 Test configuration - Supercapacitor Bank 2

The second capacitor bank again used 6 capacitors connected in series, but of higher capacitance. The capacitors used were Maxwell Energy Products Inc PC 2500, of value 2500F, 2.7V [84]. The total capacitance of the 6 capacitors in series was therefore (calculated) 417F.

10.3.3 Capacitance tests

Capacitors are manufactured with a wide capacitance tolerance, so charge and discharge tests of the bank were carried out in order to establish the actual capacitance experimentally.

The capacitors were charged from 1V to a terminal voltage of 15V using a constant current of 2A. Subsequently the pack was discharged using a constant current 2A load to 1V (1V being used as it allowed headroom for the constant current load). Calculations of stored charge (Coulombs) were then carried out in order to establish capacitance values (Table 20).

Table 20. Capacitance test results

	Bank 1 charge	Bank 1 discharge	Bank 2 charge	Bank 2 discharge
Charge (coulombs)	**658**	**652**	**8418**	**7152**
Capacitance (F)	**47**	**46.6**	**601.3**	**510.9**

10.3.4 Test system description – parallel network PRBS tests

The test system used in the earlier tests was modified with the addition of further input from a total of five channels of measurement (Figure 113). The channels comprised battery terminal Voltage and offset measurement to determine any voltage dropped in the system wiring, and 3 channels of current measurement (capacitor current, battery current and total current).

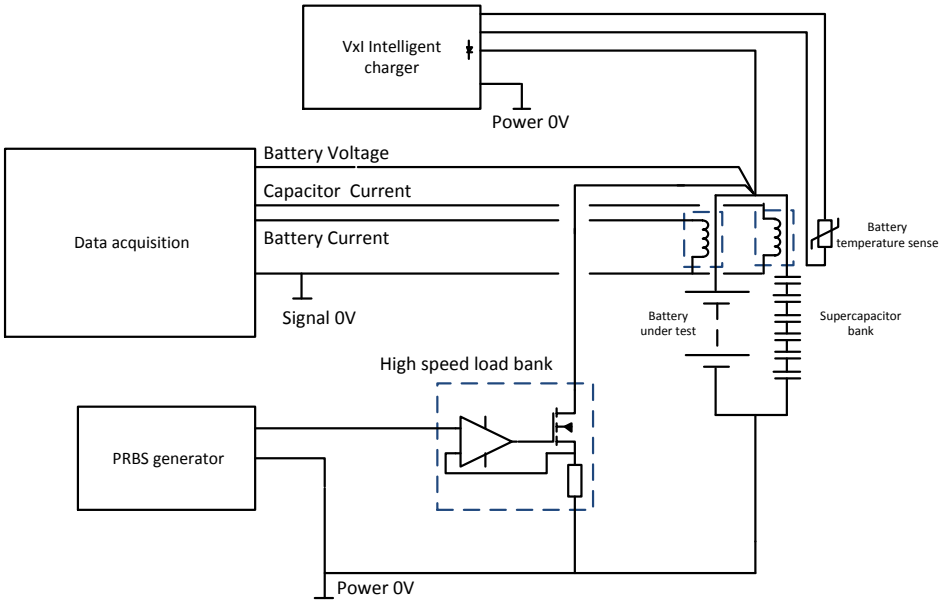

Figure 113. Test system block diagram

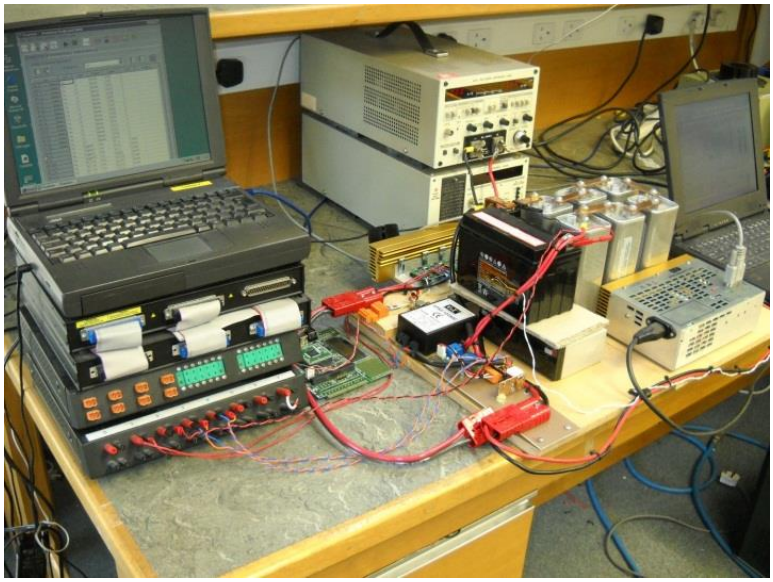

Figure 114. Test system photograph, battery/supercapacitor bank 2

Figure 114 shows the test system photograph. To the left of the picture the data acquisition system is seen, and referring to the aerial view in Figure 115 we can see the parallel connection of the battery and the smaller supercapacitor bank.

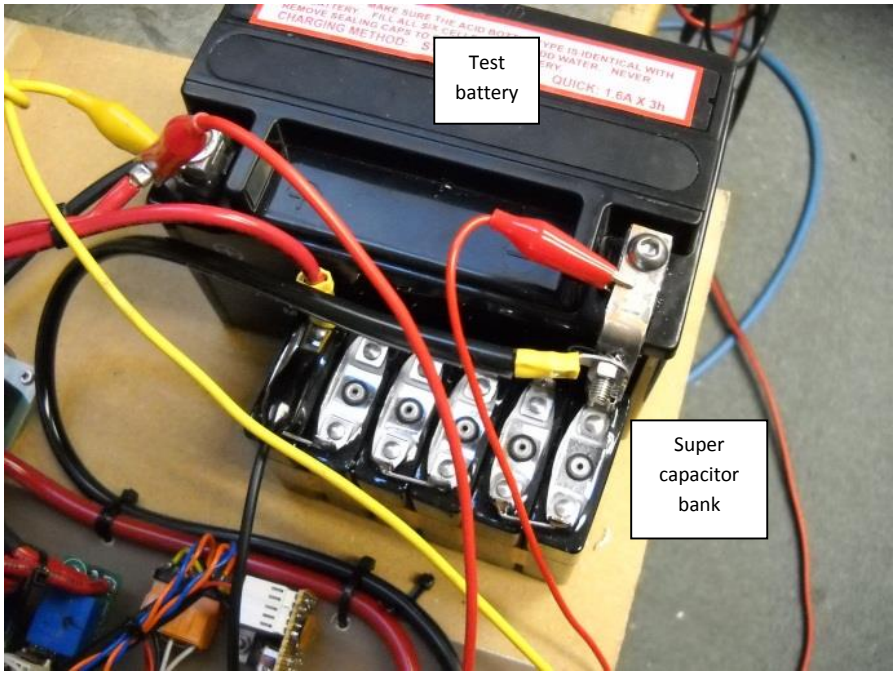

Figure 115. Battery/supercapacitor test setup, bank 1

Figure 116 shows more detail of the test system with capacitor bank 2. (The twisted wires from the charger to battery are the temperature sensor for the battery temperature compensation).

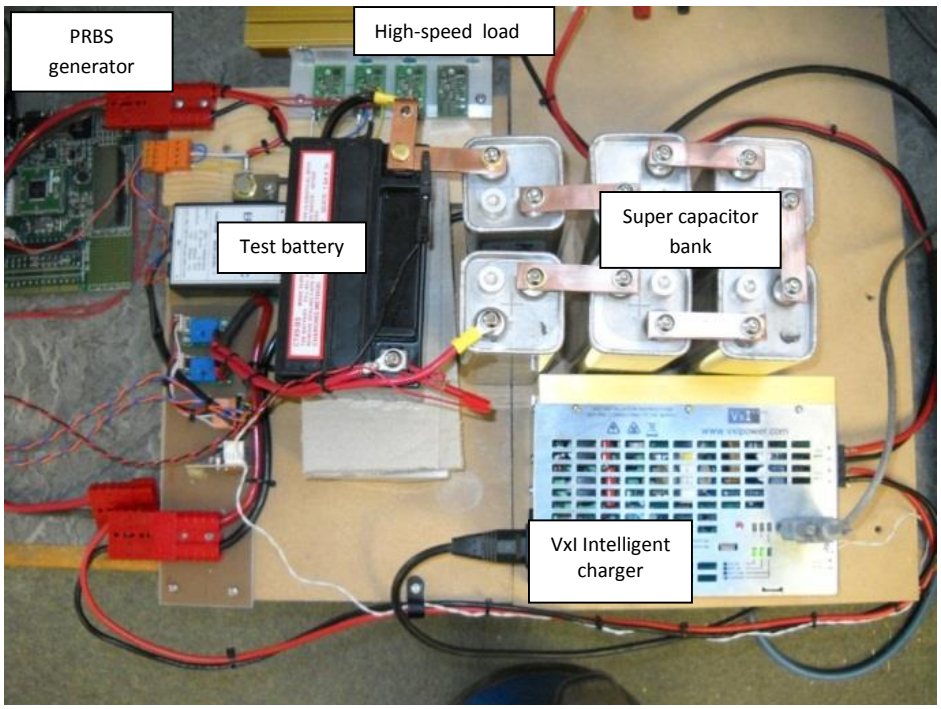

Figure 116. Battery/supercapacitor test setup, bank 2

10.3.5 PRBS application to the energy storage networks

Tests on the capacitor/battery parallel combination were carried out in the same way as the tests discussed in the previous chapters, with additional information gathered regarding the current profiles. Current measurement was carried out on each parallel branch, in addition to total current flowing in the PRBS load. Analysis of these current responses was carried out in order to gain insight into

the range of frequencies over which the supercapacitor offers performance improvements over the battery alone.

10.3.6 Analysis of the complementary energy stores

Prior to carrying out frequency domain analysis of the acquired data, the data was plotted in the time domain to allow inspection of the waveforms.

Analysis of the current flows during the tests gave an insight into the interaction of the capacitor and battery. The capacitor/battery combination is intended to address the issues associated with rapid changes of current direction, and as such the PRBS test allows some examination of this performance.

Prior to the test the battery/capacitor combination was charged at a cyclic charge level [17], (2.4 Volts per Cell (VpC) at 20 °C), as this was considered to be closer to the conditions under which the parallel combination would be used in application. The discharge PRBS perturbations as applied to the test configurations were used not only to establish impedances, but the voltage and current waveforms were inspected to attempt to gain information regarding the respective roles of the two energy stores. The following section examines the plotted results for the parallel networks.

10.3.7 Battery and capacitor bank test waveforms

Figure 117 shows the overall current envelope for the parallel 33 Farad capacitor and the CTX-9 test battery. As can be seen the current sharing between the two elements reaches a pseudo steady state at just over 200 seconds.

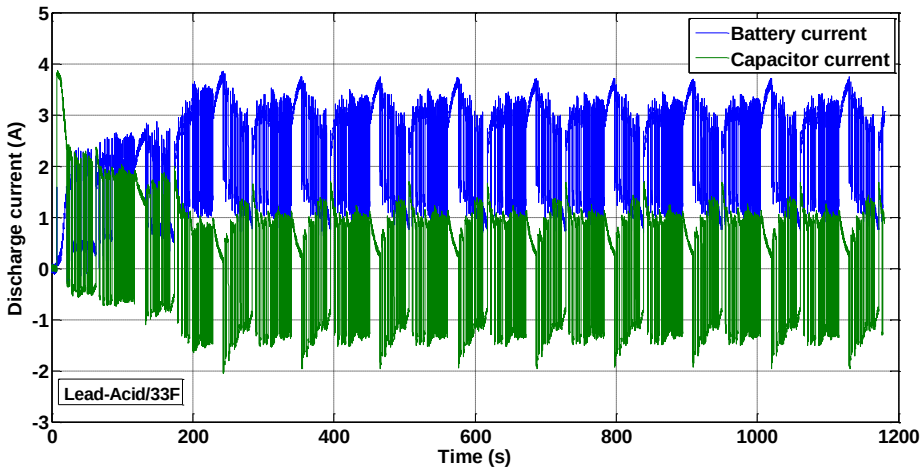

Figure 117. Relationship between battery and capacitor current over full test – bank 1.

Examination of the current envelopes for the larger capacitor bank, (Figure 118) show clear differences to the smaller capacitor bank (Figure 117). The capacitor delivers the majority of the current to the load over most of the test period.

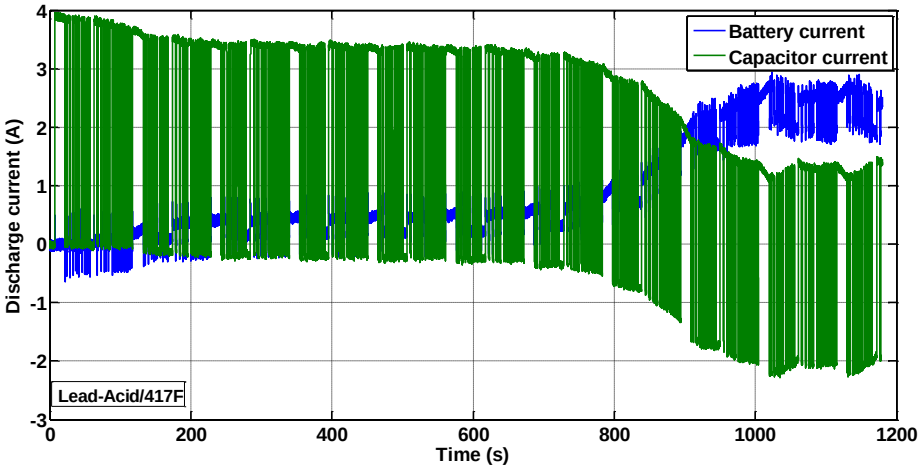

Figure 118. Relationship between battery and capacitor current over full test – bank 2.

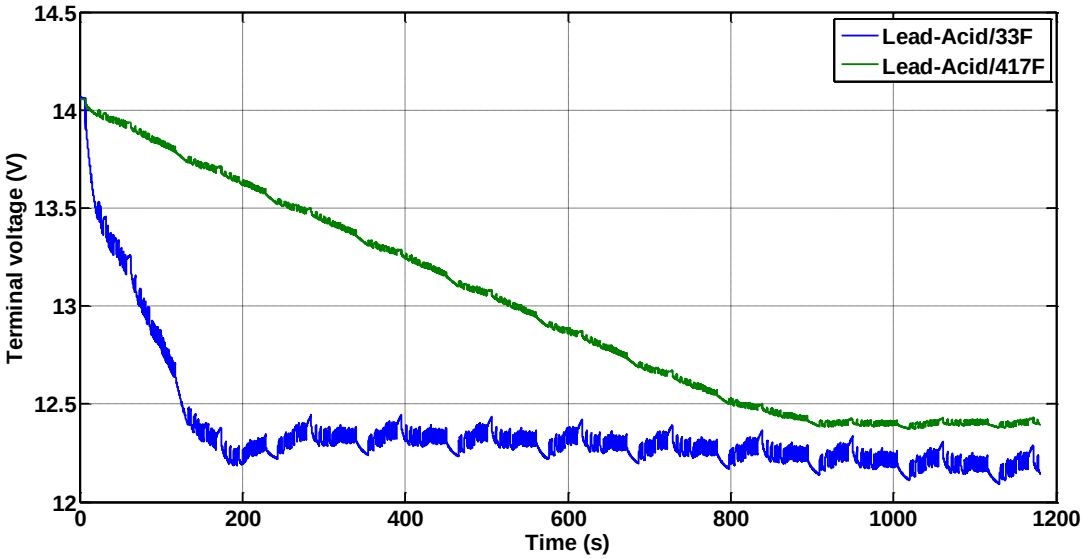

Figure 119. Overall terminal voltage during test for both capacitor banks.

The voltage overall response for both test configurations (Figure 119) shows the difference between the two networks, in terms of terminal voltage decay

and voltage amplitudes for the PRBS test pulses. Comparative current waveforms for the networks under test are shown in Figures 120 and 121.

Referring to Figure 120 the capacitor delivers the majority of the current over the course of the 100 second plot and this reduces as the capacitor discharges relative to the battery. The larger capacitor bank in Figure 121 has the effect that the capacitors are totally dominant in delivery of current over the 100 second window. Terminal voltage for the two banks can be seen in Figure 122. Figure 123 shows the transition of energy delivery from the capacitors to the battery for the bank 1 test configuration, which can be directly compared to Figure 124, which shows the similar behaviour for bank 2, in this case 800-900s into the test.

Later in the test, (1000-1100 seconds, Figures 125, 126), the battery is now supplying the bulk of the current, whilst charging the capacitor in the PRBS off period. However, the average level of ripple current seen by the battery is still much reduced by the addition of the capacitors.

The voltage response in Figure 127 now appears relatively flat as compared with the earlier plots, with the overall voltage deviations being controlled by the value of the parallel capacitance.

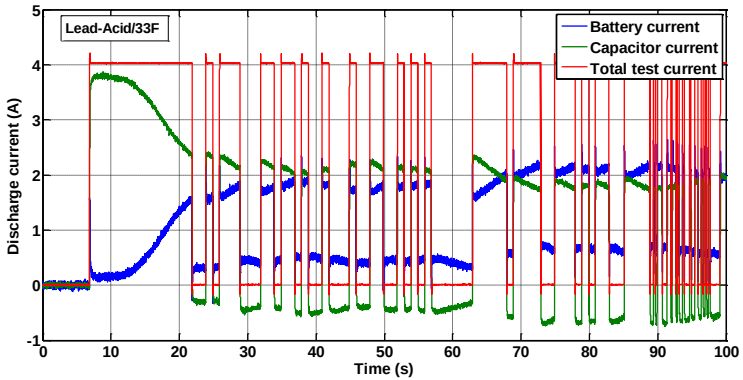

Figure 120. Capacitor, battery and total test current, 0-100s, bank 1

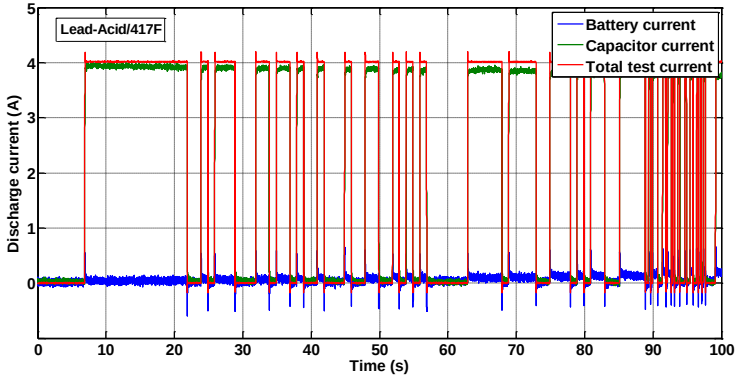

Figure 121. Capacitor, battery and total test current, 0-100s, bank 2

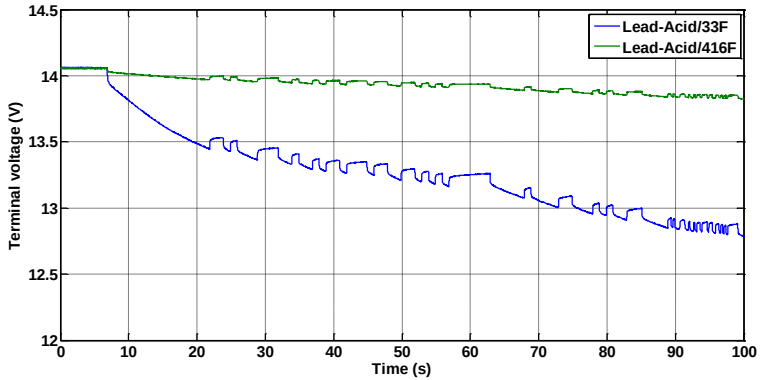

Figure 122. Terminal voltage of both parallel networks, 0-100s

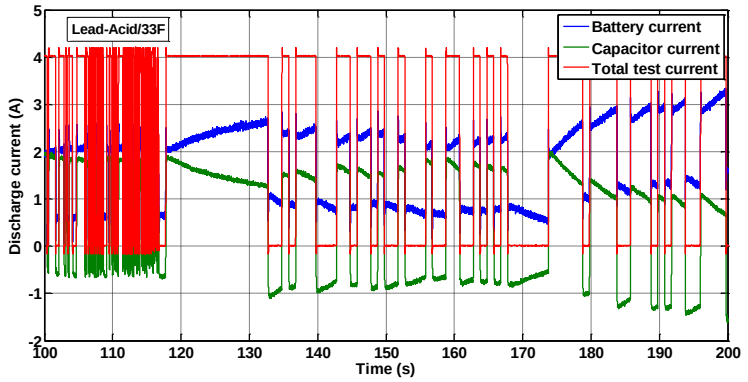

Figure 123. Capacitor, battery and total test current, 100-200s, bank 1

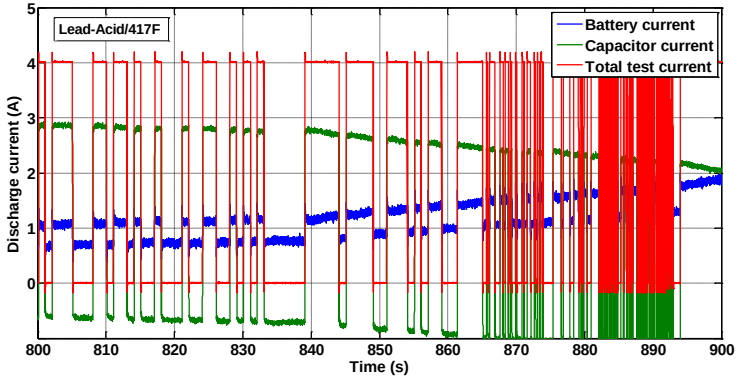

Figure 124. Capacitor, battery and total test current, 800-900s, bank 2

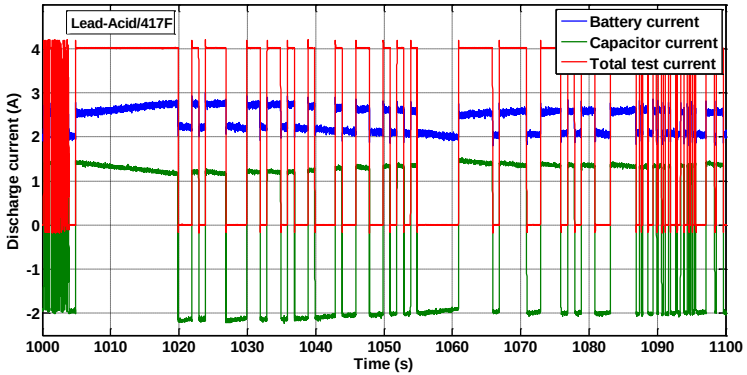

Figure 126. Capacitor, battery and total test current, 1000-1100s bank 2

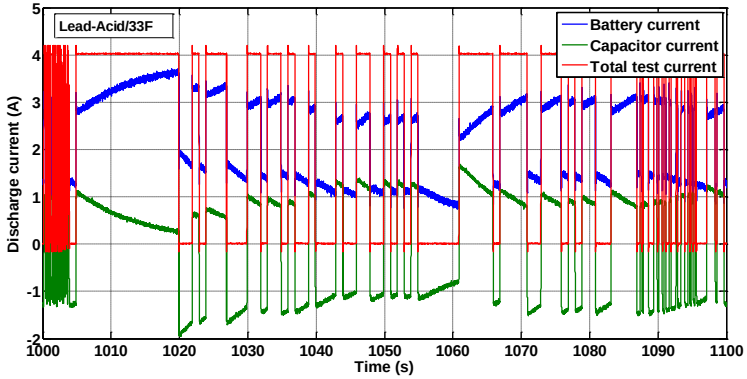

Figure 125. Capacitor, battery and total test current, 1000-1100s bank 1

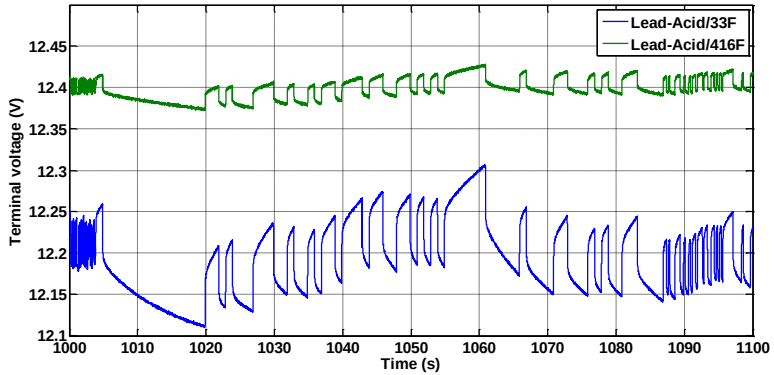

Figure 127. Terminal voltage of both parallel networks, 100-200s

10.3.8 PRBS battery test results

Impedance spectrum analysis was performed on the voltage/current waveforms of the test batteries. The impedance plots allowed separation of R_i and R_t by inspection, and were compared to simulations based on the Randles' model, resulting in a fit being established for the conventional battery which can be seen below in Figure 128.

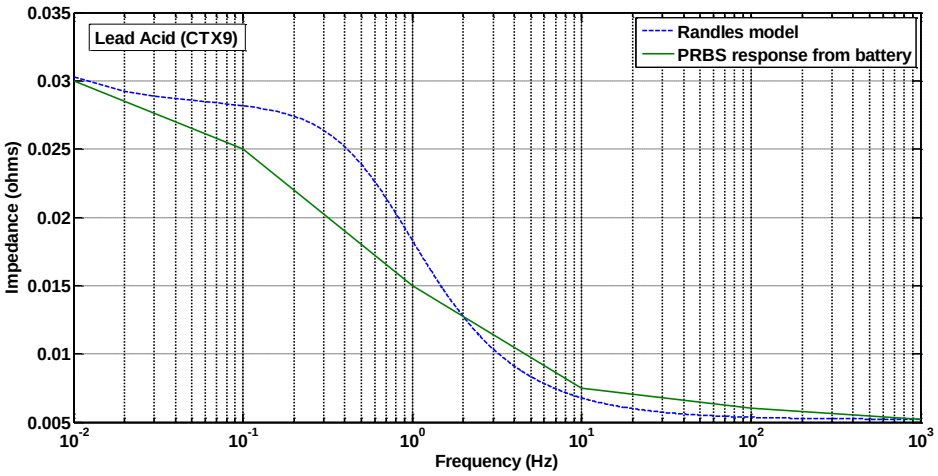

Figure 128. Impedance response (experimental) for Lead-Acid battery compared to simulation.

The UltraBattery however proved more difficult indicating a revision was required to the model. With the knowledge that the UltraBattery incorporates a capacitor in the plate design, a model was used with a parallel leg comprising a capacitor and series resistance (Figure 129).

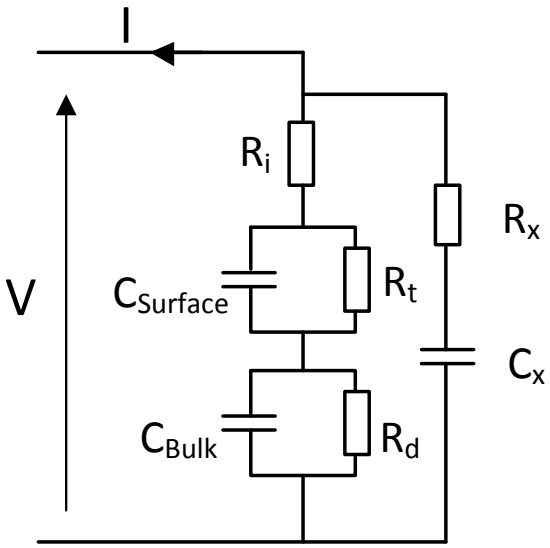

Figure 129. Modified Randles' model for the UltraBattery

The derivation for this model was previously shown on page 149 in equations 32 to 36. Parameters were then established iteratively for the simulation using the transfer function which provided a good fit to the experimental results, shown below in Figure 130.

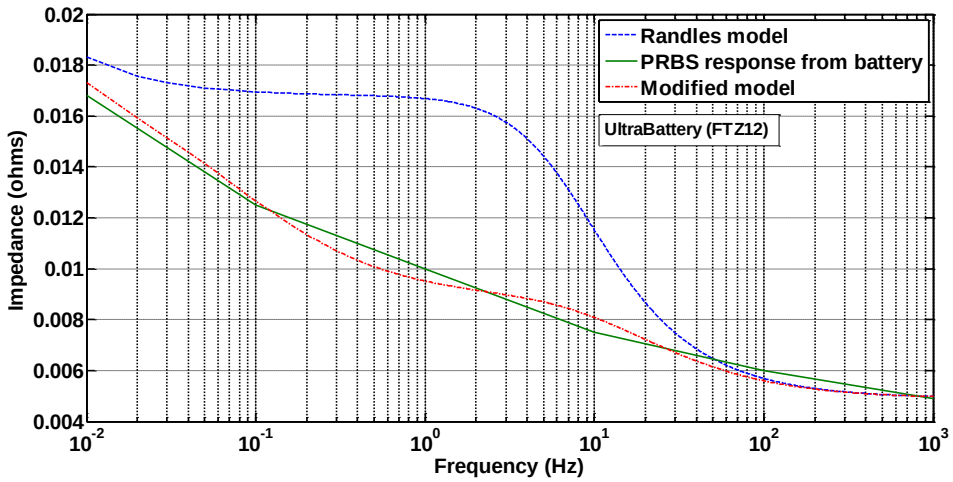

Figure 130. UltraBattery experimental response and simulation using modified model.

The modified model was then applied to the conventional battery, to see if the model predictions could be improved. Using approximate values as a starting point, an improved fit was established, which can be seen in Figure 131.

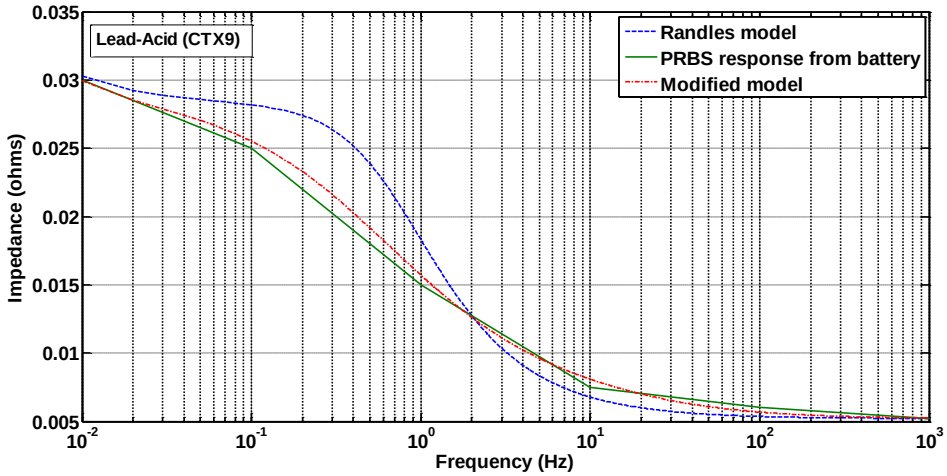

Figure 131. Lead-Acid experimental response and improved fit to modified model.

It was therefore concluded that the revised model offered benefits to establishing parameters for both batteries. Parameters established from the test results are shown in tables 21 and 22.

10.3.9 Results summary

Table 21. Battery parameters – Randles' model

Randles'model	R_i (mΩ)	R_t (mΩ)	$C_{Surface}$ (F)	C_{Bulk} (F)
Conventional	**5.2**	**23**	**2**	**7561**
UltraBattery	**4.9**	**11.9**	**3**	**10586**

Table 22. Battery parameters – modified model

Modified model	R_i (mΩ)	R_t (mΩ)	$C_{Surface}$ (F)	C_{Bulk} (F)	C_x (F)	R_x (mΩ)
Conventional	**5.2**	**23**	**2**	**7561.3**	**10**	**6**
UltraBattery	**4.9**	**11.9**	**2.5**	**10586**	**100**	**6**

The datasheet for the CTX-9 does not specify impedance directly, and states the more commonly used Cold Cranking Amps (CCA) for Starting, Lighting and Ignition (SLI) batteries. This figure is provided as 120A, which when applied to Ohm's law with Ri + Rt:

Voltage drop during starting = 120A x 28.2mΩ = 3.4V

This gives a battery voltage of 9.6V under start conditions at 20°C for a fully charged battery with a terminal voltage o 13V, which follows expectations. The Ultrabattery data was evolving as part of this work, but similarly the values of Ri and Rt reflected the intended use of the batteries, with the combined Ri + Rt being 40% less than the conventional battery, which in turn with the increased parallel capacitance lends itself to applications where rapid energy exchange is required (such as regenerative braking).

PRBS impedance results were obtained for the batteries and parallel combinations in pseudo steady-state conditions, and are shown in Figure 132.

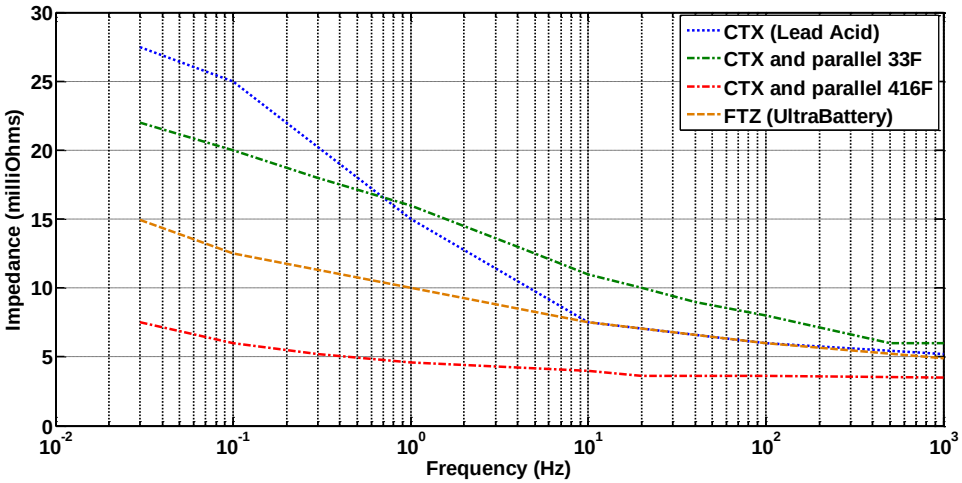

Figure 132. Respective impedances of the battery and parallel networks.

Examination of the results (Figure 132), supports the predictions of the earlier tests with the batteries alone, and the presence of the additional capacitance lowers the effective impedance response of the energy storage system, improving the transient behaviour.

The conventional battery was shown to have significantly larger impedance than the UltraBattery over the frequency range and in addition to this the response was observed to be significantly flattened by the shunting effect of the parallel capacitance. The predictions for the UltraBattery using curve fitting suggested a parallel capacitance of circa 100F. The responses in Figure 132 support the earlier calculations, with the UltraBattery response lying between the two parallel configurations, (33F and 416F).

10.4 Conclusion

The work carried out in this chapter verified the applicability of the discharge PRBS tests in establishing impedance responses and parameters for energy storage devices suitable for EV/HEV applications.

Tests carried out using the UltraBattery against the conventional Lead-Acid SLI battery showed that former was more responsive to rapid application of load, and this was demonstrated in the impedance results. Using equivalent circuit modelling it was shown that Randles' model alone is not capable of fully predicting UltraBattery behaviour. The proposed model (Randles' + parallel RC branch) provides a better fit to the experimental data. Moreover, a 10:1 difference in the capacitance value C_x which was the significant performance indicator.

Testing the conventional battery with parallel capacitances of 33F (47F measured) and 416F (510F measured) were shown to produce responses which when compared to the 100F calculated parallel capacitance of the UltraBattery, confirmed the earlier results.

Observing the PRBS current waveforms for the respective parallel battery and supercapacitor configurations allowed some insight into the benefits of using a capacitor in conjunction with a battery. It was shown clearly that during the early stages of PRBS test sequence, the supercapacitor delivers current, whilst the battery begins to undertake the chemical processes that allow discharge. The relationship between the current delivered by each energy store is dependent on the magnitude

of the parallel capacitance and prevailing dynamic loading, and changes as time progresses.

Ripple currents experienced by the battery are significantly reduced using the parallel arrangement throughout the discharge, leading to extended service life in this configuration.

Examination of the voltage responses, respective current flows and ripple currents offered opportunities for further work in defining criteria for selecting parallel capacitors in applications where transient conditions are the norm.

Chapter 11. Accelerated failure analysis of lead acid batteries

11.1 Introduction

State of Health for batteries and cells is the most difficult of the state indicators to obtain results for, as the inherent nature of the testing process requires that the battery should be assessed over its life to failure. VRLA batteries typically have a design life of 5 or 10 years, and a cycle life (typically) of around 1000 – 1500 cycles. As such, the minimum period over which a test could be carried out to cycle a battery to failure at room temperature would be in the order of 2-3 years. This is feasible within the timeframe of a research degree, but this would require all of the designed tests and test equipment to be defined at the inception of the research. Additionally, this design life is quoted to a capacity level of 80%, and as part of the investigation the remaining function beyond this defined end of life was to be assessed, extending the test period significantly. Lead–Acid batteries, do however have a characteristic behaviour that can be exploited to accelerate the test process. Battery life degrades significantly with increased temperature, and manufacturers data [17] for service life over operating temperature range presents a linear reduction of operational service above 20°C, with around 5% service life being typical for 60°C operation – 6 months for a new battery with 10 year design life. Using this as a basis, one of the original test batteries with a known history was selected, as this was already 4 years into its life cycle. It was therefore estimated that cycling the battery at 60°C under a high rate discharge and charge cycle would show significant SoH indicators over a 3 month timeframe. The motivation for this work was to examine the three PRBS tests modes

over the whole life of the battery, to examine the applicability of the charge, discharge and bipolar PRBS tests over SoH and where each method showed advantages. It was hoped that the study would provide base parameters for a statistical process controlled system, which gathers historical data from in service battery systems and modifies the predictive data to inform SoH which becomes available to the system for end-of-life battery estimation.

11.2 Cycle tests at elevated temperature

Long duration tests using batteries require automated test systems, and in order to implement the testing process to be described, a significant hardware set was developed. The battery under test was required to be cycled (charged and discharged) at elevated temperature and tests carried out to establish battery state at these intervals. Due to the long duration of the overall investigation several charge/discharge cycles (10-12) were carried out between each test and this was defined as a "cycle group".

A Montford environmental chamber was used to heat the battery to the cycling temperature, which operated under closed loop control, although active cooling was not employed – thermal runaway protection for the battery was provided for in the temperature sensing arrangement, and the control system itself.

The chamber supply was turned on and off at the beginning and end of each cycle group by the cycler controller which formed the basis of the AMM-1 test system, described in detail in the appendices. The accelerated lifetime test system evolved

naturally out of test rigs used through the research presented here, leading to an overall battery testing system facilitating long term tests using the developed techniques.

The equipment is based around a VxI Power Oracle 200E DC UPS with custom firmware, as the unit lends itself to discharge and cycling tests. The device itself is designed to run from the connected batteries in an AC fail situation and power a connected load, with inherent, adjustable low voltage disconnect for battery protection at EoD. The unit operates autonomously, but is also a Modbus slave device, allowing interaction from an external control system. On-board 12 bit A-D converters allow measurement of amongst other parameters, battery voltage and current. External TTL I/O allowed control of the peripheral equipment required, and a custom data logging user interface was developed which simply placed information obtained over the serial port into an Excel spreadsheet. Visual Basic macros were employed to allow digital control of the cycler, and the data logging functionality. The cycler interface screen can be seen in Figure 133.

The limits for the cycler can be seen on the right hand side of the interface (analogue settings). The system provides two sources of charge to the battery under test, firstly from the 200W Oracle unit (which is the charge level of 5A on the interface) and secondly, because the VxI unit is primarily being used as a control platform and the cycling needs to be more rapid than a 5A charge current would allow, an external 35A charger is enabled by the control unit.

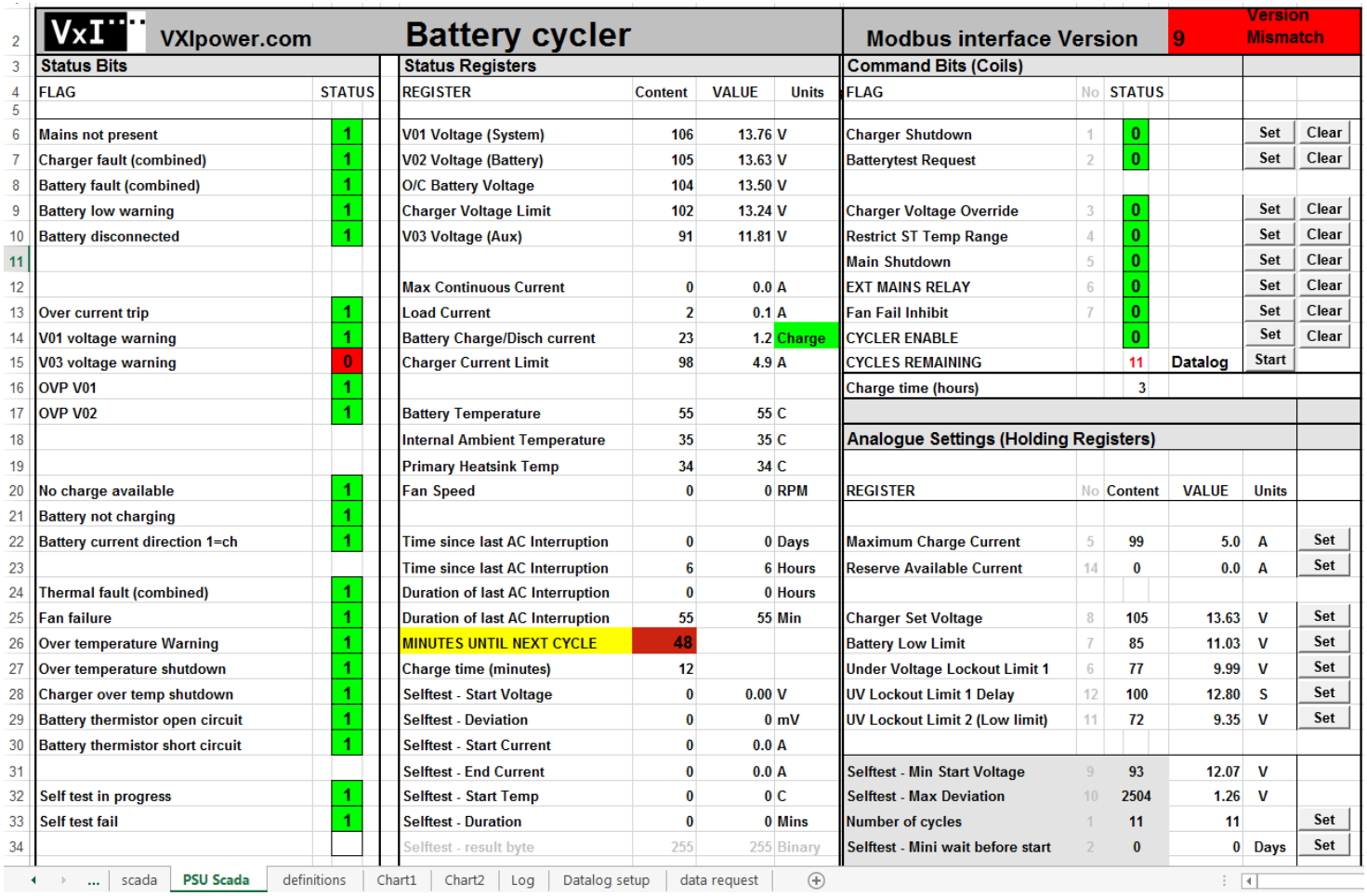

VXIpower.com

Battery cycler

Modbus interface Version 9 — Version Mismatch

Status Bits

FLAG	STATUS
Mains not present	1
Charger fault (combined)	1
Battery fault (combined)	1
Battery low warning	1
Battery disconnected	1
Over current trip	1
V01 voltage warning	1
V03 voltage warning	0
OVP V01	1
OVP V02	1
No charge available	1
Battery not charging	1
Battery current direction 1=ch	1
Thermal fault (combined)	1
Fan failure	1
Over temperature Warning	1
Over temperature shutdown	1
Charger over temp shutdown	1
Battery thermistor open circuit	1
Battery thermistor short circuit	1
Self test in progress	1
Self test fail	1

Status Registers

REGISTER	Content	VALUE	Units
V01 Voltage (System)	106	13.76	V
V02 Voltage (Battery)	105	13.63	V
O/C Battery Voltage	104	13.50	V
Charger Voltage Limit	102	13.24	V
V03 Voltage (Aux)	91	11.81	V
Max Continuous Current	0	0.0	A
Load Current	2	0.1	A
Battery Charge/Disch current	23	1.2	Charge
Charger Current Limit	98	4.9	A
Battery Temperature	55	55	C
Internal Ambient Temperature	35	35	C
Primary Heatsink Temp	34	34	C
Fan Speed	0	0	RPM
Time since last AC Interruption	0	0	Days
Time since last AC Interruption	6	6	Hours
Duration of last AC Interruption	0	0	Hours
Duration of last AC Interruption	55	55	Min
MINUTES UNTIL NEXT CYCLE	48		
Charge time (minutes)	12		
Selftest - Start Voltage	0	0.00	V
Selftest - Deviation	0	0	mV
Selftest - Start Current	0	0.0	A
Selftest - End Current	0	0.0	A
Selftest - Start Temp	0	0	C
Selftest - Duration	0	0	Mins
Selftest - result byte	255	255	Binary

Command Bits (Coils)

FLAG	No	STATUS		
Charger Shutdown	1	0	Set	Clear
Batterytest Request	2	0	Set	Clear
Charger Voltage Override	3	0	Set	Clear
Restrict ST Temp Range	4	0	Set	Clear
Main Shutdown	5	0	Set	Clear
EXT MAINS RELAY	6	0	Set	Clear
Fan Fail Inhibit	7	0	Set	Clear
CYCLER ENABLE		0	Set	Clear
CYCLES REMAINING		11	Datalog	Start
Charge time (hours)		3		

Analogue Settings (Holding Registers)

REGISTER	No	Content	VALUE	Units	
Maximum Charge Current	5	99	5.0	A	Set
Reserve Available Current	14	0	0.0	A	Set
Charger Set Voltage	8	105	13.63	V	Set
Battery Low Limit	7	85	11.03	V	Set
Under Voltage Lockout Limit 1	6	77	9.99	V	Set
UV Lockout Limit 1 Delay	12	100	12.80	S	Set
UV Lockout Limit 2 (Low limit)	11	72	9.35	V	Set
Selftest - Min Start Voltage	9	93	12.07	V	
Selftest - Max Deviation	10	2504	1.26	V	
Number of cycles	1	11	11		Set
Selftest - Mini wait before start	2	0	0	Days	Set

... | scada | PSU Scada | definitions | Chart1 | Chart2 | Log | Datalog setup | data request

Figure 133. Battery cycler user interface showing available measurement and control

Battery limits can be seen in the analogue group - the most important being the Under Voltage Lock Out (UVLO) limits. These voltages define the point at where the battery will be disconnected from the load thereby preventing permanent damage. The 9.99V limit is a time delayed threshold, and this limit needs to be breached for circa 10 seconds before the battery is disconnected from the load and the cycle resets. The lower threshold (9.35V) is immediate, and provides for the battery terminal voltage "crashing" – typical of a battery in depleted state of health.

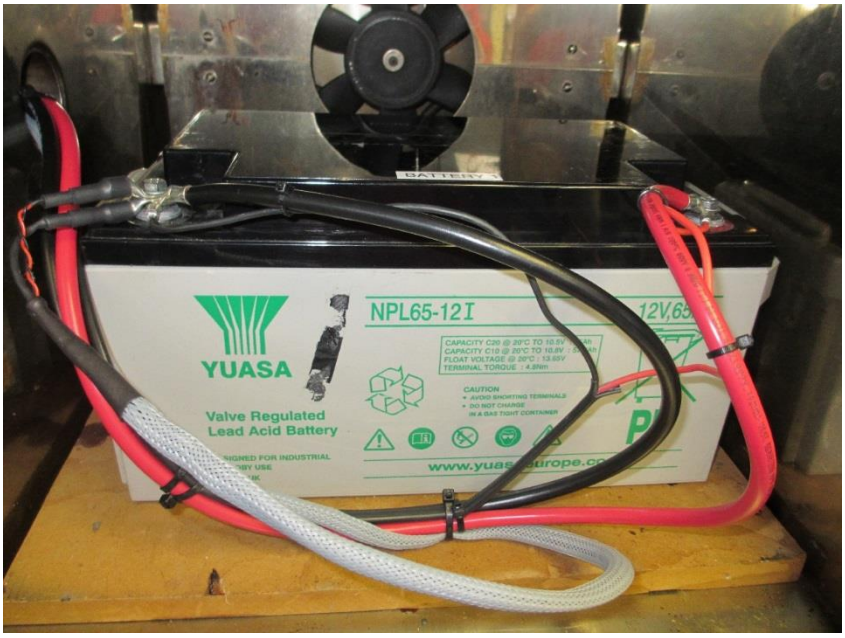

Figure 134. Test battery within the environmental chamber (door removed)

The test system incorporated battery terminal voltage sensing at the battery, independent of the load cables (Figure 134), with temperature sensing of the battery being implemented primarily to ensure correct charging voltage levels (Figure 135), whilst additionally reporting any elevations in battery temperature beyond the programmed chamber temperature, allowing the system to shut down automatically.

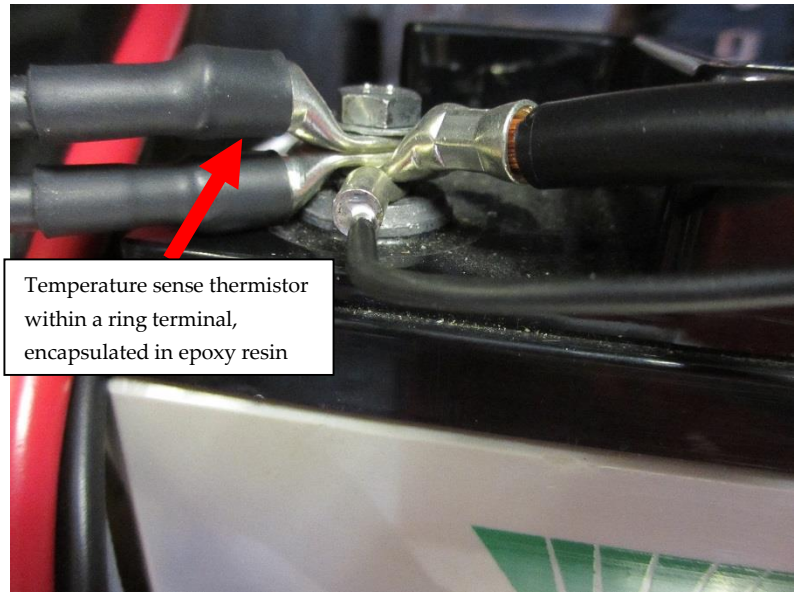

Figure 135. Close up of battery terminal showing temperature sensing arrangement

11.3 Battery test schedule

The test schedule for the accelerated failure testing of the battery was designed to take advantage of all of the techniques investigated up to this point. As such all three modes (discharge, charge and bipolar) were used to evaluate the battery performance at each group of ten cycles.

The tests were carried out 100% SoC, 85% and 0% SoC, reflecting the tests carried out in the earlier experimental investigations. Discharge, charge and bipolar PRBS tests were carried out at each test interval, along with a full discharge at the $c_r/20$ rate with data logging. The flow chart shown in Figure 136 shows the test procedure in more detail.

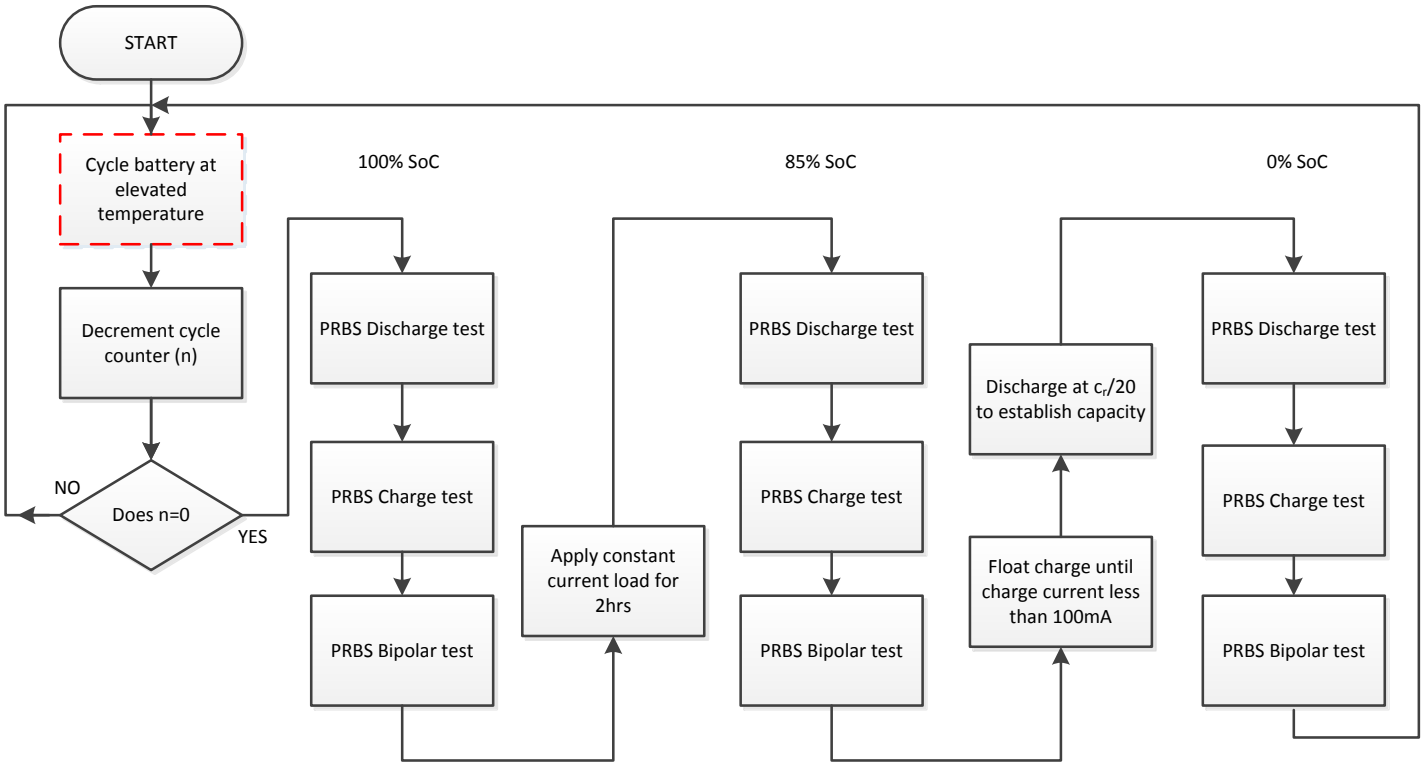

Figure 136. Overall test schedule flowchart, accelerated failure tests

Figure 137 shows the cycler block (cycle battery at elevated temperature) from Figure 136 broken out into its component processes:

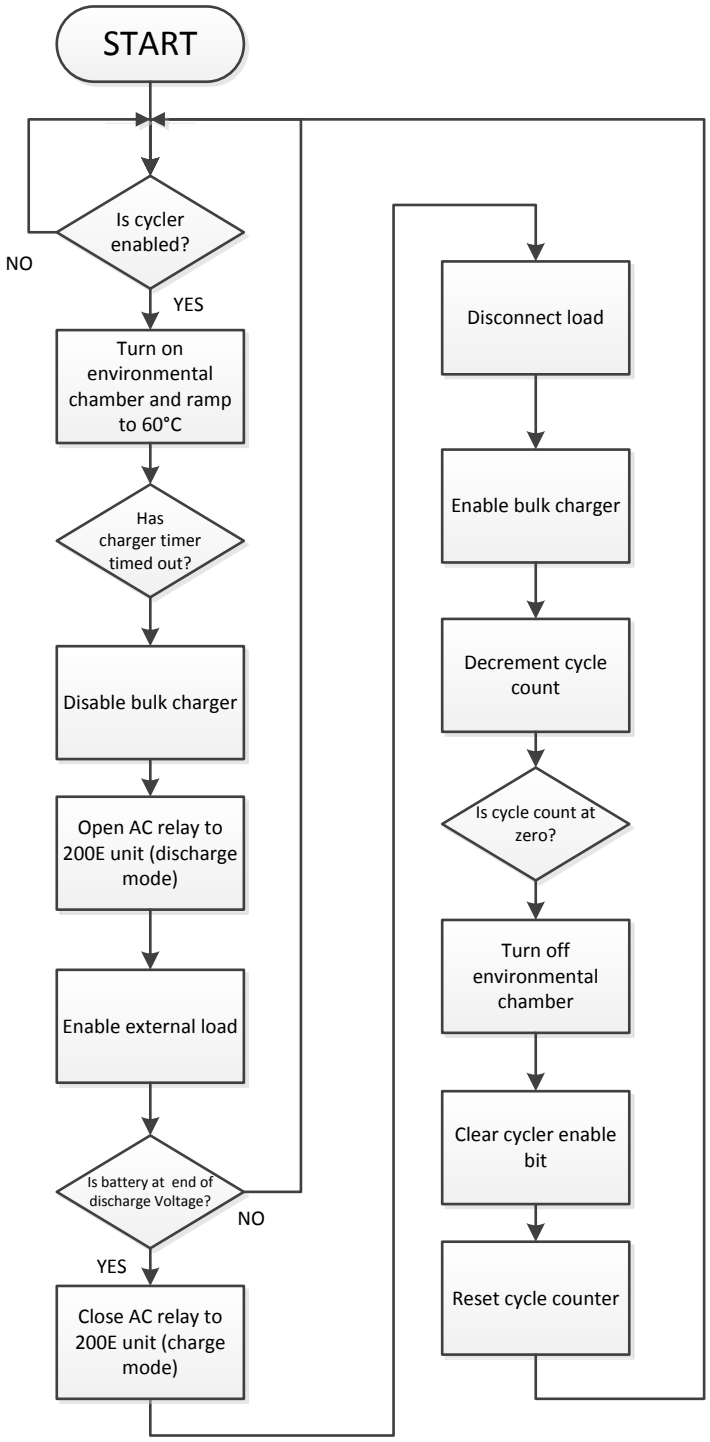

Figure 137. Battery cycler flowchart

11.4 Test results

The test battery was subjected to close to 200 cycles, at a rate approaching 1C and at a temperature of 55-60°C, with the complete test period covering 314 days.

The cycler data log in Figure 138 shows the low speed acquisition data from the AM-1 battery test system, which was used to acquire the capacity results - note the Figure shows an overall cycle group. The initial ramping up of the battery temperature can be seen at the early part of the data, and despite the thermal capacity of the oven (3kW heating) the internal battery temperature took 4 hours to reach the programmed temperature of 60°C.

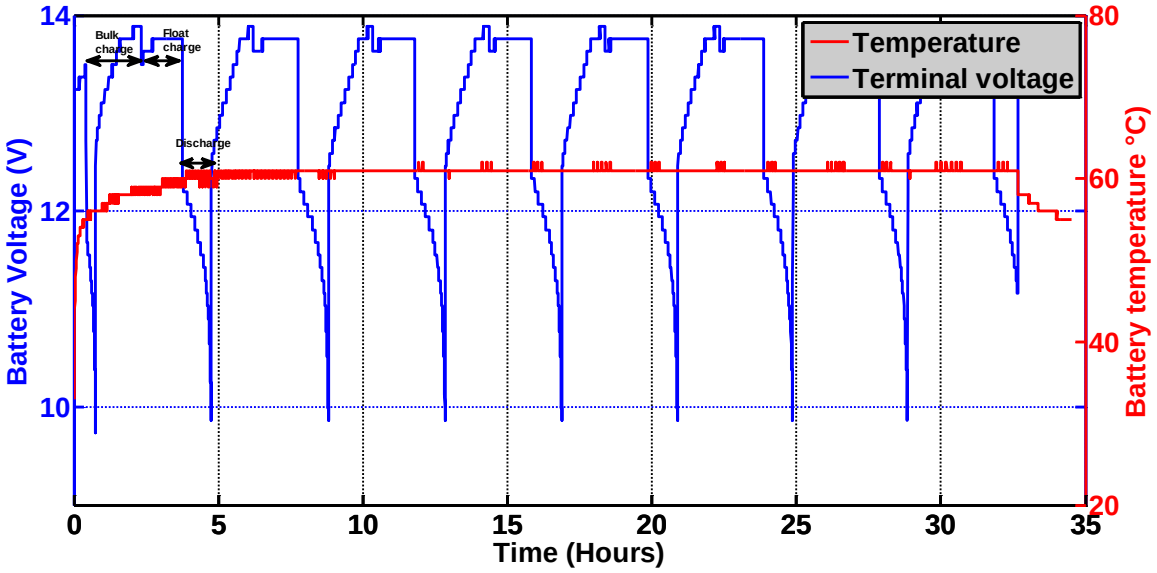

Figure 138. Battery cycler data log temperature and voltage data over complete cycle period between PRBS tests

The charge and discharge profiles for the battery can also be seen from the figure. The battery undergoes an initial "bulk" charge (constant current, 30A transitioning

to constant voltage 14.4V/20°C) from the charger module, and the transition to "float" charge (constant voltage, 13.65V/20°C).

The PRBS tests were carried periodically after each cycle group, with the developed tests envisaged to collect more data than necessarily required for the investigation, bearing in mind the difficulty in repeating the experiments. It was decided from the outset that the base parameters over battery life would be derived from the bipolar tests at a stable SoC, with the other modes examined to reinforce the findings.

11.4.1 Battery capacity results

The battery capacity over the test period is shown in Figure 139, and as expected, battery capacity generally reduced over the course of the experiment.

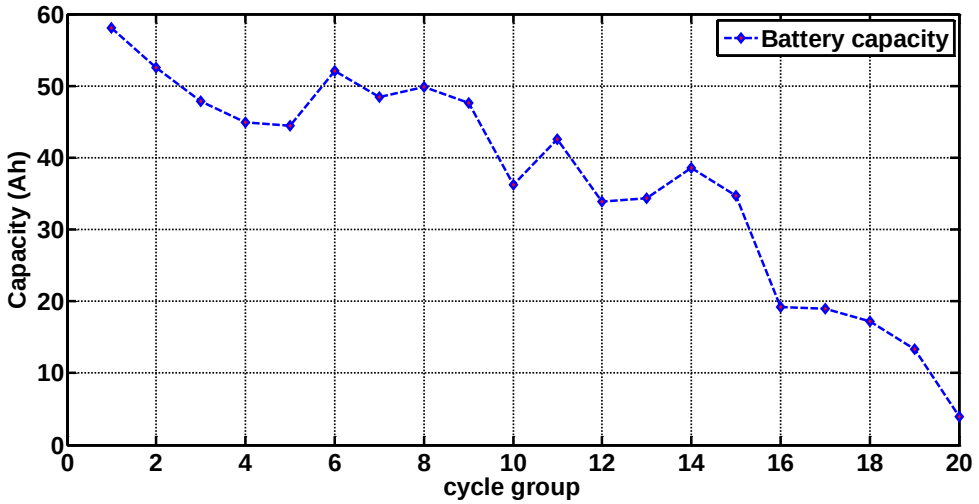

Figure 139. Battery capacity over accelerated life cycle tests

The results obtained were used to calculate C_{Bulk}, and these values can be found in table 23. The capacity reduction of the battery follows a reasonably

predictable pattern until cycle group 14, where the onset of the final decline occurs.

11.4.2 Battery impedance over accelerated life cycle

The impedance results in Figure 140 show the general trends that were obtained by using the bipolar results at 85% SoC for the battery. The rationale for using these results this was that the bipolar test method was the least intrusive and the 85% state avoided the elevated impedances at high and low states-of-charge, which can be confused with declining health. The results from the final test group were not presented in the impedance responses as the severe changes in impedance offered little more information than the battery was now unusable.

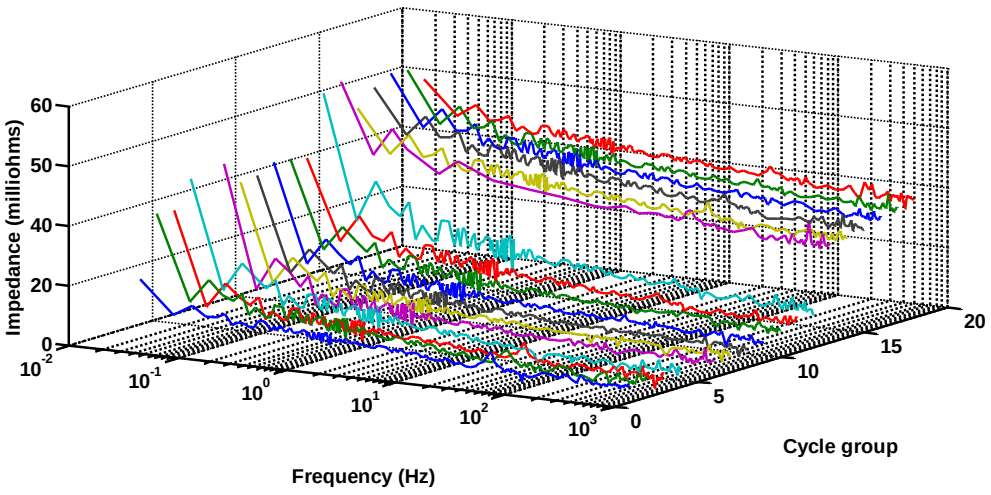

Figure 140. Battery impedance over accelerated life cycle testing, bipolar test, 85% SoC

The impedance plots demonstrate the declining health of the battery over the accelerated tests. The battery continues to be useful beyond the normal end of life point, but experiences a step decline at cycle group 12. As such, observing

the behaviour of the battery up to this point is crucial in determining when this failure occurs, and this is discussed in the following sections.

11.4.3 Battery parameters over accelerated life cycle

The parameters over the battery life cycle were obtained by iterative curve fitting to the models developed in chapter 8 (Figure 90, page 186) using the impedance results from the bipolar tests at 85% SoC. At this stage of the research many of the MATLAB processing routines were combined to assist in processing the large amounts of data automatically. An example of this is crunch1.m (appendices 15.8.7) which was created to load the data from saved MATLAB workspaces relating to the tests carried out. The routine then processed the multiple PRBS sequences to produce an impedance plot, which was then used for the iterative curve fit. Figure 141 shows the trends in R_i and R_e (electrolyte resistance) which clearly show the step change as the battery fails.

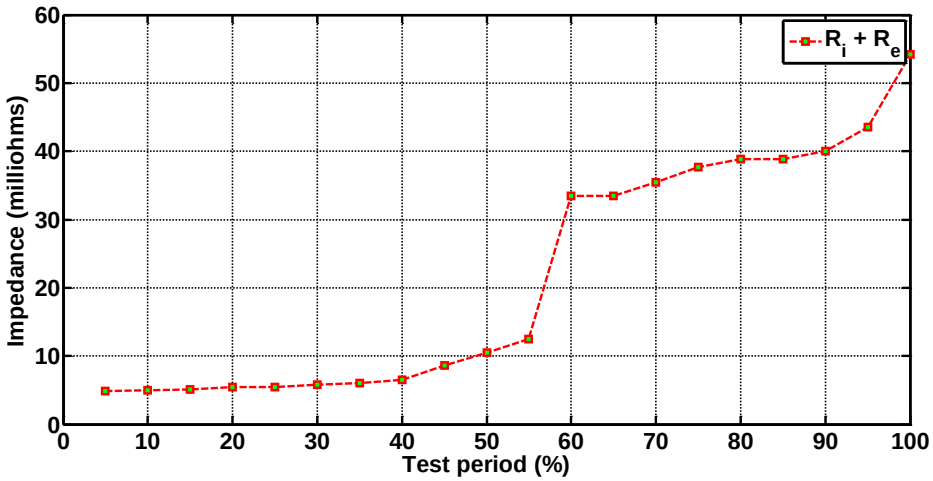

Figure 141. Major series impedance over test period

The parameters for the battery are shown in Table 23. Examining the results it the onset of terminal failure of the battery can be seen from cycle group 9 (45% into the test period).

Table 23 – Battery parameters, bipolar tests, 85% SoC

Cycle Group	C_{Bulk} (F)	Ri (mΩ)	R_t (mΩ)	$C_{Surface}$ (F)	Rx1 (mΩ)	Cx1 (F)
1	92516	4.9	10	4.5	11	50
2	83722	5	14	4.5	17	45
3	76282	5.1	14	4.5	13	45
4	71486	5.5	16	4.5	7	45
5	70857	5.5	16	4.5	7	45
6	83005	5.5	15	4.5	7	40
7	77220	5.9	15	4.5	7	40
8	79500	6.1	16	4	7	40
9	75915	6.5	16	2	7	30
10	57655	8.7	16	0.9	6	25
11	67742	10.5	16	0.8	6	15
12	53945	12.5	20	0.4	6	12
13	54805	33.4	20	0.4	5.5	12
14	61433	33.5	20	0.4	5	12
15	55251	35.5	20	0.4	5	10
16	30621	37.7	20	0.4	7	12
17	30270	38.9	20	0.4	7	35
18	27434	40	20	0.4	7	35
19	21189	43.6	300	0.4	7	2
20	6229	542.2	85	0.06	25	5

The manufacturer's data sheet for the battery (shown in appendices, 15.7.1), offers impedance at 1 kHz (5mΩ) which equates to R_i, and 10.51mΩ internal resistance which equates to R_i+R_t for a new battery at 20°C. The parameters in red are in the terminal phase of the battery life. As is seen with other modes of

reduced SoF of batteries and cells the general trends include a reduction in effective capacitance, and increases in series impedance.

11.4.4 Observed trends over states of charge during battery lifetime

Further to the observations from the parameter estimation, the results for the charge, discharge and bipolar tests were examined for trends at the test charge states. It had been noted previously that the bipolar testing provides an overall picture of the battery impedance for charge and discharge, however, comparative results for the three modes of test at each test step, yield some interesting trends. The test data was examined for all three modes of test at the test states of charge (100%, 85% and 0%). The cycle groups chosen were 1 and 13, 1 being the healthiest state at the start of the test, with cycle group 13 clearly into the terminal phase of the battery performance.

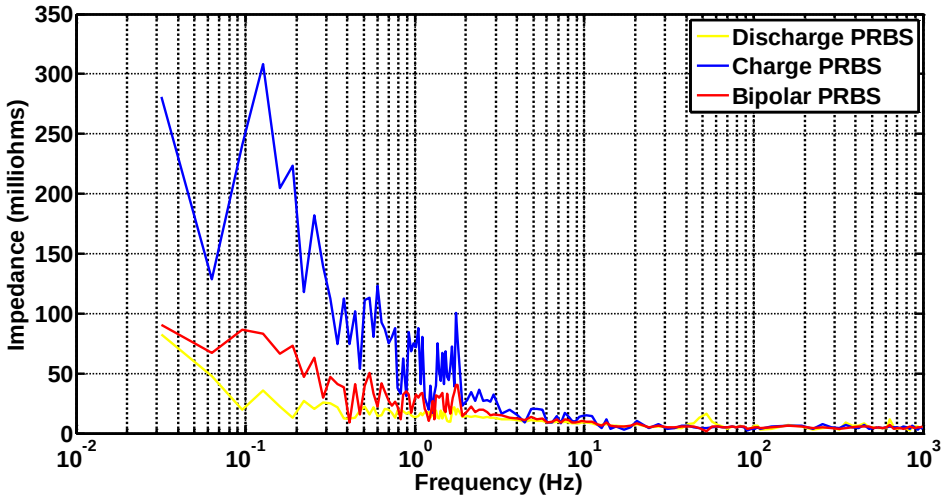

Figure 142. 100% SoC cycle group 1

Figure 142 shows the comparative plots at 100% SoC at the start of the life test. Work in previous chapters has identified the charge PRBS as a charge stage transition indicator, and that the discharge PRBS can give indeterminate results. It is only when the three modes are observed together that a trend emerges for indicating battery state. The general trend for 100% SOC is that the overall impedance of the charge based PRBS is greatest at this state, whilst the three methods tend to converge at high frequency. Figure 143 shows the same plot for cycle group 13, and the trend remains valid, although the overall magnitudes have increased.

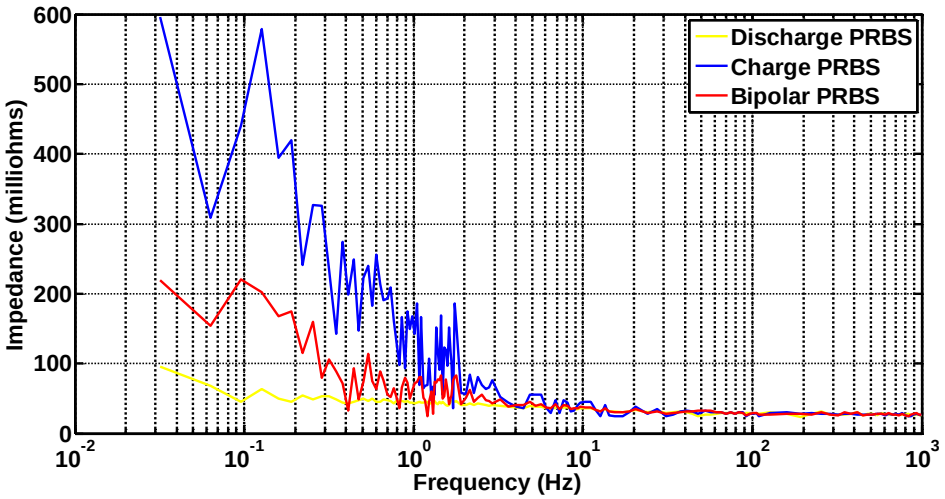

Figure 143. 100% SoC cycle group 13

The change by 85% SoC (Figure 144) is clear and the 3 modes of test largely converge at this battery state. There is some divergence at low frequency, and this is due to the charge and discharge test modes having some effect on the battery, but it is clear the battery is in a different SoC solely by inspection.

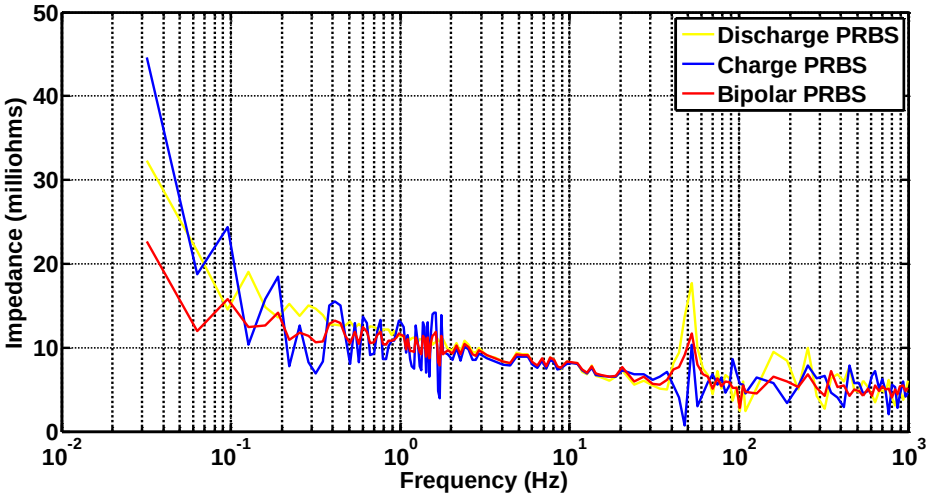

Figure 144. 85% SoC, cycle group 1

Figure 145 shows the same plot for cycle group 13. The overall trend is convergent, but there are some difference between the high frequency discharge impedance and the other tests.

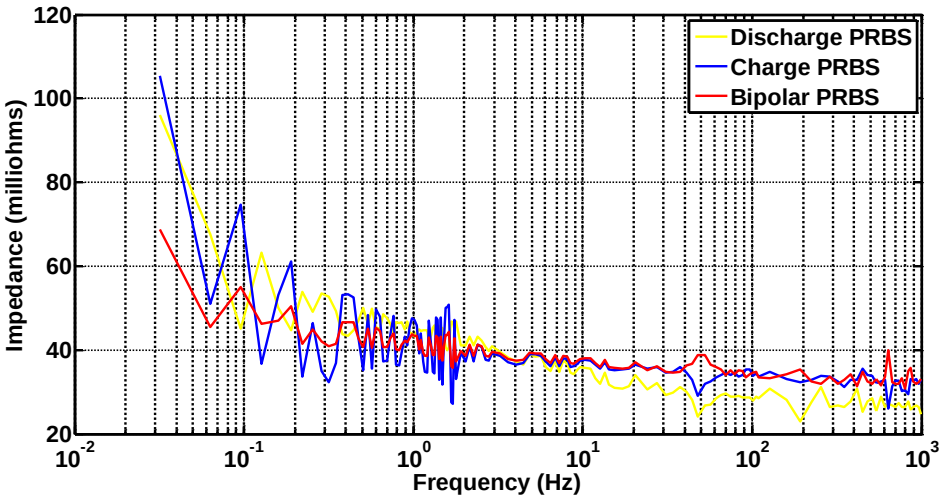

Figure 145. 85% SoC, cycle group 13

The plot in Figure 146 is very interesting, in that at 0% SoC the relative impedances of the discharge and charge PRBS have changed places and the discharge PRBS now has the highest overall impedance. In a blind battery

test it would therefore be possible to establish the SoC just by the relationship of the three test mode impedances.

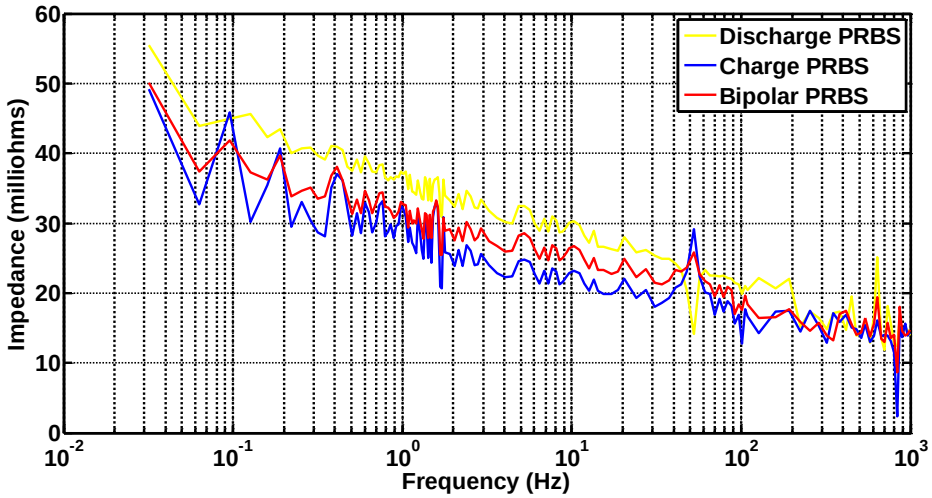

Figure 146. 0% SoC cycle group 1

The findings are further reinforced with the results show in Figure 147, which show impedance plots in the same order as for the healthy battery, but the characteristic impedances have further diverged. The information contained in this plot is a clear indicator of battery SoC and SoH.

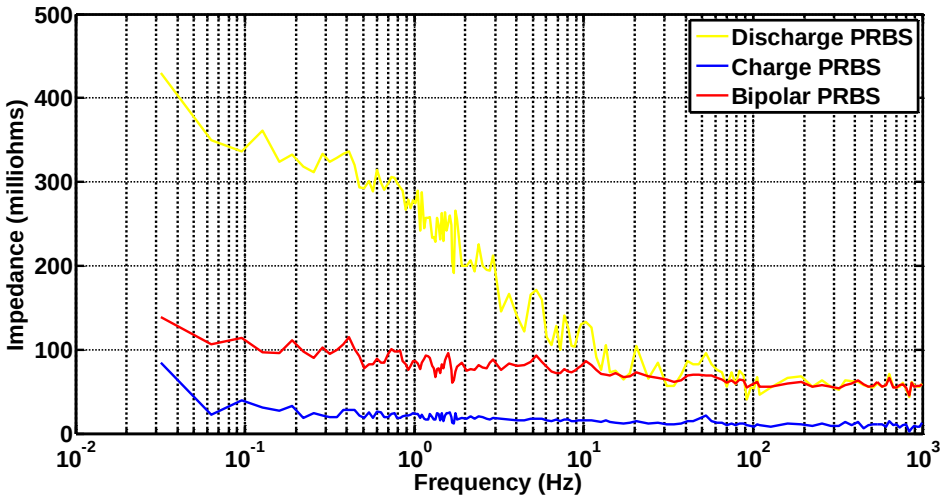

Figure 147. 0% SoC, cycle group 13

11.4.5 Mean DC terminal voltage

During the work in chapter 7, it was indicated that observing the mean DC terminal voltage during a bipolar PRBS test could be used to support state indication. Experiments in chapter 8 over state-of-charge confirmed this parameter as useful in differentiating impedance responses at differing charge states.

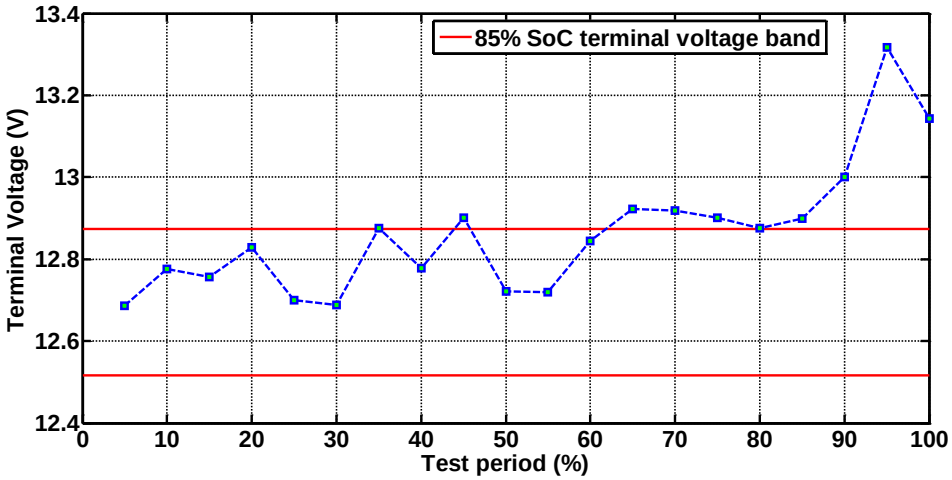

Figure 148. DC mean terminal voltage over the cycle test period (85% SoC).

Figure 148 shows the mean DC terminal voltage of the test battery, at 85% SoC throughout the test period. The observed general trend for the battery was that the mean terminal voltage increased with declining SoH. This is somewhat counter intuitive, and may have been different altogether with a different failure mode in declining SoH (a shorted cell for example). However, the increase in impedance coupled with a decrease in surface capacitance led to the battery being more responsive to changes in terminal voltage with current, as the PRBS tended to excite a much smaller capacitor,

in addition to the ability of the battery to transition between charge and discharge states being affected by the reduction in battery function.

The overall peak to peak voltage deviations at the battery terminals were significantly increased as reported in the impedance results. The mean voltage gradient over a bipolar PRBS test is linked to battery efficiency, and this in itself is a useful indicator in measuring SoH. Further batteries would need to be tested to validate these findings, with different modes of failure examined to characterise the observations made in these tests.

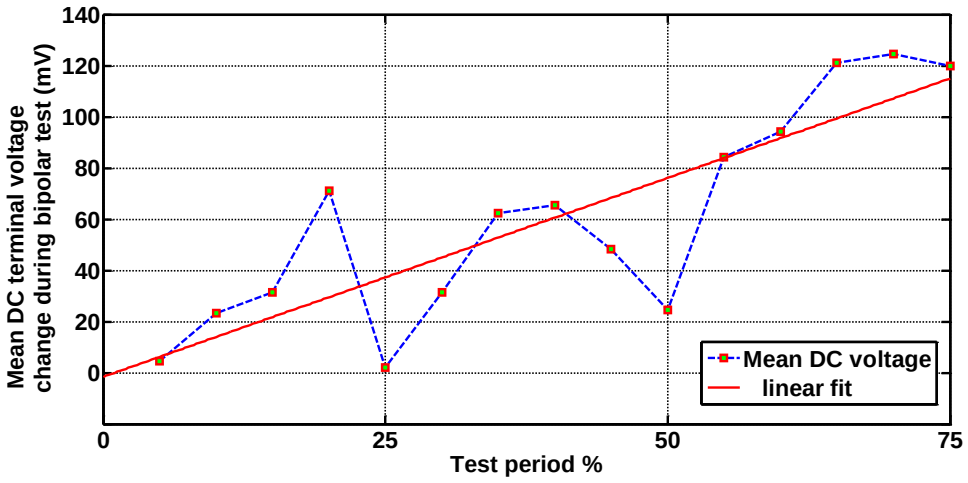

Figure 149. Changes in Mean DC voltage during bipolar tests (battery efficiency)

Figure 149 shows the progression of mean terminal voltage reduction over the test period to cycle group 15 (to 75% of the overall test period), during the bipolar tests at 85% SoC. The bipolar test presents a net zero energy exchange with the battery, so in ideal conditions the mean DC terminal voltage at the start of the test compared to that at the end of any bipolar PRBS test period, should be the same. Any deviations from this can be attributed to battery

efficiency. The trend in Figure 149 is generally that this change in voltage increases with time and declining SoH. The linear fit is not wholly appropriate but the trend is clear that as the battery ages the efficiency decreases.

11.4.6 Examination of internal battery condition

The opportunity arose to inspect the internal condition of the battery at the end of the testing. The battery was weighed prior to the inspection and was found to have a mass of 21.2kg compared to 22kg when new, indicating significant loss of electrolyte, which indicated that battery mass could possibly support SoH indication.

The battery case also suffered significantly during the tests and was distorted during the high temperature cycling (Figures 150, 151).

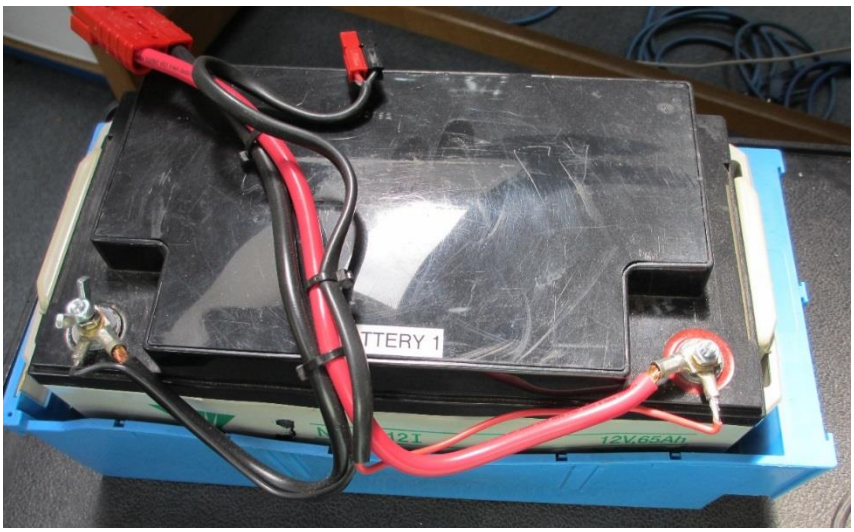

Figure 150. Battery at end of testing within containing "bund" in case of electrolyte leakage

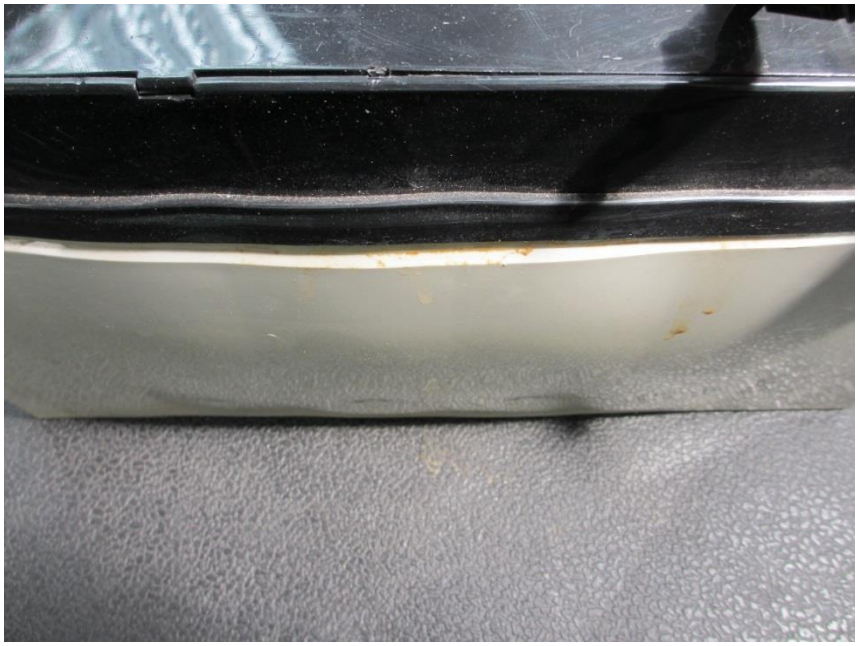

Figure 151. Case distortion of the battery during the elevated temperature tests

The top of the battery case was cut away to expose the individual cells, allowing individual cell voltages to be measured and the general condition of the battery to be examined. Figure 152 shows the battery with the case top removed. Significant corrosion can be seen on the inter-cell links, indicative that such undesirable reactions have occurred elsewhere within the battery. The cells appeared almost dry of electrolyte, and using a non-metallic "dip stick" in the void at the end of the cells, it was found that the electrolyte was completely expended apart from that remaining in the absorbent material between the plates.

Figure 152. Test battery with case top removed exposing the individual cells

Refering to Figure 152 the cells were numbered 1 to 6, left to right and the individual cell voltages measured. The findings are shown in table 24.

Table 24. Individual cell voltages for subject battery at the end of the test.

Cell number	Voltage (V)
1	2.0764
2	1.4714
3	1.2593
4	1.1709
5	1.1348
6	1.9200

The outer cells in the battery appear to have retained terminal voltages approaching that of healthy cells where cells 2-5 have significantly reduced cell voltages.

The battery had, prior to the measurements, been charged to its prevailing 100% capacity, and left for a period of several months in order that an estimate

for R_d could be made. Surprisingly, the self discharge of the battery remained in a healthy state, bearing in mind the measured residual capacity was 3.91Ah.

Based on the period elapsed between the end of the tests and the battery dissection, the self discharge resistance was estimated at still being in excess of 15 KΩ based on a linear interpolation.

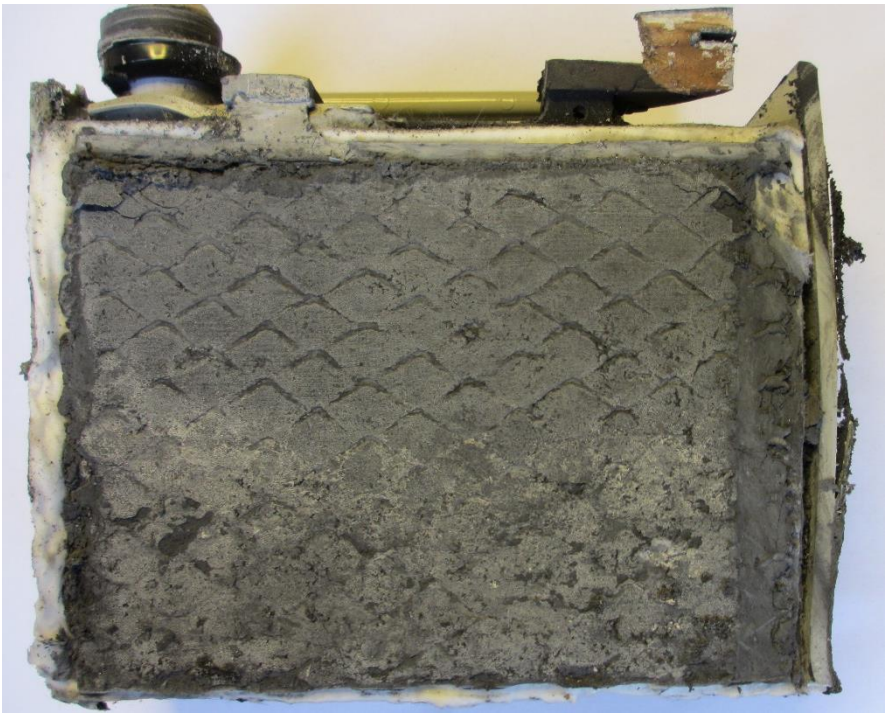

Figure 153. Plate condition of one of the failed cells

The photograph in Figure 153 shows the condition of the cell plates. The upper area of the cell plate appears from inspection to be in a good condition, but the lower part of the plate is covered with a salty deposit which appears to be sulphation. The separators and absorbent mats in which the electrolyte were suspended remained damp but no significant quantity of electrolyte was in evidence.

11.5 Conclusion

Accelerated lifetime tests on the subject battery revealed insights into the process of degradation with electrochemical cells as a result of undesirable reactions between the electrolyte and the cell plates. As expected, reductions in available capacity were manifest, and these reductions in performance were found to correspond to specific parameter indications using PRBS testing to establish frequency response. The modes of reduction in performance observed showed a gradual change in key parameters, with a sharp increase in loss of performance at end of life.

The reduction in $C_{Surface}$ could be seen as the battery degraded, which is envisaged to relate to a loss in available plate area and active material as the battery tends towards end of life. In conjunction to this an increasing in electrolyte resistance for both charge and discharge conditions was shown to be apparent. As the battery degraded the suitability of a single model is diminished, and at this point the reporting of parameters is somewhat diluted. The value of reporting parameters when the battery has a significant loss of function is dominated by overall increases in impedance, or in individual cell failure.

Importantly, characteristics of the PRBS tests were identified which could directly be applied to a SoH/SoC evaluation system, specifically:

Comparison of PRBS test modes (charge, discharge and bipolar) can be used to identify SoC as the observed trend was that at high state-of-charge the charge PRBS would give a generally increased impedance with the discharge PRBS reporting the

lowest result. The bipolar tests, as previously observed fall between these two test modes.

Specific findings from the tests:

- The results converge at medium states of charge.
- The trend reverses at low states of charge.
- The trend is valid over SoH, and is amplified.

Again the examination of mean DC terminal voltage over the test period yielded some interesting results. The findings from the bipolar tests at 85% SoC shows a mean DC terminal voltage that increased over time with declining SoH. This was mainly attributed to the increased impedance of the battery and reduced capacitive elements, resulting in overall time constants that were much reduced. The battery therefore was able to change in terminal voltage more rapidly as health declined, with, for these tests, a characteristic upswing in the mean DC terminal voltage at the onset of irreversible failure (Figure 148).

DC terminal voltage was also used to establish some measure of battery efficiency at the test conditions above. The observed trend for a generally increasing differential between the mean DC terminal voltage at the start and end of a bipolar test showed clear indications that the bipolar PRBS was increasingly responsible for energy removal from the battery, and as such could be correlated to the battery charge efficiency.

It is expected that batteries cycled to end of life during more conventional durations (several years) may experience slightly different failure characteristics, and these

characteristics will also be tied in with whole-life average temperature, and rate of charge and discharge.

However, the value in the testing is the ability to inform prediction of end of life through parameter analysis using the following metrics:

- observations of increased overall impedance (R_i and R_t)
- corresponding changes in mean terminal voltage
- reduction in elements of surface capacitance

Which have been demonstrated during the accelerated failure tests.

Chapter 12. PRBS battery state evaluation using an embedded processor

12.1 Introduction

The research within this thesis was carried out in conjunction with a sponsoring industrial partner (VxI Power Ltd), and as such a deployable version of the developed hardware was one of the desirable objectives of the investigations.

This chapter therefore explores the implementation of the PRBS tests devised during the body of this research within an embedded processor, with the PRBS generation, signal acquisition and data processing using FFT all carried out in software within the chosen embedded processor. The project was directed by the author of this thesis, with the embedded software development carried out as the focus of an MSc final year project by a member of staff from the sponsoring industrial partner [169]. Development of the test hardware, analysis of the batteries using the developed embedded solution, and the verification against the test systems developed for the larger body of work were carried out by the author of this thesis.

In implementing the technology some trade-offs in the capability of the measurement and state evaluation process were anticipated, and would be subject to some boundaries, specifically the computational capability of the microcontroller itself.

The motivation for this short study was therefore to explore the suitability of commercially available microcontrollers for this type of battery analysis, and to provide a proof of concept which could be used in an evolving on-board battery test system within larger electrical equipment such as a battery charger or industrial UPS.

12.2 Embedded processor selection

In selecting the processor for the test system, perhaps the largest constraints of the whole body of work came into play. The processor chosen needed to be reflective of a device which could feasibly be incorporated into a product costing $500. It was required to have a digital signal processing "engine", and library functions should be available from the manufacturer in order that robust, efficient code could be developed in a short time frame. Since both the author and the sponsor had considerable experience with Microchip embedded processors the devices examined were members from the Microchip dsPIC family, and the 16 bit 33fJ256GP710A [157] was chosen as the target processor. These devices have a price around $6 in quantity at the time of writing.

It was recognised that the timing of the acquisition was important in maintaining the integrity of the PRBS, and this required some element of parallel processing.

The chosen microcontroller was able to transfer data from the ADC to memory outside of the CPU operation by using the on-board Direct Memory Access (DMA) data bus. This was an important factor in the selection of the device, as the PRBS generation, and the acquisition of the battery data would need to be carried out as concurrent events.

12.3 Limitations associated with embedded devices

Embedded processors have become powerful devices over the 20 years or so of their existence, and embedded digital signal processing is a feature of many consumer audio devices. That being said, there are limitations in the computational capability of microcontrollers in mathematically intense applications. Despite having a high "million instructions per second" (MIPS) rating operations like FFT require that a large number of instructions be carried out, requiring efficient implementation of the software and its execution.

As mentioned, the dsPIC33fJ256GP710A has (DMA) allowing data transfer between on board RAM and a peripheral independently of the CPU execution, and further to optimise this operation the Microchip FFT libraries are written in assembly language to be more code efficient. However, limitations on memory and fixed point arithmetic lead to the device being only able to process 1024 FFT samples, restricting the resolution of the impedance results.

12.4 Development and testing

A basic specification was devised for the system it was very much considered that this was a proof of concept and within the limitations of the microcontroller the system should perform the following tasks:

Concurrent actions

a. Generate a 6 bit PRBS sequence at a selected frequency to drive an off-board power stage.

b. Acquire PRBS current and voltage PRBS data synchronised with (a)

c. Store the data externally to the main processor.

d. Processed the acquired data using an on board maths engine (FFT)

e. Store the data as an impedance response for the test battery.

In order to optimise the acquisition of the data within the constraints of the device, it was necessary to address the problems of capturing data from battery tests. The data of interest within the acquired voltage signal from the battery is typically 200 mV-1V on a DC level of circa 12.5V. The resolution of the dsPIC33fJ256GP710A ADC is up to 12 bits dependent on the number of channels used, so for the two channels required the available resolution available was 10-bit. As such, acquiring the DC part of the terminal voltage would reduce the effective resolution, so a hardware solution was adopted to improve the quality of the acquired data.

As part of the signal conditioning, a differential amplifier was used with a stable DC voltage set at one input to the amplifier. This effectively "dialled out" the DC offset of the battery, facilitating measurement of the resulting PRBS perturbation with a FSD of 3.3V rather than a scaled 15V FSD (Figure 154).

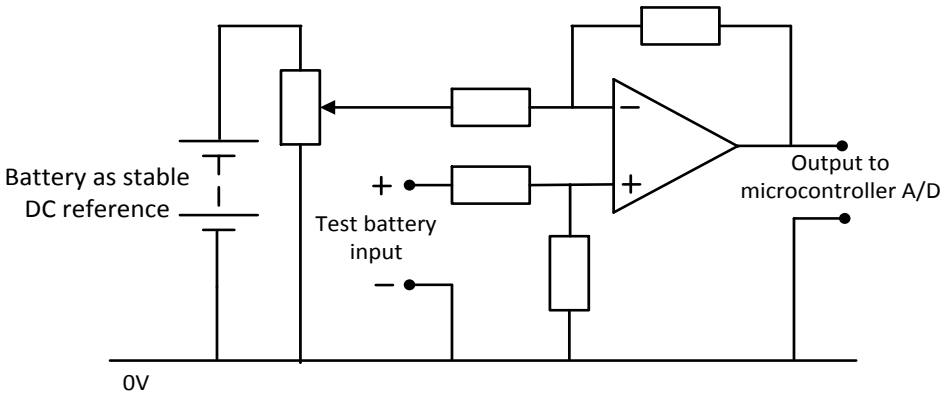

Figure 154. Improving battery test measurement resolution by introducing a stable DC offset

The DC reference was a small VRLA battery that was in a steady stage condition (previously charge several weeks before). The potentiometer used for dividing down the battery voltage was of a sufficiently high resistance that during the test the battery voltage should not be affected. It was envisaged that in the commercialisation of the techniques that this arrangement would be replaced with a precision reference and digital potentiometer, controlled by the dsPIC.

The test system block diagram is shown in Figure 155. The 16 Hz, 6 bit PRBS is generated from an array, and a single digital pin (RB1) changes state on a timer interrupt. Clearly, the acquisition needs to proceed at the same time and this is facilitated by the DMA. The ADC acquisition uses multiple sample and hold channels to sample the inputs at the same time, with the conversion subsequently performed sequentially. The addressing scheme used by the DMA module allows storage of the acquired data in separate blocks addressed by the channels as sampled, rather than in the order of conversion.

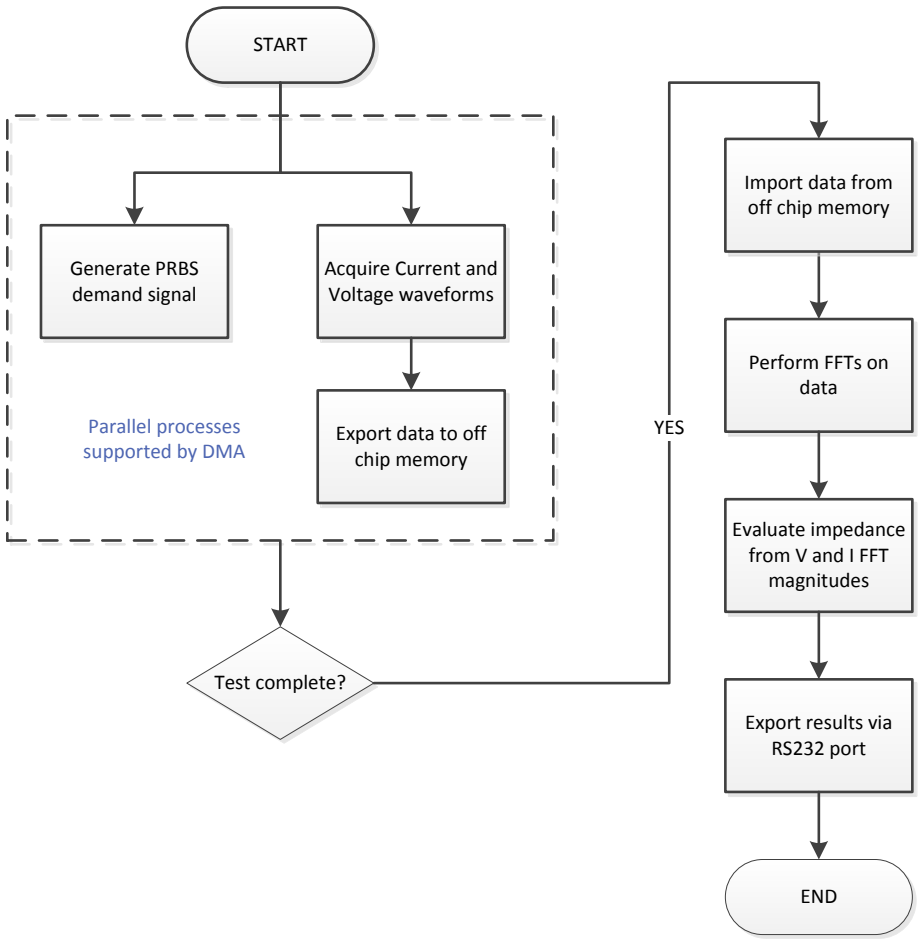

Figure 155. dsPIC test system flowchart

During this part of the process, the acquired data is being exported to the external flash (Amic A25L032), and the speed at which this occurs and the amount of available memory control the rate at which the dsPIC can acquire.

Subsequent to the data acquisition operation, the data is imported back into the microcontroller and the data processed using the Microchip DSP library FFT function.

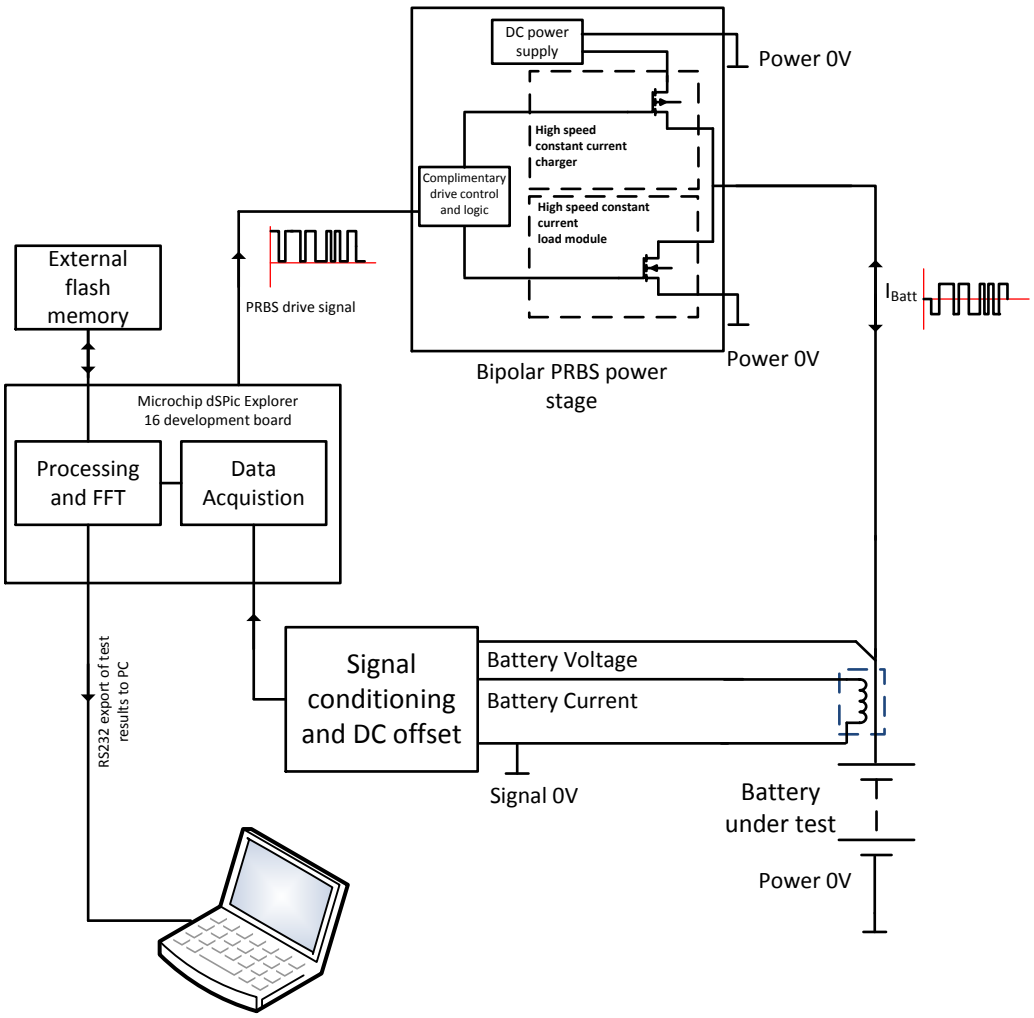

Figure 156. PRBS system block diagram

Figure 156 shows the system block diagram. (Full schematics are included in the appendices). The test equipment uses the power stage developed for the larger work, being driven by the dsPIC development board, and acquiring to it (Figure 157).

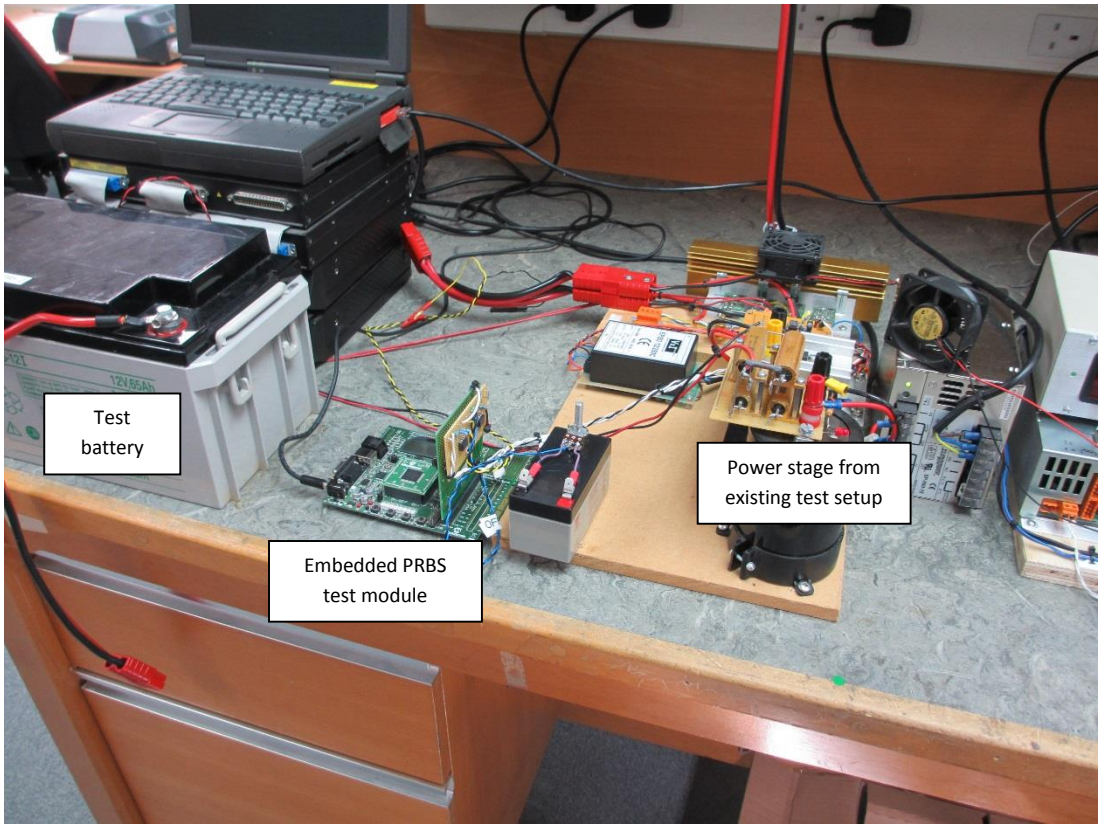

Figure 157. Photograph of prototype test apparatus

As such the board is autonomous with a single button press to start the test. Test results are exported via RS 232 to a local computer, but equally, these could be stored in RAM for historical trend analysis of batteries in application. A close up of the system board is shown in Figure 158. The essential digital components, along with the analogue signal processing could be shrunk to a much smaller board area, and the power stage used for the testing carries the dimensional overhead of multi-functional test hardware. It was estimated that the complete hardware including power devices but excluding power supplies could be accommodated on a double sided printed circuit board of dimensions 50mm x 75mm.

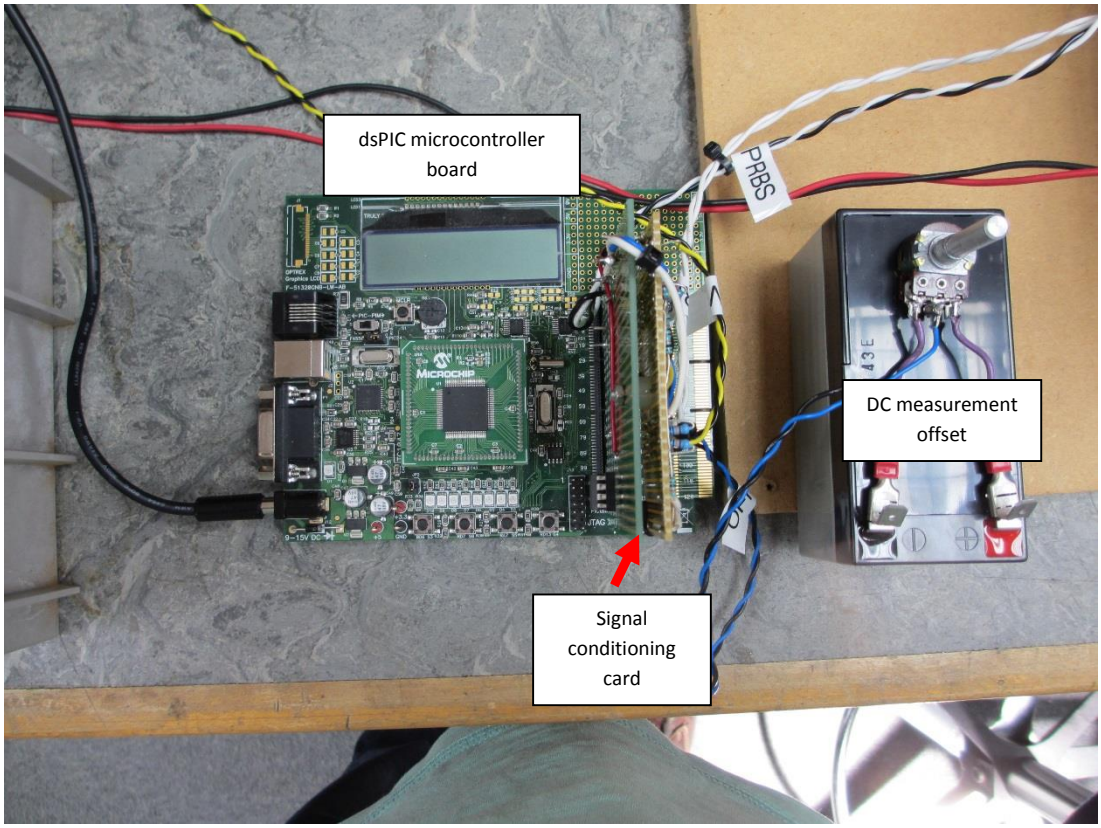

Figure 158. Close up of microcontroller card and signal processing hardware

12.5 Test results

The tests carried out were initially intended to verify the system could identify battery health, and as such the selected test batteries which were chosen for their very different SoH. Both of the batteries were Yuasa NP65-12 types, both with known histories. The better of the two batteries was less than 6 months old, and had been used for some of the PRBS tests in other chapters. The charging and discharging of this battery had been carefully controlled, and it had completed few cycles. As such it was deemed to be in a good SoH. The second battery was a similar type, but had been a "lab" battery for over ten years, and used in battery test profiling and general

duty in testing battery chargers during this time. In terms of SoH, the battery retained around only 20% of its original capacity, so was beyond the defined end of life for lead-acid batteries generally. Both batteries were in a fully charged state at the start of the tests.

The batteries are referred to as 'New Battery' and 'Aged Battery' in the test results.

Figure 159 shows the respective voltage profiles for the test batteries when subjected to the PRBS perturbation. The results shown in the figure are captured results from the microcontroller.

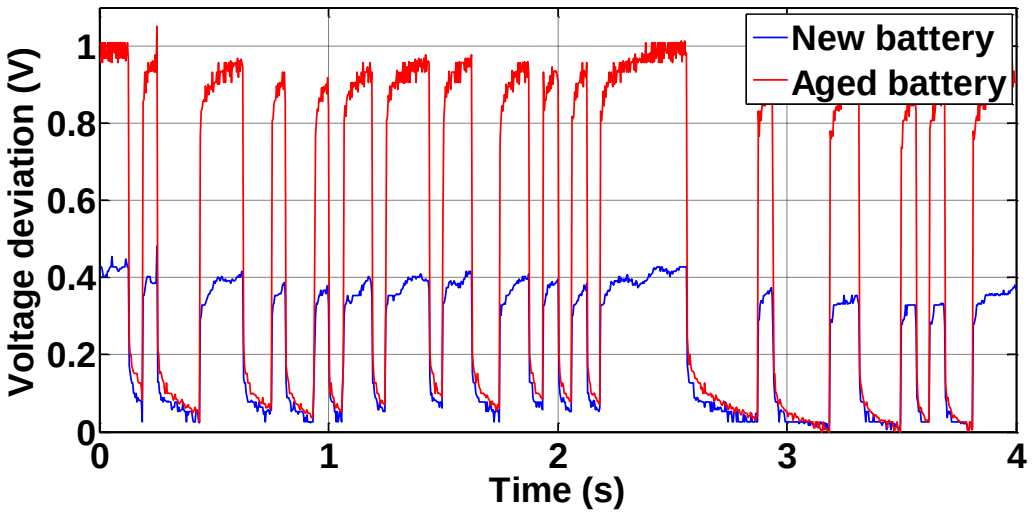

Figure 159. New and aged battery voltage profiles acquired by the dsPIC

The impedance results from the test, delivered by the microcontroller are shown in Figure 160. The responses are noisy but show the clear trends, and this can be observed more clearly in the filtered response in Figure 161.

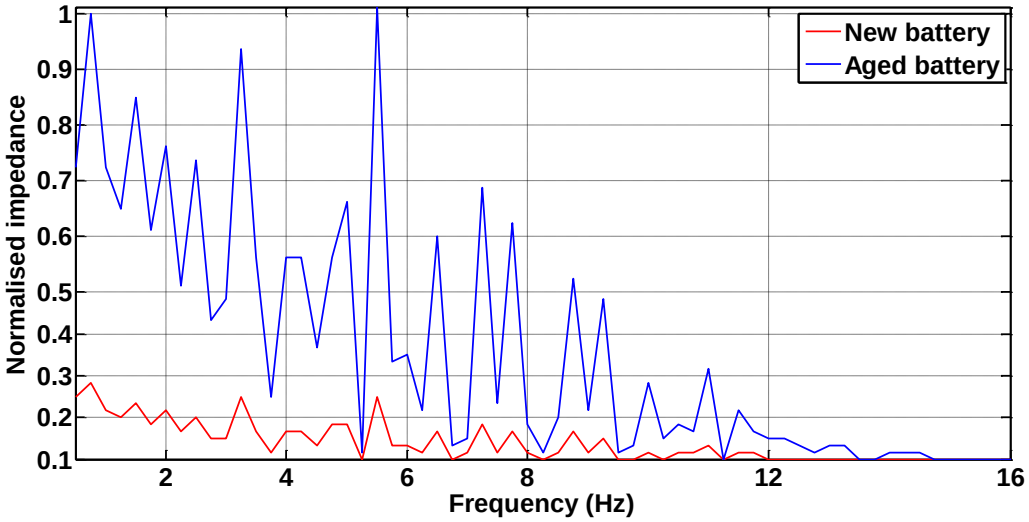

Figure 160. Raw normalised impedance results, new and aged battery

Figure 161 shows the raw FFT results after application of an 8 point moving average filter. It is clear from the results that the aged battery has a significantly increased impedance over the new battery indicating the known, poor SoH.

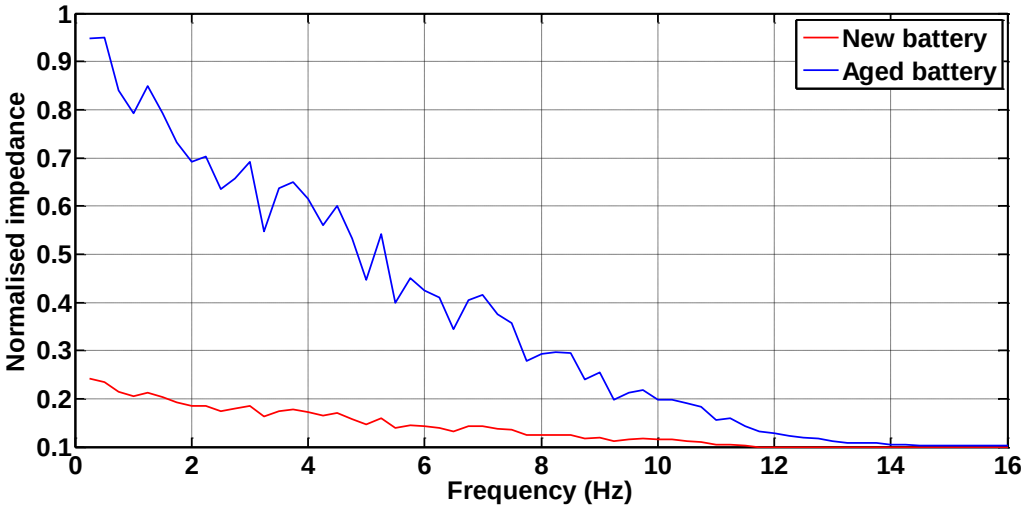

Figure 161. Normalised impedance results, both test batteries, 8 point moving average filter

12.6 Conclusion

This chapter has summarised initial attempts to embody the previously discussed battery characterisation tests within an early stage proof of concept commercial product prototype. The systematic design of an embedded processor was described and the compromise design choices in terms of cost and performance were given. Ideally the chosen processor would have more than the 1024 data samples of the dsPIC used, however experimental test results obtained from the prototype system show impedance responses indicating SoH can be extracted using a low-cost PRBS test module based on such a device. The tests were concluded at the proof of concept stage, as the system itself is to be developed further for incorporation into a deployed product. With the information gathered from this study the use of the dsPIC in evaluating battery performance using PRBS was demonstrated, and even with the limitations of the microcontroller, the SoH evaluation system developed could be used directly within a product to report this state. The system has benefits over the pulse battery testing used at present within these products in that even over the narrow band frequency spectrum used in the study, more information can be gathered than by single frequency analysis alone.

Comparatively, the PRBS test is fast, with the test time being just over 4 seconds for the clock frequency chosen, to capture an impedance spectrum, compared to 15-30 seconds for a two pulse battery test, which only yields a single result at the chosen step duration.

The embedded implementation of the PRBS battery evaluation technique involved overcoming some challenges in measurement resolution, and those of the FFT itself. The maximum number of samples for the FFT (1024) reduced the overall resolution of the result, but it was shown to be adequate to produce comparative results for test batteries of diverse states and effective capacities. The system was not used to produce models at this stage in development, as further work is required in characterising the results against known states.

It is intended that this characterisation of batteries will be part of the ongoing research, and with the technology incorporated into a commercial battery charger with Ethernet connectivity, potential exists for data collection from many deployed units operating with batteries over the lifecycle of the equipment. Periodic battery testing from the cradle to the grave for deployed batteries could provide a basis for a SoH/SoC measurement system. This in-field data could then be used as an input to the state prediction system introduced in chapter 8.

Chapter 13. Conclusions and further work

13.1 Conclusions

This thesis has described a novel series of experiments using PRBS perturbation signals in discrete and mixed modes to obtain state indicators and equivalent circuit parameters for Lead-Acid batteries, hybridised Lead-Acid, and battery/supercapacitor parallel networks.

Chapter 1 introduced the motivation for the study and the outstanding technical challenges to be addressed, in developing test systems to investigate battery state evaluation using a range of test modes over life and performance envelopes for the test batteries, and examining trends in and across the test modes.

The need to establish models for the test batteries based on these experiments was identified allowing correlations to be made between battery state and equivalent circuit components.

Furthermore, the partnering of the research with industry, required the realisation of this technology in a deployable format which could be incorporated in a battery connected device.

Within chapter 2 the current state of energy storage technologies was reviewed, and this combined with the research carried out in chapter 3 in examining performance characteristics and limitations of batteries, were used to inform the design of battery tests during the main study.

Battery test methods themselves were examined in chapter 4, culminating in the adoption of frequency rich signals examined in the frequency domain as the testing scheme for the work.

The work carried out within chapter 5 examined the discharge mode PRBS, developing techniques that would be used throughout the research. This early work examined batteries in differing SoH and formed the basis for much of the investigations that followed.

Chapter 6 was concerned with investigating the charge mode PRBS, and opened up applications for the technique with the results obtained. Using the charge mode technique it was discovered that by control of the charge voltage headroom high states of charge were clearly identified, and by using the prevailing charge voltage threshold, charge stage transition could be detected in multi-stage charge profiles.

Whilst reporting this SoC, the charge based PRBS was also suitable for reporting SoH, indicating via high frequency impedance the series impedance of the battery. The charge PRBS could be used to measure impedance over the full range of charge and therefore finds application as a state evaluation system that can be incorporated with a battery charger with minimal additional hardware, predominantly requiring an embedded processor to carry out the analysis.

Specific findings:

- Charge PRBS reports SoC
- At high SoC charge stage transitions can be detected
- Can be incorporated with minimal hardware into a battery charger

The investigations carried out in chapter 7 looked at the bipolar mode PRBS and the specific advantages of applying a net-zero perturbation signal to the battery. It transpired that the technique was not only the least intrusive, it brought with this additional indicators in the form of mean DC terminal voltage as an indicator.

Specific findings:

- Bipolar PRBS net zero energy perturbation signal facilitating longer tests
- Allows examination of mean DC terminal voltage as an addition SoC indicator
- Mean terminal voltage can also be used to indicate battery efficiency over a bipolar test period

The study in chapter 8 was concerned with examining the test battery parameters over SoC and encompassed some early work using the discharge PRBS along with the later developed bipolar tests. The investigation demonstrated that bipolar PRBS battery testing could be used for SoC indication and gave very clear identification of 100% and 0% charge states.

At intermediate charge states, state indications could further be observed, but as in all SoC indication techniques the observations are more subtle and benefit from being supported by additional indicators or historic state information.

The use of `mean terminal voltage measurement was further explored subsequent to the discoveries in chapter 7, and mapping this parameter over the full range of charge states confirmed that the parameter could be used at an input to a state evaluation system.

Specific findings:

- Bipolar PRBS most representative of battery impedance at 100% SoC
- Able to identify SoC through parameter identification
- Facilitates bipolar mean terminal voltage SoC indication

Chapter 9 investigated the effect of temperature on battery parameters and led on directly from the work in chapter 8. Again early work using the discharge PRBS was examined in conjunction with a later study using the bipolar PRBS. The testing obtained parameters for the test battery and further investigation of the bipolar testing was carried out.

Specific findings:

- Low temperature performance reduction observed by parameter identification
- Mean DC voltage from bipolar tests could be correlated to series impedance

Within the work carried out in Chapter 10 novel experiments were developed to examine the performance of a hybridised battery with integral supercapacitor. Tests using parallel networks comprising conventional batteries and supercapacitors allowed some insight into the respective roles of the capacitor and battery. Analysis of the current waveforms for each component allowed some estimations regarding the effectiveness of the Ultrabattery in EV/HEV duty showing the battery was more

responsive to rapid application of load, than its conventional counterparts and this was further shown in the impedance results. Using the PRBS tests, parameter estimation was carried out, and the battery was discovered to exhibit increased equivalent circuit surface capacitance to the conventional type by a factor 10:1.

Testing the conventional battery with parallel capacitances were shown to produce responses which when compared to the calculated parallel capacitance of the UltraBattery, confirmed the PRBS results.

The work was presented at the 13th European Lead Battery Conference (Paris, 2012) and was published in the Journal of Power Sources [160].

Specific findings:

- PRBS discharge testing applicable to parallel energy storage networks
- Parameter identification indication of 10:1 surface capacitance of hybridised battery compared to conventional Lead-Acid
- Results verified by testing comparable capacitor- battery parallel storage networks

The work carried out in chapter 11 comprised the most comprehensive series of tests running for over 120 days, and generating some 65 GByte of test data. A test battery was driven to accelerated failure, and all of the developed test modes were applied to the battery periodically during this time.

Lead-Acid Batteries are rated generally in terms of their lifetime to 80% capacity. It was clear from the tests that battery remained in a usable state beyond this capacity, and it was possible to observe the onset of total functional failure of the battery when reviewing the results.

This had implications in that if SoH and in turn the impact on SoF of the subject battery is fully understood, the useful life of the battery can be extended. It is vital that the end of life of the battery is predictable in these conditions, but the impact of being able to extend useful life of batteries is far reaching in terms of cost and environmental impact of the production of batteries.

It was observed that evaluating three test modes together in consecutive tests led to a deeper understanding of the prevailing state of the battery.

The following figures show with linear representations the observed trends.

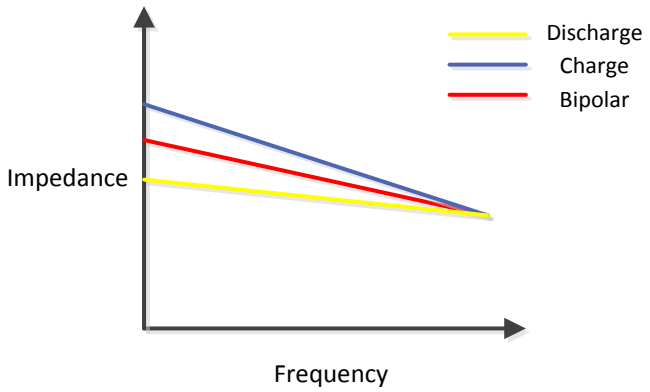

Figure 162. General impedance trends for the 3 modes of test at 100% SoC

At 100% SoC (figure 162) the discharge PRBS has a higher average impedance than the Charge PRBS. As charge state declines the three modes of test largely converge (Figure 163).

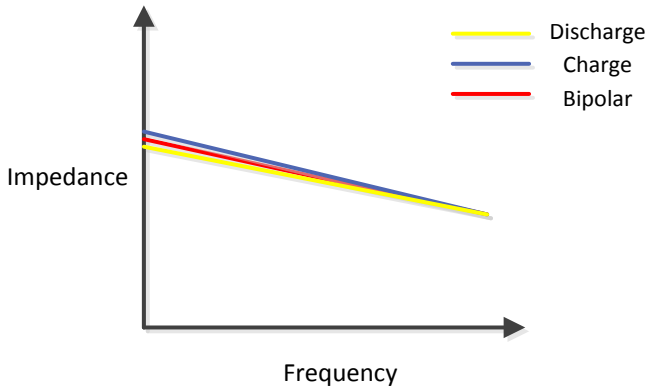

Figure 163. General impedance trends for the 3 modes of test at 85% SoC

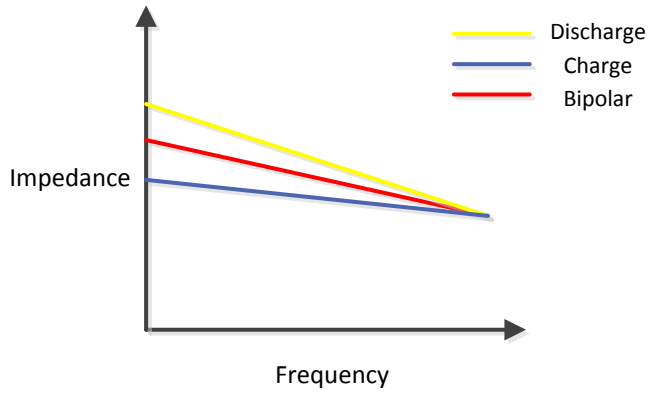

Figure 164. General impedance trends for the 3 modes of test at 0% SoC

Finally as the battery progresses to 0% SoC (Figure 164) the trend reverses and the discharge PRBS has the highest overall impedance. The trends were verified over battery SoH, with the observation that the impedance of a healthy battery generally converges at all states-of-charge at high frequency for all test modes. A battery in

poor state of health followed the trends observed in the figures, but overall amplitudes for impedance were increased.

It should be noted that only one mode of failure was examined in these tests, and other types of premature failure would require investigation to further inform the evaluation of SoH. Further investigation of the use of historic mean terminal voltage measurements under bipolar PRBS testing would also be desirable in order to further characterise this promising performance measure.

Specific findings:

- Parameter identification observations identify battery failure
- Mean bipolar DC terminal voltage identified declining battery health
- Mean bipolar DC terminal voltage identified declining battery efficiency
- Comparison of the three modes of test identified direct identification of battery SoC

The work carried out in chapter 12 proved the commercial viability of the developed tests by incorporating the PRBS generation, measurement, acquisition and FFT processing into a Microchip dsPIC. The exercise was a proof of concept, and the system itself will be developed further for incorporation into a deployed product.

The developed hardware and software facilitated identification of batteries in differing states of health. The types of low cost test hardware at which the study was targeted would typically employ pulse tests to carry out the battery evaluation and would generally report SoH only. The system showed benefits over this type of

testing in that even over the narrow band frequency spectrum used in the study, more information can be gathered than by single frequency analysis alone.

Specific benefits of the embedded system were identified:

- Comparatively, the PRBS test was fast, with the test time being just over 4 seconds, compared to 15-30 seconds for a two pulse battery test, which only yields a single result at the chosen step duration.
- The test system can be incorporated at minimal cost into a product which already employs pulse testing
- The investigations into the charge based technique would allow the embedded hardware to be used within a battery charger, modulating the charge current
- Data export allows historic trends to be identified

Comparison and applications of the PRBS test modes

The PRBS test schemes described in the previous sections have attributes that make them more suitable for some test modes than others. Table 25 summarises the relative benefits of each test type.

Table 25. Comparison of PRBS test modes

PRBS test method	Discharge	Charge	Bipolar
Mode	Current	Current/Voltage	Current
Advantages	Low hardware count	Can be implemented as part of the charge process. Can be run continuously in this mode.	Close to zero net effect on battery state. Long duration tests are possible. Facilitates mean DC terminal voltage measurement.
Disadvantages	Consumes energy, discharges battery to some extent. Long duration tests not possible.	Can only be used while a charge source is available.	Most complex to implement.
Indicators	SoC, SoH, SoF less effective at 100% SoC	SoC, SoH, SoF, charge phase endpoint detection	SoC, SoH, SoF, battery efficiency
Applications	Portable equipment, hand held battery test apparatus.	Battery chargers, UPS systems	Battery chargers, UPS systems, standalone battery evaluation systems.

13.2 Further work

The work carried out within this research has yielded much information regarding the application of diverse modes of frequency rich signals to test batteries. Opportunities for further work now exist in expanding and refining these techniques with in application test data. The developed commercial module as discussed in chapter 13 will form a basis for pushing the work further, as despite the limitations on the processing capability of commodity microcontrollers the deployment of a mass produced unit with the ability of returning field data represents a massive opportunity for system refinement. Referring to the block diagram in Figure 165, improvement of the existing developed hardware is required, and algorithms

developed to exploit the discoveries relating to mean terminal voltage, impedance trends over the test methods with SoC, and the effects of temperature.

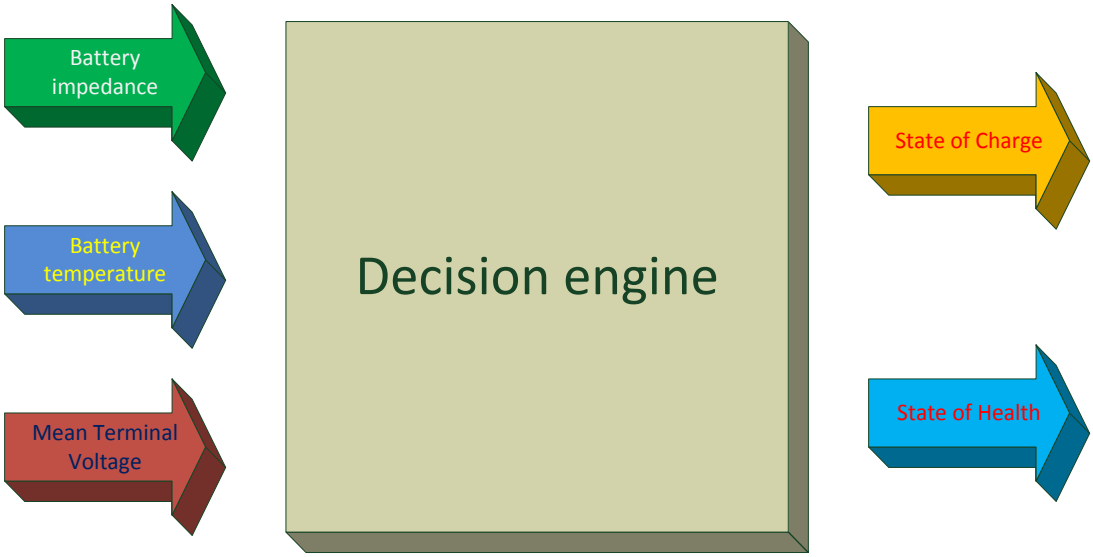

Figure 165. SoH/SoC evaluation system

The development of genetic algorithms for this system improvement itself would form the basis of a body of work which could be expanded to encompass increasing data as the hardware evolves with falling costs of processing and memory. Opportunities for further work exist in repeating the experiment with a lower chamber temperature (over a longer period) to reinforce the results and inform further analysis of the battery types. Using automated testing gives opportunities for driving batteries to failure at rated ambient temperatures, as the cycle life of the subject batteries may only be in the 1200-1500 range for these types. As such it is feasible to drive a battery to failure at 20°C ambient in under a year. Furthermore, realisation of the developed tests within a marketable product could inform these

techniques with the use of SPC and data collection from the field. The features unique to each of the load, charge and bipolar techniques when combined form a powerful addition to the pre-existing battery testing technologies, and further work in exploiting the charge end point detection capability of the charge technique shows great promise.

The increased capability of microprocessors generally has facilitated the growth of the "internet of things" and this in turn opens up opportunities for more accurate methods of battery testing. The ability to export historical data to a host system now allows evolution of battery test algorithms based on this data. Additionally, the ability to upload new firmware into these systems not only allows the evolution of the data interpretation, but enables the testing schemes themselves to evolve throughout the life of their operation.

.

14. References

1. Ribeiro, P.F., et al., *Energy storage systems for advanced power applications.* Proceedings of the IEEE, 2001. **89**(12): p. 1744-1756.

2. Skyllas-Kazacos, M. and C. Menictas. *The vanadium redox battery for emergency back-up applications*. in *Telecommunications Energy Conference, 1997. INTELEC 97., 19th International*. 1997.

3. Williams, B.R. and T. Hennessy, *Energy oasis [vanadium redox battery system in power distribution application].* Power Engineer, 2005. **19**(1): p. 28-31.

4. European Photovoltaic Industry Association. *Self consumption of PV electricity*. Updated: 2013 [cited 2013 27/09/2013]; Available from: http://www.epia.org/fileadmin/user_upload/Position_Papers/Self_and_direct_consumption_-_position_paper_-_final_version.pdf.

5. Poonpun, P. and W.T. Jewell, *Analysis of the Cost per Kilowatt Hour to Store Electricity.* Energy Conversion, IEEE Transactions on, 2008. **23**(2): p. 529-534. DOI: 10.1109/tec.2007.914157.

6. Porsche. *Ferdinand Porsche*. Updated: 2013 [cited 2013 27/09/2013]; History of Porsche]. Available from: http://www.porsche.com/uk/accessoriesandservice/classic/philosophyandclassicworld/world/tradition/ferdinand/.

7. Porsche Cars North America. *Prof. Ferdinand Porsche created the first functional hybrid car*. Updated: 2013 [cited 2013 26/10/2013]; Available from: http://press.porsche.com/news/release.php?id=642.

8. Nissan USA. *Nissan Leaf webpage*. Updated: 2015 [cited 2015 19/03/2015]; Available from: http://www.nissanusa.com/electric-cars/leaf/charging-range/battery/.

9. J Gartner, C.W. *Electric Vehicle Batteries - Lithium Ion Batteries for Plug-in Hybrid and Battery Electric Vehicles: Market Analysis and Forecasts*. Updated: 2009 26th November 2010; Available from: https://www.pikeresearch.com/wp-content/uploads/2009/12/EVB-09-Executive-Summary.pdf.

10. House of Lords European Union committee. *"The EU's Target for Renewable Energy: 20% by 2020"*. Updated: 2008 10/12/2010; Available from: http://www.publications.parliament.uk/pa/ld200708/ldselect/ldeucom/175/175.pdf.

11. Evonik Industries AG. *"Evonik developing the world's largest lithium ceramic battery"*. Updated: 2010 10/12/2010; Available from: http://corporate.evonik.com/en/media/press_releases/pages/news-details.aspx?newsid=10312.

12. Bush, S. (2014) *More on: Toshiba supplies UK with 1MW smart grid battery*. Electronics Weekly, Available from: http://www.electronicsweekly.com/news/design/power/toshiba-supplies-uk-1mw-smart-grid-battery-2-2014-07/.

13. Coleman, M., et al., *State-of-Charge Determination From EMF Voltage Estimation: Using Impedance, Terminal Voltage, and Current for Lead-Acid and Lithium-Ion Batteries.* Industrial Electronics, IEEE Transactions on, 2007. **54**(5): p. 2550-2557. DOI: doi:10.1016/j.apenergy.2008.11.021.

14. Nguyen, K.S., et al., *Enhanced coulomb counting method for estimating state-of-charge and state-of-health of lithium-ion batteries.* Applied Energy, 2009. **86**(9): p. 1506-1511.

15. Gruber, P.W., et al., *Global Lithium Availability.* Journal of Industrial Ecology, 2011. **15**(5): p. 760-775. DOI: 10.1111/j.1530-9290.2011.00359.x.

16. Linden, D. and T.B. Reddy, *Handbook of batteries*. 4th ed. McGraw-Hill handbooks. 2010, New York: McGraw-Hill. 1 v. (various pagings).007162421-X

17. Yuasa Battery Europe. *Yuasa NP Valve Regulated Lead Acid Battery Manual*. NP VRLA Application Manual [Application Manual] Updated: 1999 1/12/99; 1:[1, 2, 5, 6, 7, 8, 9, 12, 22, 24, 27, 29]. Available from: http://www.yuasa-battery.co.uk/industrial/downloads.html.

18. ABB. *GM and ABB demonstrate Chevrolet Volt Battery Reuse – world's first use of electric vehicle batteries for homes* Updated: 2012 [cited 2013 27/09/2013]; Available from: http://www.abb.co.uk/cawp/seitp202/8cb38a9d23816174c1257ab500497848.aspx.

19. BMW group. *BMW Group and Vattenfall start a new research project for the secondary use of high-voltage storage from electric vehicle. Enlarging the global test program under real application conditions - batteries from the MINI E and the BMW ActiveE will be used as a stationary power storage.* Updated: 2013 [cited 2013 27/9/2013]; BMW Group press release]. Available from: https://www.press.bmwgroup.com/pressclub/p/de/pressDetail.html?title=bmw-group-und-vattenfall-starten-neues-forschungsprojekt-zur-zweitverwendung-von-hochvoltspeichern&outputChannelId=7&id=T0145187DE&left_menu_item=node__2367.

20. Elsevier. *Scopus website*. Updated: 2013 [cited 2013 14th June 2013]; Available from: www.scopus.com.

21. UK Government Department for Transport. *Number of newly registered ultra low emissions vehicles*. Updated: 2013 [cited 2013 27/09/2013]; Available from: https://www.gov.uk/government/publications/number-of-newly-registered-ultra-low-emissions-vehicles.

22. Rolls Battery Engineering. *Rolls Battery Engineering Battery User Manual*. Updated: 2014 [cited 2015 16/03/15]; Available from: http://rollsbattery.com/public/docs/user_manual/Rolls_Battery_Manual.pdf.

23. Trojan Battery Company. *Trojan Battery Company website*. Updated: 2013 [cited 2013 17/8/2013]; Available from: http://www.trojanbattery.com/Tech-Support/TechSupport.aspx.

24. EnerSys Reserve Power. *Cyclon Application Manual*. Updated: 2004 [cited 2013 24/08/2013]; 5th Edition:[US-CYC-AM-005]. Available from:

http://www.enersysreservepower.com/pdfs/US-CYC-AM-005_0604%20Application%20Manual.pdf.

25. Ma, H., F. Cheng, and J. Chen, *Nickel-Metal Hydride (Ni-MH) Rechargeable Batteries*, in *Electrochemical Technologies for Energy Storage and Conversion*. 2011, Wiley-VCH Verlag GmbH & Co. KGaA. p. 175-237.9783527639496

26. Battery Council International. *Battery Council website*. Updated: 2013 [cited 2013 05/07/2013]; Available from: http://batterycouncil.org/?page=Battery_Recycling.

27. Yuasa Battery, E. *Yuasa Battery Europe Web site*. Updated: 2014 [cited 2015 08/03/2015]; Available from: http://www.yuasaeurope.com/en-gb/.

28. Westbrook, M.H., *The electric car : development and future of battery, hybrid and fuel-cell cars*. 2001, London: Institution of Electrical Engineers.0852960131 : [1]36.00

29. Ji, K., et al., *Electrodeposited lead-foam grids on copper-foam substrates as positive current collectors for lead-acid batteries.* Journal of Power Sources, 2014. **248**(0): p. 307-316. DOI: http://dx.doi.org/10.1016/j.jpowsour.2013.09.112.

30. Moseley, P.T., D.A.J. Rand, and B. Monahov, *Designing lead–acid batteries to meet energy and power requirements of future automobiles.* Journal of Power Sources, 2012. **219**(0): p. 75-79. DOI: http://dx.doi.org/10.1016/j.jpowsour.2012.07.040.

31. Rand, D.A.J., *Valve-regulated lead-acid batteries*. 1st ed. 2004, Amsterdam ; Boston: Elsevier. xxv, 575 p.0444507469

32. Ohmae, T., et al., *Advanced technologies in VRLA batteries for automotive applications.* Journal of Power Sources, 2006. **154**(2): p. 523-529. DOI: http://dx.doi.org/10.1016/j.jpowsour.2005.10.049.

33. Bentley, P. and D.A. Stone. *The parallel combination of a valve regulated lead acid cell and supercapacitor for use as a hybrid vehicle peak power buffer*. in *Power Electronics and Applications, 2005 European Conference on*. 2005. DOI: http://dx.doi.org/10.1109/EPE.2005.219586.

34. Bentley, P., *The use of Valve Regulated Sealed Lead Acid Batteries in Hybrid Electric Vehicles*, in *Department of Electrical Machines and Drives*. 2004, University of Sheffield: Sheffield

35. Ebonex Technologies Ltd. *Atraverda Batteries website*. Updated: 2010 [cited 2010 29/11/2010]; Available from: http://www.atraverda.co.uk.

36. Bullock, K.R., *Carbon reactions and effects on valve-regulated lead-acid (VRLA) battery cycle life in high-rate, partial state-of-charge cycling.* Journal of Power Sources, 2010. **195**(14): p. 4513-4519. DOI: http://dx.doi.org/10.1016/j.jpowsour.2009.10.027.

37. Moseley, P.T., R.F. Nelson, and A.F. Hollenkamp, *The role of carbon in valve-regulated lead–acid battery technology.* Journal of Power Sources, 2006. **157**(1): p. 3-10. DOI: http://dx.doi.org/10.1016/j.jpowsour.2006.02.031.

38. Pavlov, D. and P. Nikolov, *Capacitive carbon and electrochemical lead electrode systems at the negative plates of lead–acid batteries and elementary processes on cycling.* Journal of Power Sources, 2013. **242**(0): p. 380-399. DOI: http://dx.doi.org/10.1016/j.jpowsour.2013.05.065.

39. Devitt, J., *An account of the development of the first valve-regulated lead/acid cell.* Journal of Power Sources, 1997. **64**(1–2): p. 153-156. DOI: http://dx.doi.org/10.1016/S0378-7753(96)02516-5.

40. Optima Batteries. *Optima batteries website*. Updated: 2013 [cited 2013 14/11/13]; Available from: http://www.optimabatteries.com/us/en/technology/spiralcell-technology/.

41. Bhangu, B.S., et al. *Observer techniques for estimating the state-of-charge and state-of-health of VRLABs for hybrid electric vehicles*. in *Vehicle Power and Propulsion, 2005 IEEE Conference*. 2005.

42. Lam, L.T. and R. Louey, *Development of ultra-battery for hybrid-electric vehicle applications.* Journal of Power Sources, 2006. **158**(2): p. 1140-1148. DOI: 10.1016/j.jpowsour.2006.03.022.

43. Furukawa Electric. *Furukawa review no. 43*. Updated: 2013 [cited 2015 8/3/2015]; Available from: http://www.furukawa.co.jp/review/fr043/fr43_02.htm#searchform.

44. East Penn Manufacturing. *East Penn Manufacturing, UltraBattery*. Updated: 2014 [cited 2015 8/3/2015]; Available from: http://www.eastpennmanufacturing.com/tag/deka-ultrabattery/.

45. Jungner, E.W., *Process of making active material for accumulator-plates*. 1901, Google Patents

46. Panasonic Industrial Batteries. *Panasonic Industrial Batteries website*. Updated: 2013 [cited 2013 17/08/2013]; Available from: http://www.panasonic.com/industrial/batteries-oem/oem/lithium-ion.aspx.

47. EUROPEAN, T.E.P.A.T.C.O.T. and UNION, *DIRECTIVE 2006/66/EC OF THE EUROPEAN PARLIAMENT AND OF THE COUNCIL on batteries and accumulators and waste batteries and accumulators and repealing Directive 91/157/EEC*, E. Union, Editor. 2006: Strasbourg DOI: 6th September 2006.

48. Alcad Ltd. *Alcad Batteries website*. Updated: 2013 17/08/13]; Available from: http://www.alcad.com/Products/Nickel-Cadmium-single-cell-batteries.

49. Sato, Y., et al., *Possible Cause of the Memory Effect Observed in Nickel-Cadmium Secondary Batteries.* Journal of The Electrochemical Society, 1996. **143**(10): p. L225-L228. DOI: 10.1149/1.1837152.

50. Power-Sonic Inc. *Power-Sonic Inc NiCd & NiMH Batteries and chargers*. Updated: 2015 [cited 2015 21/03/15]; Available from: http://www.power-sonic.com/nickel_cadmium_n_nimh.php.

51. K.D. Beccu, B.-G., *Elektrode zur Speicherung und Aktivierung von Wasserstoff"*. 1973: Switzerland

52. Bergveld, H.J., W.S. Kruijt, and P.H.L. Notten, *Battery management systems : design by modelling*. Philips Research v. 1. 2002, Dordrecht ; Boston: Kluwer Academic. xxv, 295 p.1402008325 (hb alk. paper)

53. Bumblebee Batteries LLC. *Bumblebee Batteries LLC website*. Updated: 2015 [cited 2015 13/03/2015]; Bumblebee Batteries - Honda Insight]. Available from: http://bumblebeebatteries.com/honda-hybrid-batteries/.

54. Toyota Motor Sales, U.S.A.I. *Toyota Safety and Quality communications webpage - batteries*. Updated: 2015; Available from: http://www.toyota.com/esq/vehicles/batteries/nickel-metal-hydride.html.

55. Al-Thyabat, S., et al., *Adaptation of minerals processing operations for lithium-ion (LiBs) and nickel metal hydride (NiMH) batteries recycling: Critical review.* Minerals Engineering, 2013. **45**(0): p. 4-17. DOI: http://dx.doi.org/10.1016/j.mineng.2012.12.005.

56. Larsson, K., C. Ekberg, and A. Ødegaard-Jensen, *Dissolution and characterization of HEV NiMH batteries.* Waste Management, 2013. **33**(3): p. 689-698. DOI: http://dx.doi.org/10.1016/j.wasman.2012.06.001.

57. Sony Corporation. *Expanding from the Development of Olivine-Type Lithium-Ion Iron Phosphate Storage Batteries to Include Other Peripheral Devices*. Updated: 2014 [cited 2015 21/03/2015]; Available from: http://www.sony.net/SonyInfo/csr_report/environment/climate/ghg/products/index4.html.

58. Commission, I.E., *IEC 60086-2 Primary batteries: Physical and Electrical specifications*. 2006, IEC: Geneva

59. Jaffe, S. (2013) *The Lithium Ion Inflection point*. Battery Power Magazine, Available from: http://www.batterypoweronline.com/main/articles/the-lithium-ion-inflection-point/.

60. Wang, Q., et al., *Thermal runaway caused fire and explosion of lithium ion battery.* Journal of Power Sources, 2012. **208**(0): p. 210-224. DOI: http://dx.doi.org/10.1016/j.jpowsour.2012.02.038.

61. Yufei, C., S. Li, and J.W. Evans. *Modeling studies on battery thermal behaviour, thermal runaway, thermal management, and energy efficiency*. in *Energy Conversion Engineering Conference, 1996. IECEC 96., Proceedings of the 31st Intersociety*. 1996. DOI: 10.1109/iecec.1996.553943.

62. A123 systems LLC. *"A123 Systems Opens the Largest Lithium Ion Automotive Battery Manufacturing Plant in North America"*. Updated: [cited 2010 7/12/10]; Available from: http://ir.a123systems.com/releasedetail.cfm?ReleaseID=506787.

63. Ying, W. and C. Guozhong, *Nanostructured materials for advanced Li-Ion rechargeable batteries.* Nanotechnology Magazine, IEEE, 2009. **3**(2): p. 14-20.

64. Altair Nanotechnologies. *Altairnano's advanced energy storage systems provide fundamental advantages over existing, traditional lithium-ion battery designs*. Updated: 2010 [cited 2015 22/03/2015]; Available from: http://www.altairnano.com/products/performance/.

65. Lee, S.W., et al., *High-power lithium batteries from functionalized carbon-nanotube electrodes.* Nat Nano, 2010. **5**(7): p. 531-537. DOI: http://www.nature.com/nnano/journal/v5/n7/abs/nnano.2010.116.html#supplementary-information.

66. Mirzaeian, M. and P.J. Hall. *Nano structure carbons for energy storage in lithium oxygen batteries*. in *Sustainable Power Generation and Supply, 2009. SUPERGEN '09. International Conference on*. 2009.

67. Moriguchi, K., et al., *Nano-tube-like surface structure in graphite particles and its formation mechanism: A role in anodes of lithium-ion secondary batteries.* Journal of Applied Physics, 2000. **88**(11): p. 6369-6377.

68. Hanafusa, H., *SANYO's SMART ENERGY SYSTEM CONSISTS OF 1.5 MWh Li-ion BATTERY AND 1 MW PV SOLAR SYSTEM*, in *Electrical Energy Storage Applications & Technologies (EESAT) Conference 2011*. 2011: San Diego, CA

69. Lombardi, C. (2009) *Mazda, Think, EnerDel partner on electric rentals*. CNET, Available from: http://www.cnet.com/uk/news/mazda-think-enerdel-partner-on-electric-rentals/.

70. Graber, K. (2012) *Electrovaya Delivers 1.5 MWH Lithium Ion Battery-Based Energy Storage System to Arizona Public Service Company*. Available from: http://www.electrovaya.com/pdf/PR/2012/PR20120223.pdf.

71. Mitsubishi Heavy Industries. *MHI to Introduce Large-capacity Lithium-ion Battery Energy Storage System To Power Grid of Orkney Islands in UK, Jointly with SSE*. Updated: 2012 [cited 2015 22/03/2015]; Available from: https://www.mhi-global.com/news/story/1211221593.html.

72. Valence advanced energy storage solutions. *Backup Power for UPS and Micro Grid*. Updated: 2014 [cited 2015 22/03/2015]; Available from: https://www.valence.com/solutions/backup/.

73. Kang, D.H.P., M. Chen, and O.A. Ogunseitan, *Potential Environmental and Human Health Impacts of Rechargeable Lithium Batteries in Electronic Waste.* Environmental Science & Technology, 2013. **47**(10): p. 5495-5503. DOI: 10.1021/es400614y.

74. Xu, J., et al., *A review of processes and technologies for the recycling of lithium-ion secondary batteries.* Journal of Power Sources, 2008. **177**(2): p. 512-527. DOI: http://dx.doi.org/10.1016/j.jpowsour.2007.11.074.

75. Mizushima, K., et al., *LixCoO2 (0<x<-1): A new cathode material for batteries of high energy density.* Materials Research Bulletin, 1980. **15**(6): p. 783-789. DOI: http://dx.doi.org/10.1016/0025-5408(80)90012-4.

76. Yoon, Y., et al., *Lattice orientation control of lithium cobalt oxide cathode film for all-solid-state thin film batteries.* Journal of Power Sources, 2013. **226**(0): p. 186-190. DOI: http://dx.doi.org/10.1016/j.jpowsour.2012.10.094.

77. Sakuda, A., A. Hayashi, and M. Tatsumisago, *Electrochemical performance of all-solid-state lithium secondary batteries improved by the coating of Li2O–TiO2 films on LiCoO2 electrode.* Journal of Power Sources, 2010. **195**(2): p. 599-603. DOI: http://dx.doi.org/10.1016/j.jpowsour.2009.07.037.

78. Zero Motorcycles Specification. *Zero motorcycles product specification*. [Manufacturers web page] Updated: 2013 [cited 2013 22/11/2013]; Available from: http://www.zeromotorcycles.com/zero-s/specs.php.

79. Lu, L., et al., *A review on the key issues for lithium-ion battery management in electric vehicles.* Journal of Power Sources, 2013. **226**(0): p. 272-288. DOI: http://dx.doi.org/10.1016/j.jpowsour.2012.10.060.

80. Super B Batteries. *Super B Batteries*. Updated: 2013 [cited 2013 4/10/2013]; Available from: http://www.super-b.com.

81. Krieger, E.M., J. Cannarella, and C.B. Arnold, *A comparison of lead-acid and lithium-based battery behavior and capacity fade in off-grid renewable charging applications.* Energy, 2013. **60**(0): p. 492-500. DOI: http://dx.doi.org/10.1016/j.energy.2013.08.029.

82. Fenton, D.E., J.M. Parker, and P.V. Wright, *Complexes of alkali metal ions with poly(ethylene oxide).* Polymer, 1973. **14**(11): p. 589. DOI: http://dx.doi.org/10.1016/0032-3861(73)90146-8.

83. Tobishima, S.I. and J.I. Yamaki, *A consideration of lithium cell safety.* Journal of Power Sources, 1999. **81-82**: p. 882-886.

84. Maxwell Technologies. *Maxwell Technologies website*. Updated: 2015 [cited 2015 8/03/2015]; Available from: http://www.maxwell.com/products/ultracapacitors.

85. Liyan, Q. and Q. Wei, *Constant Power Control of DFIG Wind Turbines With Supercapacitor Energy Storage.* Industry Applications, IEEE Transactions on, 2011. **47**(1): p. 359-367. DOI: 10.1109/tia.2010.2090932.

86. Miller, J.M. *Energy storage technology markets and application’s: ultracapacitors in combination with lithium-ion*. in *Power Electronics, 2007. ICPE '07. 7th Internatonal Conference on*. 2007. DOI: 10.1109/icpe.2007.4692343.

87. Conway, B.E., *Electrochemical supercapacitors : scientific fundamentals and technological applications*. 1999, New York: Plenum Press. xxviii, 698 p.0306457369

88. Wima Spezialvertrieb elektronischer Bauelemente GmbH & Co.KG. *Wima SuperCap R product webpage*. Updated: 2015 [cited 2015 8/03/2015]; Available from: http://www.wima.cn/EN/supercap_r_1.htm.

89. Burke, J.R.M.a.A.F., *Electrochemical Capacitors: Challenges and Opportunities for Real-World Applications.* The Electrochemical Society's Interface, 2008. **17**(1).

90. Ellis, M.W., M.R. von Spakovsky, and D.J. Nelson, *Fuel cell systems: efficient, flexible energy conversion for the 21st century.* Proceedings of the IEEE, 2001. **89**(12): p. 1808-1818. DOI: 10.1109/5.975914.

91. Burke, K.A., *High energy density regenerative fuel cell systems for terrestrial applications.* Aerospace and Electronic Systems Magazine, IEEE, 1999. **14**(12): p. 23-34. DOI: 10.1109/62.811091.

92. Aso, S., M. Kizaki, and Y. Nonobe. *Development of Fuel Cell Hybrid Vehicles in TOYOTA*. in *Power Conversion Conference - Nagoya, 2007. PCC '07*. 2007. DOI: 10.1109/pccon.2007.373179.

93. Hua, T., et al., *Status of hydrogen fuel cell electric buses worldwide.* Journal of Power Sources, 2014. **269**(0): p. 975-993. DOI: http://dx.doi.org/10.1016/j.jpowsour.2014.06.055.

94. Kohler, J., et al. *Infrastructure investment for a transition to hydrogen road vehicles*. in *Infrastructure Systems and Services: Building Networks for a Brighter Future (INFRA), 2008 First International Conference on*. 2008. DOI: 10.1109/infra.2008.5439664.

95. Stolten, D. and B. Emonts, *Fuel cell science and engineering : materials, processes, systems and technology*. 2012, Weinheim: Wiley-VCH ; [Chichester : John Wiley, distributor].9783527330126

96. Srinivasan, S., *Fuel cells : from fundamentals to applications*. 2006, New York, N.Y.: Springer.9780387251165 (hbk.) : ¹59.00

97. Symons, P.C., *Process for electrical energy using solid halogen hydrate*, U.S.P. Office, Editor. 1973: United States of America

98. Garche, J., *Encyclopedia of electrochemical power sources*. 2009, Boston, MA: Elsevier.9780444520937

99. Sumitomo Electric Industries Ltd. *Sumitomo Electric Commences the Demonstration of Megawatt-Class Power Generation/Storage System at Yokohama Works* Updated: 2012 [cited 2013 09/08/2013]; Press release, Sumitomo Electric Industries Ltd]. Available from: http://global-sei.com/news/press/12/prs069_s.html.

100. Renewable Energy Dynamics Technology Ltd. *REDT Website*. Updated: 2013 [cited 2013 17/08/2013]; REDT company website]. Available from: http://www.poweringnow.com/.

101. Mohamed, M.R., S.M. Sharkh, and F.C. Walsh. *Redox flow batteries for hybrid electric vehicles: Progress and challenges*. in *Vehicle Power and Propulsion Conference, 2009. VPPC '09. IEEE*. 2009. DOI: 10.1109/vppc.2009.5289801.

102. Smith, G., *Storage batteries; including operation, charging, maintenance and repair*. 2nd ed. 1971, London,: Pitman. xiii, 231 p.0273360876

103. Lam, L.T., et al., *VRLA Ultrabattery for high-rate partial-state-of-charge operation.* Journal of Power Sources, 2007. **174**(1): p. 16-29. DOI: 10.1016/j.jpowsour.2007.05.047.

104. Cooper, A., et al., *The UltraBattery—A new battery design for a new beginning in hybrid electric vehicle energy storage.* Journal of Power Sources, 2009. **188**(2): p. 642-649. DOI: 10.1016/j.jpowsour.2008.11.119.

105. Csiro. *Csiro website - Ultrabattery FAQs*. Updated: 2013 [cited 2013 24/08/13]; Available from: http://www.csiro.au/en/Outcomes/Energy/Renewables-and-Smart-Systems/Ultra-Battery-FAQs.aspx.

106. Saft Battery Group. *Saft Battery Website*. Updated: 2015 [cited 2015 18/03/2015]; Available from: http://www.saftbatteries.com/.

107. Horowitz, P. and W. Hill, *The art of electronics*. 1989: Cambridge University Press

108. Samsung SDI. *Samsung Lithium Ion battery products websit*. Updated: 2015 [cited 2015 17/03/2015]; Available from: http://www.samsungsdi.com/lithium-ion-battery/overview.

109. Amperex Technology Ltd. *Amperex Technology Ltd Website*. Updated: 2015 [cited 2015 17/03/2015]; Available from: http://www.atlbattery.com/products/en/product-1.htm.

110. E-One Moli Energy. *Molicel Rechargeable Lithium-Ion Batteries*. Updated: 2008 [cited 2010 29/10/10]; Available from: http://www.molicel.com/ca/products.html.

111. Varta Microbattery GmbH. *Varta Microbattery Products Website*. Updated: 2015 [cited 2015 17/03/2015]; Available from: http://www2.varta-microbattery.com/en/oempages/product_data/poductdata_types.php?output=typedata&segment=RechLiFlatPoly.

112. Elmer, T., et al., *Fuel cell technology for domestic built environment applications: State of-the-art review.* Renewable and Sustainable Energy Reviews, 2015. **42**(0): p. 913-931. DOI: http://dx.doi.org/10.1016/j.rser.2014.10.080.

113. Joerissen, L., et al., *Possible use of vanadium redox-flow batteries for energy storage in small grids and stand-alone photovoltaic systems.* Journal of Power Sources, 2004. **127**(1–2): p. 98-104. DOI: http://dx.doi.org/10.1016/j.jpowsour.2003.09.066.

114. Pascoe, P.E. and A.H. Anbuky, *The behaviour of the coup de fouet of valve-regulated lead–acid batteries.* Journal of Power Sources, 2002. **111**(2): p. 304-319. DOI: http://dx.doi.org/10.1016/S0378-7753(02)00316-6.

115. de Oliveira, C.P. and M.C. Lopes, *Early stages of the lead-acid battery discharge.* Journal of Power Sources, 2004. **138**(1–2): p. 294-300. DOI: http://dx.doi.org/10.1016/j.jpowsour.2004.06.009.

116. Berndt, D. and E. Voss. *Proceedings of the Fourth International Symposium*. 1964. Brighton.

117. Pavlov, D., et al., *Hydration and Amorphization of Active Mass PbO2 Particles and Their Influence on the Electrical Properties of the Lead-Acid Battery Positive Plate.* Journal of The Electrochemical Society, 1989. **136**(11): p. 3189-3197. DOI: 10.1149/1.2096424.

118. Pavlov, D., *The Lead-Acid Battery Lead Dioxide Active Mass: A Gel-Crystal System with Proton and Electron Conductivity.* Journal of The Electrochemical Society, 1992. **139**(11): p. 3075-3080. DOI: 10.1149/1.2069034.

119. Manenti, A., S. Onori, and Y. Guezennec. *A new modeling approach to predict 'Peukert effect' for lead acid batteries*. in *IFAC Proceedings Volumes (IFAC-PapersOnline)*. 2011. DOI: 10.3182/20110828-6-it-1002.03659.

120. Peukert, W., *Über die Abhängigkeit der Kapazität von der Entladestromstärke bei Bleiakkumulatoren.* Elektrotechnische Zeitschrift 20, 1897.

121. Doerffel, D. and S.A. Sharkh, *A critical review of using the Peukert equation for determining the remaining capacity of lead-acid and lithium-ion batteries.* Journal of Power Sources, 2006. **155**(2): p. 395-400.

122. Serrao, L., et al. *An aging model of Ni-MH batteries for hybrid electric vehicles*. in *Vehicle Power and Propulsion, 2005 IEEE Conference*. 2005. DOI: 10.1109/vppc.2005.1554536.

123. Swoboda, C.A., et al., *Development of an Ultrasonic Technique to Measure Specific Gravity in Lead-Acid Battery Electrolyte.* Sonics and Ultrasonics, IEEE Transactions on, 1983. **30**(2): p. 69-77. DOI: 10.1109/t-su.1983.31389.

124. Nagai, Y., Y. Tomokuni, and T. Matsui. *Optical-Type Hydrometer for Lead-Acid Batteries and its Applications*. in *Telecommunications Energy Conference, 1987. INTELEC '87. The Ninth International*. 1987. DOI: 10.1109/intlec.1987.4794631.

125. Fairweather, A.J., *Analysis of false battery failure reporting in single load pulse battery test schemes*. 2000, Bulgin Power Source PLC: Lincoln, UK

126. Coleman, M., W.G. Hurley, and L. Chin Kwan, *An Improved Battery Characterization Method Using a Two-Pulse Load Test.* Energy Conversion, IEEE Transactions on, 2008. **23**(2): p. 708-713.

127. Ashley, G.H., *Proposed battery testing methods for the Ulyssees project* 1999, Bulgin Power Source: Lincoln

128. Bolgeo, R.T., *IEEE Recommended Practice for Maintenance, Testing, and Replacement of Vented Lead-Acid Batteries for Stationary Applications.* IEEE Std 450-1995, 1995: p. 1-32. DOI: 10.1109/ieeestd.1995.79541.

129. Cantor, W.P., *IEEE Recommended Practice for Maintenance, Testing, and Replacement of Valve-Regulated Lead-Acid (VRLA) Batteries for Stationary Applications.* IEEE Std 1188-1996, 1996: p. i. DOI: 10.1109/ieeestd.1996.81039.

130. Leksono, E., et al. *State of charge (SoC) estimation on LiFePO<inf>4</inf> battery module using Coulomb counting methods with modified Peukert*. in *Rural Information & Communication Technology and Electric-Vehicle Technology (rICT & ICeV-T), 2013 Joint International Conference on*. 2013. DOI: 10.1109/rICT-ICeVT.2013.6741545.

131. Barsoukov, E. and J.R. Macdonald, *Impedance spectroscopy : theory, experiment, and applications*. 2nd ed. 2005, Hoboken, N.J. [Chichester]: Wiley-Interscience. xvii, 595 p.0471647497 (hbk.)

132. Hioki EE Corporation. *BATTERY HiTESTER 3554*. Updated: 2009 [cited 2015 13/03/2015]; Hioki EE Website]. Available from: https://www.hioki.com/products/lcr_resistance_signal/lcr_resistance_meters/544.

133. J.L. Jespersen, A.E.T., K. Nørregaard, L. Overgaard, F. Elefsen. *Capacity Measurements of Li-Ion Batteries using AC Impedance Spectroscopy*. in *EVS24*. 2009. Stavanger, Norway.

134. Yi-Feng, L., et al. *AC impedance technique for dynamic and static state of charge analysis for Li-ion battery*. in *Consumer Electronics (ISCE), 2013 IEEE 17th International Symposium on*. 2013. DOI: 10.1109/isce.2013.6570268.

135. Texas Instruments. *bq77PL900 Five to Ten Series Cell Lithium-Ion or Lithium-Polymer Battery Protector and Analog Front End*. Updated: 2008 [cited 2015 19/03/2015]; Available from: http://www.ti.com/lit/ds/symlink/bq77pl900.pdf.

136. Texas Instruments. *bq34z100 Wide range fuel gauge with impedance track technology*. Updated: 2012 [cited 2015 19/03/2015]; Available from: http://www.ti.com/lit/ds/symlink/bq34z100.pdf.

137. Taylor, H.O., *Telephone Receivers and Radio Telegraphy.* Radio Engineers, Proceedings of the Institute of, 1918. **6**(1): p. 37-58. DOI: 10.1109/jrproc.1918.217354.

138. Suwarno and F. Donald. *Frequency response analysis (FRA) for diagnosis of power transformers*. in *Electrical Engineering/Electronics Computer Telecommunications and Information Technology (ECTI-CON), 2010 International Conference on*. 2010.

139. Bingham, C.M. and A.J. Fairweather, *PhD Project meeting, use of PRBS in frequency domain analysis of batteries*. 2009: Sheffield

140. Cedric, T.M.M., R.W. Adi, and I. McLoughlin. *Data concealment in audio using a nonlinear frequency distribution of PRBS coded data and frequency-domain LSB insertion*. in *TENCON 2000. Proceedings*. 2000.

141. Jamieson, D.G. and T. Schneider, *Electroacoustic evaluation of assistive hearing devices.* Engineering in Medicine and Biology Magazine, IEEE, 1994. **13**(2): p. 249-254.

142. Vermeulen, H.J., J.M. Strauss, and V. Shikoana. *On-line estimation of synchronous generator parameters using PRBS perturbations*. in *Power Engineering Society General Meeting, 2003, IEEE*. 2003.

143. Melkonian, L. *Improving A/D Converter Performance Using Dither*. Updated: 1992 [cited 2015 11/04/2015]; Available from: http://www.ti.com/lit/an/snoa232/snoa232.pdf.

144. Davies, W.D.T., *System identification for self-adaptive control*. 1970, London, New York,: Wiley-Interscience. xiv, 380 p.0471198854

145. Alfke, P. (1996) *Efficient Shift Registers, LFSR, Counters, and Long Pseudo-Random Sequence Generators*. Available from: http://www.xilinx.com/support/documentation/application_notes/xapp052.pdf.

146. Hampton, R.L.T., *A hybrid analog-digital pseudo-random noise generator*, in *Proceedings of the April 21-23, 1964, spring joint computer conference*. 1964, ACM: Washington, D.C. p. 287-301 DOI: 10.1145/1464122.1464152.

147. Davidson, J.N., et al., *Improved bandwidth and noise resilience in thermal impedance spectroscopy by mixing PRBS signals.* Power Electronics, IEEE Transactions on, 2013. **PP**(99): p. 1-1. DOI: 10.1109/tpel.2013.2288936.

148. Tlili, C., et al., *Electrochemical impedance probing of DNA hybridisation on oligonucleotide-functionalised polypyrrole.* Talanta, 2005. **68**(1): p. 131-137.

149. Feliu, S., et al., *The determination of the corrosion rate of steel in concrete by a non-stationary method.* Corrosion Science, 1986. **26**(11): p. 961-965, 967-970.

150. Randles., J.E., *Kinetics of rapid electrode reactions.* Discuss. Faraday Soc. , 1947(1): p. 11.

151. Bhangu, B.S., et al., *Nonlinear observers for predicting state-of-charge and state-of-health of lead-acid batteries for hybrid-electric vehicles.* Vehicular Technology, IEEE Transactions on, 2005. **54**(3): p. 783-794.

152. Cverna, F., *ASM ready reference. Thermal properties of metals*. 2002, Materials Park, Ohio: ASM International.0871707683

153. VxI Power Ltd. *Oracle 200E product webpage*. Updated: 2012 [cited 2012 20/07/2012]; Oracle 200E product webpage]. Available from: http://www.vxipower.com/product_pdetail_200-Watt---Oracle-III-200e_140.htm.

154. Pintelon, R. and J. Schoukens, *System identification : a frequency domain approach*. 2001, New York: IEEE Press. xxxviii, 605 p.0780360001

155. Schwarzenbach, J. and K.F. Gill, *System modelling and control*. 2nd ed. 1984, London ; Baltimore, Md.: E. Arnold. xi, 322 p.0713135182 (pbk.)

156. Microchip Technology Inc. *Explorer 16 Development Board User's Guide*. Updated: 2005 [cited 2010 20/6/2010]; Available from: http://ww1.microchip.com/downloads/en/DeviceDoc/51589a.pdf.

157. Microchip Technology Inc. *dsPIC33F Family Data Sheet*. [Manufacturer's datasheet] Updated: 2005 23/06/14; DS70165A:[Available from: http://ww1.microchip.com/downloads/en/DeviceDoc/70165a.pdf.

158. Salameh, Z.M., M.A. Casacca, and W.A. Lynch, *A mathematical model for lead-acid batteries.* Energy Conversion, IEEE Transactions on, 1992. **7**(1): p. 93-98. DOI: 10.1109/60.124547.

159. Bingjun, X., S. Yiyu, and H. Lei. *A universal state-of-charge algorithm for batteries*. in *Design Automation Conference (DAC), 2010 47th ACM/IEEE*. 2010.

160. Fairweather, A.J., D.A. Stone, and M.P. Foster, *Evaluation of UltraBattery™ performance in comparison with a battery-supercapacitor parallel network.* Journal of Power Sources, 2013. **226**(0): p. 191-201. DOI: http://dx.doi.org/10.1016/j.jpowsour.2012.10.095.

161. Jossen, A., *Fundamentals of battery dynamics.* Journal of Power Sources, 2006. **154**(2): p. 530-538. DOI: http://dx.doi.org/10.1016/j.jpowsour.2005.10.041.

162. Li, J. and M.A. Danzer, *Optimal charge control strategies for stationary photovoltaic battery systems.* Journal of Power Sources, 2014. **258**(0): p. 365-373. DOI: http://dx.doi.org/10.1016/j.jpowsour.2014.02.066.

163. Stevens, J.W. and G.P. Corey. *A study of lead-acid battery efficiency near top-of-charge and the impact on PV system design*. in *Photovoltaic Specialists Conference, 1996., Conference Record of the Twenty Fifth IEEE*. 1996. DOI: 10.1109/pvsc.1996.564417.

164. Armenta-Deu, C. and M.V. Calvo-Baza, *The initial voltage drop in lead–acid cells: the influence of the overvoltage.* Journal of Power Sources, 1998. **72**(2): p. 194-202. DOI: http://dx.doi.org/10.1016/S0378-7753(97)02733-X.

165. Fairweather, A.J., M.P. Foster, and D.A. Stone, *State-of-Charge Indicators for VRLA Batteries Utilising Pseudo Random Binary Sequences (PRBS)*, in *PCIM Europe 2011*. 2011: Nuremberg, Germany

166. Fairweather, A.J., M.P. Foster, and D.A. Stone, *Modelling of VRLA batteries over operational temperature range using Pseudo Random Binary Sequences.* Journal of Power Sources, 2012. **207**(0): p. 56-59. DOI: 10.1016/j.jpowsour.2012.02.024.

167. Sangyoung, P., K. Younghyun, and C. Naehyuck. *Hybrid energy storage systems and battery management for electric vehicles*. in *Design Automation Conference (DAC), 2013 50th ACM / EDAC / IEEE*. 2013.

168. Jayasinghe, S.D.G., D.M. Vilathgamuwa, and U.K. Madawala. *A direct integration scheme for battery-supercapacitor hybrid energy storage systems with the use of grid side inverter*. in *Applied Power Electronics Conference and Exposition (APEC), 2011 Twenty-Sixth Annual IEEE*. 2011. DOI: 10.1109/apec.2011.5744773.

169. Purvis, L., *Frequency Domain Analysis of Batteries in an Embedded Systems Environment*, in *Department of computer Science*. 2013, University of Leicester: Leicester

170. Continental Batteries. *Continental Batteries products website*. Updated: 2012 [cited 2015 15/04/2015]; Available from: http://www.continentalbattery.com/products/87?q=ctx.

15. Appendices

15.1 AM-1 Combined mode battery test system

During the course of the research, several hardware and software based experimental test systems were developed, which progressively evolved into the AM-1 combined mode battery test system. The test system comprises battery charging and cycling systems which operate autonomously, with the opportunity for external real time control via a pc running an appropriate software control system, such as National Instruments LabView™. The block diagram for the system can be seen in Figure 166.

The control system with the AM-1 is centred on a VxI Power Oracle 200E intelligent power supply using custom firmware to autonomously control the system operation from within the AMM-1 battery cycler module.

The firmware was written in assembly language to the on-board Microchip 16F877 microcontroller. The microcontroller card has external A-D conversion allowing 12 bit resolution measurements of voltage and current from within the power supply itself and the connected batteries. D-A conversion is also available within the unit which allows control of the internal battery charger. Within the VxI unit, a constant current load module is provided for pulse battery testing, driven by digital I/O from the microcontroller. A serial port is provided, allowing external control and monitoring of the system parameters. Running the Modbus protocol, digital status indications, digital inputs and analogue I/O are available via this port.

15.1.1 AM-1 system block diagram

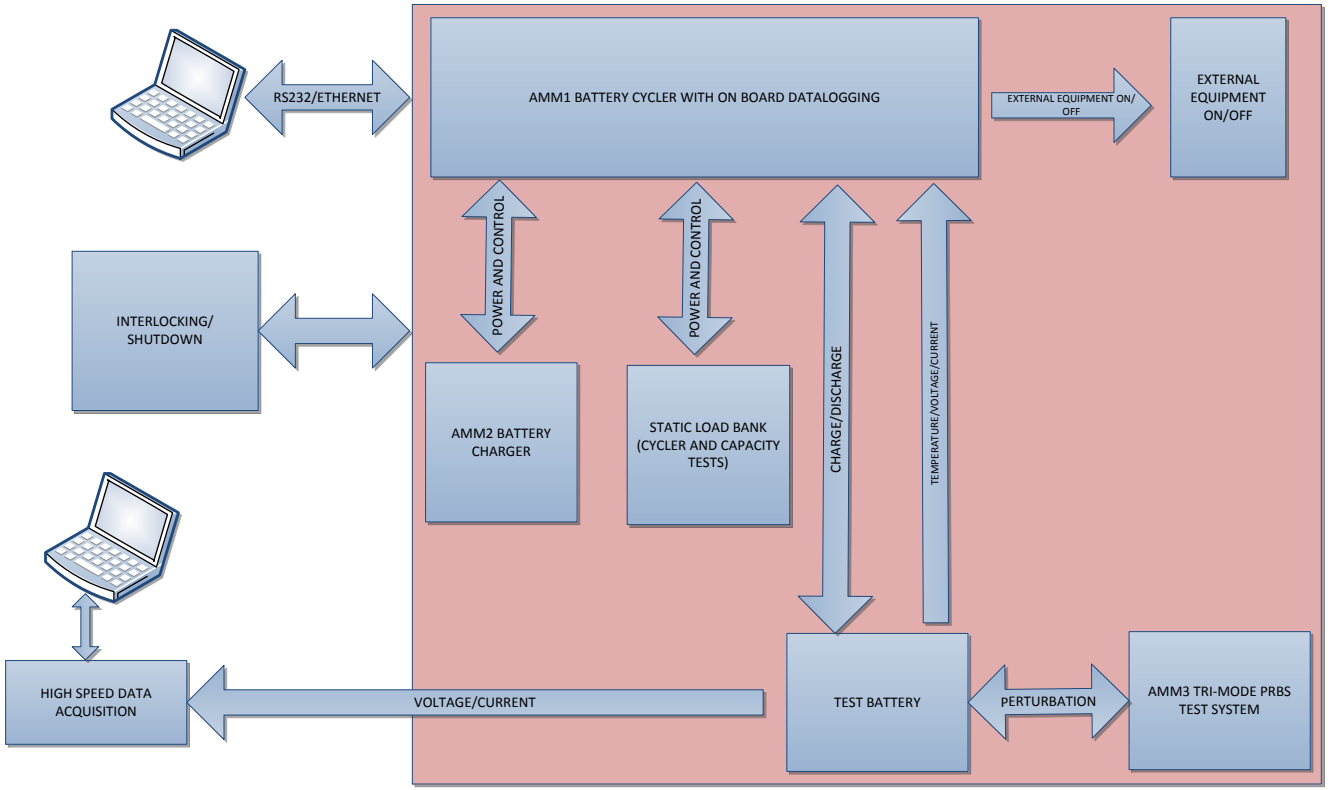

Figure 166. Overall system block diagram, AM-1 battery test system

The firmware written for the cycler uses the Oracle 200E digital outputs and analogue inputs to control the cycler itself. User input from the connected pc allows setting of the number of cycles, enabling of the cycle mode, battery charge current, battery disconnect point among other parameters.

In cycler mode the control from the Oracle unit controls the overall rack using 4 digital outputs which control the external loads and battery charger.

The cycler operates in 3 primary modes:

Mode 1 - Battery cycler with pre-set number of cycles

In the battery cycler mode the on board charger within the VxI unit is supplemented with an external charger, controlled by the firmware. An external load, again controlled by the firmware is used for the discharge portion of the cycle.

On initiation of a battery cycling test, the software enables the charging system for a period of three hours. Additionally, if the test uses the external environmental chamber this is also switch on by the firmware. After the charge timer has elapsed, the chargers are disabled and the system enters discharge mode by connecting the external load. The voltage of the battery is monitored via a 4 wire measurement system during the discharge process, and is disconnected from the load at the EoD voltage (an analogue setting within the user interface). At this point the charge cycle begins again and the cycler counter is decremented. Once the cycler counter reaches zero, the cycle count resets and the systems prepares the battery for the PRBS testing. This comprises of turning the environmental chamber off, enabling the bulk and float

chargers, and recharging the battery. The bulk charge is enabled for three hours, and then the system reverts to the float charger where it remains, charging the battery to 100% SoC.

Mode 2 - Single shot battery capacity measurement with deep discharge protection

In this mode the user sets the "charge disable" via the PC interface and enables the discharge test. The software then enables the external load and the battery discharges to the EoD Voltage at which point the load is disconnected. Optionally the equipment can be set to automatically recharge the battery to 100% SoC, or remain at the EoD state.

Mode 3 -Temperature compensated battery charger

This is the default mode of the system on power up. The system will charge the connected battery via the on board charger to the float voltage level, which can be set by the user, along with the magnitude of battery charge current.

The interface used for the system was based on Microsoft Excel with a third party software package carrying out the Dynamic Data Exchange (DDE) between the spreadsheet and the serial port communicating with the equipment. The interface can be seen in figure 167.

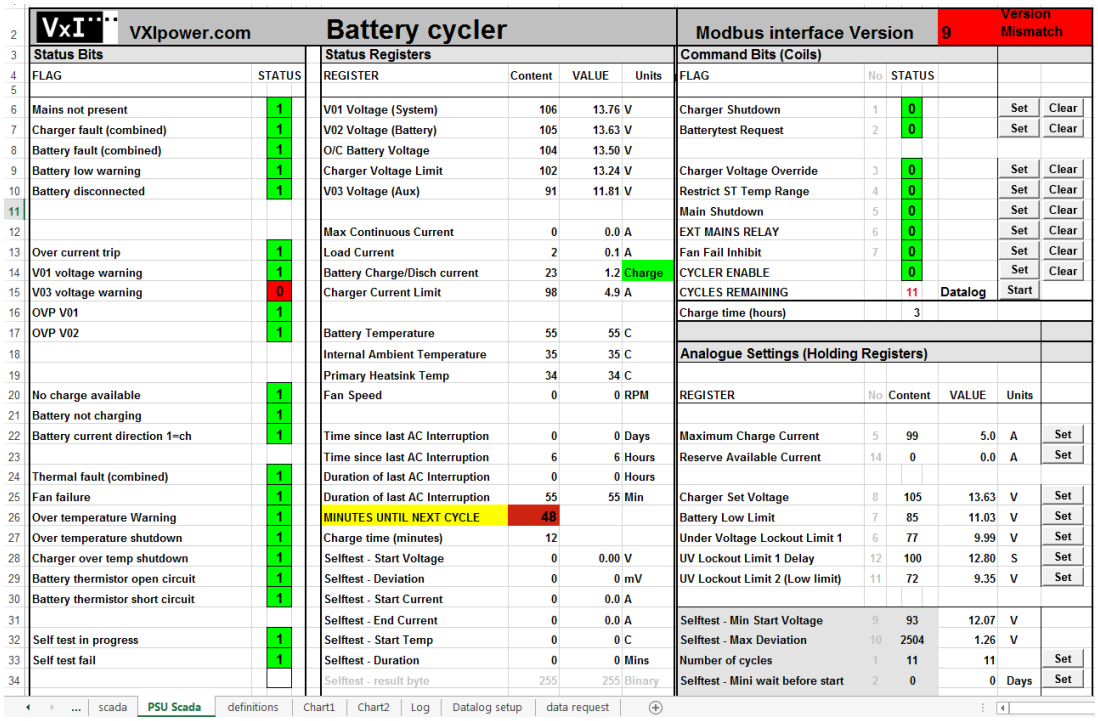

VXIpower.com

Battery cycler

Modbus interface Version 9 — Version Mismatch

Status Bits

FLAG	STATUS
Mains not present	1
Charger fault (combined)	1
Battery fault (combined)	1
Battery low warning	1
Battery disconnected	1
Over current trip	1
V01 voltage warning	1
V03 voltage warning	0
OVP V01	1
OVP V02	1
No charge available	1
Battery not charging	1
Battery current direction 1=ch	1
Thermal fault (combined)	1
Fan failure	1
Over temperature Warning	1
Over temperature shutdown	1
Charger over temp shutdown	1
Battery thermistor open circuit	1
Battery thermistor short circuit	1
Self test in progress	1
Self test fail	1

Status Registers

REGISTER	Content	VALUE	Units
V01 Voltage (System)	106	13.76	V
V02 Voltage (Battery)	105	13.63	V
O/C Battery Voltage	104	13.50	V
Charger Voltage Limit	102	13.24	V
V03 Voltage (Aux)	91	11.81	V
Max Continuous Current	0	0.0	A
Load Current	2	0.1	A
Battery Charge/Disch current	23	1.2	Charge
Charger Current Limit	98	4.9	A
Battery Temperature	55	55	C
Internal Ambient Temperature	35	35	C
Primary Heatsink Temp	34	34	C
Fan Speed	0	0	RPM
Time since last AC Interruption	0	0	Days
Time since last AC Interruption	6	6	Hours
Duration of last AC Interruption	0	0	Hours
Duration of last AC Interruption	55	55	Min
MINUTES UNTIL NEXT CYCLE	48		
Charge time (minutes)	12		
Selftest - Start Voltage	0	0.00	V
Selftest - Deviation	0	0	mV
Selftest - Start Current	0	0.0	A
Selftest - End Current	0	0.0	A
Selftest - Start Temp	0	0	C
Selftest - Duration	0	0	Mins
Selftest - result byte	255	255	Binary

Command Bits (Coils)

FLAG	No	STATUS			
Charger Shutdown	1	0		Set	Clear
Batterytest Request	2	0		Set	Clear
Charger Voltage Override	3	0		Set	Clear
Restrict ST Temp Range	4	0		Set	Clear
Main Shutdown	5	0		Set	Clear
EXT MAINS RELAY	6	0		Set	Clear
Fan Fail Inhibit	7	0		Set	Clear
CYCLER ENABLE		0		Set	Clear
CYCLES REMAINING		11	Datalog	Start	
Charge time (hours)		3			

Analogue Settings (Holding Registers)

REGISTER	No	Content	VALUE	Units	
Maximum Charge Current	5	99	5.0	A	Set
Reserve Available Current	14	0	0.0	A	Set
Charger Set Voltage	8	105	13.63	V	Set
Battery Low Limit	7	85	11.03	V	Set
Under Voltage Lockout Limit 1	6	77	9.99	V	Set
UV Lockout Limit 1 Delay	12	100	12.80	S	Set
UV Lockout Limit 2 (Low limit)	11	72	9.35	V	Set
Selftest - Min Start Voltage	9	93	12.07	V	
Selftest - Max Deviation	10	2504	1.26	V	
Number of cycles	1	11	11		Set
Selftest - Mini wait before start	2	0	0	Days	Set

... | scada | PSU Scada | definitions | Chart1 | Chart2 | Log | Datalog setup | data request

Figure 167. Battery cycler interface screen

The interface incorporates a data log function allowing recording of any desired group of analogue or digital parameters available on the RS232 port. The sampling rate of the acquisition is typically in the 1 – 10 second range in line with recording data during cycling and discharge tests of long duration. High speed acquisition is carried out by the external IOTech data aquisition system (figure 168). Full specifications for the system are found in appendix 15.6.

Figure 168. IOTech Daqbook 200 data acquisition system used for the high frequency tests

Photographs of the AM-1 test system are shown in figures 169, 170 and 171 showing the key parts of the system and the interconnections. Note the modules are connected via Anderson SB connectors which allow rapid reconfiguration of the system to allow alternative DC loads and charging systems to be rapidly adopted.

Figure 169. AM-1 test system photograph showing installed modules and rear interconnectivity

Key to figure 169.

a. Emergency stop and power distribution panel.

b. Battery and charger status panel (charger panel to the left, overall battery current and battery terminal voltage indicated by the panel meters on the right).

c. AMM-2 battery charge module.

d. AMM-1 battery cycling system

e. AMM-3 PRBS battery test system

f. Electronic loads for long duration discharge and cycling tests.

g. Ethernet port (from RS232 system communication port).

h. Controlled AC mains outlet (for external oven control or similar. (A controlled 24V output is also provided.)

i. Battery current measurement (low speed) this measurement is fed to the front panel meter and also the low speed acquisition of the VxI Oracle unit).

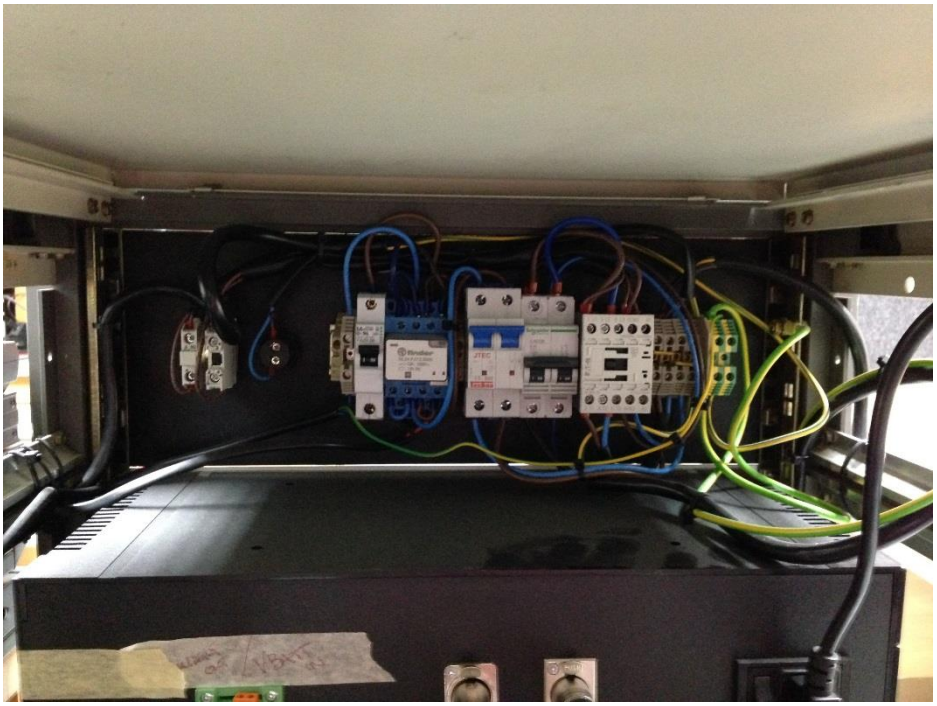

Figure 170. AM-1 AC distribution, circuit protection and emergency stop wiring

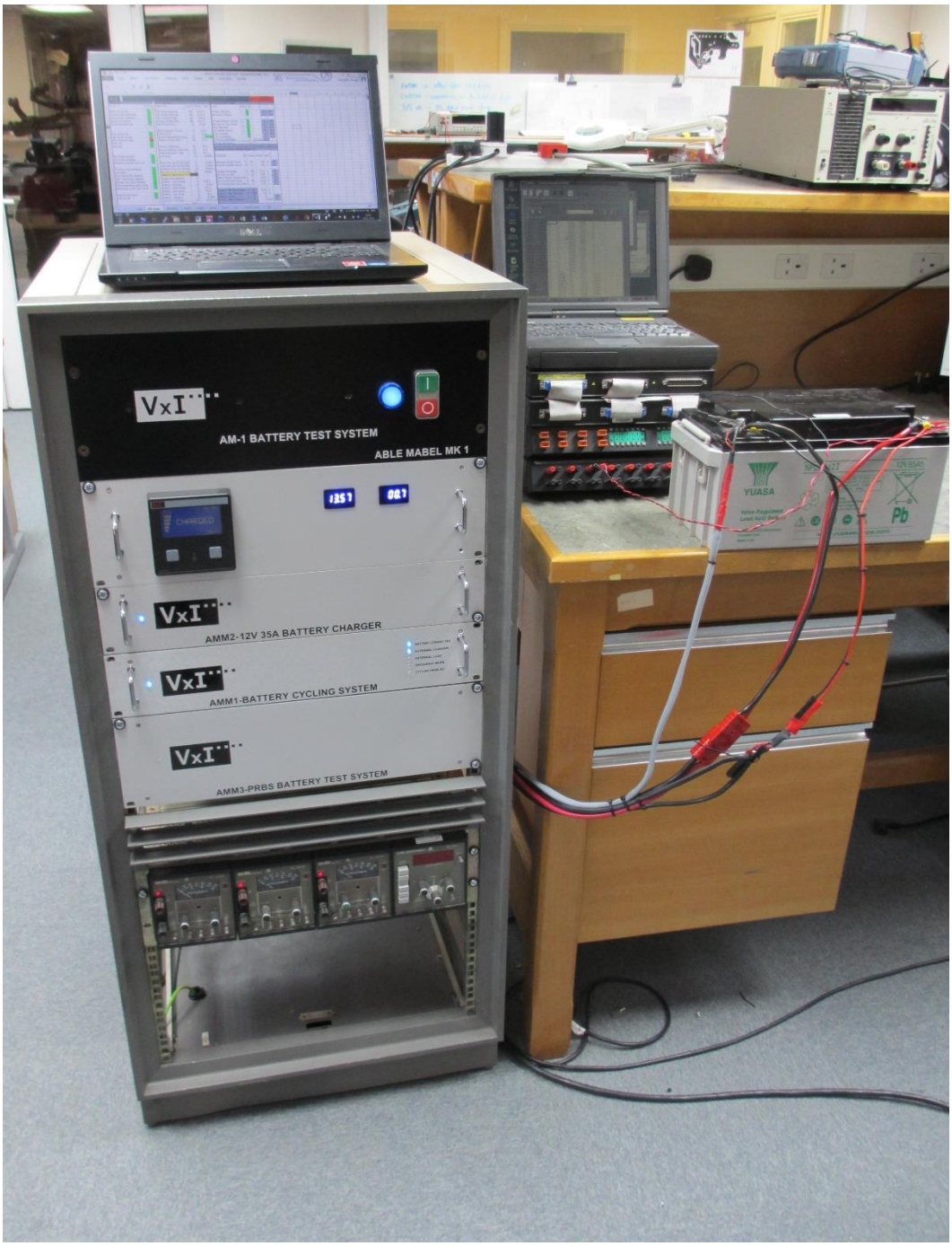

Figure 171. Wider shot of the test system showing the high speed data acquisition, control PC and battery under test

15.1.2 AMM-1 Battery cycler and system controller

Figure 172 shows the internal view of the AMM-1 cycler controller. Under control of the VxI unit the module marshals the battery current to the connected loads and chargers whilst being capable of charging the battery itself at a digitally controlled charge current of up to 10A.

Controlled discharges are carried out again via the control and monitoring of the VxI unit with battery disconnect voltage (EoD voltage) being programmable via the RS232 port. Figure 173 shows the rear connections that are made to the unit.

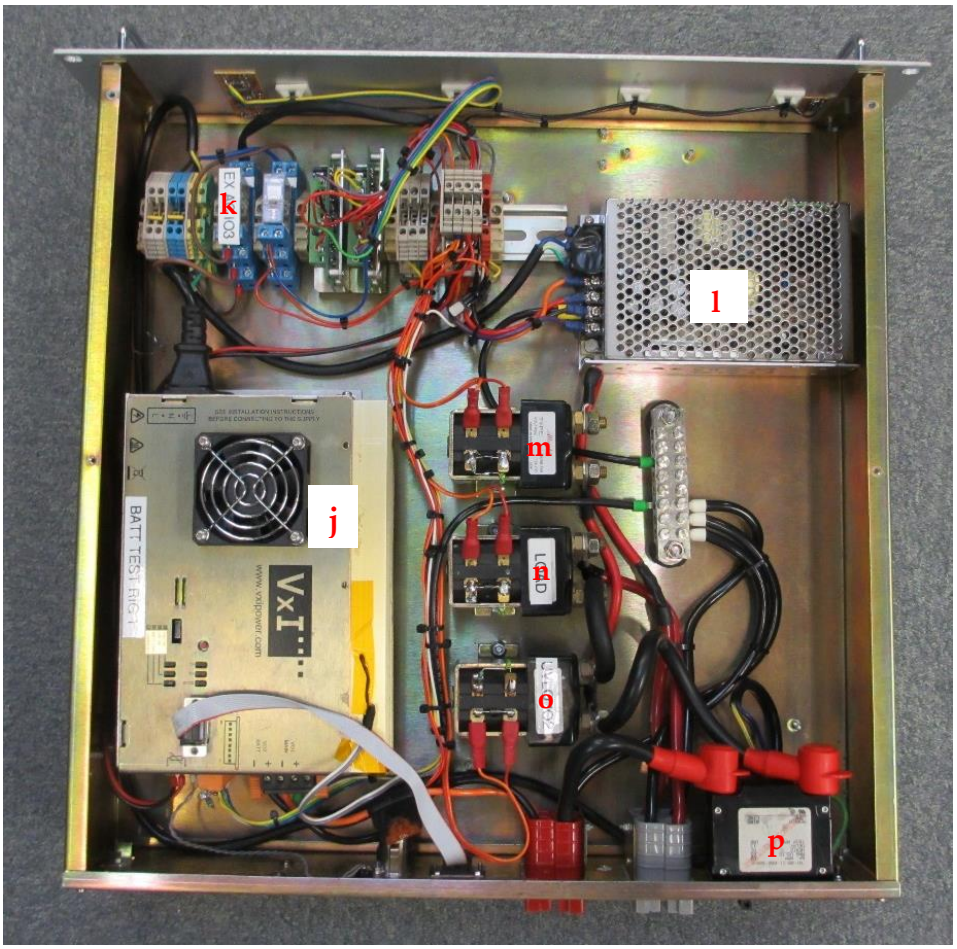

Figure 172. AMM-1 battery cycler and controller

Key to figure 172.

j. VxI Power Oracle 200E unit (system controller)

k. Relay control and logic (driven from system controller)

l. Housekeeping DC power supply

m. External charger contactor

n. External load contactor

o. Battery contactor

p. Battery breaker (100A DC curve)

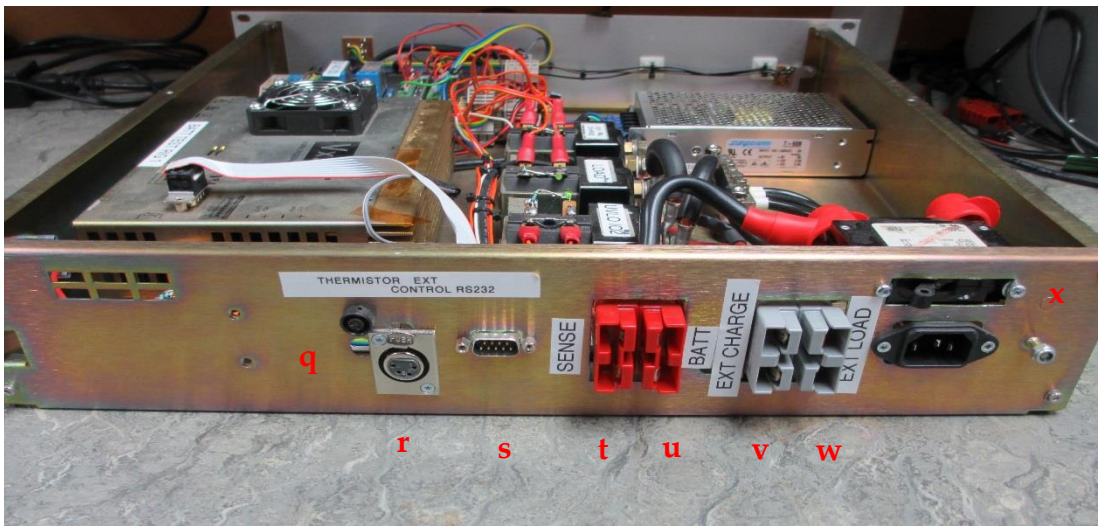

Figure 173. Rear of AMM-1 battery cycler showing connections to other modules

Key to figure 173.

q. Battery temperature sense thermistor connector

r. External equipment control (switched 24V DC)

s. RS232 port

t. Battery voltage sense

u. Main battery connector (charge and load)

v. External charger connector

w. External load connector

x. Battery breaker (100A DC)

Figure 174 show shows the block diagram of the cycler module, figure 175 the block diagram of the VxI Oracle 200E unit with the cycler schematic in figure 176.

15.1.2.1 AMM-1 Battery cycler and controller block diagram

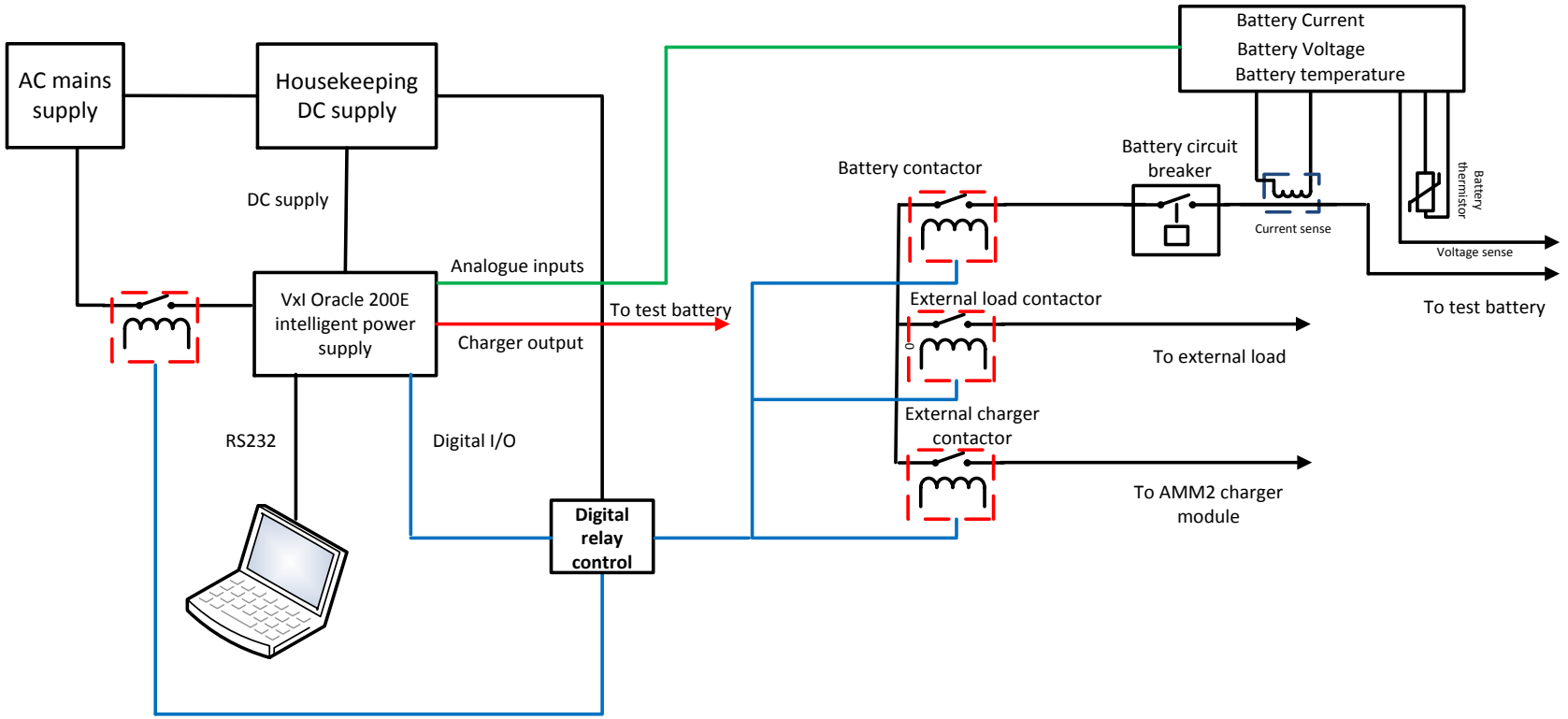

Figure 174. AMM-1 Battery cycler and controller block diagram

15.1.2.2 VxI Power Oracle 200E power supply block diagram (system controller)

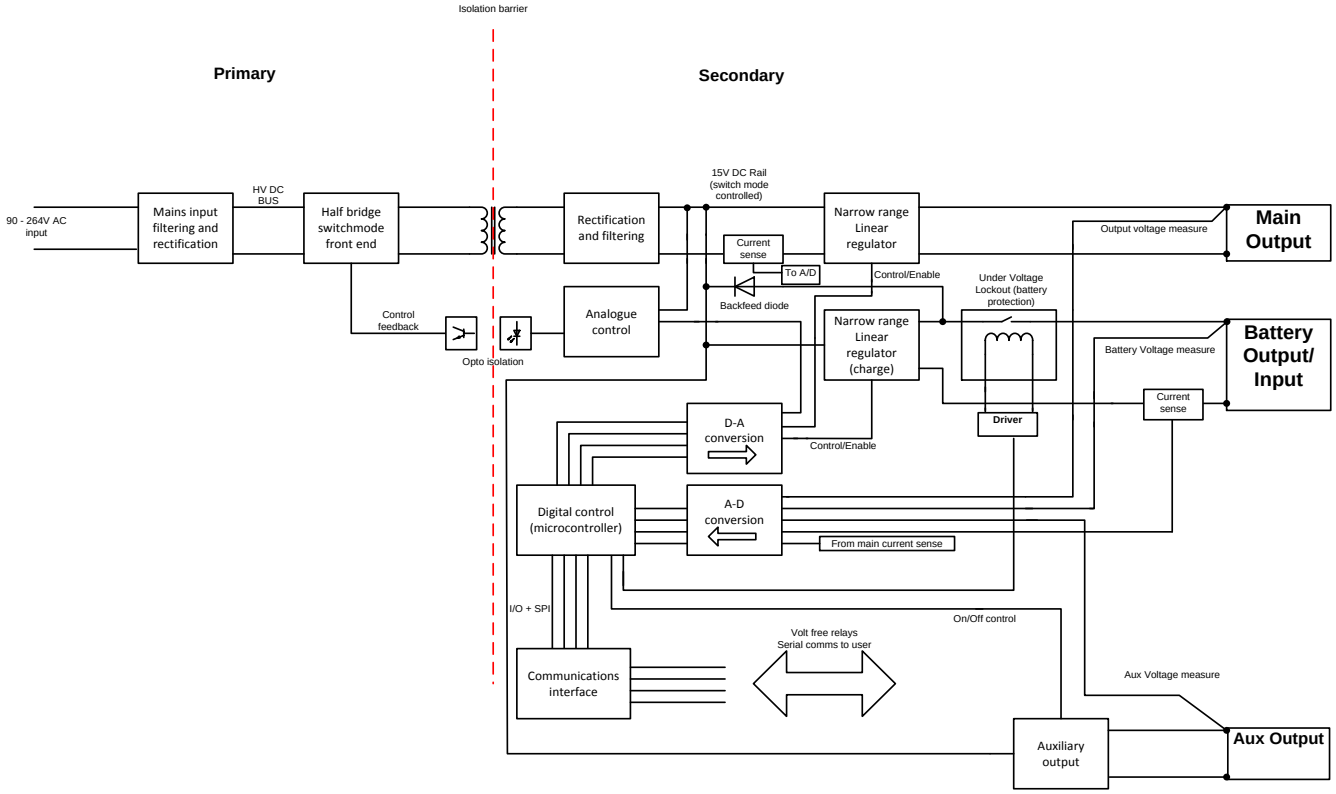

Figure 175. Block diagram – VxI Oracle 200E psu (system controller)

15.1.2.3 AMM-1 Battery cycler and controller schematic

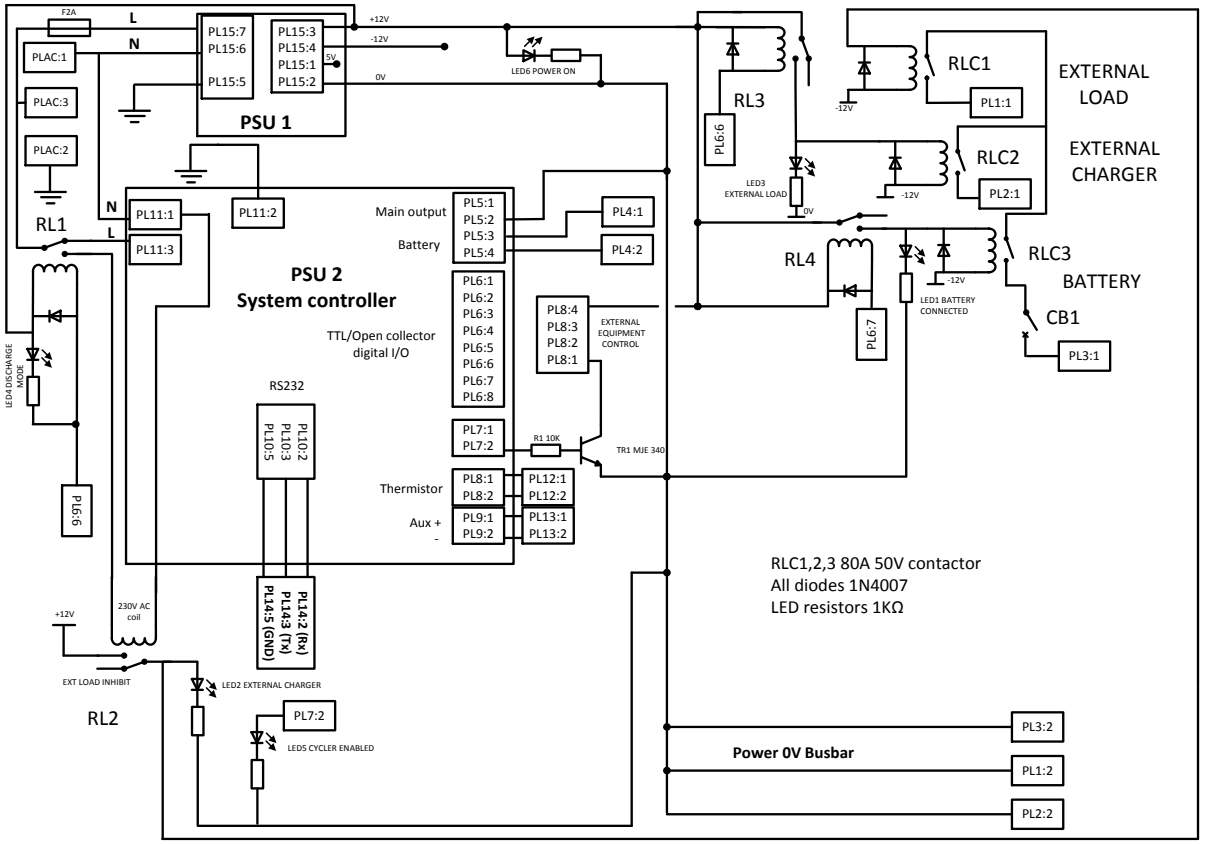

Figure 176. AMM-1 Battery cycler and controller schematic

15.1.3 AMM-2 12V 35A Battery charger

The AMM-2 module (figure 177) comprises a 3 stage microprocessor controller cyclic battery charger and is used for recharging the battery during cycler tests, operating in parallel with the on-board charger of the AMM-1 battery cycler. Charging is automatic and temperature compensated with an optional "Equalise" charge mode that can be enabled periodically for flooded batteries. Figure 178 shows the with the block diagram for the module.

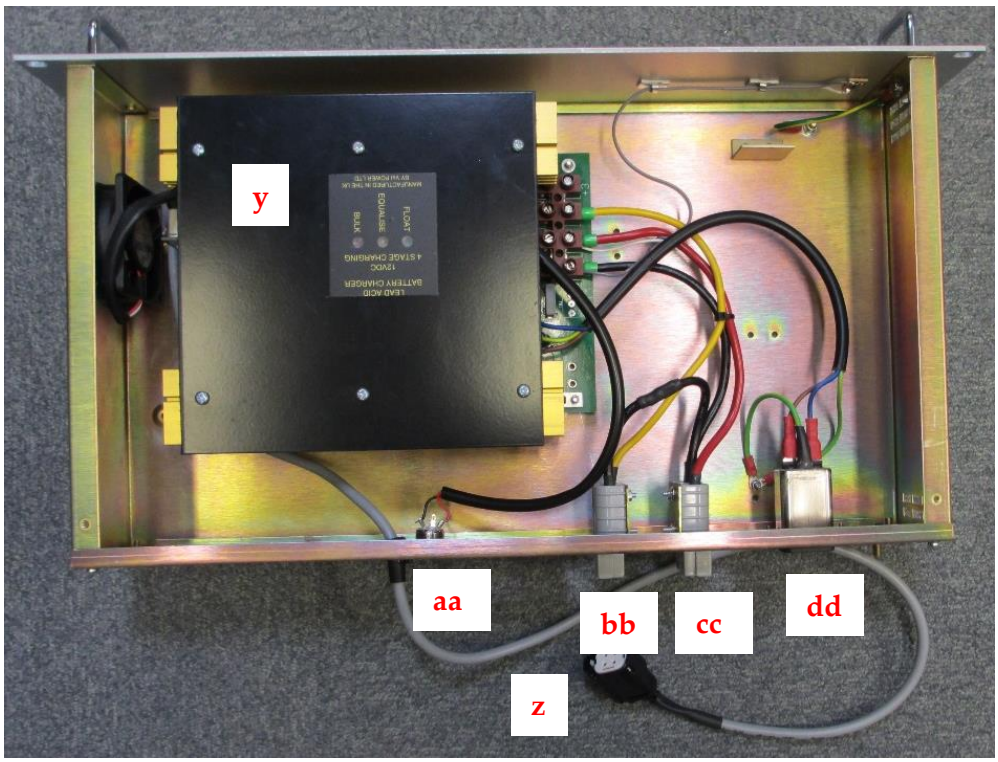

Figure 177. AMM-3 bulk battery charge module internal view

Key to figure 177.

y. Charger electronics

z. Display cable (RS232) or to host computer.

aa. Battery temperature sense thermistor

bb. Not used

cc. Charger output

dd. AC mains input

15.1.3.1 AMM-2 12V 35A Battery charger block diagram

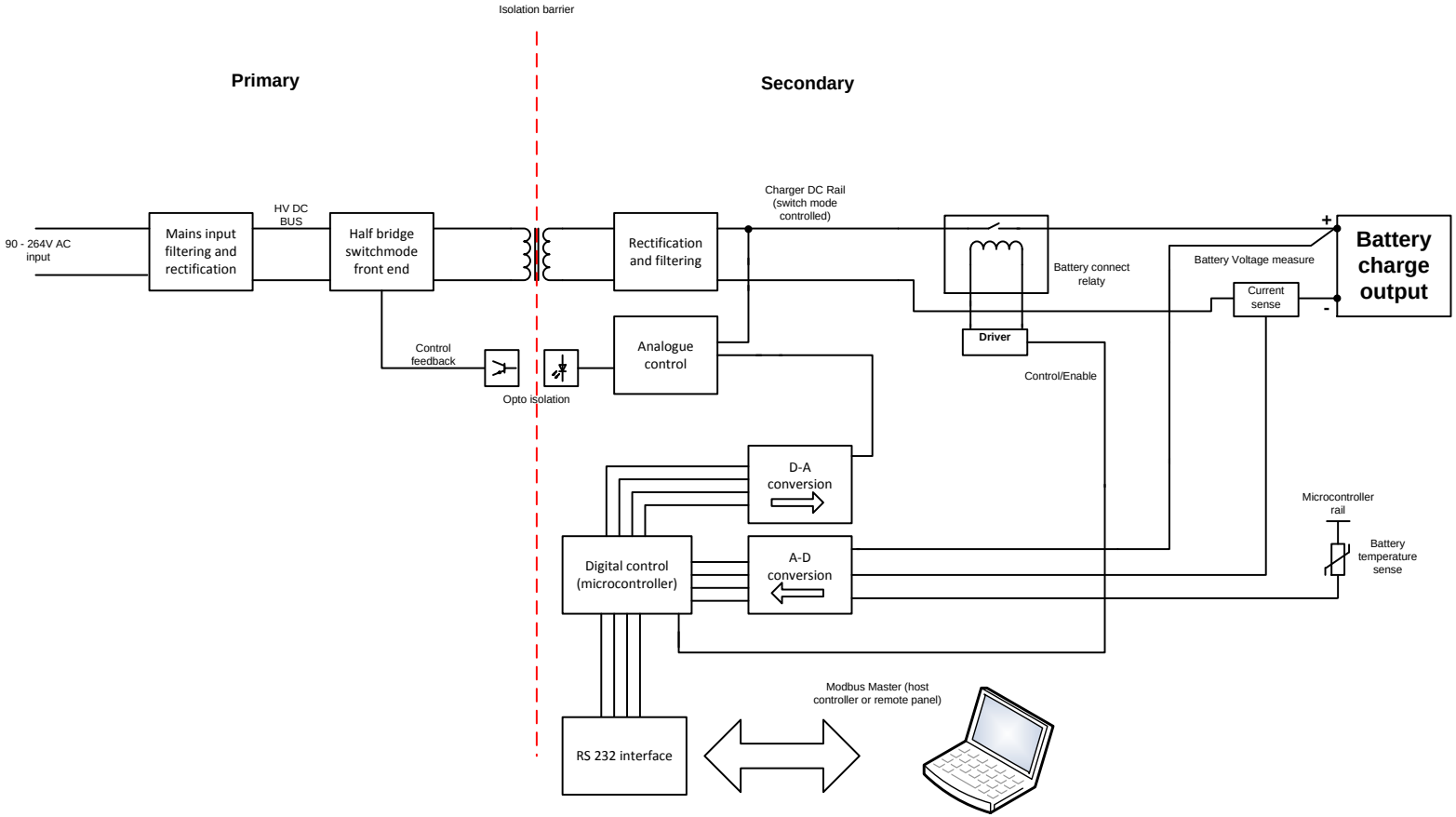

Figure 178. AMM-4 12V 35A Battery charger block diagram

15.2 AMM-3 Tri-mode PRBS battery test module

The AMM-3 module comprises the perturbation and power stages of the PRBS test equipment. Complementary charge and load power stages are provided which nominally provide +/-4A current source/sink to the test battery, but are further programmable up to +/-10A. The power stage can operate in charge, discharge or bipolar modes, at frequencies up to 5 kHz.

Perturbation signal is provided by either external signal input, or via internal microcontroller.

Figure 179 shows the block diagram for the module with schematics in figures 180-182.

15.2.1 AMM-3 Tri-mode PRBS battery test module block diagram

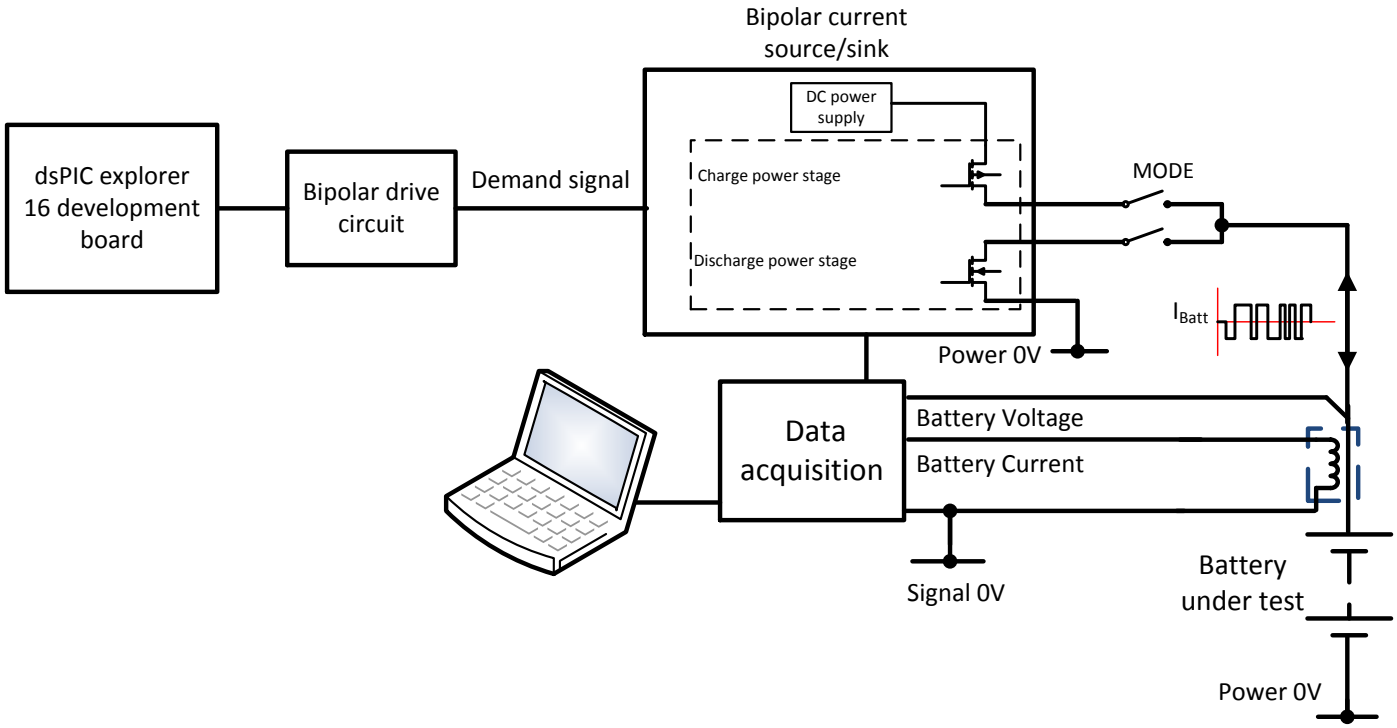

Figure 179. AMM-3 Tri-mode PRBS battery test module block diagram

15.2.2 AMM-3 Tri-mode PRBS battery test module schematic

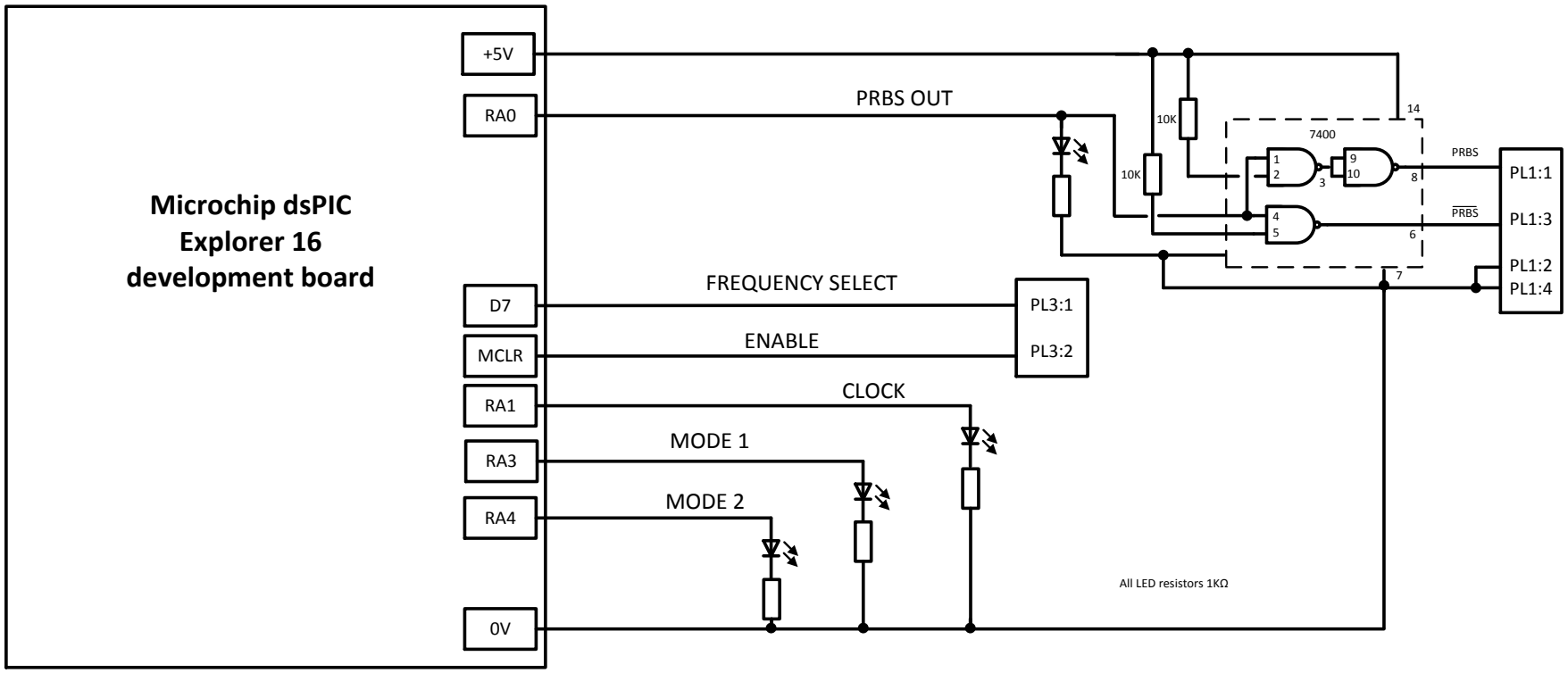

Figure 180. AMM-3 microcontroller board schematic (digital board)

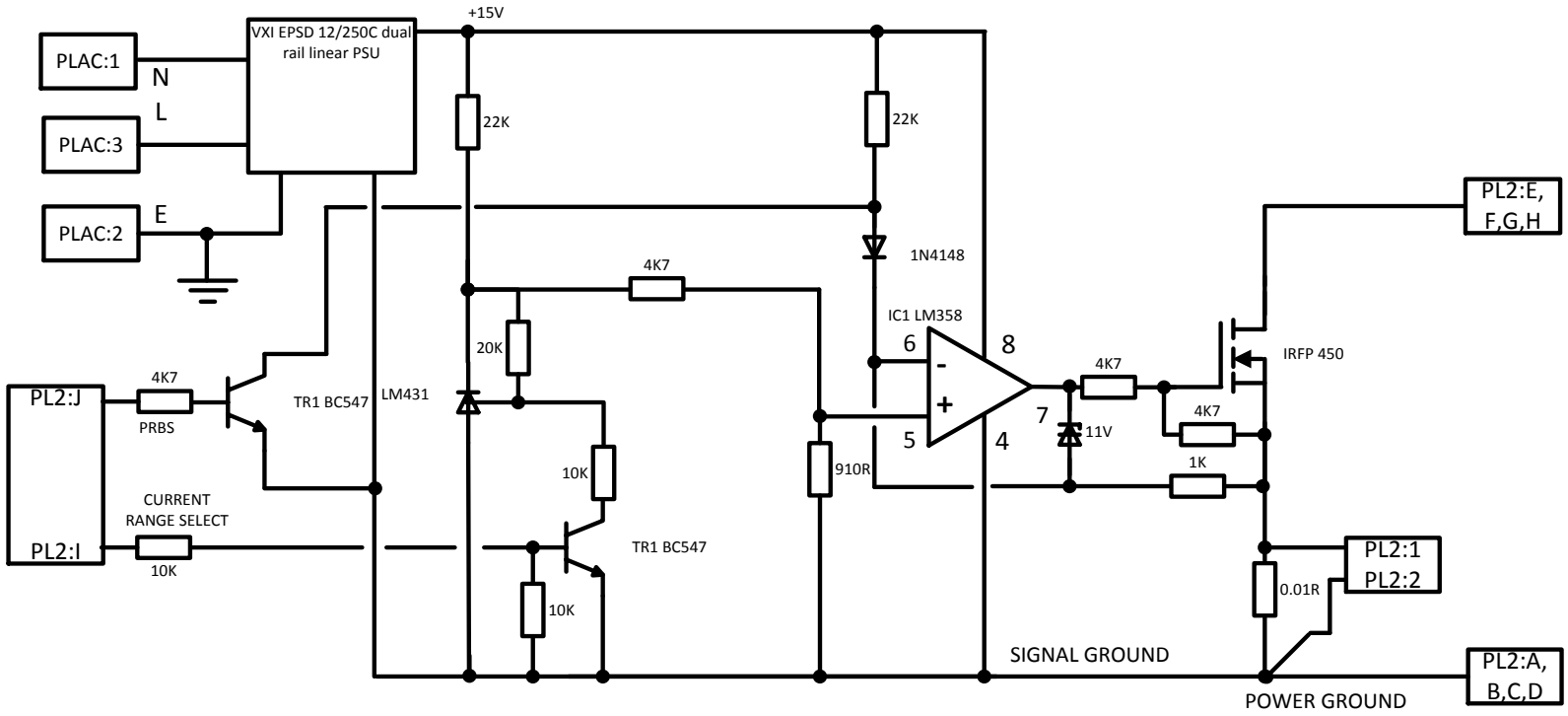

Figure 181. AMM-3 Tri-mode PRBS battery test module schematic (power stage, discharge)

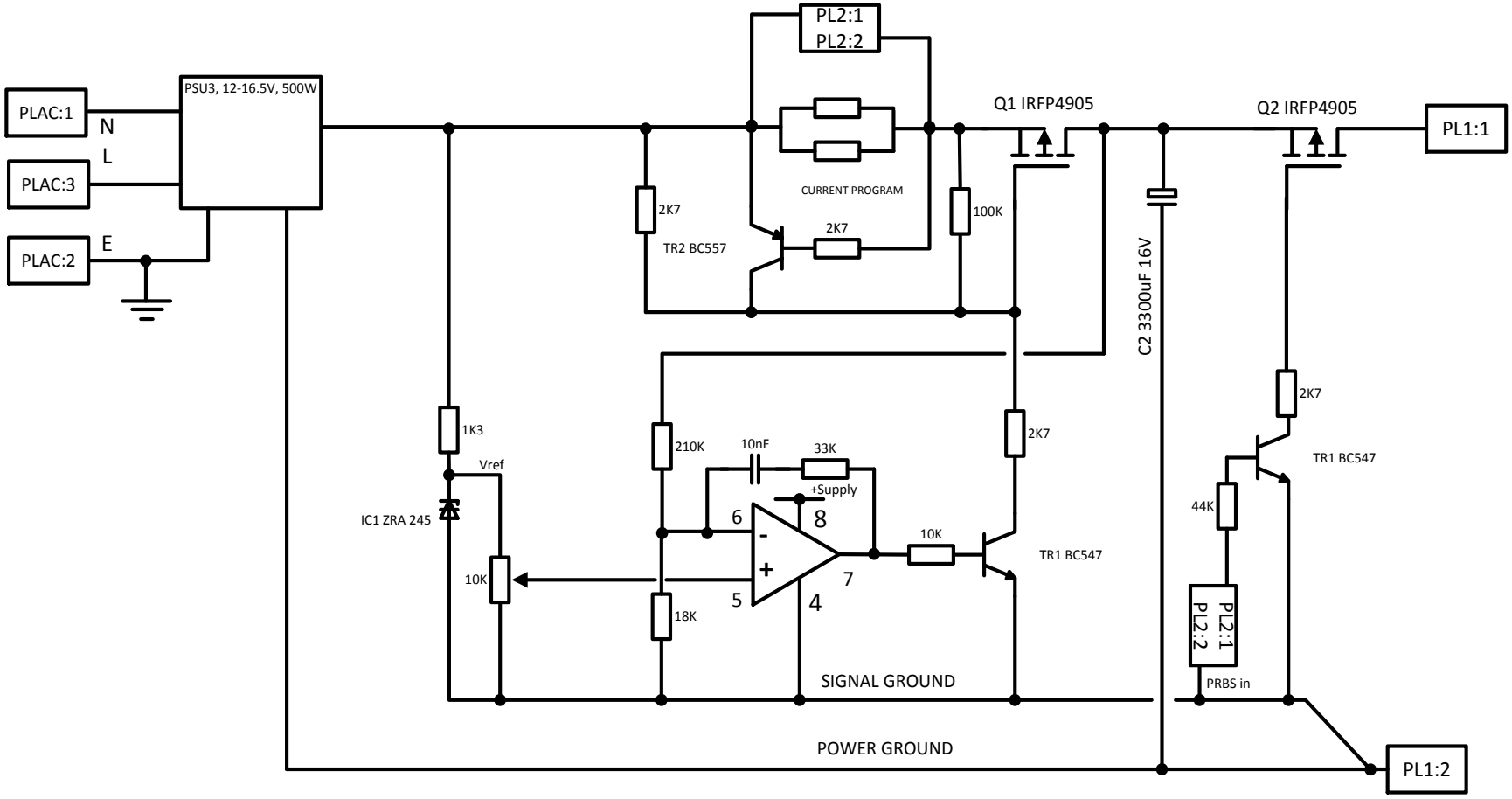

Figure 182. AMM-3 Tri-mode PRBS battery test module schematic (power stage, charge)

15.3 Environmental chambers

The system comprised two environmental chambers, used for long duration heating and cooling tests.

15.3.1 Heat/cool temperature chamber

The environmental chamber (figure 183) used for these tests is a combined heat/cool device with a closed loop PID controller with the ability to be controlled with an external program or profile via LabView™. The heating of the chamber is effected by conventional electrical means, with a fan in the rear of the chamber to distribute the heated or cooled air. Cooling occurs by evaporation of carbon dioxide delivered from pressurised cylinders with internal syphon tubes which ensure that liquid CO_2 is delivered to the pressure reduction matrix within the delivery system.

15.3.1.1 Heat/cool temperature chamber specification

Chamber type	Montford
Controller type	Anglicon
Thermal capacity (Heating)	3kW
Thermal capacity (cooling)	500W (approx.)

Maximum temperature 150°C

Minimum temperature -50°C

Figure 183. Photograph of Heat/Cool temperature chamber

15.3.2 Long duration low temperature test chamber

The long duration low temperature test chamber (figure 184) was used for longer duration tests at low temperature. The downside of the conventional environmental chamber is that a gaseous refrigerant is consumed. The issues with this are two fold, in that the tests become expensive, and secondly the

refrigerant may not last for the duration of the test. An alternative approach was developed using a domestic freezer and an industrial PID temperature controller. Employing a solid state relay as the switching element, the controller interrupts the supply to the freezer to effect temperature control. During the initial cooling phase a thermocouple connected to the controller hangs in free air within the freezer compartment. After the batteries are introduced to the chamber the thermocouple can be attached to the negative battery terminal in order to improve the response of the system.

Although this chamber provides no positive heating, the differential between the internal and external temperatures allows the necessary control to be maintained by relying on thermal losses of the appliance insulating material.

15.3.2.1 Extended low temperature chamber specification

Chamber type

VxI Power design using domestic freezer with external PID controller

Thermal capacity (cooling)

60W

Internal volume

60 litres

Controller

CAL 9900 PID controller with solid state relay control of chamber compressor.

RS232 port for data logging and cool profile

Maximum temperature 0°C

Minimum temperature -30°C

Figure 184. (a) Photograph of extended low temperature chamber, and (b) battery in situ within the chamber with thermocouple attached

15.4 Peripheral test hardware

15.4.1 Timed discharge apparatus

The timed discharge apparatus was built to increase the capacity of the test hardware, in that it was used to carry out controlled discharges from test batteries whilst the AM-1 system was otherwise engaged with longer duration tests. The overall simplicity of the equipment was a design requirement, in that setup would be minimal, and a battery could be connected and the discharge started from a single button without interaction of a host computer or control system. The system photograph is shown in figure 185, with the block diagram shown in figure 186.

Figure 185. Timed discharge apparatus photograph

15.4.1.1 Timed discharge apparatus block diagram

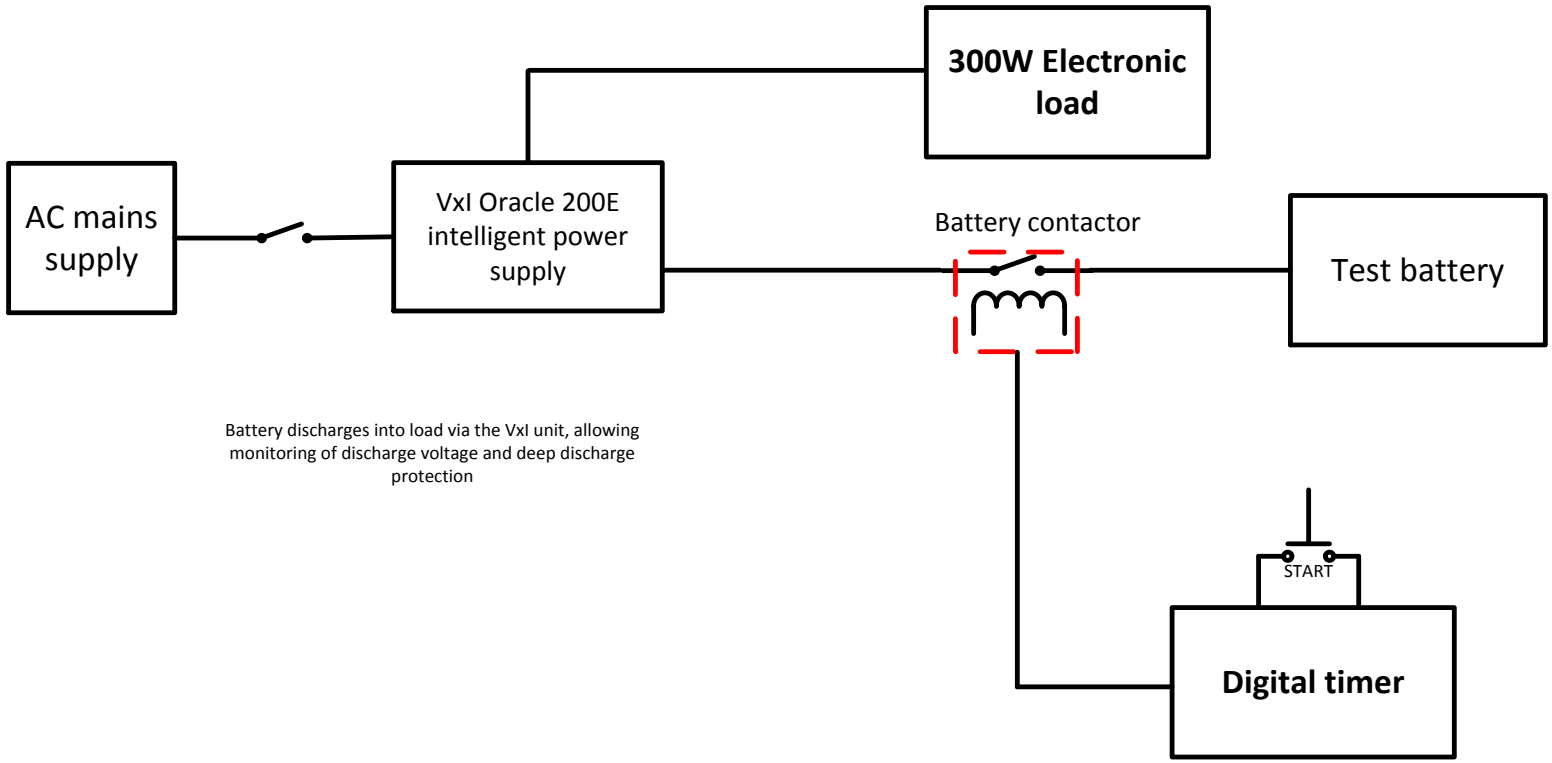

Figure 186. Timed discharge apparatus block diagram

15.5 Embedded PRBS battery test system

The embedded PRBS battery test system digital hardware (figure 187, 188) was based around a Microchip PIC Explorer 16 development board, using a dsPIC33fJ256GP710A. An external SPI flash memory chip (Amic A25L032) was used on a PICTAIL™ prototype card plugged into the main board, which served as storage for the acquired battery test data, which was subsequently imported back into the dsPIC™ for FFT analysis and filtering.

External to the microcontroller card, signal conditioning was provided, incorporating differential measurement including DC offset to improve the system resolution.

The power stage used for the system was the hardware described in 15.2.

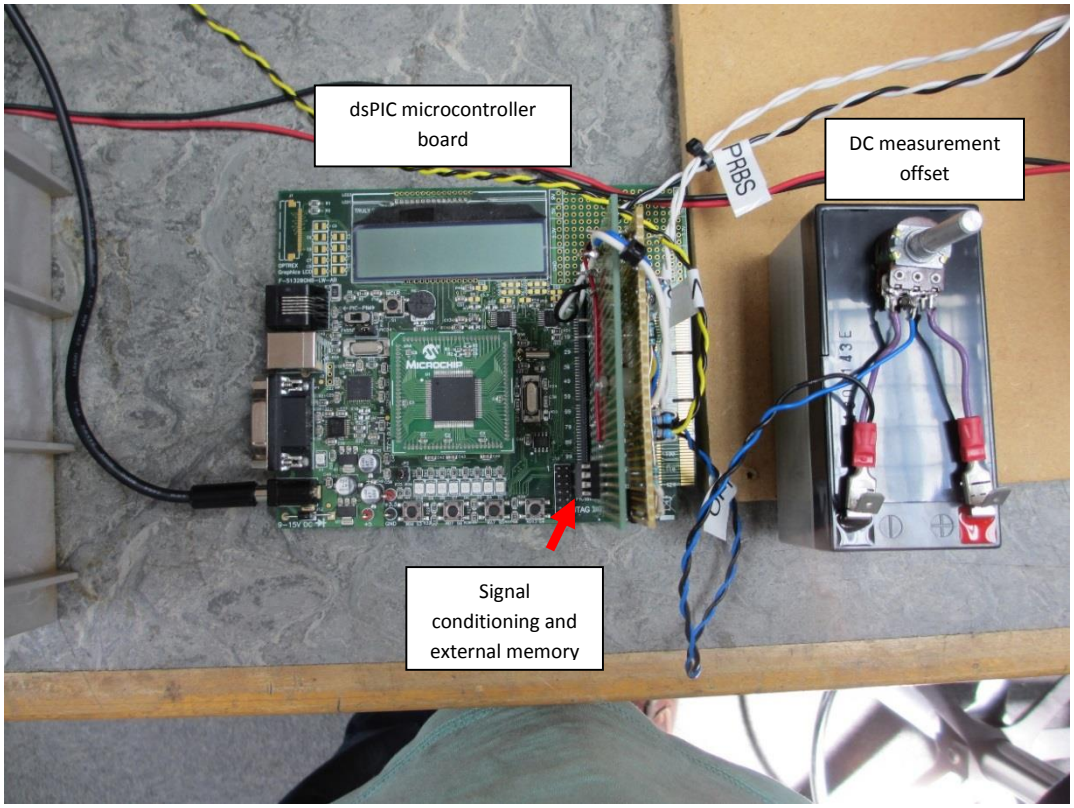

Figure 187. Embedded PRBS test system photograph (power stage not shown)

15.5.1 Embedded PRBS test system circuit diagram

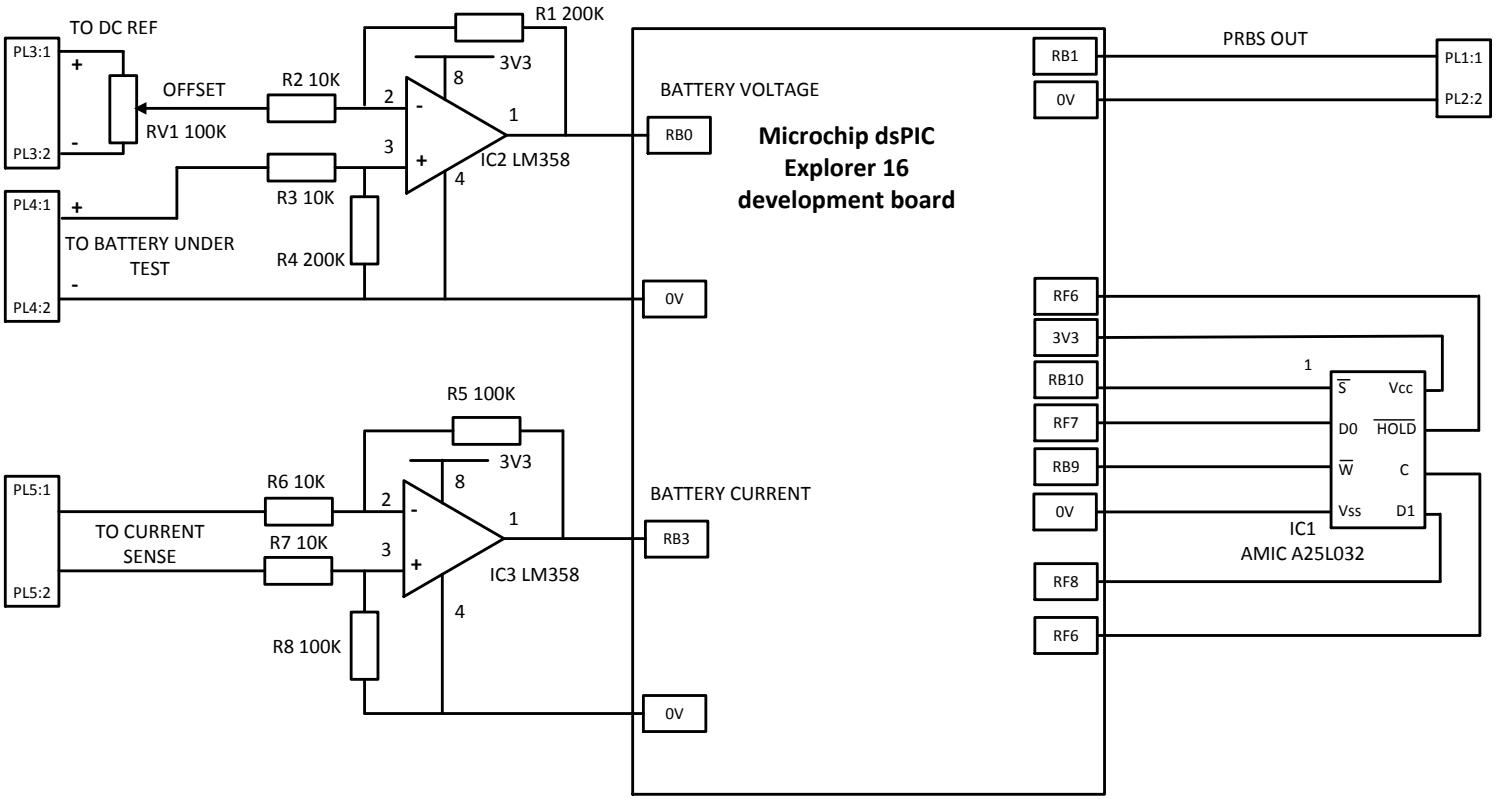

Figure 188. Embedded PRBS test system circuit diagram

15.6 IoTech Daqbook 200 data acquisition system specification

General

Power Consumption
620 mA @ 12 VDC
Operating Temperature: 0° to 50°C
Storage Temperature: 0° to 70°C
Humidity: 0 to 95% RH, non-condensing
Dimensions: 285 mm W x 220 mm D x 35 mm H
(11" x 8.5" x 1.375")
Weight: 2.2 kg (5 lbs)

A/D Specifications

Type: Successive approximation
Resolution: 16 bit
Conversion Time: 8 µs
Monotonicity: No missing codes
Linearity: ±1 bit
Zero Drift: ±10 ppm/°C max
Gain Drift: ±30 ppm/°C max

Sample & Hold Amplifier

Acquisition Time: 2 µs
Aperture Uncertainty: 100 ps

Analog Inputs

Channels: 16 single-ended, 8 differential, expandable up to 256 differential; single-ended/differential operation is software programmable per system
Connector: DB37 male, P1
Resolution: 16 bits
Accuracy: ±0.025% FS
Ranges
Unipolar/bipolar operation is software programmable on a per-channel basis
Unipolar: 0 to +10V, 0 to +5V, 0 to +2.5V, 0 to +1.25V
Bipolar: ±5V, ±2.5V, ±1.25V, ±0.625V
Maximum Overvoltage: 30 VDC
Input Current
Differential: 150 pA typ; 0.2 µA max
Single-Ended: 250 pA typ; 0.4 µA max
Input Impedance: 100M Ohm in parallel with 100 pF
Gain Temp. Coefficient: 3 ppm/°C typ
Offset Temp. Coefficient: 12 µV/°C max

Triggering

Analog Trigger
Programmable Level Range: 0 to ±5V
Trigger to A/D Latency: 10 µs max
Digital Trigger
Logic Level Range: 0.8V low/2.2V high
Trigger to A/D Latency: 10 µs max
Software Trigger
Trigger to A/D Latency: Dependent on PC
Pre-Trigger: Up to 65,536 scans

Sequencer

Randomly programmable for channel and gain on unipolar/bipolar ranges
Depth: 512 location
Channel to Channel Rate: 10 µs/channel, fixed
Maximum Repeat Rate: 100 kHz
Minimum Repeat Rate: 10 hours
Expansion Channel Sample Rate:
Same as on-board channels, 10 µs/channel

Analog Outputs

Channels: 2
Connector: DB37 male, P1
Resolution: 12 bits

Voltage Ranges: 0 to 5 VDC with built-in reference;
0 up to ±10 VDC with external reference
Maximum Output Current: 10 mA

General Purpose Digital I/O

24 I/O channels, expandable up to 192
Connector: DB37 male, P2
Device: 82C55
Output Voltage Levels
Minimum "1" Voltage: 3.0 @ 2.5 mA sourcing
Maximum "0" Voltage: 0.4 @ 2.5 mA sinking
Output Current
Maximum Source Current: 2.5 mA
Maximum Sink Current: -2.5 mA
Input Voltage Levels
Minimum Required "1" Voltage Level: 2V
Maximum Allowed "0" Voltage Level: 0.8V
Output Float Leakage Current: 10 µA

High-Speed Digital Inputs

16 input lines
Connector: DB37 male, P3
Maximum Sampling Rate: 100 Kwords/s
Input Low Voltage: 0.8V max
Input High Voltage: 2V min
Input Low Current: 10 nA
Input High Current: -10 µA

Counter/Timer

5 counter/timer channels
Connector: DB37 male, P3
Frequency/Pulse Counting Mode:
Up or down, binary or BCD
Maximum Pulse Count: 80-bit binary
(5 channels cascaded)
Maximum Input Rate: 7 MHz
Minimum High Pulse Width: 70 ns
Minimum Low Pulse Width: 70 ns
On-board Time Base: 1 MHz

15.7 Battery and capacitor datasheets

15.7.1 Yuasa NPL65-12i datasheet

Data Sheet

NPL-Series - Valve Regulated Lead Acid Battery

NPL65-12I (FR)

SPECIFICATIONS		
Nominal voltage	12	V
20-hr rate Capacity to 10.5V at 20°C	65	Ah
10-hr rate Capacity to 10.8V at 20°C	57.2	Ah
DIMENSIONS		
Length	350 (±0.7)	mm
Width	166 (±0.5)	mm
Height	174 (±0.5)	mm
(height over terminals)	N/A	mm
Mass (typical)	23.0	kg
TERMINAL TYPE		
Female threaded terminal	M6	mm
Torque	4.8	Nm
OPERATING TEMPERATURE RANGE		
Storage (in fully charged condition)	-20°C to +50°C	
Charge	-15°C to +50°C	
Discharge	-20°C to +60°C	
STORAGE		
Capacity loss per month at 20°C (approx)	-3	%
CASE MATERIAL		
Standard Option	ABS (UL.94:HB)	
Flame retardant option (FR)	ABS (UL94:V0)	
CHARGE VOLTAGE		
Float charge voltage at 20°C	13.65 (±1%) 2.275 (±1%)	V V/cell
Float Charge voltage temperature correction factor (for variations from the standard 20°C)	-3	mV/cell/°C
Cyclic (or Boost) charge at 20°C	14.5 (±3%) 2.42 (±3%)	V V/cell
Cyclic Charge voltage temperature correction factor (for variations from the standard 20°C)	-4	mV/cell/°C
CHARGE CURRENT		
Float charge current limit	No limit	A
Cyclic (or Boost) charge current limit	16.25	A
MAXIMUM DISCHARGE CURRENT		
1 second	800	A
1 minute	500	A
SHORT-CIRCUIT CURRENT & INTERNAL RESISTANCE		
(according to EN IEC 60896-21)		
Internal resistance	10.51	mΩ
Short-Circuit current	1375	A
IMPEDANCE		
Measured at 1 kHz	5	mΩ
PERFORMANCE & CHARACTERISTICS		
Refer to the technical manual	NPL	
DESIGN LIFE		
EUROBAT Classification: High performance	10 to 12	years
Yuasa design life @ 20°C	up to 10	years
SAFETY		
Installation Can be installed and operated in any orientation except permanently inverted		
Handles Batteries must not be suspended by their handles (where fitted)		
Vent valves Each cell is fitted with a low pressure release valve to allow gasses to escape and then reseal.		
Gas Release VRLA Batteries release hydrogen gas which can form explosive mixtures in air. Do not place inside a sealed container		
Recycling YUASA's VRLA batteries must be recycled at the end of life in accordance with local and national laws and regulations		

LAYOUT

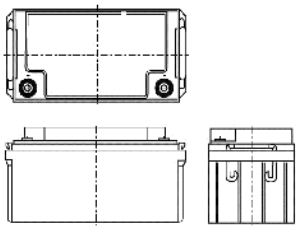

This battery type must never be installed permanently suspended by their handles

3RD PARTY CERTIFICATIONS

ISO 9001 - Quality Management Systems
ISO 14001 - Environmental Management Systems
EN 18001 - OHSAS Management Systems
UNDERWRITERS LABORATORIES Inc.

STANDARDS

IEC61056
IEC60896-21/22

ALL DATA IS SUBJECT TO CHANGE WITHOUT NOTICE
Issue No.: V.3 / Issue Date: September 2012

YUASA BATTERY SALES UK LTD.
Unit 13, Hunts Rise
South Marston Industrial Estate
Swindon
SN3 4TG
UK

www.yuasaeurope.com NPL

15.7.2 Maxwell PC2500 Ultracapacitor datasheet

Features:

- Delivers up to 100 times the energy of conventional capacitors and delivers ten times the power of ordinary batteries
- Is optimized for individual applications through its capacity to repeatedly charge and discharge
- Designed for smaller and lighter-weight products
- Offers instantaneous ride-through power
- UL recognized

PC2500

BOOSTCAP® Ultracapacitor

BOOSTCAP® Ultracapacitors provide extended power availability, allowing critical information and functions to remain available during dips, sags, and outages in the main power source. In addition, it can relieve batteries of burst power functions, thereby reducing costs and maximizing space and energy efficiency. The ultracapacitor features a cylindrical design and an electrostatic storage capability that can cycle hundreds of thousands of charges and discharges without performance degradation.

BATTERY vs. ULTRACAPACITOR vs. CAPACITOR COMPARISON

Available Performance	*Lead Acid Battery*	*Ultracapacitor*	*Conventional Capacitor*
Charge Time	1 to 5 hours	0.3 to 30 seconds	10-3 to 10-6 seconds
Discharge Time	0.3 to 3 hours	0.3 to 30 seconds	10-3 to 10-6 seconds
Energy (Wh/kg)	10 to 100	1 to 10	<0.1
Cycle Life	1,000	>500,000	>500,000
Specific Power (W/kg)	<1000	<10,000	<100,000
Charge/discharge efficiency	0.7 to 0.85	0.85 to 0.98	>0.95

15.7.3 Wima Supercap R datasheet

WIMA SuperCap R

Double-Layer Capacitors in Rectangular Metal Case with very High Capacitances in the Farad Range

Special Features

- Storage capacitors with very high capacitance values from 100 F to 600 F and a rated voltage of 2.5 VDC
- Discharge current up to 800 A
- Maintenance-free
- With rectangular metal case
- Series connection possible
- According to RoHS 2002/95/EC

Typical Applications

Suitable for support, protection or replacement of batteries in the field of new traction technologies in

- Automotive
- Railway technology
- Wind power systems
- Uninterruptible power systems (UPS)

Construction

Internal construction:

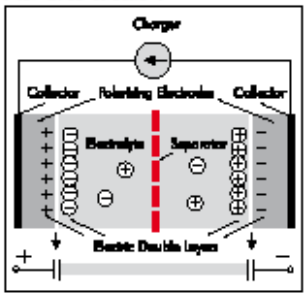

Encapsulation:
Rectangular aluminium case, sealed by laser welding
Terminations:
FS 6.3 slip-on terminations according to DIN 46244.
Marking:
Colour: Black. Marking: Gold

Technical Data

Capacitance:	C_N	**100 F**	**200 F**	**300 F**	**400 F**	**600 F**
Capacitance tolerance:	–	±20%	±20%	±20%	±20%	±20%
Rated voltage:	U_R	2.5 V	2.5 V	2.5 V	2.5 V	2.5 V
Rated current:	I_C	30 A	45 A	50 A	80 A	100 A
Pulse current:	I_P	up to 200 A	up to 350 A	up to 400 A	up to 600 A	up to 800 A
Internal resistance:	R_{DC}	12 mΩ	7 mΩ	6 mΩ	4 mΩ	3 mΩ
Max. stored energy: ±20%	$E_{max.}$	313 J	625 J	938 J	1250 J	1875 J
Operating temperature:	T_{op}	–30° C ... +65° C				
Storage temperature:	T_{st}	–40° C ... +70° C				
Weight:	m	40 g	62 g	90 g	95 g	120 g
Volume:	V	0.028 l	0.047 l	0.075 l	0,075 l	0,1 l

Additional Data

Case:	–	$Al_{99.5}$	$Al_{99.5}$	$Al_{99.5}$	$Al_{99.5}$	$Al_{99.5}$
Lug terminals:	–	Brass	Brass	Brass	Brass	Brass

Comparative Data

Density of capacitance:						
gravimetric	C_d	2500 F/kg	3200 F/kg	3400 F/kg	4300 F/kg	6400 F/kg
volumetric	C_V	3600 F/l	4600 F/l	4400 F/l	5900 F/l	6660 F/l
Energy density:						
gravimetric	E_d	2.2 Wh/kg	2.8 Wh/kg	3.0 Wh/kg	3.8 Wh/kg	4.5 Wh/kg
volumetric	E_V	3.2 Wh/l	3.7 Wh/l	4.0 Wh/l	5.4 Wh/l	6.0 Wh/l

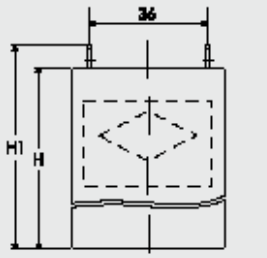

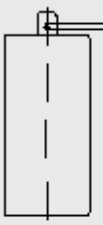

Capacitance	W	H	H1	L
100 F	16.5	36	45	48
200 F	16.5	59	66	48
300 F	26.5	59	66	48
400 F	26.5	59	66	48
600 F	26.5	80	87	48

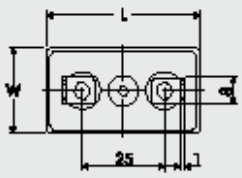

Dims. in mm.

Lug terminals for 6.3 mm slip-on connection.

When connected in series cases should be kept isolated.

New values

11.08

15.7.4 Furukawa FTZ12-HEV UltraBattery data

Operating voltage window	14.7 to 10.5V
Max voltage	16V
Discharge end voltage at 1C rate	10.02V (@ 20°C)
Float Voltage	13.62 V (@ 20°C)
Float Current, after 24 hr at 13.62V	9.3 mA
Charge Regulation Voltage	14.7 V
Maximum Charge Current	20 A
Maximum Pulse Current	80 A
Maximum Constant Current	20 A
DC Ohmic resistance	20 mΩ (@ 25°C)
Capacity, 1C rate to 10.5V	7.8 Ah
Energy density	30 Wh/kg 77Wh/L
Dimensions, (mm)	110 x 87 x 150
Mass	3.787 kg

15.7.5 Continental batteries CTX-9 battery data

Battery type	AGM maintenance free battery
Voltage	12V
Dimensions	150mm x 87mm x 105 mm
Capacity rating	8Ah
Cold-start performance CCA (EN)	120A

Information obtained from manufacturer's website [170].

15.8 MATLAB code

15.8.1 sdm1a.m

```
%%%%%%%%%%%%%%%%%%%%%%
% Filename sdm1a.m
% Date 03/07/09
% Sampled data model of Randle's battery model
% used to rapidly generate PRBS data
% Randle's model is represented in state-variable format
%%%%%%%%%%%%%%%%%%%%%%
% Generates a PRBS and applies it to the battery model
%%%%%%%%%%%%%%%%%%%%
%%%%%%%%%%%%%%%%%%%%

%Ri     Randles model parameter
%Rt     Randles model parameter
%Cs     Randles model parameter
%Cb     Randles model parameter
%Rd     Randles model parameter
%N      PRBS bit length
%t_prbs PRBS time clock pulse period

function sdm_1a(Ri,Rt,Cs,Rd,Cb,N,t_prbs);
%number of samples per pulse period
n_sam=60

%actual simulation time step
t_step=t_prbs/n_sam

%total number of samples
n_tot=(2^N-1)*n_sam

%initial prbs sequence
disp('Generating PRBS')
%call mls - generates the PRBS sequence
prbs1=mls(N);

%generate actual sequence taking sampling into account
%prbs2 is the prbs input to the model
prbs2(1:n_tot)=0;
for ind1=0:(2^N-2)
    for ind2=1:n_sam
        prbs2(n_sam*ind1+ind2)=prbs1(ind1+1);
    end
end

%%%%%%%%%%%%%%%%%%%%
%model matrices
%state vector is x=[vcs,vcb]

A=[-1/(Cs*Rt),0;0,-1/(Cb*Rd)]
B=[1/Cs;1/Cb]
C=[1 1]
```

```
D=Ri

I=expm(A*t_step)
R=inv(A)*(I-eye(2))*B

%%%%%%%%%%%%%%%%%%%
%sampled data loop to generate data
%initialise voltage vector
Vbat(1:n_tot)=0;

%initial conditions
x_prev=[0;0]

%perform voltage calculation
for ind=2:n_tot
    x_next=I*x_prev+R*prbs2(ind);
    Vbat(ind)=C*x_next+D*prbs2(ind);
    x_prev=x_next;
end

time=(0:n_tot)*t_step;

%%%%%%%%%%%%%%%%%%%%%%%%%%%%%%%%%%
% Analyse data

%plot time waveform and fft of vbat
%plot(time,Vbat)
%xlabel('Time (s)')
%ylabel('Battery terminal voltage (V)')

%extract impedance response from data using ffts
figure
[in]=four(time,prbs2',0);
xlabel('Frequency (Hz)')
%ylabel('FFT of Iin')
set(gca,'XScale','log')

figure
[out]=four(time,Vbat',0);
xlabel('Frequency (Hz)')
%ylabel('FFT of VBat')
set(gca,'XScale','log')

in=in';
out=out';
w=in(:,1);
min=in(:,2);
mout=out(:,2);
mag=mout./min;
figure
plot(w/2/pi,mag)
xlabel('Frequency (Hz)')
%ylabel('Z')
set(gca,'XScale','log')
axis([0,1000,0,0.015]);
grid
```

15.8.2 mls.m

```
%Generates a Maximum Length Sequence of n bits by utilizing a
%linear feedback shift register with an XOR gate on the tap
bits
%
%Function can accept bit lengths of between 2 and 24
%
%y is a vector of 1's & -1's that is (2^n)-1 in length.
%
%optional flag is:

%  1 for an initial sequence of all ones (repeatable)
%  0 for an initial sequence that is random (default)
%
%
%reference:
%   Davies, W.D.T. (June, July, August, 1966). Generation and
%properties of maximum-length sequences. Control, 302-4, 364-
5,431-3.
%
%Spring 2001, Christopher Brown, cbrown@phi.luc.edu

%n=bit length of PRBS
function  y = mls(n,flag)
flag=0;

switch n            %assign taps which will yield a maximum
case 2              %length sequence for a given bit length
   taps=2;
   tap1=1;          %there's a list of appropriate tap values in
   tap2=2;          %Vanderkooy, JAES, 42(4), 1994.
case 3
   taps=2;
   tap1=1;
   tap2=3;
case 4
   taps=2;
   tap1=1;
   tap2=4;
case 5
   taps=2;
   tap1=2;
   tap2=5;
case 6
   taps=2;
   tap1=1;
   tap2=6;
case 7
   taps=2;
   tap1=1;
   tap2=7;
case 8
   taps=4;
   tap1=2;
   tap2=3;
   tap3=4;
```

```
   tap4=8;
case 9
   taps=2;
   tap1=4;
   tap2=9;
case 10
   taps=2;
   tap1=3;
   tap2=10;
case 11
   taps=2;
   tap1=2;
   tap2=11;
case 12
   taps=4;
   tap1=1;
   tap2=4;
   tap3=6;
   tap4=12;
case 13
   taps=4;
   tap1=1;
   tap2=3;
   tap3=4;
   tap4=13;
case 14
   taps=4;
   tap1=1;
   tap2=3;
   tap3=5;
   tap4=14;
case 15
   taps=2;
   tap1=1;
   tap2=15;
case 16
   taps=4;
   tap1=2;
   tap2=3;
   tap3=5;
   tap4=16;
case 17
   taps=2;
   tap1=3;
   tap2=17;
case 18
   taps=2;
   tap1=7;
   tap2=18;
case 19
   taps=4;
   tap1=1;
   tap2=2;
   tap3=5;
   tap4=19;
case 20
   taps=2;
   tap1=3;
   tap2=20;
case 21
```

```
   taps=2;
   tap1=2;
   tap2=21;
case 22
   taps=2;
   tap1=1;
   tap2=22;
case 23
   taps=2;
   tap1=5;
   tap2=23;
case 24
   taps=4;
   tap1=1;
   tap2=3;
   tap3=4;
   tap4=24;

otherwise
   disp(' ');
   disp('input bits must be between 2 and 24');
   return
end
if (nargin == 1)
    flag = 0;
end
if flag == 1
    abuff = ones(1,n);
else
    rand('state',sum(100*clock))
    while 1
        abuff = round(rand(1,n));
        %make sure not all bits are zero
        if find(abuff==1)
            break
        end
    end
end

for i = (2^n)-1:-1:1
   i   ;
   xorbit = xor(abuff(tap1),abuff(tap2));       %feedback bit
   if taps==4
      xorbit2 = xor(abuff(tap3),abuff(tap4));
      %4 taps = 3 xor gates & 2 levels of logic
      xorbit = xor(xorbit,xorbit2);
      %second logic level
   end
    abuff = [xorbit abuff(1:n-1)];
    y(i) = (-2 .* xorbit) + 1;
   %yields one's and negative one's (0 -> 1; 1 -> -1)
    xnum=numel(y);
    x=(1:xnum);
    stairs(x,y);
    axis([0,250,-2,2]);
    time=(0:(2^n-2))*(1/500);
    simin.signals.values=y';
    simin.time=time';
end
```

15.8.3 four.m

```
%four.m
%performs FFT on an input signal
%with the specific window function below
%time = time data
%inp = input data
%winder = select window function or not
function out=four(time,inp,winder)
global amp freqout mag
[m,n]=size(inp);
tsam=(time(2)-time(1));
%tsam=time(10)-time(1)
if winder
%window function (hanning)
k=-m/2:m/2-1;
wind=0.5+0.5*cos(2*pi*k/m);
%window function (hamming)
%wind=0.54+0.46*cos(2*pi*k/m);
%window function (blackman)
%wind=0.42-0.6*cos(2*pi*k/(m-1))+0.08*cos(4*pi*k/(m-1));
size(wind);
size(inp);

%performs fft
freqs=fft(wind'.*inp,m)/m;
else
freqs=fft(inp,m)/m;
%extract only positive frequencies
end
if mod(m,2)==0
    n=m/2;
else
    n=(m+1)/2;
end

%magnitude
mag=2*abs(freqs(1:n));
mag(1)=mag(1)/2;

%fundamental frequency of fft or frequency step
w1=2*pi/(tsam*m);
w=0:n-1;
w=w*w1;
freqout=w/2/pi;
amp=20*log10(mag);
figure
plot(freqout,mag);
grid
set(gca,'XScale','log')

%phase
ph=180/pi*unwrap(angle(freqs(1:n)));
size(w);
size(mag);
size(ph);
out=[w;mag';ph'];
```

15.8.4 fourseq.m

```
% fourseq - modified from four.m
% Andrew Fairweather 2008-2014
% checks a selected data set for a clean current FFT
% which in turn checks PRBS is correct
% sampling and clock have no jitter
% a textbook PRBS FFT should be evident
% ref WDT Davies system identification for self adaptive
control
% note plots are for inspection only and are unscaled

function out=fourseq(time,inp,winder,start,sample,N,trim)
length=(N*sample)
start=start+trim;
global indplt1 indplt2 pltnum
finish=start+length
prb=inp(start:finish);
tt=time(start:finish);
ttt=time(start:finish)*25000;
subplot(indplt1,indplt2,pltnum),plot(ttt,prb);
pltnum=pltnum+1
grid
time=time(start:finish);
inp=inp(start:finish);
 [m,n]=size(inp);
tsam=(time(2)-time(1));
if winder
 %window function
 k=-m/2:m/2-1;
 wind=0.5+0.5*cos(2*pi*k/m);
 figure
 plot(wind)
 size(wind);
 size(inp);

 %performs fft
 freqs=fft(wind'.*inp,m)/m;
 else
 freqs=fft(inp,m)/m;
 %extract only positive frequencies
 end
 if mod(m,2)==0
    n=m/2;
 else
    n=(m+1)/2;
end

%magnitude
mag=2*abs(freqs(1:n));
mag(1)=mag(1)/2;

%fundamental frequency of fft or frequency step
w1=2*pi/(tsam*m);
w=0:n-1;
w=w*w1;
freqout=w/2/pi;
amp=20*log10(mag);
```

```
%figure
subplot(indplt1,indplt2,pltnum),plot(freqout,mag);
pltnum=pltnum+1
grid
set(gca,'XScale','log')
finish
%phase
ph=180/pi*unwrap(angle(freqs(1:n)));
size(w);
size(mag);
size(ph);
```

15.8.5 evalprbs.m

```
%%evalprbs1-5 - Andrew Fairweather 17th July 2009
%% this routine evaluates the results of imported data from a
PRBS battery
%% experiment - the length below is used to specify how much
data is used,
%%  and should be set to a data set that corresponds to 1
complete PRBS sequence

%V          voltage data
%I          current data
%time       time
%winder     FFT window select
%ylim       ylimit on outplut plot
%start      data start
%N          PRBS 'N' (N=2^n-1)
%sample     data sample rate
%trim       data trim

function
result=evalprbs5(V,I,time,winder,ylim,start,N,sample,trim,dozca
lc);
start=start+trim;
finish=((N*sample)+start)

close all;

iin=I(start:finish);

vout=V(start:finish);
tout=time(start:finish);
vin=iin;
tin=time(start:finish);

four(tin,vin,winder);

figure;
four(tout,vout,winder);
grid;
axis([0,100,-10,10]);
[infft]=four(tin,vin,winder);
[outfft]=four(tout,vout,winder);
incomp=infft(2,:).*(cos(infft(3,:))+i*sin(infft(3,:)));
outcomp=outfft(2,:).*(cos(outfft(3,:))+i*sin(outfft(3,:)));
tfcomp=outcomp./incomp;

figure;
xxxx=(infft(1,:)/2/pi);
yyyy=(abs(tfcomp));
semilogx(xxxx,yyyy);

axis([0,1000,0,ylim]);
```

```
grid;
xlabel('Hz');
ylabel('Z');

%%  Do Z Calc - this calculates CSurface and Rt from two points
in the results
%%
%%  needs complex impedance so embedded in evalprbs

while dozcalc==1     %option to select this bit of code
%% frequency points in response
%freq1
freq1=10
%freq2
freq2=300
%Find these freqs in the data
n1=find(xxxx>freq1)
n=n1(1)-1
n2=find(xxxx>freq2)
nn=n2(1)-1
% and the corresponding impedance
Zt1=yyyy(n)
Zt2=yyyy(nn)
Znum=(1/(Zt1-Ri))-(1/(Zt2-Ri))
w1=xxxx(n)*2*pi
w2=xxxx(nn)*2*pi
%Csurface
Csurf=Znum/(i*w1-i*w2)
%Rt

XCs1=1/(i*w1*Csurf)
denom=(1/(Zt1-Ri))-1/(XCs1)
Rt=1/denom

else
end
```

15.8.6 find_datastart.m

```
%% find_datastart
%% this finds the start of the PRBS waveform
%% in the acquired test data to allow accurate processesing
%% for all modes of test used in the thesis

%sample = 25000
freq=2
samp = input('Sampling freq khz? ');
mode = input('1=discharge, 2=charge, 3=bipolar, 4=bipolar LF
');
trim = input('at a trim value in single pulses  ');

sample=samp*1000;
header_length=0

%*****************************
 a=data(:,1);
 b=data(:,2);
 c=data(:,3);
 numel(c)
 time=(1:ans)/sample;
 close all
 %*****************************
 if mode==1
 x=a;
 else
 end
 if mode==2
 x=-c+0.15;
 else
 end
 if mode==3
 x=a;
 else
 end
 if mode==4
 x=a;
 freq=0.5
 else
 end
 trim1=trim*sample/freq
 header=(header_length*sample/freq)+trim1

 fin=numel(x)
 % find the rising edge
 d=find(x>0.15);
 rising=d(2)

 % find the falling edge - offset by "header" pushes it into
 the
 %middle of the header bit so the next transition is -ve - the
 start
 XXX=x(header:fin);
 e=find(XXX<0.05);
```

```
falling=e(2)+header

pulsewidth=falling-rising

yfalling=[-0.1 0 0.1 0.2 0.3]
xfalling=[falling falling falling falling falling]
xs=(1:(numel(x)));
start=falling

figure
plot(xs(start:fin/10),x(start:fin/10),xfalling,yfalling)
%plot(xs,x,xfalling,yfalling)
grid
hold on
%%%%%%%%%%%%%%%%%%%%%%%%%%%%%%%%
start=falling
clear yfalling xs xfalling t2 t1 pulsewidth header rising XXX
fin falling
```

15.8.7 crunch1.m

```
% crunch1

% this routine loads matlab workspaces that have been created
% to process battery test data then calls multiprbs which
% processes them to provide impedance responses
% the workspaces contain the raw acquired current and voltage
% data for the PRBS tests time data for the waveforms
% and data start sample point
% workspaces are set up using laterresultssetup.m
% and find_datastart.m
% this code can be modified to process other data workspaces


 close all
 clear time
 clear data
 clear a
 clear b
 clear c
 clear ans
 testnum = input('Which test to evaluate? ');
 global testnum
 if testnum==1
 load('2105141.mat')
 %load 2105141
 else
 end
 if testnum==2
 load('2105142.mat')
 else
 end
 if testnum==3
 load('2105143.mat')
 else
 end
 if testnum==4
 load('2105144.mat')
 %load 2105141
 else
 end
 if testnum==5
 load('2105145.mat')
 else
 end
 if testnum==6
 load('2105146.mat')
 else
 end
 if testnum==7
 load('2105147.mat')
 %load 2105141
 else
 end
 if testnum==8
 load('2105148.mat')
```

```
else
end
if testnum==9
load('2105149.mat')
else
end
if testnum==10
load('21051410.mat')
else
end
if testnum==11
load('21051411.mat')
else
end
if testnum==12
load('21051412.mat')
else
end
if testnum==13
load('21051413.mat')
else
end
if testnum==14
load('21051414.mat')
else
end
if testnum==15
load('21051415.mat')
else
end
if testnum==16
load('21051416.mat')
else
end
if testnum==17
load('21051417.mat')
else
end
if testnum==18
load('21051418.mat')
else
end
if testnum==19
load('21051419.mat')
else
end
if testnum==20
load('21051420.mat')
else
end
if testnum==21
load('21051421.mat')
else
end
if testnum==22
load('21051422.mat')
else
end
if testnum==23
load('21051423.mat')
```

```
else
end
if testnum==24
load('21051424.mat')
else
end
if mod(testnum,2)
   disp('odd')
  multiprbs(a,b,c,time,start,0.1,1,1,0,0)
else
   disp('even')
   multiprbs(a,b,c,time,start,0.1,0,1,0,0)
end
stitchprbs(0.05,0)
```

15.8.8 multiprbs.m

```
%%multiprbs - Andrew Fairweather 29th May 2014
%% this uses evalprbs 2 to process a batch of results and plot
the graphs
%% it is written for a frequency changing prbs with no header
% a is discharge current +ve
% b is prbs terminal voltage
% c is charge current    -ve
% range selects the samples for HF or LF results (1=HF)
% evaluate does the impedance fftss and calcs if selected
function
result=multiprbs(a,b,c,time,start,ylim,range,bipolar,charge,dis
charge);
ylim1=0.05
ylim2=0.05
ylim3=0.05
ylim4=0.05
ylim5=0.05
ylim6=0.05
ylim7=0.05
ylim8=0.05
indplt1=3
indplt2=3
global indplt1 indplt2 pltnum graphnum
v=b;
N=63;
graphnum=1
winder=0
if range
 samp1=2501
 samp2=626.2
 samp3=196.44
 samp4=100.1
 samp5=46.39
 samp6=23.2
 samp7=18.08+0.66
 samp8=2.6
else
 samp1=2501*8
 samp2=625*16
 samp3=5000
 samp4=2500
 samp5=1250
 samp6=625
 samp7=312.5
 samp8=156.25/50
end

%starts
s1=start
s2=s1+(N*samp1)
s3=s2+(N*samp2)
s4=s3+(N*samp3)
s5=s4+(N*samp4)
s6=s5+(N*samp5)
s7=s6+(N*samp6)
```

```
s8=s7+(N*samp7)

%finishes
f1=s2
f2=s3
f3=s4
f4=s5
f5=s6
f6=s7
f7=s8
f8=s8+(N*samp8)

dischargei=a*20;
chargei=c*30.77;
bipolar_i=-1*(dischargei+chargei);
pltnum=1;
figure
subplot(indplt1,indplt2,pltnum),plot(time,v)
grid
pltnum=pltnum+1;
subplot(indplt1,indplt2,pltnum),plot(time,bipolar_i)
grid
pltnum=pltnum+1;
%fourseq(time,dischargei,0,start,2501,63,0)
fourseq(time,dischargei,0,start,samp1,63,0)
%pltnum=pltnum+1;
fourseq(time,chargei,0,start,samp1,63,0)
%pltnum=pltnum+1;
fourseq(time,bipolar_i,0,start,samp1,63,0)

pltnum=pltnum+1;

if bipolar
 evalprbs2(v,bipolar_i,time,ylim1,s1,samp1,N,winder);
 legend('bipolar PRBS')
 evalprbs2(v,bipolar_i,time,ylim2,s2,samp2,N,winder);
 legend('bipolar PRBS')
 evalprbs2(v,bipolar_i,time,ylim3,s3,samp3,N,winder);
 legend('bipolar PRBS')
 evalprbs2(v,bipolar_i,time,ylim4,s4,samp4,N,winder);
 legend('bipolar PRBS')
 evalprbs2(v,bipolar_i,time,ylim5,s5,samp5,N,winder);
 legend('bipolar PRBS')
 evalprbs2(v,bipolar_i,time,ylim6,s6,samp6,N,winder);
 legend('bipolar PRBS')
 evalprbs2(v,bipolar_i,time,ylim7,s7,samp7,N,winder);
 legend('bipolar PRBS')
 evalprbs2(v,bipolar_i,time,ylim8,s8,samp8,N,winder);
 legend('bipolar PRBS')
 %%%fft full results
%evalprbs2(v,bipolar_i,time,1,s1,(f8/N),N,winder);
 f8
else
end

if charge
 evalprbs2(v,chargei,time,1,s1,samp1,N,winder);
 evalprbs2(v,chargei,time,ylim,s2,samp2,N,winder);
 evalprbs2(v,chargei,time,ylim,s3,samp3,N,winder);
```

```
  evalprbs2(v,chargei,time,ylim,s4,samp4,N,winder);
  evalprbs2(v,chargei,time,ylim,s5,samp5,N,winder);
  evalprbs2(v,chargei,time,ylim,s6,samp6,N,winder);
  evalprbs2(v,chargei,time,ylim,s7,samp7,N,winder);
  evalprbs2(v,chargei,time,ylim,s8,samp8,N,winder);
 else
 end

if discharge
  evalprbs2(v,dischargei,time,1,s1,samp1,N,winder);
  evalprbs2(v,dischargei,time,ylim,s2,samp2,N,winder);
  evalprbs2(v,dischargei,time,ylim,s3,samp3,N,winder);
  evalprbs2(v,dischargei,time,ylim,s4,samp4,N,winder);
  evalprbs2(v,dischargei,time,ylim,s5,samp5,N,winder);
  evalprbs2(v,dischargei,time,ylim,s6,samp6,N,winder);
  evalprbs2(v,dischargei,time,ylim,s7,samp7,N,winder);
  evalprbs2(v,dischargei,time,ylim,s8,samp8,N,winder);
  else
  end
```

15.8.9 evalprbs2.m

```
%% evalprbs1 - Andrew Fairweather 17th July 2009
%% evalprbs2 - 2010 - 2014 modified to process later test data
%% 2014 called by multi PRBS
%% this routine evaluates the results of imported data from a
PRBS battery
%% experiment - data starts are pre defined in the test data
%% workspace

function result=evalprbs2(V,I,time,ylim,start,sample,N,winder);
%close all;
finish=((N*sample)+start)
xlim=(1/sample)*10000;
global graphnum
iin=I(start:finish)*1; %% scaling for LEM 50mV/Amp
vout=V(start:finish);
tout=time(start:finish);
vin=iin;
tin=time(start:finish);
[infft]=four(tin,vin,winder);
[outfft]=four(tout,vout,winder);
incomp=infft(2,:).*(cos(infft(3,:))+i*sin(infft(3,:)));
outcomp=outfft(2,:).*(cos(outfft(3,:))+i*sin(outfft(3,:)));
tfcomp=outcomp./incomp;

xxxx=(infft(1,:)/2/pi);
yyyy=(abs(tfcomp));
infftmag=infft(2,:);
outfftmag=outfft(2,:);
ifreqw=infft(1,:);
ifr=ifreqw/2/pi;
ofreqw=outfft(1,:);
ofr=ofreqw/2/pi;

figure
subplot(6,2,1),plot(vin)
grid
subplot(6,2,2),plot(vout)
grid
subplot(6,2,3),semilogx(ifr,infftmag)
grid
subplot(6,2,4),semilogx(ofr,outfftmag)
grid
subplot(6,2,5),semilogx(xxxx,yyyy);
axis([0,xlim,0,ylim]);
grid;
title([' start ' num2str(start) ' Sample size ' num2str(sample)
]);
xlabel('Hz');
ylabel('Z');
tightfig


%% this bit stores the variables for use in plotting the
%% graphs
```

```
%% graphnum is a counter which increments each time the
%% evalprbs is called

global xout1 xout2 xout3 xout4 xout5 xout6 xout7 xout8
global yout1 yout2 yout3 yout4 yout5 yout6 yout7 yout8
if graphnum==1
xout1=xxxx
yout1=yyyy
else
end
if graphnum==2
xout2=xxxx
yout2=yyyy
else
end
if graphnum==3
xout3=xxxx
yout3=yyyy
else
end
if graphnum==4
xout4=xxxx
yout4=yyyy
else
end
if graphnum==5
xout5=xxxx
yout5=yyyy
else
end
if graphnum==6
xout6=xxxx
yout6=yyyy
else
end
if graphnum==7
xout7=xxxx
yout7=yyyy
else
end
if graphnum==8
xout8=xxxx
yout8=yyyy
else
en
graphnum=graphnum+1
```

15.8.10 curve_fit.m

```
%%%%%%%%%%%%%%%%%%%%%%
% Filename curve_fit.m
% Loads a previously saved impedance response
% then compares to the chosen model
% with parameters chosen by the user
% to provide an iterative curve fit
% by inspection

%Models
%1 = Randles
%2 = Parallel model developed during Ultrabattery work
%3 = Parallel branch model with Ri outside of the parallel
branch

%notes added 16/05/2015 reference Thesis chapters and models
used
%Chapter 5  - Model 1 (no specific curve fits used in text)
%Chapter 6  - Model 2 (with Ri = Rec + Rint OR Ri = Red + Rint)
%Chapter 7  - Model 2 (with Ri = Rec + Rint OR Ri = Red + Rint)
%Chapter 8  - Model 3 (with Ri = Re + Ri)
%Chapter 9  - Model 3 (with Ri = Re + Ri)
%Chapter 10 - Model 2 (with Ri = Rec + Rint OR Ri = Red + Rint)
%Chapter 11 - Model 3 (with Ri = Re + Ri)



impplot = input('Input filename of impedance plot ');
modelno = input('Which model to use?  1=Randles, 2=Parallel
model (Ultrabattery), 3=Parallel branch model ')
modelparams=input('Input model parameters in brackets separated
by a space in order Ri,Rt,Cs,Rd,Cb,Cparallel,Rparallel ');
% use a zero for Cparallel, Rparallel if not used
%C1=Cparallel;
%R1=Rparallel;

Ri=modelparams(1)
Rt=modelparams(2)
Cs=modelparams(3)
Rd=modelparams(4)
Cb=modelparams(5)
C1=modelparams(6)
R1=modelparams(7)
%example array = [5e-3 6e-3 15 5000 88400 1 5e-3]
%example array = [5e-3 5e-3 15 5000 88000 0.1e-6 5e-3]

H = HGLOAD(impplot)

hold on% allow figure to overlay on impedance plot

f=logspace(-6,4,500);
for ind=1:500

    if modelno==1
```

```
%    Randles
     s=2*pi*f(ind)*i;
     Xs=1/(s*Cs);
     Zs=1/(1/Rt+1/Xs);
     Xb=1/(s*Cb);
     Zb=1/(1/Rd+1/Xb);
     Z(ind)=Ri+Zs+Zb;
     else
end

     if modelno==2
%  Ultrabattery model

     s=2*pi*f(ind)*i;
     Xs=1/(s*Cs);
     Zs=1/(1/Rt+1/Xs);
     Xb=1/(s*Cb);
     Zb=1/(1/Rd+1/Xb);
     Zr=Ri+Zs+Zb;
 %parallel branch
     Xc1=1/(s*C1);
     Zp=R1+Xc1;

     Z(ind)=(Zp*Zr/Zp+Zr);
     else
end

  if modelno==3
     %additional series network between cbulk and csurface
     %zx is the impedance of c1 and r1 in the new network

     s=2*pi*f(ind)*i;
     Xs=1/(s*Cs);
     Zs=1/(1/Rt+1/Xs);
     Xb=1/(s*Cb);
     Zb=1/(1/Rd+1/Xb);
     %addition of parallel cx rx
     Xc1=1/(s*C1);
     Zp=R1+Xc1;


     Zr1=Zs+Zb
     Zt=Ri+(Zr1*Zp)/(Zr1+Zp);

    % Z(ind)=Zt;
     Z(ind)=Ri+(Zr1*Zp)/(Zr1+Zp);
     else
end
end
```

15.9 Embedded PRBS code

15.9.1 prbs3.c

```
//*****************************************************************************
//          PRBS gen with frequency change
//          Hardware: Microchip DSpic explorer 16 development board
//          Andrew Fairweather
//              26/02/2010
//*****************************************************************************
//*****************************************************************************

//modified to run with /8 prescale in timer 1 init allowing lower frequency PRBS
// multi prbs3.c - modified to remove header
// multi prbs4.c - comments added for clarity
//#include <p30f6014.h> //processor include
#include <p33FJ256GP710.h>
#include "lcd.h"
#include "common.h"

_FOSCSEL(FNOSC_PRIPLL);
_FOSC(FCKSM_CSDCMD & OSCIOFNC_OFF & POSCMD_XT);
_FWDT(FWDTEN_OFF);


//  program start
int main(void)

{

//****** initialise and setup port **********


int loop_1;
int n;
int nn;
int nnn;
int nnnn;
int seq_len;
int freq;
int tt;



int a;
int b;
int c;
int d;
int e;
int f;
int g;
int h;
int switch_flag1;
int switch_flag2;
int debounce;
int z;

a=0x0001;
b=0x0001;
c=0x0001;
d=0x0001;
e=0x0001;
f=0x0001;
g=0x0001;
h=0x0001;

z = 0;
rtc_lcd_update = 0;
timer_2_flg = 0;
switch_flag1=0;
```

```
switch_flag2=0;


//PRBS Arrays

//*****************************4 bit PRBS array*********************************
//  unsigned char
prbs out 1[15]={1,1,1,0,1,1,0,0,1,0,1,0,0,0,0};

//*****************************6 bit sequence with 16 bit header*****************
//  unsigned char
prbs_out_1[80]={1,1,1,1,1,1,1,1,1,1,1,1,1,1,1,1,0,0,1,0,1,1,1,0,0,0,1,1,0,1,1,0,1,0,0
,1,0,0,0,1,0,0,1,1,0,0,1,0,1,0,1,0,0,0,0,0,0,1,1,1,1,1,0,1,1,1,1,0,0,1,1,1,0,1,0,1,1,
0,0,0};//1 bit added because the seqence terminates early


//*************************6 bit sequence with no header (Bipolar)*****************
    unsigned char
prbs_out_1[64]={0,0,1,0,1,1,1,0,0,0,1,1,0,1,1,0,1,0,0,1,0,0,0,1,0,0,1,1,0,0,1,0,1,0,1
,0,0,0,0,0,0,1,1,1,1,1,0,1,1,1,1,0,0,1,1,1,0,1,0,1,1,0,0,0};//1 bit added because the
seqence terminates early


    //TRISD=0x00;   //set the port as outputs
    loop_1=10;
//  seq len=80;                                         //actual sequence is 15 but loop
adds 1
    seq_len=64;                                         //actual sequence is 15 but loop
adds 1

    n=1;
    nn=1;
    nnn=1;
    nnnn=1;
    freq=0;
    debounce=0;


    TRISA=0x00; //set the port as outputs
    TRISD=0XFF; //set port D as inputs
    PORTA=0x00;                                         // clear port B

    //PORTAbits.RA6=1;
    Init_Timer1();
    Init_Timer2();

    while(1)                                            //run forever
        {


//Switch1 code
*************************************************************************
    if (PORTDbits.RD6==0)
        {
        PR1= 0x0800;
        PORTA=0x00;
        }
        else
        {
        }

            if (PORTDbits.RD7==1)      //switch code (PRBS mode set, HF/LF)

            {

                    if (PORTDbits.RD7&&switch_flag1==1)
                    {
                    switch_flag1=0;
                //  debounce=0;
                    }
                    else
                    {
                    switch_flag1=1;
                    //debounce=0;
                    }
```

```
                    }
                    else

              if (switch_flag1==1)
              {
              PORTAbits.RA2=1;
              }
              else
              {
              PORTAbits.RA2=0;
              }

//Switch2 code
*************************************************************************

              if (PORTDbits.RD6==1)                    //switch code (ON/OFF)

              {
                  if (PORTDbits.RD6&&switch_flag2==1)
                    {
                    switch_flag2=0;
                    }
                    else
                    {
                    switch_flag2=1;
                    }
                    }
                    else

              if (switch_flag2==1)
              {
              //PORTAbits.RA3=1;
              }
              else
              {
              //PORTAbits.RA3=0;
              }
//*************************************************************************************
**

//Frequency select
*********************************************************************

//if (switch flag1)
//if (z)
if (PORTDbits.RD7)
        {
        PORTAbits.RA3=1;
        PORTAbits.RA4=0;
        a=0x4000;
        b=0x2000;
        c=0x1000;
        d=0x0800;
        e=0x0400;
        f=0x0200;
        g=0x0100;
        h=0x0001;
        }
        else
        {
        PORTAbits.RA4=1;
        PORTAbits.RA3=0;
        a=0x0800;
        b=0x0200;
        c=0x00A0;
        d=0x0051;
        e=0x0025;
        f=0x0012;
        g=0x00E;
        h=0x0001;
        }
```

```
//PRBS section
**********************************************************************
        if (rtc_lcd_update)
                {


                {
                if (PORTAbits.RA1==1)                   //clock indicator
                {
                PORTAbits.RA1=0;
                }
                else
                {
                PORTAbits.RA1=1;
                }
                }
            {
            PORTAbits.RA0=prbs_out_1[n];
        //  PORTA=prbs out 1[n];                        //porta loaded with variable
n from array
             n++;
            }
        rtc_lcd_update = 0;
        timer_2_flg =0;
        }
        if (n==seq_len)
        {
    //  PORTA=0;
        n=1;
        nn=1;
        nnn=1;
        nnnn=1;


        if (PR1==h)
        PR1 = a;
        else if(PR1==a)
        PR1 = b;
        else if(PR1==b)
        PR1 = c;
        else if(PR1==c)
        PR1= d;
        else if(PR1==d)
        PR1= e;
        else if(PR1==e)
        PR1= f;
        else if(PR1==f)
        PR1= g;
        else if (PR1==g)
        PR1= h;
        }
        }
}
```